Computational Approximation of Mesoscale Field Dislocation Mechanics at Finite Deformation

Submitted in partial fulfillment of the requirements for

the degree of

Doctor of Philosophy

in

Computational Mechanics

Rajat Arora

B. Tech., Mechanical Engineering, Indian Institute of Technology Kanpur
M. Tech., Mechanical Engineering, Indian Institute of Technology Kanpur
M.S., Computational Mechanics, Carnegie Mellon University

Carnegie Mellon University
Pittsburgh, PA

May, 2019

This page intentionally left blank.

Keywords: Dislocation, Finite deformation, Patterning, Size effect, Strain gradient plasticity, Mechanics, Inelasticity, Nonlinear elasticity, Large strains.

This page intentionally left blank.

Dedicated to

my father

Mr. Vinod Arora

and my mother

Mrs. Poonam Arora

This page intentionally left blank.

Acknowledgments

I would like to take this opportunity to thank people whole helped me in my research, leading to submission of this thesis. Foremost, I would like to express my sincere thanks and gratitude to my thesis advisor Prof. Amit Acharya for his continuous support and encouragement. I am grateful for his guidance and advice throughout the work and for providing me enough opportunities and proper environment to explore the fascinating subject of Continuum Mechanics. I also want to thank my committee members Prof. Robert Suter, Prof. Jacobo Bielak, Prof. Rahul Panat, and Prof. Matteo Pozzi for their time and suggestions on this thesis. I am grateful to Prof. Jorge Vinãls for providing access to computational resources at Minnesota Supercomputing Institute (MSI). I also thank Dr. Xiaohan Zhang for his time and discussions, especially during the early phase of the work.

My deepest thanks goes to my family, especially my parents, my brother Rohit, and my wife Shipra for the continuous support and encouragement, without which this wouldn't have been possible. I shall remain forever indebted to them. They were, and are, always the source of inspiration and motivation for me.

I am thankful to all my friends - Sabyasachi, Esteban, Chiqun, Xiaohan, Ankit, Utsav, Afreen, Sneha, Pratik, Vaibhav, Arnab, and Kshiteej for their help and moral support which made my stay at CMU enjoyable and memorable. There have been times when I have been disheartened by failures, but it was these friends who always managed to bring a smile back on my face and kept me going.

My special thanks go to Maxine Leffard for her effort in making my graduate life in CEE

rich and wonderful. The funding of Dean's Fellowship provided by Civil and Environmental Engineering Department is highly appreciated.

I acknowledge support from Army Research Office grant number ARO-W911NF-15-1-0239. This work used also the Extreme Science and Engineering Discovery Environment (XSEDE) [TCD+14], through generous XRAC grants of supercomputing resources, which is supported by National Science Foundation grant number ACI-1548562. The computing resources provided by the Pittsburgh Supercomputing Center [NLRS15], and the Minnesota Supercomputing Institute (URL: http://www.msi.umn.edu) are gratefully acknowledged.

Abstract

This work involves the modeling and understanding of mechanical behavior of crystalline materials using finite deformation Mesoscale Field Dislocation Mechanics (MFDM). MFDM is a Partial Differential Equation (pde) based model to understand meso-macroscale plasticity in solids as it arises from dislocation motion, interaction, and nucleation within the material. Specifically, the work is divided into the following two parts:

- The first part of the work deals with the development of a novel, parallel computational framework for finite deformation MFDM. Beyond the development, implementation, and verification of novel algorithms for the stated purpose, the computational framework involves the use of various state-of-the-art open source libraries such as Deal.ii, PetSc, P4est, MUMPS, ParMetis, and MPI. This accomplishment stands as a first computational implementation of a partial differential equation based model of the mechanics of dislocations at finite deformations in the whole literature, including time-dependent behavior.

- The second part involves the verification and qualitative validation of the developed MFDM framework by applying it to study problems of significant scientific and technological interest. We compare the stress fields obtained from finite deformation FDM with the small deformation analytical result for fields of screw and edge dislocations embedded in an infinite medium. The code is also verified against the sharply contrasting predictions of geometrically linear and nonlinear theories for the stress field of a spatially homogeneous dislocation distribution in the body. This ability to calculate stress

fields for an arbitrary distribution of dislocation density in the geometrically nonlinear setting is then used to quantify the change in volume of the body upon introduction of dislocations, and to study the stress-field path followed in a body corresponding to the presence of a sequence of dislocation configurations comprising a single dislocation to a stress-free dislocation wall (or a grain boundary). Stringent verification tests of the time-dependent numerics are also undertaken such as i) studying the evolution of a prescribed dislocation density in the absence of a flux of dislocations ii) accurately reproducing classical hyperelastic response, including the prediction of no hysteresis in a loading-unloading cycle, all up to finite ($\approx 100\%$) strains. The model is also used to predict size effects, dislocation patterning, and the occurrence of stressed dislocation microstructures both under applied loads and in unloaded bodies using crystal and J_2 plasticity MFDM. Finally, we demonstrate the potential of the computational tool by modeling the longitudinal propagation of localized bands of plastic deformation in metals, in particular, shear bands.

This research presents results of a first computational framework of (mesoscale) plasticity of unrestricted geometric and material nonlinearities with the following features:

1. Computation of finite deformation stress fields of arbitrary (evolving) dislocation distributions in finite bodies of arbitrary shape and elastic anisotropy, under general statically admissible traction boundary conditions;

2. Prediction of size effect and stressed dislocation pattern formation including dipolar dislocation walls under load;

3. Prediction of stress-free dislocation microstructures and unloaded stressed metastable dislocation microstructures;

4. Modeling of longitudinal propagation of plastic wavefront as a fundamental kinematical feature of plastic flow;

5. No involvement of a multiplicative decomposition of the deformation gradient, a plastic distortion tensor, or a choice of a reference configuration to describe the micromechanics of plasticity arising from dislocation motion and predicts plastic spin with isotropic J_2 plasticity assumptions.

This page intentionally left blank.

Contents

List of Figures

This page intentionally left blank.

List of Tables

This page intentionally left blank.

Chapter 1

Motivation and outline

This chapter presents a brief introduction and the motivation for undertaking the present research. Section 1.2 reviews the notation and terminology used in the document. The outline of the document and a brief summary of each chapter are discussed in Sec. 1.3.

1.1 Introduction

Plastic deformation in many metals takes place due to the motion of dislocations under applied stresses. It can be shown on dimensional grounds that no material length scale enters the equations of conventional plasticity theories. Therefore, predictions of the elasto plastic response of homogeneous bodies based on any conventional theory is size independent. However, it is now well-established in the literature, e.g. [FMAH94, LHT+12, SWBM93, EA66, MC95, SE98], that metals exhibit strong size effects at micron to submicron length scales. For example, there is a strong size effect in the measured indentation hardness of single crystals when the indenter size goes below 10 microns [MC95, SWBM93]. It was observed [EA66, KN63] that for a given volume fraction of hard particles, the strengthening of the metal is greater for smaller particle size. Another example is that under torsional loading of copper wires the scaled shear strength, as a function of average shear strain, has been shown to increase by a factor of around 3 as the wire diameter goes down from 100 microns to 10 microns [FMAH94, LHT+12]. However, these wires showed negligible size effect under tensile load. These examples demonstrate that the size effect strongly depends on the gradients of plastic strain.

The underlying idea is that the material flow strength is dependent upon the total stored dislocation density. Dislocations are stored for two reasons:

1. When a single crystal is strained uniformly, dislocations mostly accumulate by random trapping. They are referred to as statistically stored dislocations or geometrically redundant dislocations [Ash70]. There is no simple theory to predict the density of SSDs but they have been investigated experimentally by various researchers like [BB66]

and the references therein.

2. When the crystal is subjected to any gradient of (inverse) elastic distortion that gives a non-zero curl, the dislocations that are stored in the body are referred to as geometrically necessary dislocations (GNDs). The density of GNDs can be estimated from the curl of the (inverse) elastic distortion tensor, which can be experimentally measured.

Direct support for the notion that GNDs lead to enhanced hardening comes from the experiments performed in [RA70]. Therefore, when the characteristic length scale of deformation is large, strain gradients are small resulting in small density of GNDs and conventional theories suffice to model material response. However, as the length scale associated with deformation becomes smaller, it becomes necessary to incorporate strain gradients for an accurate prediction of the mechanical response of the material.

Dislocations in the material are also found to arrange themselves in different patterns, e.g. cells [MW76], labyrinths [JW84], or walls [Mur89]. The presence of this dislocation microstructure along with cell size and its orientation can have a strong influence on the macroscopic response of materials. An example is the formation of subgrain boundaries in high temperature nickel alloys, which triggers recrystallization and causes microstructural degradation, leading to decrease in the life of turbine blades [HH12, Ree06]. The ability to synthesize new materials with desired microstructure distribution using laser powder-bed-fusion technique for additive manufacturing enables such materials to exhibit a combination of yield strength and tensile ductility which surpasses those of conventional materials [WVM+18].

It is currently impossible to model elastic-plastic material response and microstructure development at realistic time scales and mesoscopic length scales with Discrete Dislocation Dynamics and Molecular Dynamics due to computational expense. Conventional elasto-plastic theory does not explicitly account for the motion of GNDs in the domain along with corresponding boundary conditions and therefore cannot predict realistic microstructure. Hence, developing a continuum scale model that can overcome the limitations of conventional

theories, which include modeling size effects and predicting microstructure development in the material is an actively pursued research area. This research elaborates on the development of one such model by developing a mechanics based, novel parallel computational tool to make finite element method based computational predictions of finite deformation dislocation plasticity. This framework has the ability to model the properties of materials with complicated microstructural features, thereby providing a tool to help in the design of new state-of-the-art materials developed using additive manufacturing [WVM+18].

1.2 Notation and terminology

Vectors and tensors are represented by bold face lower and upper-case letters, respectively. The action of a second order tensor $\boldsymbol{A}$ on a vector $\boldsymbol{b}$ is denoted by $\boldsymbol{Ab}$. The inner product of two vectors is denoted by $\boldsymbol{a} \cdot \boldsymbol{b}$ and the inner product of two second order tensors is denoted by $\boldsymbol{A} : \boldsymbol{B}$. A superposed dot denotes a material time derivative. A rectangular Cartesian coordinate system is invoked for ambient space and all (vector) tensor components are expressed with respect to the basis of this coordinate system. $(\cdot)_{,i}$ denotes the partial derivative of the quantity $(\cdot)$ w.r.t. the x_i coordinate direction of this coordinate system. $\boldsymbol{e}_i$ denotes the unit vector in the x_i direction. Einstein's summation convention is always implied unless mentioned otherwise. All indices span the range 1-3 unless stated otherwise. The condition that any quantity (scalar, vector, or tensor) a is defined to be b is indicated by the statement $a := b$ (or $b =: a$). The symbol $|(\cdot)|$ represents the magnitude of the quantity $(\cdot)$. E, μ, and ν will always denote the Young's Modulus, Shear Modulus, and Poisson's ratio of the material under consideration, respectively. $det(\boldsymbol{A})$ denotes the determinant of the second order tensor $\boldsymbol{A}$.

The current configuration and its external boundary is denoted by Ω and $\partial\Omega$, respectively. $\boldsymbol{n}$ denotes the unit outward normal field on $\partial\Omega$. The symbols $grad$, div, and $curl$ denote the gradient, divergence, and curl on the current configuration. For a second order tensor

$\boldsymbol{A}$, vectors $\boldsymbol{v}$, $\boldsymbol{a}$, and $\boldsymbol{c}$, and a spatially constant vector field $\boldsymbol{b}$, the operations of div, $curl$, and cross product of a tensor ($\times$) with a vector are defined as follows:

$$
\begin{aligned}
(div\boldsymbol{A}) \cdot \boldsymbol{b} &= div(\boldsymbol{A}^T\boldsymbol{b}), \qquad \forall\ \boldsymbol{b} \\
\boldsymbol{b} \cdot (curl\boldsymbol{A})\boldsymbol{c} &= \left[curl(\boldsymbol{A}^T\boldsymbol{b})\right] \cdot \boldsymbol{c}, \quad \forall\ \boldsymbol{b}, \boldsymbol{c} \\
\boldsymbol{c} \cdot (\boldsymbol{A} \times \boldsymbol{v})\boldsymbol{a} &= \left[(\boldsymbol{A}^T\boldsymbol{c}) \times \boldsymbol{v}\right] \cdot \boldsymbol{a} \quad \forall\ \boldsymbol{a}, \boldsymbol{c}.
\end{aligned}
$$

In rectangular Cartesian coordinates, these are denoted by

$$
\begin{aligned}
(div\boldsymbol{A})_i &= A_{ij,j}, \\
(curl\boldsymbol{A})_{ri} &= \varepsilon_{ijk}A_{rk,j}, \\
(\boldsymbol{A} \times \boldsymbol{v})_{ri} &= \varepsilon_{ijk}A_{rj}v_k,
\end{aligned}
$$

where ε_{ijk} are the components of the third order alternating tensor $\boldsymbol{X}$. The corresponding operations on the reference configuration are denoted by the symbols $Grad$, Div, and $Curl$. $\boldsymbol{I}$ is the second order Identity tensor whose components w.r.t. any orthonormal basis are denoted by δ_{ij}. The vector $\boldsymbol{X}(\boldsymbol{AB})$ is defined by

$$
[\boldsymbol{X}(\boldsymbol{AB})]_i = \varepsilon_{ijk}A_{jr}B_{rk}.
$$

In this document, we qualitatively define *patterning* as the appearance of inhomogeneous distributions of dislocation density, more or less in the entire domain.

1.3 Dissertation outline

This research aims at developing a theoretical-computational continuum framework for modeling dislocation-mediated plastic deformation in ductile materials. Specifically, this document is organized as follows:

- Related literature on implementations of some gradient plasticity models involving dislocation density transport in some form is briefly reviewed in Chapter 2.

- Chapter 3 presents a self-contained introduction to the governing equations of finite deformation (Mesoscale) Field Dislocation Mechanics (M)FDM theory. Constitutive statements for the Cauchy stress $\boldsymbol{T}$, the plastic distortion rate $\boldsymbol{L}^p$, and the dislocation velocity $\boldsymbol{V}$ that are consistent with the requirement of non-negative dissipation are then discussed in Sec. 3.3. The boundary and the initial conditions for the theory are then discussed in Sections 3.4 and 3.5, respectively.

- The details of the finite element discretization of the equations of finite deformation (M)FDM are then presented in Chapter 4. The staggered computational algorithm for the problems within the quasi-static and dynamic (with inertia) settings and the criteria for choosing time increments for discretely evolving the system in time are described in Section 4.2. The details of the developed framework framework are presented in Sec. 4.3. The present parallel implementation has been written chronologically by Dr. X. Zhang [Zha15] and I (R. Arora), utilizing prior work of Dr. S. Puri [Pur09] (related to the purely static elastic case) and a (serial) algorithmic modification incorporating the rate equilibrium equation suggested by Prof. Acharya. I (Arora) am responsible for the development to the current state, including all debugging and verification done to date.

- Chapter 5 presents results for various problems studied using the developed framework. These results include: i) accurately predicting homogeneous hyperelastic response with no hysteresis in an elastic loading-unloading cycle (Sec. 5.1), ii) comparing small deformation analytical stress field solutions for edge and screw dislocations to the finite deformation stress fields (Sec. 5.2) computed from FDM, iii) testing for Burgers vector conservation and evolution of corresponding dislocation density in the absence of any flux of dislocations (Sec. 5.3), iv) calculating stress fields of homogeneous dislocation

distribution (Sec. 5.4) and grain boundary walls (Sec. 5.6) for geometrically linear and nonlinear FDM theories, v) quantifying the change in volume of the body upon introduction of dislocations (Sec. 5.5), and vi) modeling dynamics (with inertia) of dislocations moving with prescribed velocity in the domain (Sec. 5.7). These results are stringent test of numerics that verify the computational framework.

- Chapter 6 studies the effect of the inclusion size on the strength of the material. We present these results for the J_2 plasticity MFDM and demonstrate that for a given volume fraction of inclusions, the material strength is enhanced more for smaller inclusion sizes.

- Chapter 7 presents results for modeling size-effect, and dislocation patterning in materials using crystal plasticity MFDM theory. Sec. 7.1 focuses on the case when multiple slip systems are present in the body. The occurrence of stressed dislocation microstructure both under applied loads and in unloaded bodies is demonstrated. We also study the effect of orientation on the microstructural patterns and the macroscopic stress-strain response of the material. In Sec. 7.2 we look at the microstructural patterning and effect of orientation for the special case when only one slip system is present. Sec. 7.3 briefly discusses the convergence of microstructural patterns and overall stress-strain response with respect to mesh refinement. Sec. 7.4 presents a necessary condition for pattern formation in the model. Finally, Sec. 7.5 focuses on the effect of the length scale l (a material constant) on microstructural patterns.

- Chapter 8 demonstrates modeling longitudinally propagating shear bands in the material under quasi-static loading using FDM and small deformations. A novel scheme is developed in Sec. 8.2 to evolve the plastic distortion field in the domain. The work presented in this chapter was developed jointly with Prof. Acharya.

- Concluding remarks and future work are presented in chapter 9.

Chapter 7 and parts of Chapters 2, 3, and 9 are written jointly with Prof. Acharya for a paper that has been accepted for publication in the International Journal of Solids and Structures.

For the entire work reported in this thesis, all numerical implementations, verifications and validations were carried out by me. All scientific explorations were done by me with guidance, when necessary, from Prof. Amit Acharya.

Chapter 2

Literature review

In this chapter, we briefly review some of the vast literature on strain gradient plasticity theories. An exhaustive review of the subject is beyond the scope of this document.

Given the significance of an accurate prediction of size-effect for industries involved in the manufacturing of small scale electro-mechanical systems, and the need for a continuum scale model that enables a predictive study of dislocation mediated plastic deformation, several extensions of conventional continuum models have been proposed that incorporate one or many in-built length scales [FMAH94], [AB96, AB00a], [Gur02], and [APBB04].

One class of continuum models produce size-effects by modifying the hardening law to take into account hardening due to the presence of incompatibility in elastic distortion [AB00a, BNVdG01, Bas01, ABB03, ATSB04, AB96]. These elastic incompatibilities correspond to 'Geometrically Necessary Dislocations' (GNDs) [Ash70]. The advantage of these 'lower order gradient' theories is that the classical structure of the underlying incremental boundary-value-problem (bvp) remains unchanged, retaining all associated results on the uniqueness of solutions to the bvp of incremental equilibrium for the rate-independent (and rate-dependent) material [AS95] as obtained by Hill [Hil58].

The second class of models incorporates a dependence on length scale (or plastic strain gradients) through measures of the effective plastic strain [FMAH94, FH01, NH03]. Some formulations [KT08, APBB04, GBB06, YGVdG04] may involve additional differential equations for modeling of dislocation density evolution in the domain. These higher-order extensions of the conventional theories formulation may or may not involve higher order stresses and may require additional boundary conditions on appropriate variables.

The key ingredient in theories based on the framework of Gurtin [Gur02, Gur08, GR14] is that the classical force balance is supplemented with a statement of microforce balance based on the belief that working is associated with each kinematical process. The internal energy of the system is augmented with an additional term based on some measure of GNDs and appropriate constitutive equations are postulated for microforce fields that ensure non-negative dissipation.

All the models presented above model plastic flow through constitutive assumptions without explicitly characterizing dislocation motion. The fourth class of models [APBB04, GBB06, YGVdG04] augment the conventional elasto-plastic theories with additional equations that explicitly model dislocation motion and evolution in the domain, resulting in plastic flow. However, none of the formulations mentioned above take into account the stress field of signed dislocation density exactly under finite deformation. We now briefly discuss some of the above mentioned models.

Arsenlis et. al [APBB04] developed a micromechanical model of single crystal plasticity that incorporates a material length scale dependence in its framework. The authors developed a set of pdes for the evolution of slip system dislocation densities, one for each system. This requires constitutive assumptions for dislocation velocity, cut-off radii for annihilation, segment-length interaction matrices for each component and slip system. Although notable is the fact that these evolution equations include SSDs evolution, such a description requiring 4 pdes in 2d for each slip system for modeling dislocation density evolution can become intractable for a full 3D FCC material. The framework is applied to predict size effects in simple shear for thin films using constrained and quasi-free boundary conditions for an idealized crystalline geometry.

Geers et. al [GBB06] present another strain-gradient crystal plasticity theory which does not deviate much from conventional elasto-plastic theory. Additional equations govern the evolution of GNDs and SSDs in the domain and the back stresses due to the presence of dislocations are accounted for by using analytical integral expressions for stress fields in an infinite medium. However, such an approach results in accuracies because of finite medium approximation in the integrals, small deformations integral expression, and invalidity of integral expressions for dislocations near the boundary. Another important point to note is that satisfying equilibrium in the domain with any standard elastic-plastic constitutive statement for the stress accounts for the stress field due to the presence of any dislocations which are consistent with the elastic and the plastic plastic distortion fields. Therefore,

using additional ingredients to model the effect of the back-stress of GNDs in any model is superfluous [Ach08].

Kuroda et. al [KT08] present a finite deformation higher order strain gradient crystal plasticity formulation without introducing higher order stresses. The conventional theory is supplemented by a length scale dependent back-stress which in-turn depends on the gradients of scalar edge and screw GND densities whose evolution is governed by their respective pdes.

A finite strain generalization of the strain gradient plasticity formulation of Fleck et al. [FH01] is proposed and implemented in a finite element framework by Niordson et. al [NR04, NT05]. Numerically, the formulation requires equivalent plastic strain rate to be taken as one of the nodal variables which requires additional boundary conditions to be applied at the boundary separating parts of body loading elastically and plastically, along with boundary conditions in higher order stresses. The model is used to study necking under plane strain tension and compression [NT05], and size effects in plane strain necking of thin sheets [NR04].

[YVdGG04] propose a nonlocal version of crystal plasticity based on the statistical-mechanics description of collective behavior of dislocations [GB99, Gro97] wherein 2 coupled pdes govern the evolution of full scalar dislocation density and GNDs. The model is applied to study the shearing of a model composite material in single slip with constrained boundary conditions [YVdGG04] and bending of a single-crystal strip in plane strain [YVdGG04]. The model and computational implementation is limited to single slip deformations in 2-d problems.

Gurtin [Gur08] develops a finite deformation gradient theory of crystal plasticity involving configurational microforce balances for each slipsystem [Gur02]. A central ingredient of the theory involves inclusion of an additional term based on GND density in the free energy that characterizes work hardening associated with the accumulation of GNDs.

All these models [APBB04, GBB06, KT08, Gur08] suffer from the serious theoretical impediment which involves prescribing conditions on the scalar dislocation densities on the

boundary of grains in a multi/poly-crystal as slip system dislocation densities in different grains have different physical meanings due to the change in lattice orientation between grains.

Wang et. al [RVdVG14] presented stress field of dislocations using Toupin's gradient elasticity theory [Tou62] at finite strains wherein the defects are represented by force dipole distributions. The theory involves 4th order derivatives of displacement and therefore requires the use of Isogeometric analysis [HCB05, CHB09] for its implementation. The representation of a complex network of line defects can be onerous by dipole forces. Moreover, it is not very straightforward to postulate evolution of defects coupled to the underlying stress field, given its representation in the form of dipole forces.

A hybrid method to model dislocation core widths and their mutual interactions under quasi-static and dynamics loadings was developed in [Den04, Den07]. The approach involves a combination of Pierls-Nabarro model and Galerkin methods. However, finite deformation frameworks for these approaches have not been demonstrated.

Not only does the presence of dislocations cause additional work hardening in the material, they have also been observed to develop intricate dislocation structures such as dislocation cells [MW76, MAH79, MHS81, HH00] and labyrinths [JW84], often with dipolar dislocation walls, and mosaics [TCDH95]. These microstructures appear at mesoscopic length scales in between the atomic and macroscopic scales. It is also one of the fundamental challenges of theories and models of plasticity to predict such microstructure, with the attendant, often large, deformation and internal stress fields.

Different approaches have been used in the literature to model the development of dislocation microstructures such as [OR99, LS06, CCPS10, XEA15], and other references mentioned therein. In the work of Ortiz and Repetto [OR99], dislocation structures at finite deformation have been shown to be compatible with deformation fields that are minimizers of a pseudoelastic energy functional for a discrete time step of a rate independent crystal plasticity formulation. The predicted dislocation microstructures are necessarily stress-free

by construction with non-dipolar walls (i.e., walls with non-zero net Burgers vector), and are accompanied by slip-band deformation microstructures. A key ingredient for obtaining both the deformation and dislocation microstructures is the non-convex nature of the incremental energy functional, which in turn is the outcome of the use of strong latent hardening promoting local single-slip in their model.

Sethna and co-workers [LS06, CCPS10] demonstrate (non-dipolar) dislocation walls with and without the presence of dislocation climb, showing the formation of self-similar dislocation microstructure starting from smooth random initial conditions. Their model is 'minimal' in nature, involving geometrically linear kinematics for the displacement field, and a transport equation for the Nye tensor density [Nye53] field arising from a conservation statement for the Burgers vector. On the other hand, Xia and El-Azab [XEA15] demonstrate dislocation microstructure as an outcome of a model that assumes geometrically linear kinematics for the total deformation coupled to a system of stress-dependent, nonlinear transport equations for vector-valued slip-system dislocation densities. These slip system density transport equations involve complicated constitutive assumptions related to cross-slip, and the authors promote the point of view that dislocation patterning is necessarily related to the modeling of dislocation density transport at the level of slip system densities and the modeling of cross-slip.

In closing this brief review of related approaches we mention the Continuum Dislocation Dynamics framework of Hochrainer and collaborators; [HZG07, Hoc16, SZ15] are some representative works. These models are developed based on a kinetic theory like framework, starting from the assumption that a fundamental statement for the evolution of a number density function on the space of dislocation segment positions and orientations is available (which is in itself a non-closed statement even if one knows completely the rules of physical evolution of individual dislocations segments of connected lines). Also, what a *number* density of dislocations is supposed to mean for a tangled web of dislocation curves in a 3-d volume is not clarified. On making various assumptions for tractability, the theory

produces (non-closed) statements of evolution for the averaged dislocation density (akin to the mesoscale Nye tensor field), the total dislocation density (similar to an appropriate sum of the averaged Nye tensor density and the Statistical density) and, these densities being defined as physical scalars, an associated curvature density field. Closure assumptions are made to cut off infinite hierarchies, which is standard for averaging based on nonlinear 'microscopic equations', and further closure assumptions for constitutive statements are made based on standard thermodynamic arguments [Hoc16]. The basic framework does not account for exact geometrically nonlinear continuum mechanics of deformation and stresses appropriate for large deformation plasticity. The models have been primarily exercised in situations involving a single slip plane. The work in [SZ15] demonstrates some 'patterning' in a simplified 2-d setting where total density concentrates (by approximately 4 times) in 'blobs' (terminology of the authors) covering most of the domain, with low densities restricted to narrow 'walls', which is an inversion of what is observed in dislocation cells where high dipolar densities concentrate in narrow walls, with low densities (by orders of magnitude) arising in cell interiors.

We also note the finite deformation discrete dislocation plasticity formulation presented in the works of [DNVdG03, IRD15]. The latter work attempts to address the violation of the hypoelastic constitutive equation for stress of the dislocation fields in the computational implementation of the model proposed in [DNVdG03]. Both formulations rely heavily on the superposition of linear elastic stress fields of individual dislocations (which seems counter-intuitive in the nonlinear setting, even for small elastic strain). Unfortunately, we have found the formulation in [IRD15] to be not entirely transparent, thus hindering our understanding of the basic theory that is computationally implemented (compounded with typographical errors, e.g. equations (16) and (17) therein that are important to understanding the computation of their F^e tensor). For example, to what extent a constitutive statement like equation (32a) therein is an appropriate representation of frame-indifferent hyperelastic response, and better than the criticism leveled by the authors against the use of the (Jaumann rate-based)

hypoelastic stress response proposed in [DNVdG03], is not clear to us. Clearly, the form of the strain measure utilized in equation (32a) suggests the use of linearised elasticity out of the current configuration, and then why the classical elastic solutions for dislocations from linear elasticity should be correct for linearised elasticity out of a configuration with *stress* is not clarified - as is well-understood, the equations for linear elasticity and linearised elasticity differ when the configuration on which the problems are solved is under stress, leading to important nonlinear geometric effects like buckling instabilities.

Despite the success of conventional and strain gradient plasticity theories, a field theory that allows for the calculation of stress fields of evolutionary 3-d dislocation distribution in finite bodies under unrestricted geometric and material nonlinearity is still elusive. Moreover, rigorous homogenization of such a fine-scale model can result in a physically and kinematically faithful mesoscopic model of inelasticity tied to fundamental defect motion physics, with a desirable consistency property that when the spatial averaging length scale tends to zero, the model reduces to a theory of the collective behavior of individual dislocations. Such a mesocopic model will overcome the limitations of the conventional theories by enabling a gamut of relevant predictions like modeling size-effects, dislocation patterning, or longitudinal shear band propagation, all at finite deformation. The goal of the present research is to bridge the above gap (but without any rigorous homogenization) and present a first mesoscale model of J_2 and crystal plasticity theories with unrestricted geometric and material nonlinearities. The capabilities of such a model are demonstrated.

This work presents a broad numerical framework based on the Field Dislocation Mechanics (FDM) theory [Ach01, Ach03, Ach04]. Built on the pioneering works of Kroner [Krö81], Willis [Wil67], Mura [Mur63], and Fox [Fox66], FDM is an extension of conventional plasticity that takes into account exactly the finite deformation stress fields of dislocations and their spatio-temporal evolution, for solving general boundary value problems in finite strain dislocation based mechanics at microscopic scales. As for kinetics, the theory has Nye's dislocation density tensor [Nye53] as one of its field variables and its transport equation

is derived from the conservation of Burgers vector in a crystal with evolving dislocations. The driving force for the evolution of dislocation density is an analogue the Peach-Koehler force of classical dislocation theory [Ach04]. The equation has been shown to model salient features of dislocation transport like annihilation of dislocations, expansion of a polygonal dislocation loop and simulation of a Frank-Read source [VBAF06]. A geometrically linear version of the theory has been numerically implemented in [RA05] and is shown to successfully calculate stress fields of individual dislocations and loops, formation of slip steps upon exit of dislocations, and development of inhomogeneity from homogeneous initial and boundary conditions corresponding to homogeneous deformation in conventional plasticity [RA05].

FDM is a model that roots in the representation of defects in the lattice at the atomic scale. The theory is applicable to dislocation related phenomena in crystalline solids that appear well resolved at length scales of $10a - 10^3a$, where a is the lattice spacing in the crystal. Therefore, for the theory to be applicable to macroscopic scales, a standard space-time averaging scheme utilized in the study of multiphase flow [Bab97] was used and the resulting framework was termed as Mesoscale Field Dislocation Mechanics (MFDM) [AR06]. This averaging procedure does not provide closure equations and the resulting structure can be interpreted, for operational purposes, as the equations of FDM augmented by an extra term that takes into account the the plastic strain rates due to unresolved dislocations SSDs which is accounted for phenomenologically. Despite the phenomenology, the averaging procedure and the fine-scale theory involved impart to the coarse model a rich structure that enables a gamut of relevant predictions, with only two extra material parameters over and above conventional macroscopic continuum plasticity. It can be shown on dimensional grounds that MFDM (and FDM) has an in-built length scales.

A geometrically linear version of MFDM was numerically implemented in a finite element framework in [RA06] where it was shown to successfully model size-effect in materials, dependence of stress-strain response on sense of loading, and initial dislocation density. The

emergence of spatial inhomogeneity in dislocation density starting from homogeneous initial and boundary conditions corresponding to homogeneous deformation in conventional plasticity was demonstrated in [RA06] at small strains. An attempt to understand the emergence of microstructure in MFDM was made in [RA06, DAS16], in drastically simplified 1-d settings. The conclusion in [RA06] and [DAS16] (further substantiated in this work) was that the nature of the fundamental transport equation for Nye tensor evolution coupled to stress along with the simplest representations, from conventional plasticity theory, of the plastic strain rate due to statistical dislocations, is adequate for the emergence of dislocation microstructure in this model, while being faithful to representing the plastic strain rate of both resolved and unresolved dislocation populations. Puri et al. [PAR11, PDA11] involve a modification of the computational framework for MFDM that allows different types of grain boundary constraints to be modeled based on fundamental jump conditions [Ach07]. [PAR11] analyzed the effect of different classes of constraints to plastic flow through grain boundaries, as it relates to dislocation microstructure development and mechanical response of a bicrystal. [PDA11] studied the effect of surface passivation, grain orientation, grain boundary constraints, and film thickness on the mechanical response of multi-crystalline thin films. The finite deformation implementation of MFDM was attempted in [Pur09] and the first static, finite elastic implementation of FDM was developed there. However, the developed numerical algorithm involved a predictor-corrector approach for the evolution problem and the formulation was found to be computationally expensive and non-robust.

Here, we present a finite-element based updated Lagrangian formulation for the full finite deformation MFDM. The formulation generalizes the FEM implementation of small deformation MFDM theory developed in [RA05, RA06] to finite deformation (without the implementation of advanced jump conditions in [PAR11, PDA11]). It adopts the static finite elasticity framework developed in [Pur09]. The implementation for the evolution problem utilizes an additional equation of incremental equilibrium that enables a staggered formulation akin to the small-deformation formulations [RA05, RA06], thus overcoming the limitations

of [Pur09]. Since the equations of MFDM are identical to those of FDM except for an additional term in the plastic strain rate, denoted by $\boldsymbol{L}^p$, any algorithm and the computational framework for FDM and MFDM are similar. The formulation presented here consists of the governing equilibrium equation (and its rate form), a *div-curl* system for the elastic incompatibility, an evolution equation for the compatible part of elastic distortion tensor, and a first-order wave propagation equation for the evolution of the (spatially averaged) dislocation density. The potential and generality of the model (both FDM and MFDM) are demonstrated through several illustrative examples.

This page intentionally left blank.

Chapter 3

Theoretical framework

This chapter presents a self-contained description of the governing equations, and initial and boundary conditions of finite deformation (Mesoscale) Field Dislocation Mechanics theory.

3.1 Field Dislocation Mechanics (FDM)

The detailed derivation of the governing equations for finite deformation (M)FDM is presented in [Ach04, Ach11]. For the convenience of the reader, the formulation is briefly presented.

Field Dislocation Mechanics (FDM) was developed by Acharya in [Ach01, Ach03, Ach04] building on the pioneering works of Kroner [Krö81], Willis [Wil67], Mura [Mur63], and Fox [Fox66]. The theory is applicable to dislocation related phenomena in crystalline solids at scales when each and every dislocation is well resolved. As explained in [Ach01], the Elastic Theory of Continuously Distributed Dislocations (ECDD) theory developed by [Wil67] and [Krö81] has to be extended beyond a statement of evolution equation of dislocation density tensor to obtain unique solutions for the deformation field in the body on application of external forces. FDM enables the unique determination of such a deformation field by explicitly giving an evolution statement for the compatible part of the inverse elastic distortion tensor.

Nye's dislocation density tensor ([Nye53]) $\boldsymbol{\alpha}$ is used which when integrated over an area gives the Burgers vector of dislocation lines threading that area patch. The presence of dislocation density in the domain is related to the incompatibility of the inverse elastic distortion tensor, $\boldsymbol{F}^{e-1} \equiv \boldsymbol{W}$. This is done as follows: Consider a closed curve denoted by $C(t)$ enclosing an area $A(t)$ in the current configuration. If the curve encloses a dislocation in the material, then the image of the curve, obtained by mapping with the inverse elastic distortion tensor $\boldsymbol{W}$, in the ideal crystal lattice does not close. Instead, the closure failure gives a resulting Burgers vector of the enclosed dislocation. This closure failure relates the

incompatibility of $\boldsymbol{W}$ in the current configuration to the presence of defects, commonly called geometrically necessary dislocations. The Burgers vector content of the area patch $A(t)$, denoted by $\boldsymbol{b}_A$, is calculated as

$$\boldsymbol{b}_A = -\int_{C(t)} \boldsymbol{W}\, d\boldsymbol{x} = \int_{A(t)} \boldsymbol{\alpha}\boldsymbol{n}\, dA, \tag{3.1}$$

where the right most term in Eq. (3.1) is a representation of the same closure failure using Nye's arguments. Thus Eq. (3.1) serves as a fundamental relation connecting an argument from calculus to a physical one. Using Stokes' theorem, Eq. (3.1) can be localized to give

$$curl\boldsymbol{W} = -\boldsymbol{\alpha}. \tag{3.2}$$

The balance of linear momentum for an elasto-plastic material, in the absence of body forces, can be written as:

$$div[\boldsymbol{T}(\boldsymbol{W})] = \begin{cases} \boldsymbol{0} & \text{quasistatic} \\ \rho\,\dot{\boldsymbol{v}} & \text{dynamic.} \end{cases} \tag{3.3}$$

where $\boldsymbol{v}$ is the velocity of the material.

The governing equation for the evolution of dislocation density is derived from a statement for the conservation of Burgers vector content of any arbitrary area patch. In the absence of dislocation nucleation, the rate of change of the Burgers vector content of the area patch $A(t)$ is given by the Burgers vector content brought in/taken out by the dislocation lines entering/leaving the area patch through the curve $C(t)$. This implies

$$\frac{d}{dt}\left(\int_{A(t)} \boldsymbol{\alpha}\boldsymbol{n}\, dA\right) = \dot{\boldsymbol{b}}_A = -\int_{C(t)} (\boldsymbol{\alpha} \times \boldsymbol{V})\, d\boldsymbol{x}, \tag{3.4}$$

where $\boldsymbol{\alpha} \times \boldsymbol{V}$ represents the flux of the Burgers vector carried in/out through the curve $C(t)$. Transforming the integral on the left from the current to the reference configuration, taking

the material time derivative, and then transferring it back to the current configuration and making the choice of the current configuration being the reference gives

$$\begin{aligned}\int_{A(t)} \left(\dot{\boldsymbol{\alpha}} + \boldsymbol{\alpha}\, div\boldsymbol{v} - \boldsymbol{\alpha}\boldsymbol{L}^T\right) \boldsymbol{n}\, dA &= \int_{A(t)} -curl(\boldsymbol{\alpha} \times \boldsymbol{V})\, \boldsymbol{n}\, dA \\ \implies \mathring{\boldsymbol{\alpha}} \equiv \dot{\boldsymbol{\alpha}} + \boldsymbol{\alpha}\, div\boldsymbol{v} - \boldsymbol{\alpha}\boldsymbol{L}^T &= -\operatorname{curl}(\boldsymbol{\alpha} \times \boldsymbol{V}).\end{aligned} \tag{3.5}$$

Equation (3.5) gives the governing equation for the evolution of the dislocation density in the domain.

Equations (3.1) and (3.4) can be used to give

$$\begin{aligned}-\overline{\int_{A(t)} \boldsymbol{\alpha}\boldsymbol{n}\, dA}^{\,\cdot} &= \overline{\int_{C(t)} \boldsymbol{W}\, d\boldsymbol{x}}^{\,\cdot} \\ \int_{C(t)} (\boldsymbol{\alpha} \times \boldsymbol{V})\, d\boldsymbol{x} &= \int_{C(t)} \left(\dot{\boldsymbol{W}} + \boldsymbol{W}\boldsymbol{L}\right) d\boldsymbol{x},\end{aligned}$$

which implies

$$\dot{\boldsymbol{W}} + \boldsymbol{W}\,\boldsymbol{L} = \boldsymbol{\alpha} \times \boldsymbol{V} \tag{3.6}$$

up to a gradient. Hence, the governing equations of FDM with $\boldsymbol{W}, \boldsymbol{\alpha}$ and the current configuration (geometry) as the unknown fields can be written as:

$$\begin{aligned} curl\boldsymbol{W} &= -\boldsymbol{\alpha} \\ \dot{\boldsymbol{W}} + \boldsymbol{W}\boldsymbol{L} &= \boldsymbol{\alpha} \times \boldsymbol{V} \\ div[\boldsymbol{T}(\boldsymbol{W})] &= \begin{cases} \boldsymbol{0} & \text{quasistatic} \\ \rho\, \dot{\boldsymbol{v}} & \text{dynamic.} \end{cases}\end{aligned} \tag{3.7}$$

Equation $(3.7)_2$ constitutes a system of Hamilton-Jacobi equations and therefore is somewhat daunting to work with numerically. Hence, the theory is re-formulated in terms of other variables, $\boldsymbol{f}$ and $\boldsymbol{\chi}$, which makes it computationally amenable (although at the expense of

introducing 3 more unknown fields). This is done by using a Stokes-Helmholtz decomposition of the field $\boldsymbol{W}$.

According to the Helmholtz decomposition, $\boldsymbol{W}$ can be written as a sum of a curl free part $grad\boldsymbol{f}$, and a divergence free part, $\boldsymbol{\chi}$ (with appropriate boundary conditions). This leads us to rewrite Eq. (3.7)$_1$ as

$$\left.\begin{aligned} curl\boldsymbol{\chi} &= -\boldsymbol{\alpha} \\ div\,\boldsymbol{\chi} &= \boldsymbol{0} \end{aligned}\right\} \quad \text{on } \Omega, \tag{3.8}$$

along with the boundary condition

$$\boldsymbol{\chi}\cdot\boldsymbol{n} = \boldsymbol{0} \quad \text{on } \partial\Omega \tag{3.9}$$

to ensure vanishing of $\boldsymbol{\chi}$ in the absence of dislocations.

To get a governing equation for $\boldsymbol{f}$, Eq. (3.7)$_2$ can be re-written as

$$\begin{aligned} &\dot{\overline{\boldsymbol{\chi} + grad\boldsymbol{f}}} + (\boldsymbol{\chi} + grad\boldsymbol{f})\boldsymbol{L} = \boldsymbol{\alpha}\times\boldsymbol{V} \\ \implies &\dot{\boldsymbol{\chi}} + grad\dot{\boldsymbol{f}} - grad\boldsymbol{f}\,\boldsymbol{L} + (\boldsymbol{\chi} + grad\boldsymbol{f})\boldsymbol{L} = \boldsymbol{\alpha}\times\boldsymbol{V} \\ \implies &grad\dot{\boldsymbol{f}} = \boldsymbol{\alpha}\times\boldsymbol{V} - \dot{\boldsymbol{\chi}} - \boldsymbol{\chi}\boldsymbol{L} \\ \implies &div(grad\dot{\boldsymbol{f}}) = div(\boldsymbol{\alpha}\times\boldsymbol{V} - \dot{\boldsymbol{\chi}} - \boldsymbol{\chi}\boldsymbol{L}), \end{aligned} \tag{3.10}$$

along with the boundary conditions necessary for the existence of solutions given as

$$(grad\dot{\boldsymbol{f}})\boldsymbol{n} = (\boldsymbol{\alpha}\times\boldsymbol{V} - \dot{\boldsymbol{\chi}} - \boldsymbol{\chi}\boldsymbol{L})\boldsymbol{n}. \tag{3.11}$$

Hence, the governing equations of FDM when one chooses to work with the pair $(\boldsymbol{\chi}, \boldsymbol{f})$

instead of $\boldsymbol{W}$, can be written as:

$$
\begin{aligned}
&\boldsymbol{W} = \boldsymbol{\chi} + grad\boldsymbol{f},\ \boldsymbol{F}^e := \boldsymbol{W}^{-1} \\
&\mathring{\boldsymbol{\alpha}} \equiv (div\,\boldsymbol{v})\boldsymbol{\alpha} + \dot{\boldsymbol{\alpha}} - \boldsymbol{\alpha}\boldsymbol{L}^T = -curl\,(\boldsymbol{\alpha} \times \boldsymbol{V}) \\
&curl\boldsymbol{\chi} = -\boldsymbol{\alpha} \\
&div\boldsymbol{\chi} = \boldsymbol{0} \\
&div\left(\text{grad}\,\dot{\boldsymbol{f}}\right) = div\,(\boldsymbol{\alpha} \times \boldsymbol{V} - \dot{\boldsymbol{\chi}} - \boldsymbol{\chi}\boldsymbol{L}) \\
&div[\boldsymbol{T}(\boldsymbol{W})] = \begin{cases} \boldsymbol{0} & \text{quasistatic} \\ \rho\,\dot{\boldsymbol{v}} & \text{dynamic.} \end{cases}
\end{aligned}
\tag{3.12}
$$

3.2 Mesoscale Field Dislocation Mechanics (MFDM)

FDM is suitable for modeling the response of bodies with structural dimensions of microns or even smaller. To deal with mechanical response at the mesoscale, a commonly used space-time averaging filter used in the literature on multiphase flows [Bab97] is applied to microscopic FDM. The resulting averaged theory is called Mesoscale Field Dislocation Mechanics (MFDM). Details of the derivations can be found in [AR06, Ach11].

For any microscopic field q, the mesoscopic space-time averaged field $\bar{q}$ is given as:

$$
\bar{q} := \frac{1}{\int_{\Omega(\boldsymbol{x})}\int_{I(t)} w(\boldsymbol{x}-\boldsymbol{x}', t-t')d\boldsymbol{x}'dt'} \int_{\Lambda}\int_{B} w(\boldsymbol{x}-\boldsymbol{x}', t-t')\, q(\boldsymbol{x}', t')\, d\boldsymbol{x}'dt', \tag{3.13}
$$

where B is the body and Λ is a sufficiently large interval of time. $\Omega(\boldsymbol{x})$ is a bounded region within the body around the point $\boldsymbol{x}$ with linear dimension of the spatial resolution of the model to be developed, and $I(t)$ is a bounded interval contained in Λ. The weighting function w is non-dimensional and assumed to be smooth in the variables $\boldsymbol{x}, \boldsymbol{x}', t$, and t'. For fixed $\boldsymbol{x}$ and t, w is only non-zero in $\Omega(\boldsymbol{x}) \times I(t)$ when viewed as a function of $\boldsymbol{x}'$ and t'.

Assuming $\overline{\boldsymbol{v}} = \boldsymbol{v}$ and that the averages of products are products of averages except for

$\boldsymbol{\alpha} \times \boldsymbol{V}$, the full set of the governing equations of MFDM can be written as

$$\overset{\circ}{\overline{\boldsymbol{\alpha}}} \equiv (div\,\overline{\boldsymbol{v}})\overline{\boldsymbol{\alpha}} + \dot{\overline{\boldsymbol{\alpha}}} - \overline{\boldsymbol{\alpha}}\overline{\boldsymbol{L}}^T = -curl\left(\overline{\boldsymbol{\alpha}} \times \overline{\boldsymbol{V}} + \boldsymbol{L}^p\right) \tag{3.14a}$$

$$\left.\begin{aligned} &\overline{\boldsymbol{W}} = \overline{\boldsymbol{\chi}} + grad\overline{\boldsymbol{f}} \\ &curl\overline{\boldsymbol{W}} = curl\overline{\boldsymbol{\chi}} = -\overline{\boldsymbol{\alpha}} \\ &div\overline{\boldsymbol{\chi}} = \boldsymbol{0} \end{aligned}\right\} \tag{3.14b}$$

$$div\left(grad\dot{\overline{\boldsymbol{f}}}\right) = div\left(\overline{\boldsymbol{\alpha}} \times \overline{\boldsymbol{V}} + \boldsymbol{L}^p - \dot{\overline{\boldsymbol{\chi}}} - \overline{\boldsymbol{\chi}}\overline{\boldsymbol{L}}\right) \tag{3.14c}$$

$$div[\overline{\boldsymbol{T}}(\overline{\boldsymbol{W}})] = \begin{cases} \boldsymbol{0} & \text{quasistatic} \\ \overline{\rho}\,\dot{\overline{\boldsymbol{v}}} & \text{dynamic,} \end{cases} \tag{3.14d}$$

where $\boldsymbol{L}^p$ is defined as

$$\boldsymbol{L}^p(\boldsymbol{x},t) := \overline{(\boldsymbol{\alpha} - \overline{\boldsymbol{\alpha}}(\boldsymbol{x},t)) \times \boldsymbol{V}}(\boldsymbol{x},t) = \overline{\boldsymbol{\alpha} \times \boldsymbol{V}}(\boldsymbol{x},t) - \overline{\boldsymbol{\alpha}}(\boldsymbol{x},t) \times \overline{\boldsymbol{V}}(\boldsymbol{x},t). \tag{3.15}$$

The barred quantities in (3.14) are simply the weighted, space-time, running averages of their corresponding microscopic fields used in (3.12). The field $\overline{\boldsymbol{\alpha}}$ is the Excess Dislocation Density (ED). The microscopic density of Statistical Dislocations (SD) at any point is defined as the difference between the microscopic dislocation density $\boldsymbol{\alpha}$ and its averaged field $\overline{\boldsymbol{\alpha}}$:

$$\boldsymbol{\beta}(\boldsymbol{x},\boldsymbol{x}',t,t') = \boldsymbol{\alpha}(\boldsymbol{x}',t') - \overline{\boldsymbol{\alpha}}(\boldsymbol{x},t),$$

which implies

$$\begin{gathered} \rho_t = \sqrt{\rho_g^2 + \rho_s^2} \\ \rho_t(\boldsymbol{x},t) := \sqrt{\overline{\left(\frac{|\boldsymbol{\alpha}|}{b}\right)^2}(\boldsymbol{x},t)} \;\; ; \;\; \rho_g(\boldsymbol{x},t) := \frac{|\overline{\boldsymbol{\alpha}}(\boldsymbol{x},t)|}{b} \;\; ; \;\; \rho_s(\boldsymbol{x},t) := \sqrt{\overline{\left(\frac{|\boldsymbol{\beta}|}{b}\right)^2}(\boldsymbol{x},t)}, \end{gathered} \tag{3.16}$$

with b denoting the magnitude of the Burgers vector of a full dislocation in the material, ρ_t the

total dislocation density, ρ_g the magnitude of ED (commonly referred to as the geometrically necessary dislocation density), and ρ_s is, up to a scaling constant, the root-mean-squared SD. We refer to ρ_s as the scalar statistical dislocation density (*ssd*). It is important to note that spatially unresolved dislocation loops below the scale of resolution of the averaged model do not contribute to the ED ($\overline{\boldsymbol{\alpha}}$) on space time averaging of the microscopic dislocation density, due to sign cancellation. Thus, the magnitude of the ED is an inadequate approximation of the total dislocation density. Similarly, a consideration of 'symmetric' expansion of unresolved dislocation loops shows that the plastic strain rate produced by SD, $\boldsymbol{L}^p$ (3.15), is not accounted for in $\overline{\boldsymbol{\alpha}} \times \overline{\boldsymbol{V}}$, and thus the latter is not a good approximation of the total averaged plastic strain rate $\overline{\boldsymbol{\alpha} \times \boldsymbol{V}}$.

Similarly, when $\overline{\boldsymbol{W}}$ is used as the field variable, the governing equations can be written as:

$$
\begin{aligned}
&curl \overline{\boldsymbol{W}} = -\overline{\boldsymbol{\alpha}} \\
&\dot{\overline{\boldsymbol{W}}} + \overline{\boldsymbol{W}}\,\overline{\boldsymbol{L}} = \overline{\boldsymbol{\alpha}} \times \overline{\boldsymbol{V}} + \boldsymbol{L}^p \\
&div\,[\overline{\boldsymbol{T}}(\overline{\boldsymbol{W}})] = \begin{cases} \boldsymbol{0} & \text{quasistatic} \\ \overline{\rho}\,\dot{\overline{\boldsymbol{v}}} & \text{dynamic.} \end{cases}
\end{aligned}
\tag{3.17}
$$

In MFDM, closure assumptions are made for the field $\boldsymbol{L}^p$ and the evolution of ρ_s, as is standard in most, if not all, averaged versions of nonlinear microscopic models, whether of real-space or kinetic theory type. As such, these closure assumptions can be improved as necessary (and increasingly larger systems of such a hierarchy of nonlinear pde can be formally written down for MFDM). In this work, we adopt simple and familiar closure statements from (almost) classical crystal and J_2 plasticity theories and probe the capabilities of the models that result. As is customary, the FEM formulation and algorithm presented here is independent of the constitutive choices made for $\boldsymbol{L}^p$, $\boldsymbol{V}$, and $\boldsymbol{T}$. Following the works of Kocks, Mecking, and co-workers [MK81, EM84] we describe the evolution of ρ_s through

a statement, instead, of evolution of material strength g described by (3.33); $\boldsymbol{L}^p$ is defined by (3.25) (or (3.23)) following standard assumptions of crystal (or J_2) plasticity theory and thermodynamics. A significant part of the tensorial structure of (3.25) can be justified by elementary averaging considerations of dislocation motion on a family of slip planes under the action of their Peach-Koehler driving force [AC12].

Henceforth, we drop the overhead bars for convenience in referring to averaged quantities, and we will only refer to the 'macroscopic' fields given in (3.14). Also, $\boldsymbol{\alpha}$ will be simply referred to as the dislocation density tensor. Since the system in (3.14) is not closed, $\boldsymbol{T}$, $\boldsymbol{L}^p$, and $\boldsymbol{V}$ are to be constitutively specified response functions specific to materials.

As shown in [AZ15], (3.14a) and (3.14b) imply

$$\dot{\boldsymbol{W}} + \boldsymbol{W}\boldsymbol{L} = \boldsymbol{\alpha} \times \boldsymbol{V} + \boldsymbol{L}^p \tag{3.18}$$

up to the gradient of a vector field, which is re-written as

$$\boldsymbol{L} = \dot{\boldsymbol{F}}^e \boldsymbol{F}^{e-1} + \boldsymbol{F}^e(\boldsymbol{\alpha} \times \boldsymbol{V} + \boldsymbol{L}^p).$$

This can be interpreted as the decomposition of the velocity gradient into an elastic part, given by $\dot{\boldsymbol{F}}^e \boldsymbol{F}^{e-1}$, and a plastic part given by $\boldsymbol{F}^e(\boldsymbol{\alpha} \times \boldsymbol{V} + \boldsymbol{L}^p)$. The plastic part is defined by the motion of dislocations, both resolved and unresolved, on the current configuration and *no notion of any pre-assigned reference configuration is needed.* Of significance is also the fact that *MFDM involves no notion of a plastic distortion tensor and yet produces (large) permanent deformation.*

3.3 Constitutive equations for $\boldsymbol{T}$, $\boldsymbol{L}^p$, and $\boldsymbol{V}$

MFDM requires constitutive statements for the stress $\boldsymbol{T}$, the plastic distortion rate $\boldsymbol{L}^p$, and the dislocation velocity $\boldsymbol{V}$. We make the model consistent with the minimal, but essential,

requirement of non-negative dissipation through these choices. For this we consider the mechanical dissipation D which, in the presence of inertia and body forces, is defined as the difference between the power of the applied forces and the rate of change of the sum of the kinetic and free energies of the system:

$$D = \int_{\partial\Omega} \boldsymbol{T}\boldsymbol{n} \cdot \boldsymbol{v}\, dA + \int_{\Omega} \boldsymbol{b}_f \cdot \boldsymbol{v}\, dV - \overline{\int_{\Omega} \rho\, (\psi + \frac{1}{2}\boldsymbol{v} \cdot \boldsymbol{v})\, dV}^{\,\cdot},$$

where ψ is the specific Helmholtz free-energy of the system, and $\boldsymbol{b}_f$ is the body force density. The Helmholtz free energy of the system per unit mass, ψ, is assumed to be the sum of the elastic energy $\phi(\boldsymbol{W})$ density and a term $\Upsilon(\boldsymbol{\alpha})$ that is a heuristic representation of the averaging of a microscopic core energy, up to the mesoscale:

$$\psi = \phi(\boldsymbol{W}) + \Upsilon(\boldsymbol{\alpha}).$$

$\Upsilon(\boldsymbol{\alpha})$ is specified as

$$\Upsilon(\boldsymbol{\alpha}) = \frac{1}{2\rho^*}\epsilon\, \boldsymbol{\alpha} : \boldsymbol{\alpha},$$

where ϵ is a material constant that has dimensions of $stress \times length^2$. Using the balances of mass and linear momentum, the definition of $\Upsilon(\boldsymbol{\alpha})$, and the evolution equations for $\boldsymbol{W}$ (3.18) and $\boldsymbol{\alpha}$ (3.14a), the dissipation can be expressed as

$$\begin{aligned} D &= \int_{\Omega} \boldsymbol{T} : \boldsymbol{L}\, dV - \int_{\Omega} \rho\, \overline{(\phi(\boldsymbol{W}) + \Upsilon(\boldsymbol{\alpha}))}^{\,\cdot}\, dV \\ &= \int_{\Omega} \left[\boldsymbol{T} + \rho \boldsymbol{W}^T \frac{\partial \phi}{\partial \boldsymbol{W}}\right] : \boldsymbol{L}\, dV - \int_{\Omega} \rho \boldsymbol{X} \left[\left(\frac{\partial \phi}{\partial \boldsymbol{W}}\right)^T \boldsymbol{\alpha}\right] \cdot \boldsymbol{V} dV - \int_{\Omega} \rho \frac{\partial \phi}{\partial \boldsymbol{W}} : \boldsymbol{L}^p\, dV \\ &\quad + \frac{\epsilon}{\rho^*} \left[\int_{\Omega} \rho \left((\boldsymbol{\alpha} : \boldsymbol{\alpha})\boldsymbol{I} - \boldsymbol{\alpha}^T \boldsymbol{\alpha}\right) : \boldsymbol{L}\, dV + \int_{\Omega} \rho \boldsymbol{X} \left([curl \boldsymbol{\alpha}]^T \boldsymbol{\alpha}\right) \cdot \boldsymbol{V} dV \right. \\ &\qquad \left. + \int_{\Omega} \underbrace{\rho\, curl \boldsymbol{\alpha} : \boldsymbol{L}^p}\, dV - \int_{\partial\Omega} \rho\, \boldsymbol{\alpha} : ((\boldsymbol{\alpha} \times \boldsymbol{V} + \boldsymbol{L}^p) \times \boldsymbol{n})\, dA \right]. \end{aligned} \tag{3.19}$$

Motivated by this form of the dissipation, we therefore make the following constitutive assumptions for $\boldsymbol{T}$, $\boldsymbol{V}$, and $\boldsymbol{L}^p$ in MFDM.

3.3.1 Cauchy stress

Ensuring no dissipation in purely elastic processes, the stress is given by

$$\boldsymbol{T} = -\rho \boldsymbol{W}^T \frac{\partial \phi}{\partial \boldsymbol{W}}.$$

Saint-Venant Kirchhoff material: For a Saint-Venant Kirchhoff material, the elastic energy per unit mass is specified as

$$\begin{aligned} \phi(\boldsymbol{W}) &= \frac{1}{2\rho^*} \boldsymbol{E}^e : \mathbb{C} : \boldsymbol{E}^e \\ \boldsymbol{E}^e &= \frac{1}{2}(\boldsymbol{C}^e - \boldsymbol{I}); \quad \boldsymbol{C}^e = \boldsymbol{W}^{-T}\boldsymbol{W}^{-1}, \end{aligned} \tag{3.20}$$

where ρ^* is the mass density of the pure, unstretched elastic lattice, and $\mathbb{C}$ is the fourth order elasticity tensor, assumed to be positive definite on the space of second order symmetric tensors. The stress response for this material can be constitutively derived as

$$\boldsymbol{T} = -\rho \boldsymbol{W}^T \frac{\partial \phi}{\partial \boldsymbol{W}} \implies \boldsymbol{T} = \boldsymbol{F}^e \left[\mathbb{C} : \boldsymbol{E}^e\right] \boldsymbol{F}^{eT}. \tag{3.21}$$

Modified Neo-Hookean material: To model an incompressible Neo-Hookean material, special finite elements need to be employed to ensure incompressibility. Therefore, for the sake of simplicity, we use a compressible analog of a Neo-Hookean material whose strain energy density function per unit mass is given by

$$\phi(\boldsymbol{W}) = \frac{\mu}{2\rho^*} \left(I_1(\boldsymbol{C}^e) - ln(det\boldsymbol{C}^e)\right),$$

where μ is shear modulus, and I_1 is the first invariant of the right Cauchy-Green deformation

tensor. The stress response for this material is given as

$$\boldsymbol{T} = -\rho \boldsymbol{W}^T \frac{\partial \phi}{\partial \boldsymbol{W}} \implies \boldsymbol{T} = \mu(\boldsymbol{F}^e \boldsymbol{F}^{eT} - \boldsymbol{I}). \tag{3.22}$$

The above expressions for the Cauchy stress tensors ((3.21) and (3.22)) tacitly assume that $\frac{\rho}{\rho^*}$ is absorbed in the elastic moduli $\mathbb{C}$ (or μ), which is assumed to be spatially constant in this work.

3.3.2 Plastic strain rate

From the study of solutions to FDM it is known [AT11, ZAWB15] that the core energy provides a crucial physical regularization and therefore, we want to keep the simplest possible effect of it in MFDM, in the absence of rigorous information on the averaged structure of FDM. Based on the above terms in the dissipation Eq. (3.19), if we assume $\boldsymbol{L}^p$ to be in the direction of its driving force to ensure non-negative dissipation, then it can be observed that the presence of $curl\boldsymbol{\alpha}$ in the driving force for $\boldsymbol{L}^p$ gives rise to a term, in the evolution equation (3.14a) for $\boldsymbol{\alpha}$, of the form $-curl(curl\boldsymbol{\alpha})$ with a (possibly spatially varying) non-negative coefficient. This additional term behaves as a diffusive regularization, by a standard identity of vector calculus and the fact $div\boldsymbol{\alpha} = \boldsymbol{0}$.

Standard crystal plasticity or J_2 plasticity models assume a certain form of $\boldsymbol{L}^p$. To augment these forms with an additive term in $\epsilon\, curl\boldsymbol{\alpha}$ as motivated above requires the introduction of a mobility coefficient with physical dimensions of $(stress \times time^{-1})$. In the absence of more detailed knowledge, simplicity demands that all dissipative processes be linked to a common time scale and we do not proliferate material parameters. Thus, we assume the stress scale in the mobility to be linked to the initial yield strength g_0, and its time scale to be linked to the reciprocal of the equivalent plastic strain rates of the models. Using $l^2 := \frac{\epsilon}{g_0}$, we define $\boldsymbol{L}^p$ for the two cases of J_2 and crystal plasticity:

J_2 *Plasticity*: The plastic strain rate due to SDs is assumed to be a non-negative multiplier

of the stress deviator tensor $\boldsymbol{T}'$ in classical J_2 plasticity theory. The assumptions listed above result in the coefficient of $curl\boldsymbol{\alpha}$ in $\boldsymbol{L}^p$ to be $\frac{g_0}{\hat{\gamma}}$ (upto a factor $\frac{\rho}{\rho^*}$). $\boldsymbol{L}^p$ is assumed to be given as

$$\begin{aligned} \hat{\boldsymbol{L}}^p &= \hat{\gamma}\boldsymbol{W}\frac{\boldsymbol{T}'}{|\boldsymbol{T}'|} \\ \boldsymbol{L}^p &= \hat{\boldsymbol{L}}^p + l^2\hat{\gamma}\, curl\boldsymbol{\alpha}, \end{aligned} \tag{3.23}$$

where $\hat{\gamma}$ is a non-negative function of state representing the magnitude of the SDs slipping rate. $\hat{\gamma}$ is given by the following power law

$$\hat{\gamma} = \hat{\gamma}_0 \left(\frac{|\boldsymbol{T}'|}{\sqrt{2}\, g}\right)^{\frac{1}{m}}, \tag{3.24}$$

where $\hat{\gamma}_0$ is the reference strain rate, m is the rate sensitivity of the material, and g is the strength of the material whose evolution is given by Eq. (3.33).

Crystal Plasticity: Classical crystal plasticity assumes $\boldsymbol{L}^p$ to be a sum of slipping on prescribed slip systems (cf. [Asa83]). The coefficient of $curl\boldsymbol{\alpha}$ in $\boldsymbol{L}^p$ is taken to be $\frac{\epsilon}{g_0}\frac{1}{n_{sl}}\sum_k^{n_{sl}}|\hat{\gamma}^k|$ (up to a factor $\frac{\rho}{\rho^*}$), for the reasons mentioned above, and therefore we assume $\hat{\boldsymbol{L}}^p$ to be given by

$$\begin{aligned} \hat{\boldsymbol{L}}^p &= \boldsymbol{W}\left(\sum_k^{n_{sl}} \hat{\gamma}^k\, \boldsymbol{m}^k \otimes \boldsymbol{n}^k\right)_{sym} \\ \boldsymbol{L}^p &= \hat{\boldsymbol{L}}^p + \left(\frac{l^2}{n_{sl}}\sum_k^{n_{sl}}|\hat{\gamma}^k|\right) curl\boldsymbol{\alpha} \end{aligned} \tag{3.25}$$

where

$$\hat{\gamma}^k = sgn(\tau^k)\, \hat{\gamma}_0{}^k \left(\frac{|\tau^k|}{g}\right)^{\frac{1}{m}}. \tag{3.26}$$

In the above, $(\cdot)_{sym}$ represents the symmetric part of $(\cdot)$, $\hat{\gamma}^k$ represents the magnitude of SD slipping rate on the slip system k, n_{sl} is the total number of slip systems, and $sgn(\tau^k)$

denotes the sign of scalar τ^k. The vectors $\boldsymbol{m}^k$ and $\boldsymbol{n}^k$ represent the slip direction and the slip plane normal for the kth slip system in the current configuration. These are given as

$$\boldsymbol{m}^k = \boldsymbol{F}^e \boldsymbol{m}_0^k$$
$$\boldsymbol{n}^k = \boldsymbol{F}^{e-T} \boldsymbol{n}_0^k,$$

where $\boldsymbol{m}_0^k$ and $\boldsymbol{n}_0^k$ are the corresponding unstretched unit vectors. The resolved shear stress τ^k on the kth slip system is defined as

$$\tau^k = \boldsymbol{m}^k \cdot \boldsymbol{T} \boldsymbol{n}^k.$$

The use of the symmetrization in the definition of $\hat{\boldsymbol{L}}^p$ is not standard, but found to be necessary, following [PDA11, Sec. 5.5].

We mention here that the length scale l is not responsible for producing enhanced size effects and microstructure in MFDM. Rather, the 'smaller is harder' size effect becomes more pronounced as l decreases since its presence reduces the magnitude of the $\boldsymbol{\alpha}$ field and consequently reduces hardening (3.33). Although it is not responsible for the generation of microstructural pattern, it plays role in in defining the details of the microstructural patterns as shown in Sec. 7.5.

3.3.3 Dislocation velocity

The direction of the dislocation velocity, $\boldsymbol{d}$, is given by

$$\boldsymbol{d} = \boldsymbol{b} - \left(\boldsymbol{b} \cdot \frac{\boldsymbol{a}}{|\boldsymbol{a}|} \right) \frac{\boldsymbol{a}}{|\boldsymbol{a}|} \tag{3.27}$$

(for motivation see [AR06, AC12]) with

$$T'_{ij} = T_{ij} - \frac{T_{mm}}{3}\delta_{ij}; \quad b_i := \varepsilon_{ijk} T'_{jr} F^e{}_{rp} \alpha_{pk}; \quad a_i := \frac{1}{3} T_{mm} \varepsilon_{ijk} F^e{}_{jp} \alpha_{pk}. \tag{3.28}$$

The dislocation velocity is then assumed to be

$$\boldsymbol{V} = \zeta \frac{\boldsymbol{d}}{|\boldsymbol{d}|} \tag{3.29}$$

with

$$\zeta = \left(\frac{\mu}{g}\right)^2 \eta^2 \, b \, \hat{\gamma}_{avg}, \tag{3.30}$$

where b is as in (3.16), μ is the shear modulus, and $\eta = \frac{1}{3}$ is a material parameter. $\hat{\gamma}_{avg}$ is defined as

$$\hat{\gamma}_{avg} = \begin{cases} \hat{\gamma} & J_2 \text{ plasticity} \\ \dfrac{1}{n_{sl}} \sum_k^{n_{sl}} |\hat{\gamma}^k| & \text{Crystal plasticity.} \end{cases}$$

3.3.4 Dissipation

Defining D_{sd} as

$$D_{sd} := -\rho \frac{\partial \phi}{\partial \boldsymbol{W}} : \hat{\boldsymbol{L}}^p = \boldsymbol{F}^{eT} \boldsymbol{T} : \hat{\boldsymbol{L}}^p = \begin{cases} \hat{\gamma} |\boldsymbol{T}'| & J_2 \text{ plasticity} \\ \sum_k^{n_{sl}} \tau^k \hat{\gamma}^k & \text{Crystal plasticity,} \end{cases}$$

we note that for these choices of $\boldsymbol{T}$, $\boldsymbol{V}$, and $\boldsymbol{L}^p$

$$\begin{aligned} \lim_{\epsilon \to 0} D &= \int_\Omega \zeta \frac{\boldsymbol{d}}{|\boldsymbol{d}|} \cdot \boldsymbol{X}[\boldsymbol{T}\boldsymbol{F}^e \boldsymbol{\alpha}] \, dV + \int_\Omega D_{ssd} \, dV \\ &\geq 0 \end{aligned}$$

(assuming the multiplier of ϵ within the square parenthesis in (3.19) is bounded in the limit).

3.4 Boundary conditions

The $\boldsymbol{\alpha}$ evolution equation (3.14a), the incompatibility equation for $\boldsymbol{\chi}$ (3.14b), the $\boldsymbol{f}$ evolution equation (3.14c), and the equilibrium equation (3.14d) require specification of boundary conditions at all times.

The $\boldsymbol{\alpha}$ evolution equation (3.14a) admits a 'convective' boundary condition of the form $(\boldsymbol{\alpha} \times \boldsymbol{V} + \boldsymbol{L}^p) \times \boldsymbol{n} = \boldsymbol{\Phi}$, where $\boldsymbol{\Phi}$ is a second order tensor valued function of time and position on the boundary characterizing the flux of dislocations at the surface with unit normal field $\boldsymbol{n}$ and satisfying the constraint $\boldsymbol{\Phi n} = \boldsymbol{0}$. The boundary condition is specified in one of following two ways:

- *Constrained boundary*: A constrained boundary condition is modeled by taking $\boldsymbol{\Phi}$ to be identically zero on the boundary at all times i.e. $\boldsymbol{\Phi}(\boldsymbol{x}, t) = \boldsymbol{0}$. This makes the boundaries plastically constrained which means the dislocations cannot exit the body while only being allowed to move in the tangential direction at the external boundary. It is also referred to as the no-slip or rigid boundary condition.

- *Unconstrained boundary*: A less restrictive boundary condition where $\hat{\boldsymbol{L}}^p \times \boldsymbol{n}$ is specified on the boundary, along with the dislocation flux $\boldsymbol{\alpha}(\boldsymbol{V} \cdot \boldsymbol{n})$ specified on the inflow part of the boundary (where $\boldsymbol{V} \cdot \boldsymbol{n} < 0$) can also be used. For non-zero l, specification of $l^2 \hat{\gamma}_{ssd}(curl \boldsymbol{\alpha} \times \boldsymbol{n})$ on the boundary is also required, where $\hat{\gamma}_{ssd}$ is defined in Sec. 3.6.

The incompatibility equation (3.14b) admits a boundary condition of the form

$$\boldsymbol{\chi n} = \boldsymbol{0}$$

on the external boundary $\partial\Omega$ of the domain. Such a boundary condition along with the system (3.14b) ensures vanishing $\boldsymbol{\chi}$ in the absence of any dislocation density $\boldsymbol{\alpha}$. The $\boldsymbol{f}$

evolution equation (3.14c) requires a Neumann boundary condition of the form

$$\left(grad\dot{\boldsymbol{f}}\right)\boldsymbol{n} = (\boldsymbol{\alpha}\times\boldsymbol{V} + \boldsymbol{L}^p - \dot{\boldsymbol{\chi}} - \boldsymbol{\chi}\boldsymbol{L})\boldsymbol{n}$$

on the external boundary $\partial\Omega$. The equilibrium equation (3.14d) requires specification of standard displacement and/or statically admissible tractions on complementary parts of the boundary. Along with these, standard boundary conditions required to eliminate rigid body deformation mode during solving of equilibrium equation (or its rate form Eq. (4.2)) are required.

3.5 Initial conditions

The evolution equations for the $\boldsymbol{\alpha}$ and $\boldsymbol{f}$ fields (Eqs. (3.14a) and (3.14c), respectively) require specification of initial condition on the domain.

For the $\boldsymbol{\alpha}$ equation, an initial condition of the form $\boldsymbol{\alpha}(\boldsymbol{x}, t=0) = \boldsymbol{\alpha}_0(\boldsymbol{x})$ is required. To determine the initial the initial condition on $\boldsymbol{f}$, the problem can be more generally posed as follows: determine the $\boldsymbol{f}$ and $\boldsymbol{T}$ fields on a given configuration with a known dislocation density $\boldsymbol{\alpha}$. This problem can be solved by solving for $\boldsymbol{\chi}$ from the incompatibility equation and then $\boldsymbol{f}$ from the equilibrium equation as described by the system

$$\left.\begin{aligned} curl\boldsymbol{\chi} &= -\boldsymbol{\alpha} \\ div\boldsymbol{\chi} &= \boldsymbol{0} \\ div\left[\boldsymbol{T}(\boldsymbol{f},\boldsymbol{\chi})\right] &= \boldsymbol{0} \end{aligned}\right\} \text{ on } \Omega \tag{3.31}$$

$$\left.\begin{aligned} \boldsymbol{\chi}\boldsymbol{n} &= \boldsymbol{0} \\ \boldsymbol{T}\boldsymbol{n} &= \boldsymbol{t} \end{aligned}\right\} \text{ on } \partial\Omega \tag{3.32}$$

where $\boldsymbol{t}$ denotes the statically admissible traction field on the boundary. This determination of $\boldsymbol{\chi}$, $\boldsymbol{f}$, and $\boldsymbol{T}$ for a given dislocation density $\boldsymbol{\alpha}$ on any known configuration will be referred

to the ECDD solve on that configuration. Hence, we do the ECDD solve on the 'as-received' configuration, i.e. the current configuration at $t = 0$, to determine the initial value of $\boldsymbol{f}$ which also determines the stress $\boldsymbol{T}$ distribution at $t = 0$. For the dynamic case, an initial condition on material velocity field $\boldsymbol{v}(\boldsymbol{x}, t = 0)$ is required.

An auxiliary condition of $\dot{\boldsymbol{f}} = \boldsymbol{0}$ at a point is needed to uniquely evolve $\boldsymbol{f}$ from Eq. (3.14c) in time.

3.6 Strength evolution

The strength of the material is evolved according to (cf. [AB00b, BAC+00, AR06])

$$\dot{g} = \left[\frac{\mu^2\eta^2 b}{2(g - g_0)} k_0 \left|\boldsymbol{\alpha}\right| + \Theta_0 \left(\frac{g_s - g}{g_s - g_0}\right)\right] \left(\left|\boldsymbol{F}^e \boldsymbol{\alpha} \times \boldsymbol{V}\right| + \hat{\gamma}_{ssd}\right), \tag{3.33}$$

where Θ_0 is the Stage 2 hardening rate, k_0 is a material constant, and g_s is the saturation material strength. $\hat{\gamma}_{ssd}$ is defined as

$$\hat{\gamma}_{ssd} = \begin{cases} \hat{\gamma} & J_2 \text{ plasticity} \\ \sum_k^{n_{sl}} |\hat{\gamma}^k| & \text{Crystal plasticity.} \end{cases}$$

The material parameters $(g_0, g_s, \mu, \hat{\gamma}_0, m, \Theta_0)$ mentioned above are part of the constitutive structure of well-accepted models of classical plasticity theory. Our model requires 2 unknown fitting parameters: l, k_0, with the latter characterizing the plastic flow resistance due to ED. The material strength defines the ssd distribution (see (3.16)) as

$$\rho_s := \left(\frac{g}{\eta\mu b}\right)^2. \tag{3.34}$$

3.7 Heat equation

We currently assume that the time scale of heat diffusion is very small as compared to other time scales. Hence, under the assumption of locally adiabatic conditions, we evolve the temperature at each Gauss point according to

$$\dot{\theta} = \chi \boldsymbol{T} : (\boldsymbol{\alpha} \times \boldsymbol{V} + \boldsymbol{L}^p). \tag{3.35}$$

χ is a positive scalar parameter that can be fitted from experiments. Eq. (3.35) is a simple implementation of the idea that plastic working leads to a local increase of temperature which, in turn, softens the material of that neighborhood.

3.8 Rate independent plasticity

Rate-independent plastic response for the J_2 case may be modeled by specifying $\hat{\gamma}$ as given below:

$$\hat{\gamma} = \begin{cases} 0 & \tau < g \\ 0 & \tau = g \;\text{ and }\; \dfrac{\partial \tau}{\partial \boldsymbol{T}} : \dfrac{\partial \boldsymbol{T}}{\partial \boldsymbol{W}} : (-\boldsymbol{W}\boldsymbol{L}) < 0 \text{ unloading or neutral loading condition} \\ \hat{\gamma}_{ri} & \tau = g \;\text{ and }\; \dfrac{\partial \tau}{\partial \boldsymbol{T}} : \dfrac{\partial \boldsymbol{T}}{\partial \boldsymbol{W}} : (-\boldsymbol{W}\boldsymbol{L}) > 0 \text{ loading condition} \end{cases}$$

where

$$\tau = \frac{|\boldsymbol{T}'|}{\sqrt{2}}.$$

We can obtain $\hat{\gamma}_{ri}$ by setting $\dot{\tau} = \dot{g}$:

$$\dot{\tau} = \frac{\partial \tau}{\partial \boldsymbol{T}} : \frac{\partial \boldsymbol{T}}{\partial \boldsymbol{W}} : \dot{\boldsymbol{W}} \tag{3.36}$$

$$\frac{\partial \tau}{\partial \boldsymbol{T}} : \frac{\partial \boldsymbol{T}}{\partial \boldsymbol{W}} : (-\boldsymbol{W}\boldsymbol{L} + \boldsymbol{\alpha} \times \boldsymbol{V} + \boldsymbol{L}^p) = \left[\frac{\mu^2 \eta^2 b}{2(g - g_0)} k_0 \left| \boldsymbol{\alpha} \right| + \Theta_0 \left(\frac{g_s - g}{g_s - g_0} \right) \right] \left(\left| \boldsymbol{F}^e \boldsymbol{\alpha} \times \boldsymbol{V} \right| + \hat{\gamma}_{ri} \right). \tag{3.37}$$

We will use the following identities to evaluate the derivatives in Eq. (3.37) to obtain $\hat{\gamma}_{ri}$ for a Saint-Venant-Kirchhoff material.

$$\begin{aligned}
\frac{\partial T'_{ab}}{\partial T_{ij}} &= \delta_{ai}\delta_{bj} - \frac{1}{3}\delta_{ab}\delta_{ij} \\
T_{ij} &= F^e_{ia}\mathbb{C}_{abcd}E^e_{cd}F^e_{jb} \\
\frac{\partial F^e_{ia}}{\partial W_{pq}} &= -F^e_{qa}F^e_{ip} \\
\frac{\partial E^e_{cd}}{\partial W_{pq}} &= -\frac{1}{2}\left(F^e_{ac}F^e_{qd}F^e_{ap} + F^e_{ad}F^e_{qc}F^e_{ap}\right) \\
\frac{\partial T_{ij}}{\partial W_{pq}} &= \frac{\partial F^e_{ia}}{\partial W_{pq}}\mathbb{C}_{abcd}E^e_{cd}F^e_{jb} \\
&\quad + F^e_{ia}\mathbb{C}_{abcd}\frac{\partial E^e_{cd}}{\partial W_{pq}}F^e_{jb} \\
&\quad + F^e_{ia}\mathbb{C}_{abcd}E^e_{cd}\frac{\partial F^e_{jb}}{\partial W_{pq}}
\end{aligned}$$

We define

$$\varsigma = \left[\frac{\mu^2 \eta^2 b}{2(g - g_0)} k_0 \left| \boldsymbol{\alpha} \right| + \Theta_0 \left(\frac{g_s - g}{g_s - g_0} \right) \right]$$

and rewrite equation (3.37) as

$$\frac{\partial \tau}{\partial T_{ij}} \frac{\partial T_{ij}}{\partial W_{pq}} (-WL + \alpha \times V + L^p)_{pq} = \varsigma(\hat{\gamma}_{ri} + |\boldsymbol{F}^e \boldsymbol{\alpha} \times \boldsymbol{V}|).$$

Writing $\boldsymbol{V} = c\hat{\gamma}_{ri}\tilde{\boldsymbol{d}}$, $C_{pq} = \dfrac{\partial \tau}{\partial T_{ij}} \dfrac{\partial T_{ij}}{\partial W_{pq}}$, $\hat{\gamma}_{ri}$ is given by

$$\hat{\gamma}_{ri} = \frac{C_{pq} W_{pa} L_{aq}}{C_{pq} \epsilon_{qab} \alpha_{pa} c \tilde{d}_b + C_{pq} W_{pa} \tilde{T'}_{aq} - \varsigma \left(1 + \epsilon_{ipq} F^e_{ra} \alpha_{ap} c \tilde{d}_q\right)}, \tag{3.38}$$

where $\tilde{\boldsymbol{d}} = \dfrac{\boldsymbol{d}}{|\boldsymbol{d}|}$, $c = \eta^2 b \left(\dfrac{\mu}{g}\right)^2$, and $\tilde{\boldsymbol{T}'} = \dfrac{\boldsymbol{T}'}{|\boldsymbol{T}'|}$.

This page intentionally left blank.

Chapter 4

Numerical implementation of finite deformation (M)FDM

In this chapter, we present the weak form of the governing equations of MFDM at finite deformation for the quasistatic and dynamic (with inertia) cases. The algorithms for solving the finite deformation (M)FDM equations for both the cases are then described in Sec. 4.2. Finally, a short description of the developed code is presented in Sec. 4.3.

4.1 Variational formulations

Modeling material behavior through the use of MFDM requires the concurrent solution to coupled nonlinear system of pdes given by (3.14). To efficiently solve the system for the quasistatic case, and to be able to update the geometry while simultaneously eliminating the need for a predictor/corrector approach, we augment the system (3.14) with the rate (or incremental) form of the equilibrium equation, the derivation of which is presented below. This rate form can be solved to get the material velocity field $\boldsymbol{v}$ on the domain which can be used to (discretely) update the geometry of the body.

In the absence of body forces and inertia, the statement of local force balance (on the current configuration) w.r.t. any choice of reference configuration, can be expressed by

$$Div\boldsymbol{P} = \mathbf{0}, \tag{4.1}$$

where $\boldsymbol{P}$ represents the first Piola-Kirchhoff stress w.r.t. that reference. To get the rate form of the equilibrium equation, we take the material time derivative of Eq. (4.1)

$$\begin{aligned}\dot{\overline{Div\,\boldsymbol{P}}} = \mathbf{0} \implies & Div\,\dot{\overline{J\boldsymbol{T}\boldsymbol{F}^{-T}}} = \mathbf{0} \qquad (\boldsymbol{P} = J\boldsymbol{T}\boldsymbol{F}^{-\mathbf{T}}) \\ \implies & Div\left[Jdiv\boldsymbol{v}\,\boldsymbol{T}\boldsymbol{F}^{-T} + J\dot{\boldsymbol{T}}\boldsymbol{F}^{-T} + J\boldsymbol{T}\dot{\overline{\boldsymbol{F}^{-T}}}\right] = \mathbf{0}.\end{aligned}$$

Choosing the reference configuration to be the current configuration i.e. $\boldsymbol{F} = \boldsymbol{I}$, we write the rate form as [MR75]

$$div\left[div\boldsymbol{v}\,\boldsymbol{T} + \dot{\boldsymbol{T}} - \boldsymbol{T}\boldsymbol{L}^{T}\right] = \mathbf{0}. \tag{4.2}$$

The system of equations (3.14) is then augmented with Eq. (4.2) for the quasistatic case. For the dynamic case, the balance of linear momentum can be solved directly to give the material velocity field on the domain.

The discretization methods and statements for solving the equations for the finite deformation MFDM (3.14) are similar to the small deformation case as presented earlier in [RA05, RA06]. The following numerical schemes are used: the Galerkin FEM for the equilibrium equation (3.14d) and its rate form (4.2), and evolution equation (3.14c) for the compatible part of inverse of elastic distortion; the Least-squares FEM [Jia13] for the incompatibility equation (3.14b); and the Galerkin-Least-Squares FEM [HFH89] for the dislocation evolution equation (3.14a). Apart from the changes due to finite deformation, primary changes include the protocols needed to carefully integrate incremental reaction force rates, corresponding to imposed velocity-Dirichlet b.c.s, to obtain consistent traction b.cs. (in the weak form) for balance of linear momentum in the quasistatic case. The (finite element) mesh motion is also taken into account.

We now discuss the numerical schemes to solve the governing equations in a general case, i.e., without any specific constitutive assumptions for $\boldsymbol{T}$, $\boldsymbol{L}^p$, and $\boldsymbol{V}$. A typical time increment going from time t to $t + \Delta t$ is considered.

4.1.1 Weak form for $\boldsymbol{v}$

The Material velocity field $\boldsymbol{v}$ is required to update the geometry discretely by moving the finite element mesh. For the quasistatic case, $\boldsymbol{v}$ is obtained by solving the rate form of equilibrium equation (4.2) while for the dynamic case, it is obtained by solving the balance of linear momentum equation (3.14d).

4.1.1.1 Quasistatic case

We solve the rate form of the equilibrium equation to obtain the material velocity field $\boldsymbol{v}$ on the current configuration Ω following the assumed strain formulation of [NPR74]. We define

$\delta\bar{\boldsymbol{L}}$ to be

$$\delta\bar{\boldsymbol{L}}(\boldsymbol{x}) := grad\delta\boldsymbol{v}(\boldsymbol{x}) - \frac{1}{3}div\delta\boldsymbol{v}(\boldsymbol{x})\boldsymbol{I} + \frac{1}{3\,V(\boldsymbol{x})}\int_{B(\boldsymbol{x})} \boldsymbol{I}\, div\delta\boldsymbol{v}\, dV,$$

where $B(\boldsymbol{x})$ represents the element (in mesh) containing the point $\boldsymbol{x}$ and $V(\boldsymbol{x})$ is the volume of the element B. The weak form is then written as

$$\int_{\Omega} \delta\bar{\boldsymbol{L}} : \left[div\boldsymbol{v}\,\boldsymbol{T} + \dot{\boldsymbol{T}} - \boldsymbol{T}\bar{\boldsymbol{L}}^T\right] dV = \int_{\partial\Omega} \delta\boldsymbol{v}\cdot\dot{\boldsymbol{t}}\, dA.$$

where

$$\bar{\boldsymbol{L}}(\boldsymbol{x}) := \boldsymbol{L}(\boldsymbol{x}) - \frac{1}{3}div\,\boldsymbol{v}(\boldsymbol{x})\boldsymbol{I} + \frac{1}{3\,V(\boldsymbol{x})}\int_{B(\boldsymbol{x})} \boldsymbol{I}\, div\,\boldsymbol{v}(\boldsymbol{x})\, dV$$

and $\dot{\boldsymbol{t}}$ is the specified Neumann boundary condition of nominal traction rate based on the current configuration as the reference. Using the evolution equation for $\boldsymbol{W}$ and the identity $\boldsymbol{F}^e\boldsymbol{W} = \boldsymbol{I}$, we can get the material time derivative of $\boldsymbol{T}$ as

$$\begin{aligned}
\dot{\boldsymbol{F}}^e\boldsymbol{W} + \boldsymbol{F}^e\dot{\boldsymbol{W}} = \boldsymbol{0} \implies \dot{\boldsymbol{F}}^{\mathbf{e}} &= (\boldsymbol{L} - (\boldsymbol{F}^e\boldsymbol{\alpha})\times\boldsymbol{V} - \boldsymbol{F}^e\boldsymbol{L}^p)\,\boldsymbol{F}^e \\
\dot{\boldsymbol{T}} &= \left(\frac{\partial\boldsymbol{T}}{\partial\boldsymbol{F}^e}\right) : \dot{\boldsymbol{F}}^e \\
\dot{\boldsymbol{T}} &= \left(\frac{\partial\boldsymbol{T}}{\partial\boldsymbol{F}^e}\right) : (\boldsymbol{L} - (\boldsymbol{F}^e\boldsymbol{\alpha})\times\boldsymbol{V} - \boldsymbol{F}^e\boldsymbol{L}^p)\,\boldsymbol{F}^e.
\end{aligned}$$

The calculation of $\frac{\partial\boldsymbol{T}}{\partial\boldsymbol{F}^e}$ for the Saint-Venant Kirchhoff and the Neo-Hookean materials are shown in Secs. A.1 and A.2, respectively. Using the expression for $\dot{\boldsymbol{T}}$, the weak form is

finally rewritten as

$$\int_{\Omega} \delta\,\bar{\boldsymbol{L}} : \left[tr(\bar{\boldsymbol{L}})\boldsymbol{T} - \boldsymbol{T}\bar{\boldsymbol{L}}^T + \frac{\partial \boldsymbol{T}}{\partial \boldsymbol{F}^e} : (\bar{\boldsymbol{L}} \cdot \boldsymbol{F}^e) \right] dV = \int_{\Omega} \delta\,\bar{\boldsymbol{L}} : \left[\frac{\partial \boldsymbol{T}}{\partial \boldsymbol{F}^e} : ((\boldsymbol{F}^e \boldsymbol{\alpha}) \times \boldsymbol{V}) \right] + \int_{\Omega} \delta\,\bar{\boldsymbol{L}} : \left[\frac{\partial \boldsymbol{T}}{\partial \boldsymbol{F}^e} : \boldsymbol{L}^p \right] + \int_{\partial\Omega} \delta\bar{\boldsymbol{L}} \cdot \dot{\boldsymbol{t}}\, dA. \tag{4.3}$$

For a given state of the system ($\boldsymbol{T}, \boldsymbol{F}^e, \boldsymbol{L}^p, \boldsymbol{\alpha}, \boldsymbol{x}$, and $\boldsymbol{V}$) at time t, the weak form generates a system of linear equations which is then solved to get the velocity field $\boldsymbol{v}^t$ at time t on the configuration Ω^t at time t. It is important to note that incorporating rate-independent plasticity makes the velocity solve non-linear in nature. This is because $\hat{\gamma}$ is nonlinear in $\boldsymbol{L}$, as can be seen from the expression for $\hat{\gamma}_{ri}$ in Eq. (3.38) and the switch in the loading-unloading conditions. This is taken care of by solving the $\boldsymbol{v}$ equation by using a quasi-Newton technique where we do not modify the stiffness for each iteration.

On part of the boundary where Dirichlet conditions are applied, the nodal reaction force rates at time t^n are calculated after solving (4.2) on the configuration at t^n. The (reaction) nodal force rate field is generated by calculating $[K]\{\boldsymbol{v}\} - \{R\}$, where $[K]$ is the stiffness of the system, $\{\boldsymbol{v}\}$ is the nodal fem solution array, and $\{R\}$ is the nodal array formed after assembly of the first term on the right of (4.2). Physically, $\{R\}$ is the nodal force array from the plastic strain rate that contributes to the material velocity $\boldsymbol{v}$. For each node on this part of the boundary, this reaction force rate physically corresponds to the spatial integration of the nominal/First Piola-Kirchhoff traction rate, based on the configuration at time t^n as reference, over the area patch (on the same configuration) that contributes to the node in question. Since such a nodal force rate, viewed as a discrete function of time, corresponds to the evolving current configuration of the body (recall the definition of the First Piola-Kirchhoff stress tensor), we simply (discretely) integrate it in time and accumulate the result on the known nodal force at time t^n to obtain the nodal force (on the velocity-Dirichlet-part of the boundary) at time t^{n+1}.

4.1.1.2 Dynamic case

For the dynamic case, the balance of linear momentum equation is directly solved to obtain the velocity on the given configuration. Assuming the stresses and material velocity on the current configuration Ω are given, we solve for $\boldsymbol{v}^{t+\Delta t}$ using first order Forward Euler method as follows:

$$\begin{aligned}
\int_\Omega T_{ij,j}\delta v_i \, dV &= \int_\Omega \rho \dot{v}_i \delta v_i \\
\int_\Omega \left(T_{ij}\delta v_i\right)_{,j} \, dV - \int_\Omega T_{ij}\delta v_{i,j} \, dV &= \int_\Omega \frac{1}{\Delta t}\rho \left(v_i^{t+\Delta t} - v_i^t\right) \delta v_i \, dV \\
\int_\Omega \rho v_i^{t+\Delta t}\delta v_i \, dV = \int_\Omega \rho v_i^t \delta v_i \, dV &+ \Delta t \left(\int_{\partial\Omega} t_i \delta v_i \, dA - \int_\Omega T_{ij}\delta v_{i,j} \, dV\right)
\end{aligned} \tag{4.4}$$

4.1.2 Weak form for $\boldsymbol{\chi}$

For a given dislocation density $\boldsymbol{\alpha}$ and a configuration of the body, $\boldsymbol{\chi}$ is evaluated by solving the system (3.14b) along with the Dirichlet boundary conditions mentioned in Sec. 3.4. We use the Least-Squares finite element method to solve for $\boldsymbol{\chi}$ from the *div-curl* system (3.14b). The objective functional J for this system is written as

$$J = \frac{1}{2}\int_\Omega \left(curl\boldsymbol{\chi} + \boldsymbol{\alpha}\right) : \left(curl\boldsymbol{\chi} + \boldsymbol{\alpha}\right) \, dV + \frac{1}{2}\int_\Omega div\boldsymbol{\chi} \cdot div\boldsymbol{\chi} \, dV,$$

resulting in the weak form

$$\begin{aligned}
&\delta J|_{\delta\boldsymbol{\chi}} = 0 \\
&\int_\Omega e_{ijk}\delta\chi_{rk,j}\left(e_{imn}\chi_{rn,m} + \alpha_{ri}\right) \, dV + \int_\Omega \delta\chi_{ij,j}\chi_{im,m} \, dV = 0.
\end{aligned} \tag{4.5}$$

Therefore, solving for $\boldsymbol{\chi}$ on a given configuration Ω for a given dislocation density $\boldsymbol{\alpha}$ gives a system of linear equations which can be easily solved.

4.1.3 Weak form for $\boldsymbol{\alpha}$

The transport equation for $\boldsymbol{\alpha}$ (3.14a) exhibits nonlinear wave type solutions and therefore the solution can develop shocks and discontinuities in the domain. Numerically solving such an equation without the knowledge of upwind/downwind direction is a daunting task. To deal with this, we adopt the Galerkin-Least-Squares FEM approach as described in [HFH89] wherein the Galerkin residual is added to the least squares residual with a non-negative (may be spatially varying) scalar denoted by c. Writing $\boldsymbol{L}^p = \hat{\boldsymbol{L}}^p + \beta\, curl\boldsymbol{\alpha}$, (3.14a) can be rewritten as

$$(div\,\boldsymbol{v})\boldsymbol{\alpha} + \dot{\boldsymbol{\alpha}} - \boldsymbol{\alpha}\boldsymbol{L}^T = -curl\left(\boldsymbol{\alpha}\times\boldsymbol{V} + \hat{\boldsymbol{L}}^p + \beta curl\boldsymbol{\alpha}\right). \tag{4.6}$$

Using the first order forward Euler method (no superscript means $\boldsymbol{\alpha}^{t+\Delta t}$), the Galerkin-Least-Squares residual for Eq. (4.6) can be written as

$$\begin{aligned}
R = &\underline{\int_\Omega \delta\alpha_{ij}\left(\Delta t\, L_{pp}\alpha_{ij} - \Delta t\,\alpha_{ip}L_{jp}\right) dV} + \int_\Omega \delta\alpha_{ij}\left(\alpha_{ij} - \alpha^t_{ij}\right) dV + \Delta t \int_\Omega \varepsilon_{jqp}\,\varepsilon_{jab}\alpha_{ia}V_b\delta\alpha_{ip,q}\, dV \\
&+ \Delta t \int_\Omega \hat{L}^p_{ij}\varepsilon_{jqp}\delta\alpha_{ip,q}\, dV + \Delta t \int_\Omega \beta\varepsilon_{jab}\alpha_{ib,a}\varepsilon_{jqp}\delta\alpha_{ip,q}\, dV \\
&+ \Delta t \int_{\partial\Omega_i} B_{ij}\delta\alpha_{ij}\, dV + \Delta t \int_{\partial\Omega_o} \alpha^t_{ij}V_p n_p\delta\alpha_{ij}\, dV - \Delta t \int_{\partial\Omega} \alpha_{iq}V_j n_q\delta\alpha_{ij}\, dV \\
&- \Delta t \int_{\partial\Omega} \varepsilon_{jpq}\hat{L}^p_{ip}n_q\delta\alpha_{ij}\, dV - \Delta t \int_{\partial\Omega} \beta\varepsilon_{jpq}\varepsilon_{pba}\alpha_{ia,b}n_q\delta\alpha_{ij}\, dV \\
&+ c\Bigg[\int_{\Omega^\circ} A_{ri}\delta\alpha_{ri}\, dV + \underline{\Delta t \int_{\Omega^\circ} L_{pp}A_{ri}\delta\alpha_{ri}\, dV - \Delta t \int_{\Omega^\circ} A_{ri}\delta\alpha_{rp}L_{ip}\, dV} \\
&+ \Delta t \int_{\Omega^\circ} A_{ri}\left(\delta\alpha_{ri,q}V_q - \delta\alpha_{rq,q}V_i + \delta\alpha_{ri}V_{q,q} - \delta\alpha_{rq}V_{i,q}\right) dV \\
&+ \Delta t \int_{\Omega^\circ} A_{ri}(\beta_{,p}\delta\alpha_{ri,p} + \beta\delta\alpha_{ri,pp} - \beta_{,p}\delta\alpha_{rp,i} - \beta\delta\alpha_{rp,ip})\, dV\Bigg],
\end{aligned} \tag{4.7}$$

where

$$A_{ri} = \alpha_{ri} - \alpha^t_{ri} + \Delta t \left[\underline{\alpha^t_{ri} L_{pp} - \alpha^t_{rp} L_{ip}} + \alpha^t_{ri,q} V_q - \alpha^t_{rq,q} V_i + \alpha^t_{ri} V_{q,q} - \alpha^t_{rq} V_{i,q} + \varepsilon_{ipq} \hat{L}^p_{rq,p} + \right.$$
$$\left. + \beta_{,p} \alpha^t_{ri,p} + \beta \alpha^t_{ri,pp} - \beta_{,p} \alpha^t_{rp,i} - \beta \alpha^t_{rp,ip} \right] .$$

$\partial\Omega_i$ and $\partial\Omega_o$ represent the inflow and outflow parts of the boundary $\partial\Omega$. $\boldsymbol{B}$ is the input dislocation flux $\boldsymbol{\alpha}(\boldsymbol{V} \cdot \boldsymbol{n})$ on $\partial\Omega$. Ω° denotes the element interiors. The terms underlined in blue above are the additional terms that enter the discretization for the dislocation density evolution in the finite deformation setting.

Following [HFH89], c is a non-negative (possibly spatially varying) scalar that takes the value 1 in the convection dominated regions and is equal to the grid Péclet number in diffusion dominated regions. Since we take l to be very small, we choose $c = 1$ for MFDM calculations, unless otherwise mentioned.

4.1.4 Weak form for $\boldsymbol{f}$

For the dynamic and the quasistatic cases, $\boldsymbol{f}$ is determined in the domain at any time t by evolving equation (3.14c) in time. However for the quasistatic case, we can also determine $\boldsymbol{f}$ by solving the (nonlinear) equilibrium equation (3.14d), which could be computationally expensive to do at all increments. However, since we solve the rate form of the equilibrium equation (4.2) for the quasistatic case, force balance may not be exactly satisfied as the deformation progresses. Hence to correct for this, we periodically solve equilibrium equation (3.14d) to satisfy balance of forces which is now posed as a traction boundary value problem. These tractions are in the form of nodal reaction forces which are obtained by integrating the nodal reaction force rate array as mentioned in Sec. 4.1.1.1. Solving the equilibrium equation on a given configuration amounts to adjustment of $\boldsymbol{f}$. In the following, $\{\boldsymbol{F}\}$ represents the known nodal force array on the current configuration at time t^n.

4.1.4.1 Solve from $\boldsymbol{f}$ evolution

The evolution equation for the 'plastic position vector' $\boldsymbol{f}$, given by (3.14c), is solved on the current configuration at each time step with the natural b.c.s defined in Sec.3.4 imposed on the external boundary. Letting $\boldsymbol{Y} = (\boldsymbol{\alpha} \times \boldsymbol{V} + \boldsymbol{L}^p - \dot{\boldsymbol{\chi}} - \boldsymbol{\chi}\boldsymbol{L})$ and using a first order forward Euler scheme to update $\boldsymbol{f}$, the weak form of the (3.14c) can be given as ($\boldsymbol{Y}$ is treated as data),

$$\int_\Omega grad\, \boldsymbol{f}^{t+\Delta t} : grad\, \delta \boldsymbol{f}\, dV = \Delta t \int_\Omega \boldsymbol{Y}^t : grad\, \delta \boldsymbol{f}\, dV + \int_\Omega grad\, \boldsymbol{f}^t : grad\, \delta \boldsymbol{f}\, dV.$$

The weak form implies the satisfaction of the natural boundary conditions. We specify $\boldsymbol{f}^{t+\Delta t}$ (equivalent to $\dot{\boldsymbol{f}} = 0$) at an arbitrary point at all times to ensure a unique solution, without loss of generality.

4.1.4.2 Solve from equilibrium equation

At small deformation, the equilibrium equation is linear in $\boldsymbol{f}$ and can be solved in a single iteration. However, it is nonlinear in $\boldsymbol{f}$ at finite deformation and therefore we use the Newton-Raphson technique to solve for $\boldsymbol{f}$ at finite deformation. Here, we present the weak form for both the cases i) small deformation and ii) finite deformation.

4.1.4.3 Small Deformation

At small deformation, the stress becomes a linear function of $\boldsymbol{z}$ which is related to $\boldsymbol{f}$ as shown below in Eq. (4.8). For the linear theory, $\boldsymbol{W}$ can be written as $\boldsymbol{W} \approx \boldsymbol{I} - \boldsymbol{U}^e$ and $\boldsymbol{U}^e$ can be expressed as $\boldsymbol{U}^e = grad\boldsymbol{z} - \boldsymbol{\chi}$ which ensures $curl\boldsymbol{W} = -curl\boldsymbol{U}^e = -\boldsymbol{\alpha}$.

$$\begin{aligned} \boldsymbol{W} &\approx \boldsymbol{I} - \boldsymbol{U}^e \\ grad\boldsymbol{f} + \boldsymbol{\chi} &\approx grad\boldsymbol{x} - grad\boldsymbol{z} + \boldsymbol{\chi} \\ \implies \boldsymbol{f} &\approx \boldsymbol{x} - \boldsymbol{z} \quad \text{(upto a constant)} \end{aligned} \tag{4.8}$$

where $\boldsymbol{x}$ represents the current position of the geometry and therefore $grad\boldsymbol{x} = \boldsymbol{I}$. Once $\boldsymbol{\chi}$ is known, the equilibrium equation in the absence of body forces can be solved for $\boldsymbol{f}$ as

$$R(\boldsymbol{z}) = \int_{\partial\Omega} t_i \, \delta z_i \, dA - \int_{\Omega} T_{ij} \delta z_{i,j} \, dV. \tag{4.9}$$

Since the stress is linear in $\boldsymbol{z}$, we can get the stiffness as

$$\begin{aligned} K_T = \delta R(\boldsymbol{z})|_{d\boldsymbol{z}} &= \delta \left(\int_{\partial\Omega} t_i \, \delta z_i \, dA - \int_{\Omega} T_{ij} \delta z_{i,j} \, dV \right) \\ &= - \int_{\Omega} \frac{\partial T_{ij}}{\partial H_{ab}} dH_{ab} \, \delta z_{ij} \, dV \end{aligned} \tag{4.10}$$

where $H_{ab} = z_{a,b}$. The calculation of $\frac{\partial \boldsymbol{T}}{\partial \boldsymbol{H}}$ for the Saint-Venant Kirchhoff and the Neo-Hookean materials is shown in Sections B.1 and B.2 respectively. After solving for $\boldsymbol{z}$, $\boldsymbol{f}$ can be updated following the relation from Eq. (4.8).

4.1.4.4 Large Deformation

At large deformation, the governing equation $div\boldsymbol{T} = \boldsymbol{0}$ is nonlinear in $\boldsymbol{f}$. Therefore, we use the Newton-Raphson scheme to solve for $\boldsymbol{f}$. Following the scheme outlined in [Pur09], we write the residual at the iteration k (denoted by superscript on the left) for the non-linear Newton-Raphson scheme as

$$R({}^k\boldsymbol{f}) = \int_{\partial\Omega} t_i \delta f_i \, dA - \int_{\Omega} T_{ij} \delta f_{i,j} \, dV.$$

The guess for this Newton-Raphson solve is crucial for success in solving for the $\boldsymbol{f}$ from the equilibrium equation. We denote this guess as $\boldsymbol{f}_0$ and it is determined [ZAP18] as follows:

- For ECDD solves ($t = 0$), $\boldsymbol{f}_0$ is obtained by solving the equilibrium equation on the current configuration by assuming small deformation as shown above in Sec. 4.1.4.3.
- At all other times, $\boldsymbol{f}$ obtained by solving the evolution equation (3.14c) serves as the guess $\boldsymbol{f}_0$ for the Newton-Raphson based scheme.

The Jacobian, denoted by K_T, is calculated by taking a variation of the above residual

$$K_T = \delta R|_{d\boldsymbol{f}} = \int_\Omega \frac{\partial T_{ij}}{\partial G_{ab}} dG_{ab} \delta f_{i,j} \, dV$$

where $G_{ab} = f_{a,b}$.

We calculate $\frac{\partial \boldsymbol{T}}{\partial \boldsymbol{G}}$ as:

$$\frac{\partial \boldsymbol{T}}{\partial \boldsymbol{G}} = \frac{\partial \boldsymbol{T}}{\partial \boldsymbol{F}^e} : \frac{\partial \boldsymbol{F}^e}{\partial \boldsymbol{W}} : \frac{\partial \boldsymbol{W}}{\partial \boldsymbol{G}}.$$

The calculation of $\frac{\partial \boldsymbol{T}}{\partial \boldsymbol{F}^e}$ for the Saint-Venant Kirchhoff and the Neo-Hookean materials is shown in Sections A.1 and A.2, respectively. The other terms on the right hand side of the above equation are given as

$$\begin{aligned} \frac{\partial F^e_{mn}}{\partial W_{pq}} &= -F^e_{qn} F^e_{mp} \\ \frac{\partial W_{pq}}{\partial G_{ab}} &= \delta_{pa} \delta_{qb}. \end{aligned}$$

Therefore,

$$\begin{aligned} \frac{\partial T_{ij}}{\partial G_{ab}} &= \frac{\partial T_{ij}}{\partial F^e_{mn}} \frac{\partial F^e_{mn}}{\partial W_{pq}} \frac{\partial W_{pq}}{\partial G_{ab}} \\ &= -\frac{\partial T_{ij}}{\partial F^e_{mn}} F^e_{qn} F^e_{mp} \delta_{pa} \delta_{qb} \end{aligned}$$

We then solve the finite element system $\{K_T\}\{df\} = -\{R\}$ until the norm of the residual R is less than a certain tolerance.

4.2 Algorithm

We choose a combination of explicit-implicit schemes to evolve the system (3.14) in time. An efficient time stepping criteria based on plastic relaxation, and purely elastic and yield

strain related physical model parameters has been developed. Furthermore, to ensure robust and stable evolution of state variables, an intricate cut-back algorithm is used that carefully controls the magnitude of plastic strain in each increment.

The following notation is used for the description of the algorithm:

1. $(\cdot)^n$ means a quantity at time t^n. $\boldsymbol{x}^n$ represents the coordinates of the finite element mesh on the configuration Ω^n.

2. At any integration point q, the following state variables are stored at any given time t^n: material strength g^n, elastic distortion tensor $\boldsymbol{F}^{en}$, Cauchy stress $\boldsymbol{T}^n$, dislocation velocity $\boldsymbol{V}^n$, slip distortion rate $\boldsymbol{L}^{pn}$. We will collectively refer to them as PH^n (short for point history) of integration points.

3. Δt^n is defined as $t^{n+1} - t^n$. To evaluate Δt^n we first calculate the following variables

$$\Delta t_1 = \frac{.1\,h}{\max(|\boldsymbol{V}|)}$$

$$\Delta t_2 = \frac{.002}{\max(r) + \max(s)}$$

$$\Delta t_3 = \frac{.1\,g_0}{E\ \max(|\boldsymbol{L}|)}$$

$$\Delta t_4 = \frac{.1h}{\boldsymbol{v}_s}$$

where $\max(\cdot)$ denotes the maximum of the quantity $(\cdot)$ over all integration points in the domain, h denotes the length of the smallest edge of an element in the finite element mesh, and $\boldsymbol{v}_s$ is the shear wave speed of the material. r and s are the functions of plastic strain rate (on the current configuration) due to EDs and SDs given by

$$r = |\boldsymbol{F}^e \boldsymbol{\alpha} \times \boldsymbol{V}|,$$

$$s = \begin{cases} \hat{\gamma} & J_2 \text{ plasticity} \\ \sum_k^{n_{sl}} |\hat{\gamma}^k| & \text{Crystal plasticity.} \end{cases}$$

Δt_1 is based on the physical fact that the dislocation density can only move a fraction of h in any given time interval. Δt_2 ensures that the maximum plastic strain at any given point in a time step has an upper bound of 0.2%. Δt_3 puts a bound on the maximum strain that can be attained in a time step at any point in the domain. Δt^n is then given as

$$\Delta t^n = \begin{cases} \min\left(\Delta t_1, \Delta t_2, \Delta t_3\right) & \text{Quasistatic case} \\ \min\left(\Delta t_1, \Delta t_2, \Delta t_3, \Delta t_4\right) & \text{Dynamic case} \end{cases} \tag{4.11}$$

The algorithms for the quasistatic and dynamic cases are shown in Sections 4.1 and 4.2, respectively.

4.2.1 Quasistatic case

Given: material properties, initial conditions, boundary conditions, and applied loading conditions.
Step 1: Finding the initial stress field on the body in 'as-received' configuration - ECDD solve. • ECDD solve, mentioned in Sec. 3.5, is done on the initial configuration, i.e. current configuration at $t = 0$. • This gives us $\boldsymbol{f}$, $\boldsymbol{\chi}$, and $\boldsymbol{T}$ on the configuration of the body at $t = 0$.
Step 2: Evolution of the system: Assume that the state at time t^n is known: $\boldsymbol{x}^n$, $\boldsymbol{\alpha}^n$, $\boldsymbol{f}^n$, $\boldsymbol{\chi}^n$, $\dot{\boldsymbol{\chi}}^n$, $\boldsymbol{V}^n$, $\boldsymbol{L}^p$, Δt^n, PH^n To get the state at time step t^{n+1} the following is done:

- The rate form of the equilibrium equation (4.2) is solved on Ω^n to get the material velocity $\boldsymbol{v}^n$ in the interval $[t^n, t^{n+1}]$ as described in Sec. 4.1.1.1. $\boldsymbol{v}^n \equiv \boldsymbol{v}(\boldsymbol{\alpha}^n, \boldsymbol{L}^{pn}, \boldsymbol{V}^n, \boldsymbol{F}^{en}, \boldsymbol{x}^n)$.
- $\boldsymbol{\alpha}$ evolution equation (3.14a) is solved on Ω^n using Galerkin-Least-Squares FEM as shown in Sec. 4.1.3 to obtain $\boldsymbol{\alpha}^{n+1}$ on Ω^{n+1}. $\boldsymbol{\alpha}^{n+1} \equiv \boldsymbol{\alpha}(\boldsymbol{\alpha}^n, \boldsymbol{L}^{pn}, \boldsymbol{V}^n, \boldsymbol{F}^{en}, \boldsymbol{L}^n, \boldsymbol{x}^n)$.
- The configuration of the body is discretely updated i.e. $\boldsymbol{x}^{n+1} = \boldsymbol{x}^n + \boldsymbol{v}^n \, \Delta t^n$.
- $\boldsymbol{\chi}^{n+1}$ on Ω^{n+1} is obtained by solving Eq. (3.14b) on Ω^{n+1} as described in Sec. 4.1.2. $\boldsymbol{\chi}^{n+1} \equiv \boldsymbol{\chi}(\boldsymbol{\alpha}^{n+1}, \boldsymbol{x}^{n+1})$.
- $\boldsymbol{f}^{n+1}$ on Ω^{n+1} is obtained by doing one of the following:
  1. Solve $\boldsymbol{f}$ evolution Eq. (3.14c) on Ω^n as described in Sec. 4.1.4.1. $\boldsymbol{f}^{n+1} \equiv \boldsymbol{f}(\boldsymbol{\alpha}^n, \boldsymbol{L}^{pn}, \boldsymbol{V}^n, \dot{\boldsymbol{\chi}}^n, \boldsymbol{\chi}^n, \boldsymbol{L}^n, \boldsymbol{x}^n)$.
  2. Equilibrium equation (3.14d) is solved in alternate increments to adjust $\boldsymbol{f}^{n+1}$ on Ω^{n+1} as shown in Sec. 4.1.4.4. $\boldsymbol{f}^{n+1}$ obtained by solving Eq. (3.14c) serves as the the initial guess for the Newton Raphson scheme.
- $\dot{\boldsymbol{\chi}}^{n+1}$ is calculated as follows: $\dot{\boldsymbol{\chi}}^{n+1} = \dfrac{\boldsymbol{\chi}^{n+1} - \boldsymbol{\chi}^n}{\Delta t^n}$.
- PH^{n+1} is updated on the configuration Ω^{n+1}.

If $(r+s) \times \Delta t^n \geq 0.002$ is satisfied at any integration point on the domain:

- Go to state at time t^n.
- Use Δt^n half of the previous one.

If no cut back happens, then the state is accepted. Δt^{n+1}, based on the new state, is calculated from (4.11) and this algorithm is repeated to get state at increment t^{n+2}.

Table 4.1: Quasi-static MFDM algorithm

4.2.2 Dynamic case

Given: material properties, initial conditions, boundary conditions, and applied loading conditions.

Step 1: Finding the initial stress field on the body in 'as-received' configuration - ECDD solve.

- ECDD solve, mentioned in Sec. 3.5, is done on the initial configuration, i.e. current configuration at $t = 0$.
- This gives us $\boldsymbol{f}$, $\boldsymbol{\chi}$, and $\boldsymbol{T}$ on the configuration of the body at $t = 0$.

Step 2: Evolution of the system: Assume that $\boldsymbol{v}^{n-1}$ and the state at time t^n is known: $\boldsymbol{x}^n$, $\boldsymbol{\alpha}^n$, $\boldsymbol{f}^n$, $\boldsymbol{\chi}^n$, $\dot{\boldsymbol{\chi}}^n$, $\boldsymbol{V}^n$, $\boldsymbol{L}^p$, Δt^n, PH^n
To get the state at time step t^{n+1} the following is done:

- The balance of linear momentum Eq. (4.2) is solved on Ω^n to get the material velocity $\boldsymbol{v}^n$ in the interval $[t^n, t^{n+1}]$ as described in Sec. 4.1.1.2. $\boldsymbol{v}^{n+1} \equiv \boldsymbol{v}(\boldsymbol{f}^n, \boldsymbol{\chi}^n, \boldsymbol{v}^{n-1}, \boldsymbol{x}^n)$.
- $\boldsymbol{\alpha}$ evolution equation (3.14a) is solved on Ω^n using Galerkin-Least-Squares FEM as shown in Sec. 4.1.3 to obtain $\boldsymbol{\alpha}^{n+1}$ on Ω^{n+1}. $\boldsymbol{\alpha}^{n+1} \equiv \boldsymbol{\alpha}(\boldsymbol{\alpha}^n, \boldsymbol{L}^{pn}, \boldsymbol{V}^n, \boldsymbol{F}^{en}, \boldsymbol{L}^n, \boldsymbol{x}^n)$.
- $\boldsymbol{f}^{n+1}$ on Ω^{n+1} is obtained by solving $\boldsymbol{f}$ evolution Eq. (3.14c) on Ω^n as described in Sec. 4.1.4.1. $\boldsymbol{f}^{n+1} \equiv \boldsymbol{f}(\boldsymbol{\alpha}^n, \boldsymbol{L}^{pn}, \boldsymbol{V}^n, \dot{\boldsymbol{\chi}}^n, \boldsymbol{\chi}^n, \boldsymbol{L}^n, \boldsymbol{x}^n)$.
- The configuration of the body is discretely updated i.e. $\boldsymbol{x}^{n+1} = \boldsymbol{x}^n + \boldsymbol{v}^n \, \Delta t^n$.
- $\boldsymbol{\chi}^{n+1}$ on Ω^{n+1} is obtained by solving Eq. (3.14b) on Ω^{n+1} as described in Sec. 4.1.2. $\boldsymbol{\chi}^{n+1} \equiv \boldsymbol{\chi}(\boldsymbol{\alpha}^{n+1}, \boldsymbol{x}^{n+1})$.
- $\dot{\boldsymbol{\chi}}^{n+1}$ is calculated as follows: $\dot{\boldsymbol{\chi}}^{n+1} = \dfrac{\boldsymbol{\chi}^{n+1} - \boldsymbol{\chi}^n}{\Delta t^n}$.
- PH^{n+1} is updated on the configuration Ω^{n+1}.

If $(r + s) \times \Delta t^n \geq 0.002$ is satisfied at any integration point on the domain:

- Go to state at time t^n.
- Use Δt^n half of the previous one.

If no cut back happens, then the state is accepted. Δt^{n+1}, based on the new state, is calculated from (4.11) and this algorithm is repeated to get state at increment t^{n+2}.

Table 4.2: MFDM algorithm with inertia

4.3 Computational framework

An MPI-accelerated finite element based computational computational framework for the full finite deformation MFDM is developed using C++. The framework is based on the algorithms presented in Sec. 4.2 above and is developed using comprehensive state-of-the-art libraries Deal.ii [ABD+17], P4est [BWG11], MUMPS [ADKL01], and PetSc [BAA+17]. Integration of these libraries along with the judicious use of object oriented design creates a computational environment that is flexible and powerful enough to meet the specific requirements of the current research. The functionality obtained from their combination is suited for large scale numerical simulations using adaptive mesh refinement. The code is extensively based on Deal.ii which is an open-source framework for the numerical simulation of partial differential equations using the Finite Element Method on serial and parallel platforms. We have coupled it with PetSc for the solution of the discretized system (3.14) and with P4est for meshing the domain. Using P4est enables us to mesh the body into a collection of adaptive octrees and splits the mesh on every processor while dynamically balancing the number of unknowns on each processor. PetSc is used to efficiently store large sparse matrices and vectors using high level data structure. It also provides access to several direct and iterative solvers which are highly efficient and scalable. The code has been optimized to run on the PSC bridges supercomputer and Mesabi supercomputer of MSI.

A post-processing toolbox has been developed in Python using its Scipy [JOP+], Numpy [Oli], Pandas [M+10, McK11], Matplotlib [Hun07], and Seaborn [W+18] modules to produce publication-quality figures. The toolbox has a feature to automatically search for data files corresponding to required strain levels or iteration numbers out of thousands of output files and pass it to the 'plotting' script, greatly enhancing the efficiency in data-processing for scientific visualization. The figures presented in this document are obtained using this developed toolbox.

Chapter 5

Results and discussion: FDM

In this chapter, we present results of some selected physically meaningful verification tests for the developed FDM computational framework. To our knowledge, the results presented here are also the first fully nonlinear results (in kinematics, elasticity, and dissipation) involving dislocation mediated plasticity. The organization of the chapter is as follows:

1. In Sec. 5.1, we verify the framework by studying the problem of homogeneous elastic deformation, under simple shear and extensional loadings (both quasistatic), of a block of Saint-Venant-Kirchhoff and Neo-Hookean materials. When the velocity boundary conditions are applied for an assumed homogeneous purely elastic deformation history, it is expected that the numerics should reproduce the homogeneous deformation with no numerically induced hysteresis upon unloading. However, given the extensive use of the incremental equilibrium equation (4.2) in our scheme, it is not a priori clear that no hysteresis is induced in the numerical approximation. This overall test also verifies the algorithm for the accumulation of reaction forces due to velocity-Dirichlet boundary conditions.

2. In Sec. 5.2, we calculate the finite deformation stress fields of a screw dislocation embedded inside a body of finite extent that is assumed to behave as a variant of a Neo-Hookean material, and verify it with the analytical solution for the same case. We then calculate the finite deformation stress field of an edge dislocation embedded in a Saint-Venant Kirchhoff material. We also demonstrate large deviation from small deformation analytical stress fields in the domain by comparing it with the finite deformation solution obtained from FDM for both the screw and the edge dislocations (embedded in an infinite body).

3. In Sec. 5.3, the framework is then verified against the elastic loading of a Saint-Venant Kirchhoff material with defect evolution in the special case wherein there is no generation or motion of the defect relative to the material. The dislocation density evolution solely takes place because of coupling of the transport equation (3.14a) with the ge-

ometry and the velocity gradient in the convected derivative of the dislocation density. In the absence of any flux of dislocations, the Burgers vector content of any arbitrary area patch has to be conserved. Sec. 5.3 verifies these hypotheses under quasistatic simple shear and extensional loadings.

4. Section 5.4 presents the stress field in the domain with a spatially homogeneous dislocation distribution. We show contrasting predictions of the stress field by the linear and nonlinear FDM theory.

5. Sec. 5.5 uses FDM to calculate the change in the volume of the body with the introduction of dislocations. The linear theory predicts no volume change when the dislocations are introduced in the body which is not in agreement with experimental observations. We also calculate the reference configurations of the body with single or multiple embedded dislocations. The possibility of non-uniqueness in the reference configurations for both the cases is also demonstrated.

6. Sec. 5.6 presents the stress field in the body for a sequence of dislocation distributions comprising a single dislocation core to a full dislocation wall which constitutes a grain boundary. We demonstrate the failure of linear theory to predict the stress field and the energy in the limiting case, when the cores combine to form the grain boundary.

7. Sec. 5.7 presents results for dislocation core(s) moving in the body modeled with inertial effects taken into account, along with the geometric nonlinearity. The results are presented for the case when the dislocation velocity is uncoupled to the underlying stress field. We show the evolution of the dislocation density and plastic deformation in the body. This has implications in the phenomenon of shear band formation wherein a plastic deformation is localized in a narrow band and the band propagates (extends) longitudinally through the motion of its tip.

For all the results presented in this work, the input flux $\boldsymbol{\alpha}(\boldsymbol{V}\cdot\boldsymbol{n})$ and $curl\boldsymbol{\alpha}\times\boldsymbol{n}$ are assumed to be $\mathbf{0}$ on the boundary. Also, $\hat{\boldsymbol{L}}^p$ is directly evaluated at the boundary to calculate

$\hat{\boldsymbol{L}}^p \times \boldsymbol{n}$. All fields are interpolated using bilinear/trilinear elements in $2d/3d$, unless otherwise stated. Following Eq. (3.1), the Burgers vector content of an area patch A with normal $\boldsymbol{n}$ is given by

$$\boldsymbol{b}_A = \int_A \boldsymbol{\alpha}\boldsymbol{n}\, dA. \tag{5.1}$$

where $\boldsymbol{\alpha}$ denotes the dislocation density field in the domain. The Burgers vector of a localized dislocation distribution $\boldsymbol{\alpha}$ is given as

$$\boldsymbol{b} = \int_{A_c} \boldsymbol{\alpha}\boldsymbol{n}\, dA, \tag{5.2}$$

where A_c denotes any area patch fully enclosing the dislocation. It must be noted that $\boldsymbol{b}$ is independent of the chosen area patch A_c as any A_c encloses the full dislocation field. We refer to the magnitude of Burgers vector, $|\boldsymbol{b}|$, as the strength of the dislocation. b is a material constant which refers to the Burgers vector magnitude of a full dislocation in the material. h denotes the length of the smallest edge of an element in the finite element mesh.

The conventional plasticity solution for homogeneous deformation shown in the figures is numerically obtained by integrating the evolution equation (5.3) for the elastic distortion tensor $\boldsymbol{F}^e$ to determine the Cauchy stress response for an imposed spatially homogeneous velocity gradient history, $\boldsymbol{L}$, corresponding to the applied homogeneous deformation:

$$\begin{aligned} \dot{\boldsymbol{F}}^e &= \boldsymbol{L}\boldsymbol{F}^e - \boldsymbol{F}^e\boldsymbol{L}^p\boldsymbol{F}^e =: \tilde{\boldsymbol{f}}(\boldsymbol{F}^e, g) \\ \dot{g} &= \tilde{g}(\boldsymbol{F}^e, g) \end{aligned} \tag{5.3}$$

where $\boldsymbol{L}^p$ is defined from Eq. (3.23) or (3.25) with $l = 0$, and $\tilde{g}$ is given by (3.33) with $k_0 = 0$. For purely elastic deformations, $\boldsymbol{L}^p$ is taken as $\boldsymbol{0}$ in Eq. (5.3).

A typical schematic of the geometry is shown in Fig. 5.1. The stress-strain behavior of the body under shear loading is modeled by plotting the averaged T_{12} component of the

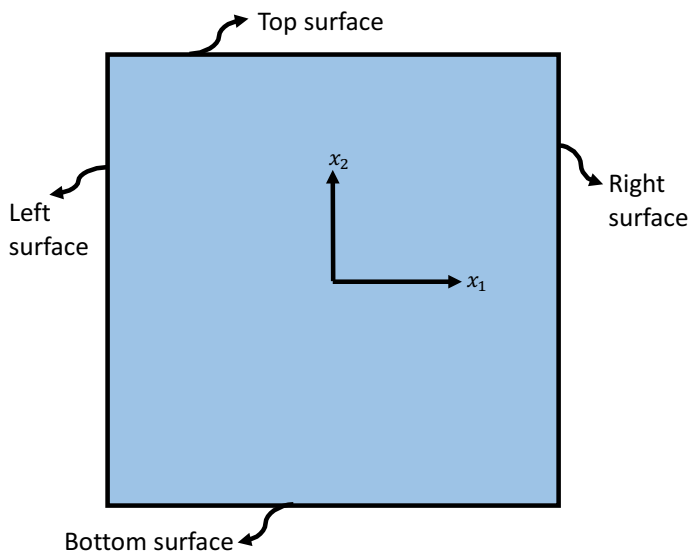

Figure 5.1: Typical schematic of the geometry.

stress tensor on the top surface, which is denoted by τ in the figures. τ is calculated by summing the tangential components of the nodal reaction force on the top surface and then dividing by the current area (line length) of the surface. The stress-strain behavior of the body under extensional loading is modeled by plotting the averaged T_{11} component of stress, on the right surface which is denoted by σ in the figures. σ is calculated by summing the normal components of the nodal reaction force on the right surface and then dividing by the current area (line length) of the surface. $\hat{\Gamma}$ represents the applied strain rate. The shear strain at any time t is denoted by Γ and it is calculated as $\hat{\Gamma}t$. The extensional strain is denoted by ϵ.

5.1 Nonlinear elasticity

Due to our interest in calculating hyperelastic stress fields of dislocations, it is essential to make sure that our scheme accurately reproduces classical hyperelastic response. This includes the prediction of no hysteresis in a loading-unloading cycle, despite the extensive use of the incremental equilibrium equation (4.2) in our algorithm, even for purely elastic problems.

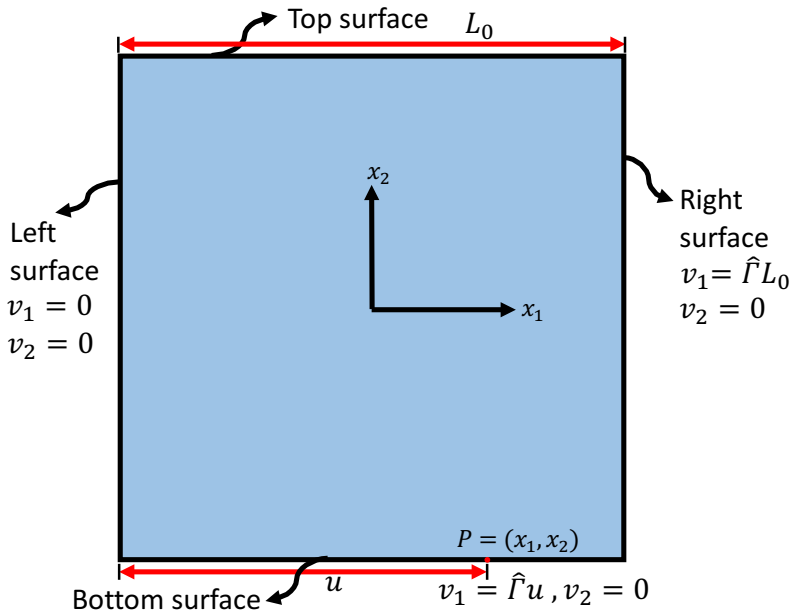

Figure 5.2: Typical schematic of the geometry for extensional loading.

A 2-d plane strain problem is set up as follows: a body of size $(1\,mm)^2$ (the size is immaterial) is set up for homogeneous extension and simple shear loadings with details below. Upon reaching 100% strain, the loading is reversed and the body is unloaded to its original configuration.

To model a purely elastic process, the dislocation velocity and the plastic strain rate due to SDs are assumed to vanish i.e. $\boldsymbol{L}^p = \mathbf{0}$ and $\boldsymbol{V} = \mathbf{0}$. The velocity boundary conditions for the simple shear loading are as follows: at any point $P = (x_1, x_2)$ on the boundary, a velocity of the form $v_2 = 0$ and $v_1 = \hat{\Gamma} y(x_2)$ is imposed, where $y(x_2)$ is the height of the point P from the bottom surface. For the extension case, at the point $P = (x_1, x_2)$, the velocity boundary conditions of the form $v_1 = \hat{\Gamma} u(x_1)$ and $v_2 = 0$ are applied, where $u(x_1)$ is the distance of the point from the left face in the reference configuration. The schematic of the set up for extensional loading is shown in Figure 5.2. Table 5.1 presents the values of the material parameters used for this simulation.

We plot the stress strain response for the Saint-Venant Kirchhoff and the Neo-Hookean materials for the extension (σ vs. ϵ) and shear (τ vs. Γ) loadings in Figures 5.3a and 5.3b,

Parameter	Value
$\hat{\Gamma}$	$1s^{-1}$
E	62.78 GPa
ν	.3647

Table 5.1: Parameter values used for homogeneous elastic deformation.

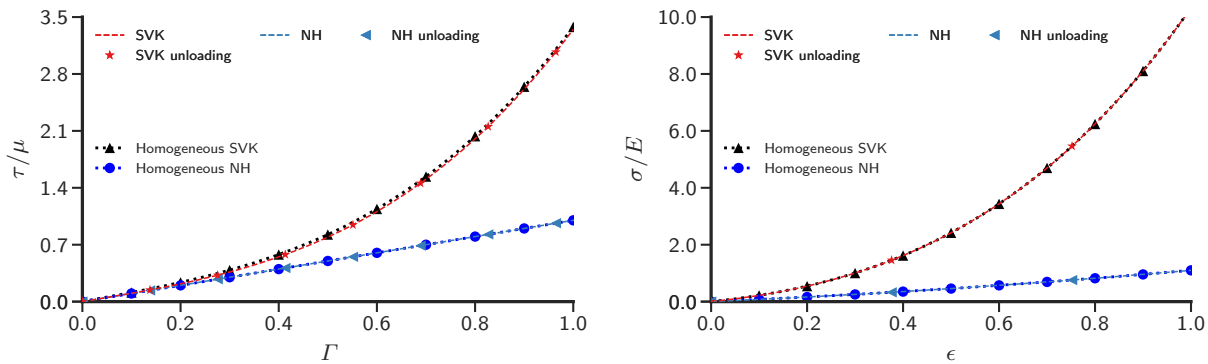

(a) (b)

Figure 5.3: Stress strain response for nonlinear elasticity a) Simple shear b) Uniaxial extension.

respectively. We notice that the stress strain plots overlap with the corresponding homogeneous solution. Moreover, the cyclic stress-strain response does not show any hysteresis.

Furthermore, we also study the effect of variation in stress with large homogeneous rigid rotations for the Saint-Venant Kirchhoff material. We calculate the stress-strain response for a superposed rigid body motion given by

$$\boldsymbol{x}^*(\boldsymbol{X}, t) = \boldsymbol{Q}(t)\boldsymbol{F}^{ss}(t)\boldsymbol{X}, \tag{5.4}$$

where $\boldsymbol{X}$ and $\boldsymbol{x}^*$ are the coordinates of the body in the reference and the current configurations, respectively. $\boldsymbol{F}^{ss}$ denotes the deformation gradient corresponding to a homogeneous simple shearing motion with $F_{12} = \hat{\Gamma}\, t$ and $F_{11} = F_{22} = F_{33} = 1$. $\boldsymbol{Q}(t)$ is the rotation tensor

written as

$$\boldsymbol{Q}(t) = \begin{bmatrix} cos(\theta(t)) & -sin(\theta(t)) & 0 \\ sin(\theta(t)) & cos(\theta(t)) & 0 \\ 0 & 0 & 1 \end{bmatrix}, \tag{5.5}$$

where $\theta(t) = \omega t$ denotes the orientation of the body at any time t and $\omega = 2\,rad.\,s^{-1}$ is the (constant) angular speed of the body about the x_3 axis. The deformation gradient of the rotated motion at any time t is given by $\boldsymbol{F}^*(t) = \boldsymbol{Q}(t)\,\boldsymbol{F}^{ss}(t)$ from Eq. (5.4). The velocity boundary conditions follow from

$$\boldsymbol{v}^*(\boldsymbol{X}, t) = \dot{\boldsymbol{Q}}(t)\boldsymbol{F}^{ss}(t)\boldsymbol{X} + \boldsymbol{Q}(t)\dot{\boldsymbol{F}}^{ss}(t)\boldsymbol{X},$$

evaluated on the boundary of the reference configuration.

Under the superposed rigid body motion defined by Eq. (5.4), the stress tensor for any frame-indifferent stress response function is given as $\boldsymbol{T}^*(t) = \boldsymbol{Q}(t)\boldsymbol{T}^{ss}(t)\boldsymbol{Q}^T(t)$, where $\boldsymbol{T}^{ss}(t)$ denotes the stress field for the simple shearing motion defined by $\boldsymbol{F}^{ss}$. We compare the maximum error in the stress up to 100% strain defined by $\max_{\boldsymbol{X}} \frac{|\boldsymbol{T}(\boldsymbol{X})-\boldsymbol{T}^*(\boldsymbol{X})|}{|\boldsymbol{T}^*(\boldsymbol{X})|} \times 100$. We find that the error accumulates at a very slow rate, leading to a maximum error of $\approx 1\%$ at $\Gamma = 1$.

We therefore conclude that the framework is capable of dealing adequately with nonlinear elasticity, without any (numerically induced) hysteresis/dissipation. Moreover, the protocol for accumulation of reaction tractions (Sec. 4.1.1.1) discretely in time is sufficiently precise in dealing with large strains and rotations.

5.2 Stress fields of single dislocations

We calculate the finite deformation stress fields of single dislocations embedded in a body which requires the solution to the ECDD system (3.31) and (3.32) as explained in Sec. 3.5.

Although we take the material to be isotropic, it is important to note that the finite deformation stress field of any distribution of dislocations in a general anisotropic material with arbitrary (but statically admissible) traction boundary conditions can be calculated without any additional complexity. Table 5.2 shows the values of the material constants used in this section.

Parameter	Value
E	200 GPa
ν	.30

Table 5.2: Parameter values used for calculating stress fields of single dislocations.

5.2.1 Screw dislocation

The material is modeled as a compressible Neo-Hookean model whose stress response is given by Eq. (3.22). A horizontal cylindrical plate, assumed to be thick in the x_3 direction and infinitely extended in the x_1-x_2 plane, has a screw dislocation embedded in it. The strength of the dislocation is assumed to be b and its line direction is assumed to be in the positive x_3 direction i.e. $\boldsymbol{b} = b\boldsymbol{e}_3$. Assuming the dislocation to be present in a cylindrical region centered on the x_3 axis, the dislocation density is modeled by specifying an $\boldsymbol{\alpha}$ field of the form

$$\alpha_{33}(x_1, x_2, x_3) = \varphi\left(\sqrt{x_1^2 + x_2^2}\right), \quad \alpha_{ij} = 0 \text{ if i} \neq 3 \text{ and j} \neq 3, \tag{5.6}$$

where φ is a positive scalar-valued function of one variable. We also assume that the front and back ends of the cylinder are capable of providing arbitrary tractions. A complete exact solution of the ECDD equations for this problem is developed in [Ach01] for the incompressible Neo-Hookean material. That solution is easily adapted here to develop the exact solution for the compressible Neo-Hookean material whose elastic response is given by Eq. (3.22). We outline the exact solution first before using it to verify our code. The particular solution $\boldsymbol{W}$ satisfying the ECDD equations (3.31) is given by $\boldsymbol{I} - H\boldsymbol{\alpha}$, where the

nonzero components of $H\boldsymbol{\alpha}$ are

$$H\alpha_{31}(x_1, x_2) = \frac{-x_2}{x_1^2 + x_2^2} \int_0^r \varphi(s) s \, ds,$$

$$H\alpha_{32}(x_1, x_2) = \frac{x_1}{x_1^2 + x_2^2} \int_0^r \varphi(s) s \, ds.$$

We make the choice

$$\varphi(r) = \begin{cases} \varphi_0 & r < r_0 \\ 0 & r > r_0. \end{cases} \tag{5.7}$$

where $r = \sqrt{x_1^2 + x_2^2}$ and φ_0 is a constant chosen to make the dislocation Burgers vector equal to $b\boldsymbol{e}_3$ by ensuring $\int_A \alpha_{33} \, dA = b$ on any cross section A perpendicular to $\boldsymbol{e}_3$ which encloses the dislocation. Thus, φ_0 is calculated as

$$\begin{aligned} b &= \int_0^{2\pi} \int_0^{r_0} \varphi(r) r \, dr \, d\theta \\ \implies \varphi_0 &= \frac{b}{\pi \, r_0^2}. \end{aligned}$$

$H\boldsymbol{\alpha}$ is then given by

$$H\alpha_{31}(r) = \begin{cases} -x_2 \dfrac{\varphi_0}{2} & r < r_0 \\ -x_2 \dfrac{\varphi_0 r_0^2}{2r^2} & r > r_0 \end{cases}$$

$$H\alpha_{32}(r) = \begin{cases} x_1 \dfrac{\varphi_0}{2} & r < r_0 \\ x_1 \dfrac{\varphi_0 r_0^2}{2r^2} & r > r_0. \end{cases}$$

The elastic distortion tensor $\boldsymbol{F}^e$ is calculated as $\boldsymbol{F}^e = \boldsymbol{W}^{-1} = \boldsymbol{I} + H\boldsymbol{\alpha}$. The analytical stress field $\boldsymbol{T}^*$, which satisfies equilibrium (without any further compensating fields) is calculated as:

$$\boldsymbol{G}^e = \boldsymbol{F}^e \boldsymbol{F}^{eT} = \begin{bmatrix} 1 & 0 & H\alpha_{31} \\ 0 & 1 & H\alpha_{32} \\ H\alpha_{31} & H\alpha_{32} & 1 + (H\alpha_{31})^2 + (H^2\alpha_{32})^2 \end{bmatrix}$$

$$\boldsymbol{T}^* = \mu \boldsymbol{G}^e - \mu \boldsymbol{I}$$

$$\implies \boldsymbol{T}^* = \mu \begin{bmatrix} 0 & 0 & H\alpha_{31} \\ 0 & 0 & H\alpha_{32} \\ H\alpha_{31} & H\alpha_{32} & (H\alpha_{31})^2 + (H\alpha_{32})^2 \end{bmatrix}. \tag{5.8}$$

To compute the stress field, the problem is set up as follows: we specify a dislocation density of the form given by Eqs. (5.6) and (5.7) in a cylinder of radius $50b$ extending from $z = 0$ to $50b$. To mimic the infinite domain size, traction boundary conditions corresponding to the analytical solution are imposed on the outer surface of the cylinder i.e. $\boldsymbol{t} = \boldsymbol{T}^* \boldsymbol{n}$ is used in Eq. (3.32) where $\boldsymbol{T}^*$ is given by Eq. (5.8).

Figure 5.4a shows the dislocation density distribution in the domain on the $z = 0$ plane. Figure 5.4b shows good comparison of the numerically and analytically calculated stress field component T_{23} plotted along $x_2 = 0$ on the $z = 0$ plane.

Figures 5.5a and 5.5b show finite deformation stress fields of the screw dislocation on the plane $z = 0$ obtained from FDM.

Figures 5.6a and 5.6b show the relative difference between numerical and analytical stress fields in the $z = 0$ plane. The regions where the analytical stress components vanish have been marked by black lines. Except for the region in the core, the error is less than 2% everywhere.

Next, for a Saint-Venant-Kirchhoff material, we compare the finite deformation stress

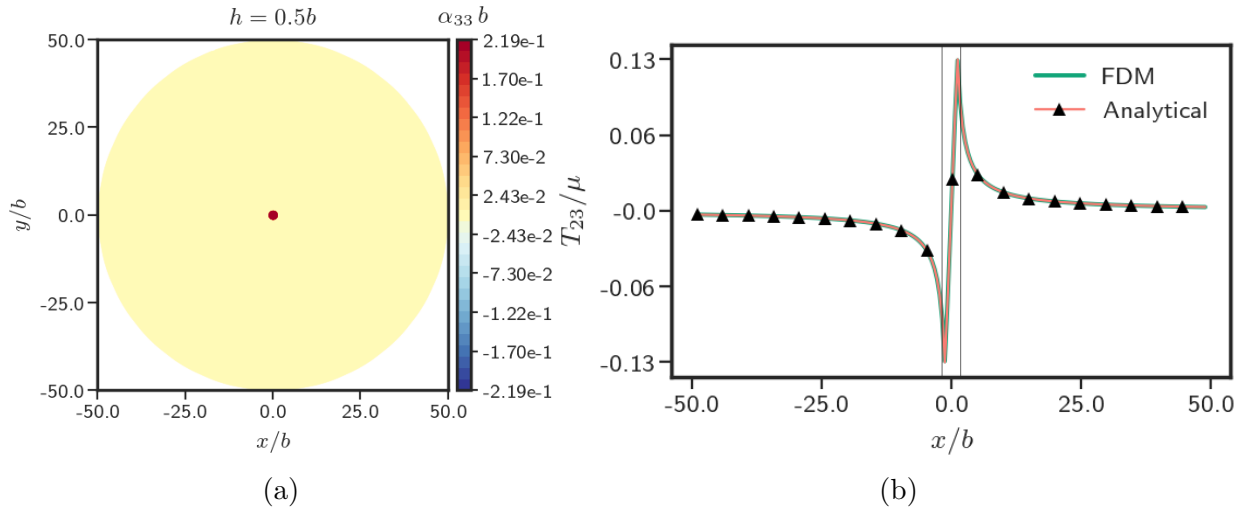

(a) (b)

Figure 5.4: a) Dislocation density, α_{33}, for the screw dislocation on $z = 0$ plane in the cylindrical body b) Comparison of analytical solution of ECDD equations (3.31) to its numerical solution for T_{23} of the screw dislocation along $x_2 = 0$.

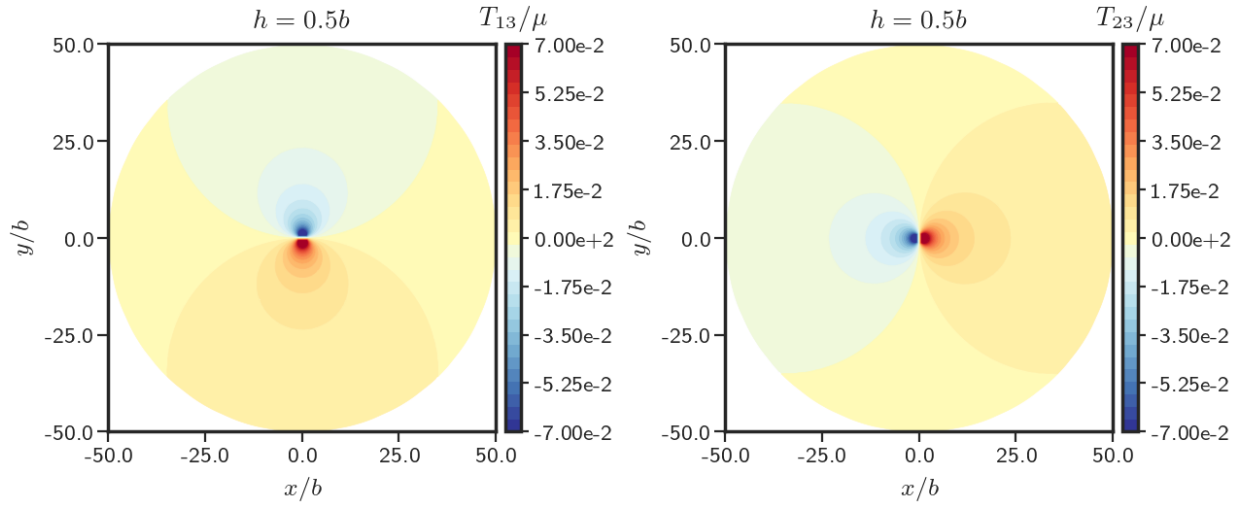

(a) (b)

Figure 5.5: Stress field of a screw dislocation embedded in the cylindrical domain behaving as a compressible Neo-Hookean material a) $\frac{T_{13}}{\mu}$ b) $\frac{T_{23}}{\mu}$.

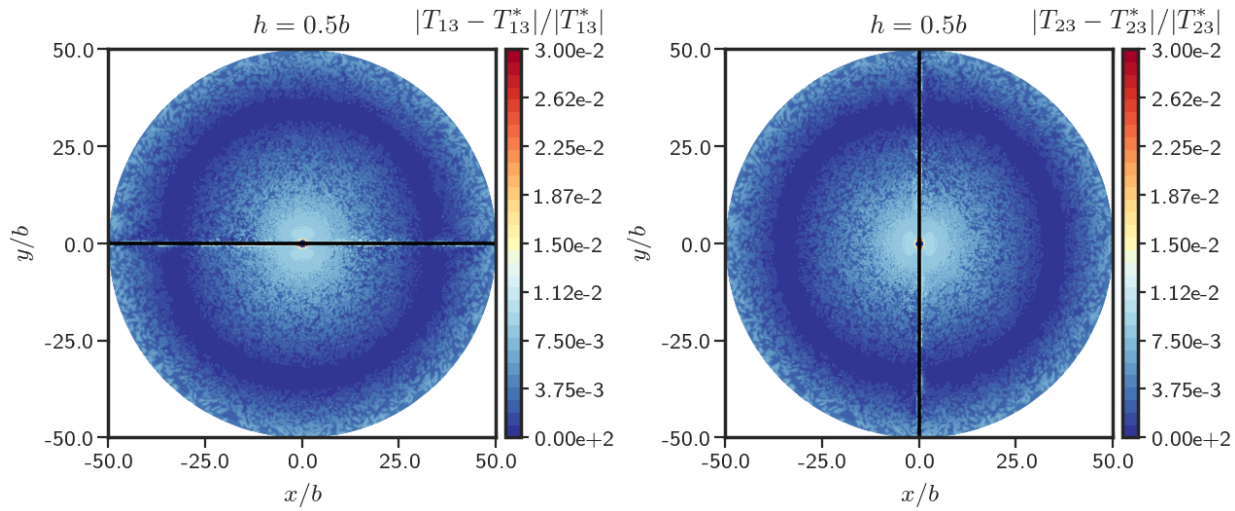

(a) (b)

Figure 5.6: Comparison of the numerical and analytical solutions of stress field of screw dislocation in the cylindrical domain on the $z = 0$ plane a) $\frac{|T_{13} - T^*_{13}|}{|T_{13}|}$ b) $\frac{|T_{23} - T^*_{23}|}{|T_{23}|}$

field of a screw dislocation with the small deformation analytical solution. The analytical solution is given by [HL82]

$$
\begin{aligned}
T^*_{13} &= -\frac{\mu b}{2\pi} \cdot \frac{x_2}{(x_1^2 + x_2^2)} \\
T^*_{23} &= \frac{\mu b}{2\pi} \cdot \frac{x_1}{(x_1^2 + x_2^2)} \\
T^*_{11} &= T^*_{22} = T^*_{33} = T^*_{12} = 0.
\end{aligned}
\tag{5.9}
$$

The problem is set up for a Saint-Venant-Kirchhoff material in the same way as above except now the tractions imposed on the outer surface of the cylinder are determined by using $\boldsymbol{T}^*$ from Eq. (5.9) in Eq. (3.32).

We define a difference measure M of the form

$$
M = \frac{|\Delta \boldsymbol{T}|}{|\boldsymbol{T}^*|} = \frac{|\boldsymbol{T} - \boldsymbol{T}^*|}{|\boldsymbol{T}^*|} \tag{5.10}
$$

where $\boldsymbol{T}$ is the stress obtained from the (finite deformation) numerical computations and $\boldsymbol{T}^*$ is the (small deformation) analytical solution. The plot of M in the domain, shown in

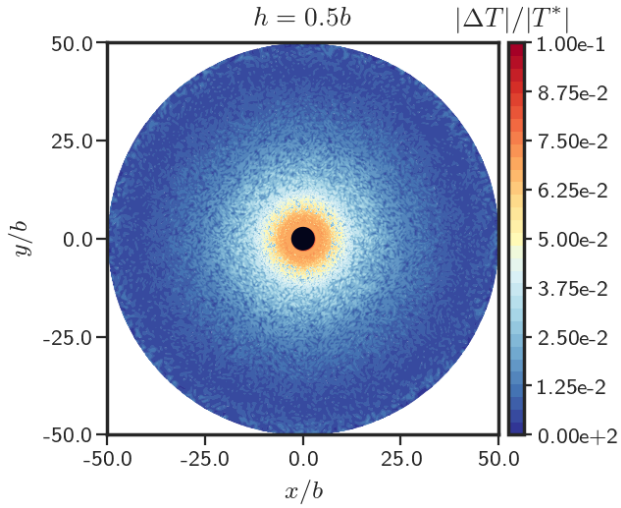

Figure 5.7: Difference between stress field given by the finite deformation FDM theory and small deformation analytical solution for a screw dislocation embedded in a cylindrical domain for a Saint-Venant-Kirchhoff material.

Figure 5.10, clearly displays that the stress fields differ in a large region around the core. Therefore, we establish that up to $\approx 6\%$ error arise as far as $10b$ from the core.

5.2.2 Edge dislocation

The material is modeled as a Saint-Venant Kirchhoff material with E and ν as specified in Table 5.2. We calculate the finite deformation stress field of a single edge dislocation in a body and compare it with the closed-form classical (small deformation) linear elastic solution for the corresponding problem. The small deformation analytical stress field $\boldsymbol{T}^*$ for a single edge dislocation at the center of an infinite cylindrical solid is given by [HL82]:

$$
\begin{aligned}
T^*_{11} &= -Dx_2\left(-\frac{2x_2^2}{(x_1^2+x_2^2)^2}+\frac{3}{(x_1^2+x_2^2)}\right)\\
T^*_{22} &= -Dx_2\left(-\frac{2x_1^2}{(x_1^2+x_2^2)^2}+\frac{1}{(x_1^2+x_2^2)}\right)\\
T^*_{12} &= Dx_1\left(-\frac{2x_2^2}{(x_1^2+x_2^2)^2}+\frac{1}{(x_1^2+x_2^2)}\right)\\
T^*_{33} &= \nu(T_{11}+T_{22}), \qquad T^*_{13}=T^*_{23}=0.
\end{aligned}
\tag{5.11}
$$

where $D = \mu b(2\pi(1-\nu))^{-1}$. x_1 and x_2 are the in-plane coordinates, measured from the center of the dislocation. The computational problem is set up in a $2d$ plane strain setting as follows: an edge dislocation with a Burgers vector $b\boldsymbol{e}_1$ and line direction $\boldsymbol{e}_3$ is assumed to be present in a domain of dimensions $[-50b, 50b] \times [-50b, 50b]$. The edge dislocation is modeled by prescribing a dislocation density $\boldsymbol{\alpha}$ at any $\boldsymbol{x} = (x_1, x_2)$ of the form

$$\alpha_{13}(x_1, x_2) = \begin{cases} \varphi_0 & |x_1| \leq b \text{ and } |x_2| \leq b \\ 0 & \text{otherwise,} \end{cases} \qquad \alpha_{ij} = 0 \text{ if } i \neq 1 \text{ and } j \neq 3. \tag{5.12}$$

In the above, the core width is assumed to be $2b$. The constant φ_0 is evaluated by making the Burgers vector of the dislocation equal to $b\boldsymbol{e}_1$, i.e. $\int_A \alpha_{13}\, dA = b\boldsymbol{e}_1$, where A is any area patch in Ω that encloses the dislocation. Tractions $\boldsymbol{t}$ on the external boundary are applied such that $\boldsymbol{t} = \boldsymbol{T}^*\boldsymbol{n}$ where $\boldsymbol{T}^*$ is given by Eq. (5.11). The stress field of the dislocation in the finite deformation setting is then calculated by solving the system (3.31) and (3.32) in the rectangular domain along with the above-mentioned traction boundary conditions.

Figure 5.8a shows the prescribed dislocation density with a Burgers vector of $b\boldsymbol{e}_1$ in the domain. Figure 5.8b compares T_{12} obtained from FDM and the closed form solution T^*_{12} along the line $x_2 = 0$ for three different mesh sizes: $h = 1b, 0.5b, 0.25b$. We see that the stress fields do not rely on the mesh sizes and a mesh size of $1b$ is adequate for stresses outside the core. The two vertical lines in Fig. 5.8b bound the small region where the analytical solution becomes large, as it is singular at the origin.

Figures 5.9a and 5.9b show the plots of T_{11} and T_{12} in the domain obtained by computing solution to the ECDD system (Eqs. (3.31) and (3.32)) for the mesh size $h = 0.25b$. It may be noted that the field plot of T_{11} is not symmetric about $y = 0$ which is in contrast with the small deformation case. We conjecture that this is because at finite deformation the elastic modulus depends on $\boldsymbol{F}^e$ as $\boldsymbol{T} = \boldsymbol{F}^e(\mathbb{C} : E^e)\boldsymbol{F}^{eT}$, and therefore the effective elastic moduli in a compressed region differ from those in a tensile region, states applicable to the dislocation

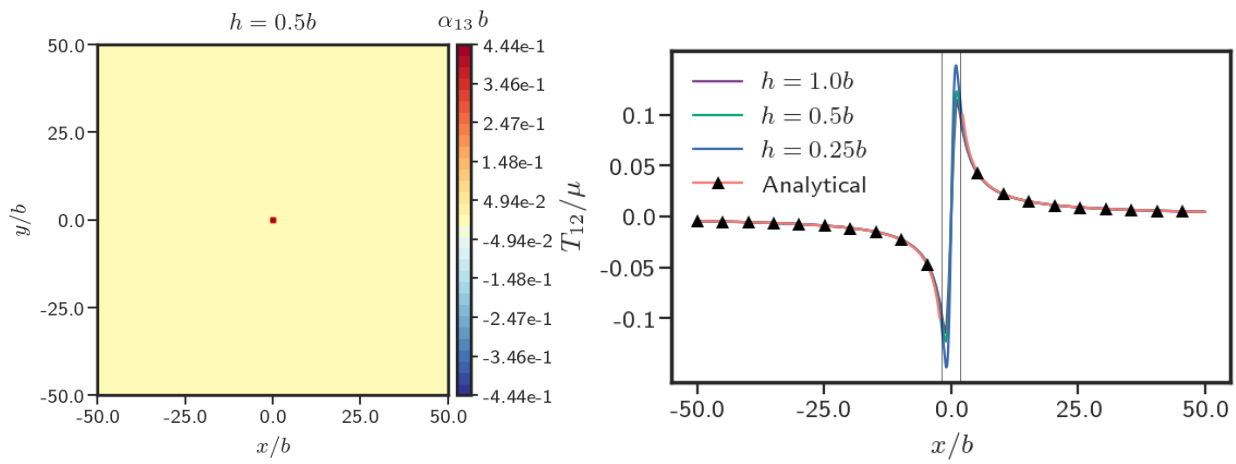

(a) (b)

Figure 5.8: a) Dislocation density, α_{13}, for an edge dislocation embedded in the body b) T_{12}, calculated from finite deformation FDM, plotted along $x_2 = 0$.

above and below $y = 0$.

We now compare the difference between stress obtained by FDM and the closed form solution for small deformation by calculating the difference measure M defined in Eq. (5.10) where $\boldsymbol{T}$ is the stress obtained from numerical computations and $\boldsymbol{T}^*$ is small deformation stress field given by Eq. (5.11). The plot of M in the domain, shown in Figure 5.10, clearly displays that the stress fields differ in a large region around the core with errors $\approx 10\%$ for up to $10b$ from the core. This is qualitatively consistent with DFT results of [IRG15] wherein they show that the energy contribution from the electronic-structure perturbations are significant up to a distance of $10b$ from the edge dislocation line where the strength of the dislocation is b. Therefore, given the large differences we see, our results suggest careful examination of the accuracy of the classical, linear elastic and our computed finite deformation stress fields of dislocations by comparison with predictions of lattice-statics calculations based on well-characterized interatomic potentials.

Given the large differences in the stress field calculated from finite deformation FDM and the classical small deformation solution, we explore the domain of validity of classical dislocation fields by varying the strength of the dislocation. To do so, we repeat the above numerical experiment for different strengths $|\boldsymbol{b}|$ of the dislocation while keeping the domain

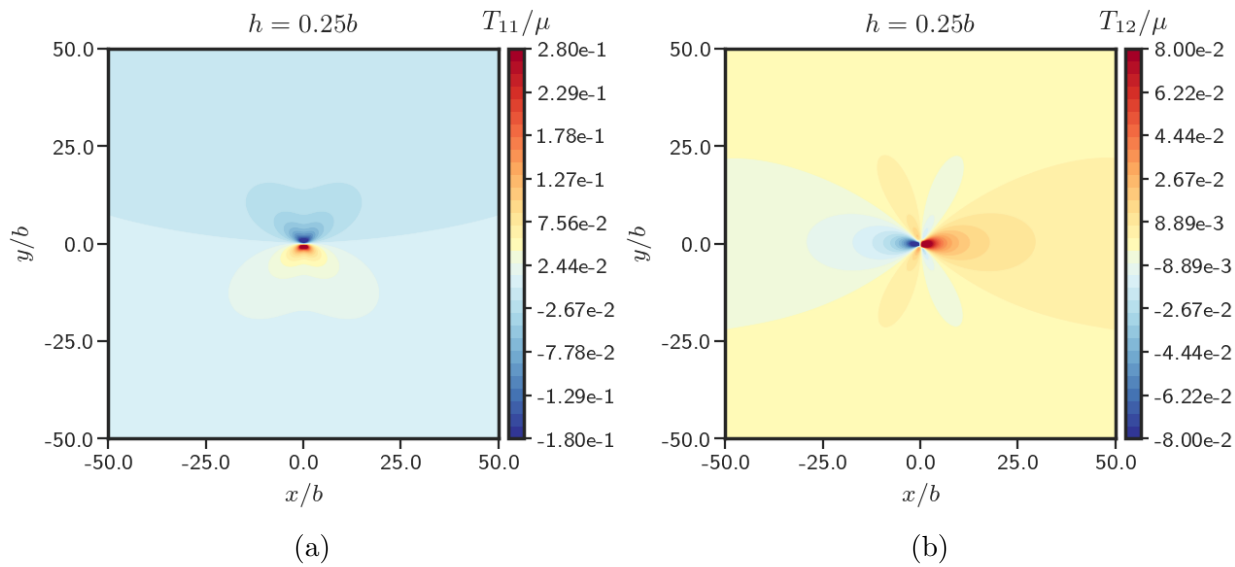

Figure 5.9: Finite deformation stress field of a single edge dislocation computed from FDM a) T_{11} b) T_{12}.

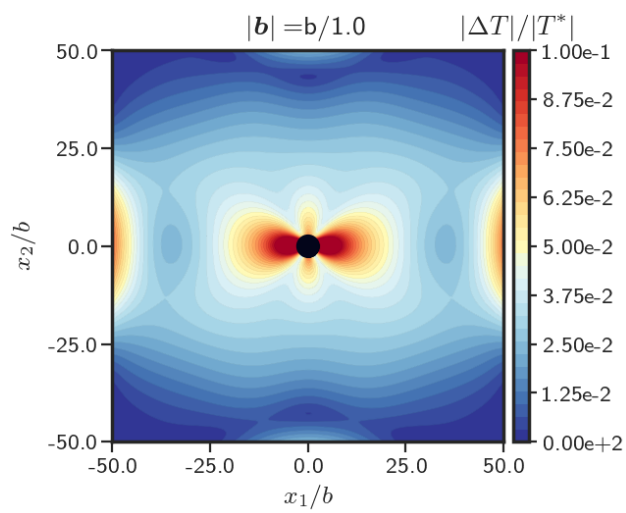

Figure 5.10: Difference in stress fields obtained from FDM and small deformation linear closed form solution given by Eq. (5.11) $\frac{|\boldsymbol{T}-\boldsymbol{T}^*|}{|\boldsymbol{T}^*|}$

size fixed and the problem set up the same as above. We show in Figure 5.11 that the error between the finite deformation FDM stress field and small deformation analytical solution becomes small as the strength of the dislocation $|\boldsymbol{b}|$ decreases, and the error is below 3% in most of the domain when $|\boldsymbol{b}|= \frac{b}{50}$. The error goes to zero only in the limit $|\boldsymbol{b}|\rightarrow 0$. This exercise also serves as a verification of our code in that the correct limiting trends are produced for small forcing.

5.3 Burgers vector constancy with dislocation density evolution in nonlinear elastic motions

Several measures have been proposed to appropriately define the dislocation content in a body as function of the elastic or plastic distortion tensor [BBS55, Esh56, Fox66, Wil67, AB00a, CG01]. Cermelli and Gurtin [CG01] advocate a single measure of GNDs based on 'physically motivated requirements'. However, as is customary in continuum mechanics, relations should always exist between any two physically meaningful measures of GNDs, it is such 'transformation rules' that are physically significant rather than superficial differences in form [Ach08].

The dislocation density tensor $\boldsymbol{\alpha}$ in (M)FDM is a two point tensor that measures the local, undeformed Burgers vector of the dislocation distribution, per unit area of the current configuration. For a given dislocation density $\boldsymbol{\alpha}$ in the domain, the Burgers vector content of an area patch $A(t)$ at any time t is given by

$$\boldsymbol{b}_A(t) = \int_{A(t)} \boldsymbol{\alpha}\boldsymbol{n}\, dA. \tag{5.13}$$

So, in the special case when there is no flux of dislocations into the material area patch, the dislocation density field $\boldsymbol{\alpha}$ has to evolve in such a way that the total Burgers vector of that material patch (given by (5.13)) remains constant. Hence, under the conditions $\boldsymbol{V} = \boldsymbol{0}$,

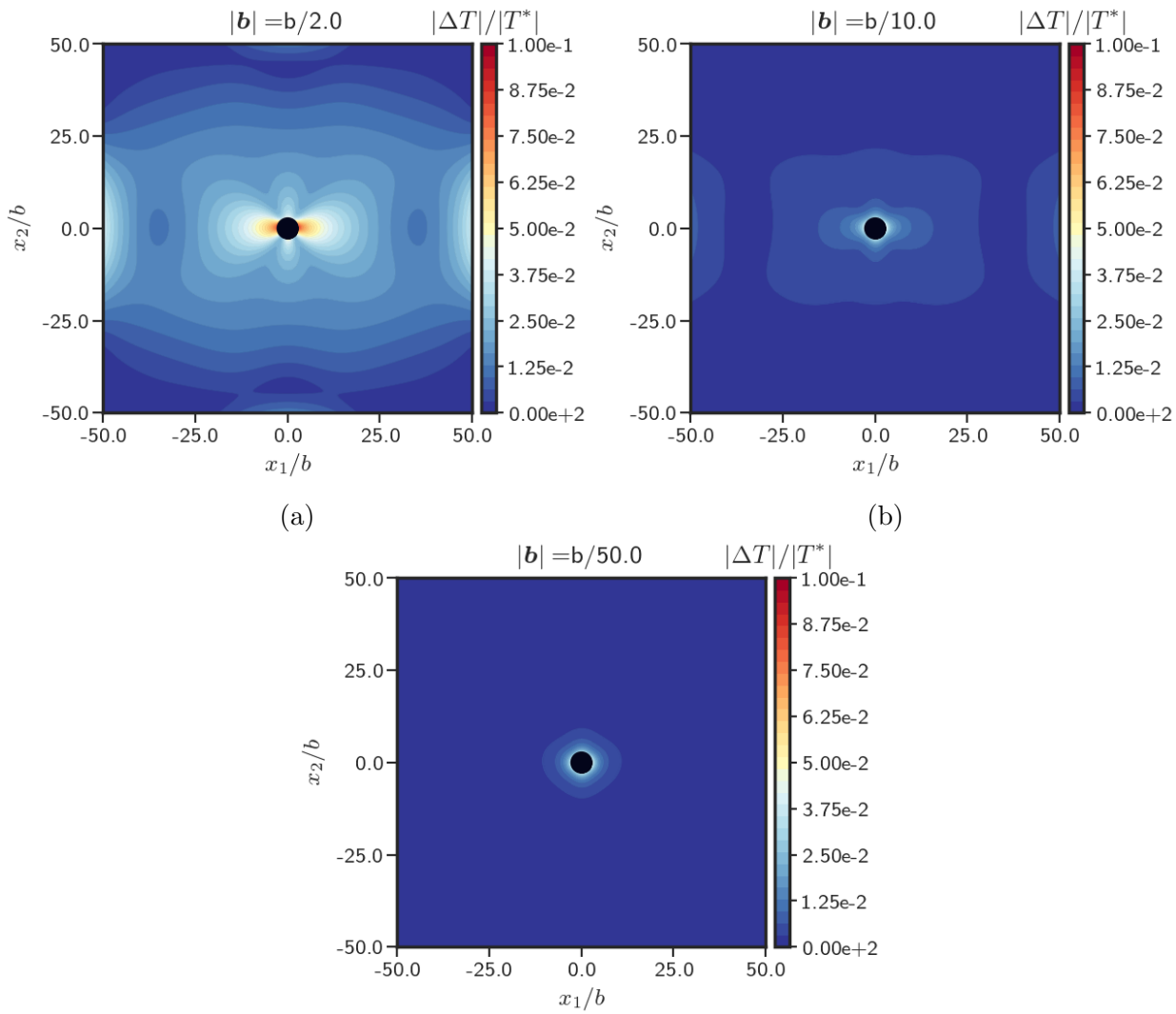

Figure 5.11: Difference in magnitude of stress fields obtained from FDM and small deformation linear closed form solution for different strength of the dislocation $|\boldsymbol{b}|$ a) $\frac{b}{2}$ b) $\frac{b}{10}$ c) $\frac{b}{50}$.

$\boldsymbol{L}^p = \mathbf{0}$, the Burgers vector of any arbitrary area patch should not change in time regardless of the total deformation magnitude i.e. at all times t,

$$\dot{\boldsymbol{b}}_A(t) = \frac{d}{dt}\int_{A(t)} \boldsymbol{\alpha}\boldsymbol{n}\, dA = \mathbf{0}, \quad \forall \quad A \in \Omega$$
$$\implies \dot{\boldsymbol{\alpha}} = \boldsymbol{\alpha}\boldsymbol{L}^T - div\boldsymbol{v}\,\boldsymbol{\alpha} \quad \text{(from Eq. 3.14a)}.$$

Furthermore, under deformations that are locally area-preserving (e.g. simple shear of a plane), the dislocation density field itself has to remain constant in time when convected with the material. We illustrate these results under large tensile and simple shear loadings below. These are stringent tests of the numerics since the dislocation density evolution is coupled to the evolving deformation through the velocity gradient by an adapted convected derivative of a 2-point tensor as shown in Eq. (3.14a). Table 5.3 presents the values of the material constants used for this verification example.

Parameter	Value
$\hat{\Gamma}$	$1s^{-1}$
E	200 GPa
ν	.30

Table 5.3: Parameter values used for the simulations.

5.3.1 Extensional loading

The problem is set up as follows: An edge dislocation is embedded in a rectangular body of dimensions $[-50b, 50b] \times [-50b, 50b]$. The dislocation line direction is assumed to be in the x_3 direction and the Burgers vector is taken as $b\boldsymbol{e}_1$. The dislocation is modeled by prescribing an initial dislocation density $\boldsymbol{\alpha}_0$ at any point $\boldsymbol{x} = (x_1, x_2)$ following Eq. (5.12). The velocity boundary conditions on the left and right faces are assumed to be $v_1 = \hat{\Gamma} L_0$ and $v_2 = 0$, where L_0 is the length of the body. On the top and bottom surfaces, $v_2 = 0$ is imposed. A uniform mesh of 50×50 elements is used to mesh the domain. The schematic of the set up

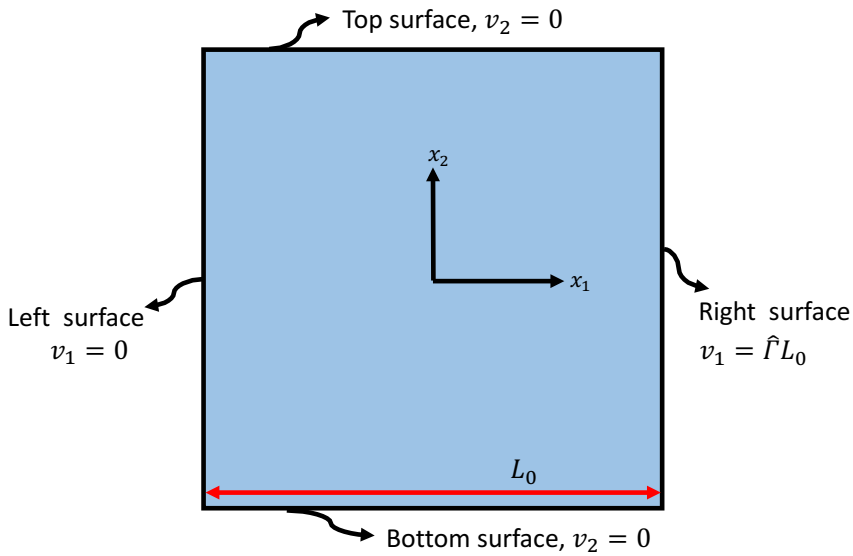

Figure 5.12: Typical schematic of the geometry.

is shown in Fig. 5.12.

Figure 5.13a shows the undeformed configuration of the body. The deformed configuration of the body at a stretch $\Lambda = 2.5$ under tensile loading is shown in 5.13b. The dislocation density is Burgers vector content per unit area and since the current area changes in the tensile loading case, the dislocation density evolves as well, as shown in Figure 5.14a. However, the change in dislocation density is such that the Burgers vector content remains constant. Figure 5.14b shows the variation of the strength of dislocation with stretch. We observe that there is virtually no change in the strength of the dislocation even at such large strains.

5.3.2 Shear loading

For shear loading, the problem is set up as follows: An edge dislocation of the form (5.12) is embedded in a body of dimensions $[-50b, 50b] \times [-50b, 50b]$. Velocity boundary conditions corresponding to overall simple shear are imposed for a plane strain problem as described in Sec. 5.1. A uniform mesh of 50×50 elements is used to mesh the domain.

Figure 5.15a shows the undeformed configuration of the body. The deformed configura-

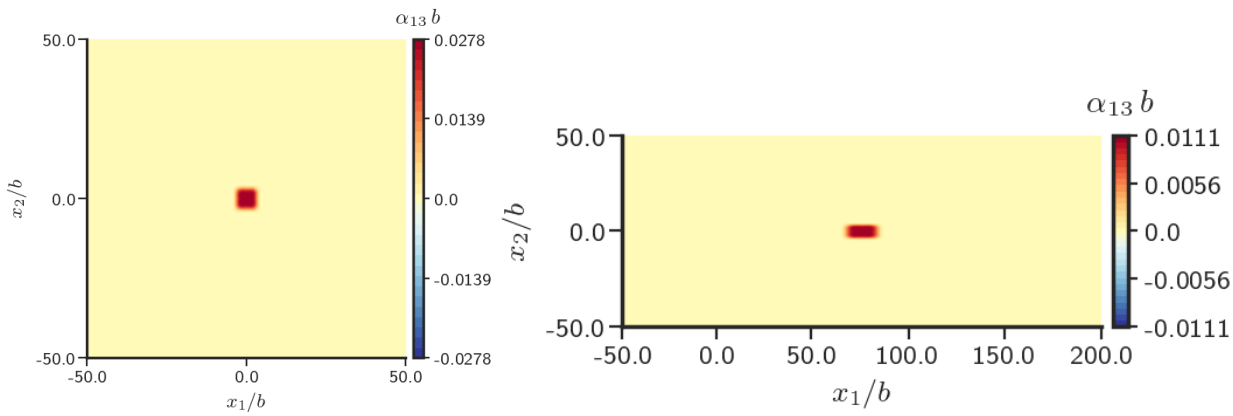

(a) (b)

Figure 5.13: Configurations (not to same scale) during tensile loading a) undeformed b) deformed

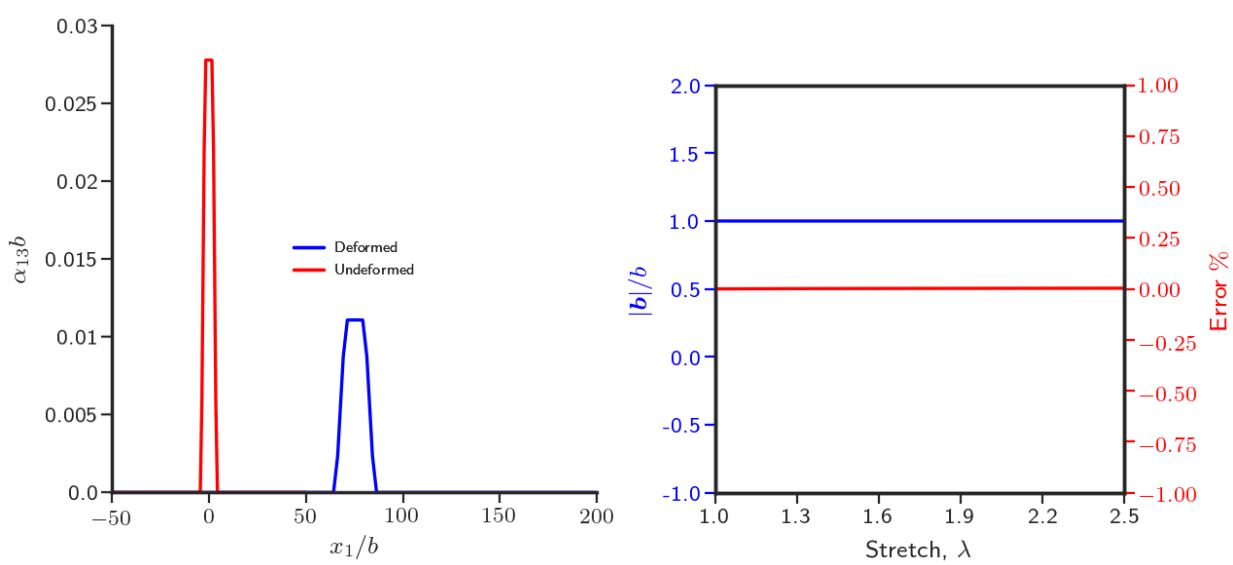

(a) (b)

Figure 5.14: Variation of a) dislocation density, α_{13} b) dislocation strength $|\boldsymbol{b}|$ along $y = 0$ with strain.

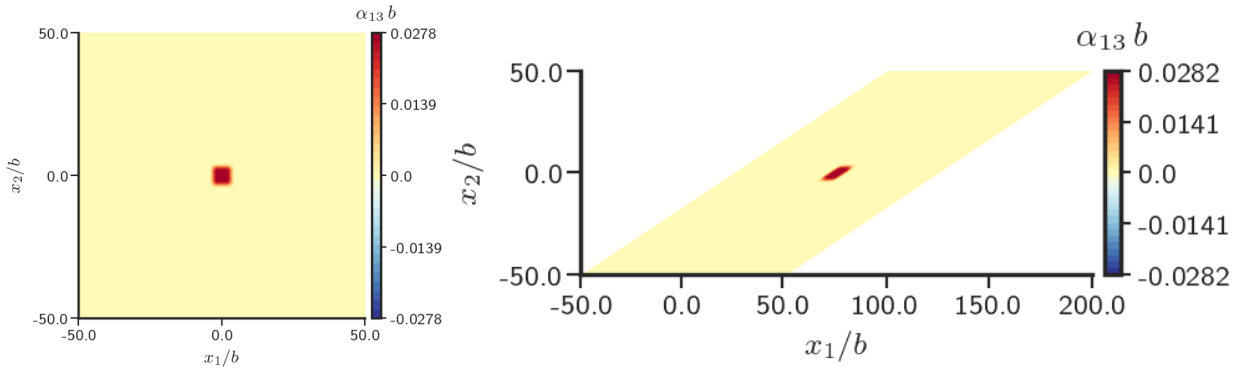

(a) (b)

Figure 5.15: Configurations (not to same scale) during shear loading a) undeformed b) deformed

tion of the body at a strain $\Gamma = 1.5$ under simple shear loading is shown in 5.15b. Since the current area does not change in simple shear loading, the dislocation density should not change as well and this is shown in Figure 5.16a. The corresponding change in the dislocation strength is shown in Figure 5.16b. We observe that there is virtually no change in the strength of the dislocation with progress of deformation over such large strains.

These examples demonstrate the robust performance of our code in stringent tests of finite deformation dislocation kinematics and also demonstrate the physical characteristics of our dislocation density measure (3.14a) [Wil67, Ach08].

5.4 Stress field of spatially homogeneous dislocation distribution

The presence of dislocations often produces long range stress field in the body even in the absence of any external loads. However, there are many dislocation distributions that produce no stress fields [Mur89, HHOT93, YG12], at least in the continuum limit wherein the dislocations are described by a continuous distribution. These stress-free dislocation distributions are physically important in the far-field description of grain boundaries, and play an important role during patterning and microstructure formation in plastic deformation.

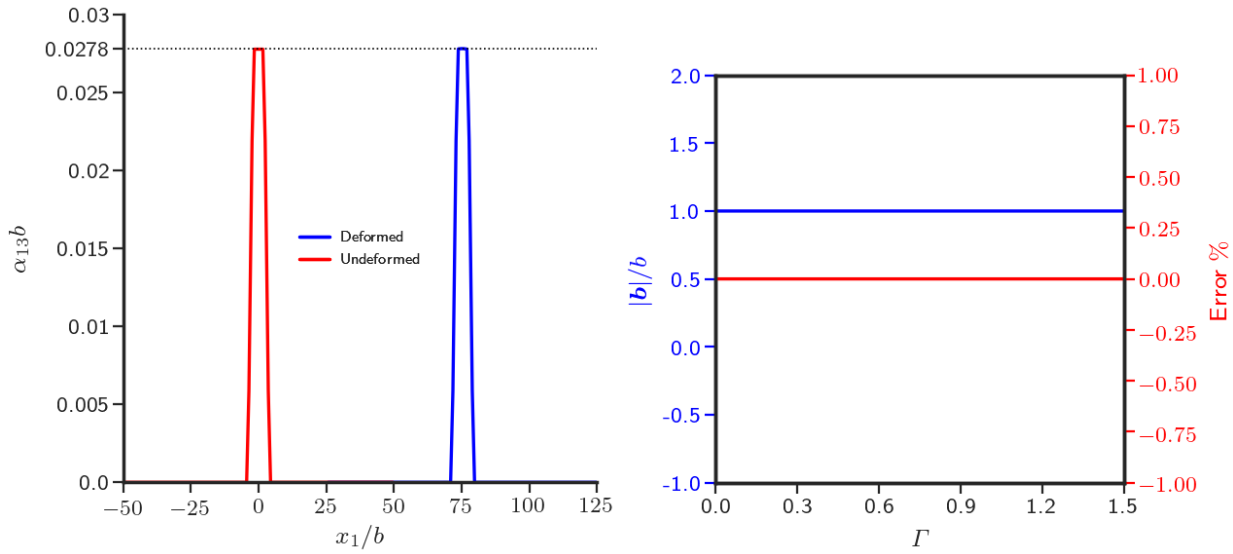

(a) (b)

Figure 5.16: Variation of a) dislocation density, α_{13} b) dislocation strength along $y = 0$ with strain.

The dislocation density tensor $\boldsymbol{\alpha}$ is related to the curl of the inverse-elastic distortion tensor. Therefore, $\boldsymbol{F}^e$ being equal to any (inhomogeneous) rotation field in the domain gives a stress free configuration with non-zero dislocation density. Correspondingly, for the linear case, the stress free dislocation distributions belong to the class such that the linearised elastic distortion tensor ($\boldsymbol{U}^e \approx \boldsymbol{F}^e - \boldsymbol{I}$) is skew-symmetric. However, it can also be shown [Mur89, HHOT93, Ach18] that any uniform distribution of dislocation density in the domain is stress free in the linear theory. This is because a spatially constant dislocation density distribution has vanishing incompatibility ($\eta := (curl((curl\boldsymbol{U}^e)^T))_{sym}$) and therefore the strain field is compatible and the body is stress free in the absence of any external forces. However, in a two-dimensional setting, such distributions are not stress free when geometric nonlinearity is taken into account [Ach18].

Here, we demonstrate this sharp contrast in the predictions for stress fields based on the linear and the (geometrically) nonlinear ECDD theories. The problem is set up in a $2d$ plane strain setting as follows: A spatially homogeneous distribution of edge dislocations α_{13} is specified in a domain with dimensions $[-50b, 50b] \times [-50b, 50b]$ as shown in Fig. 5.17.

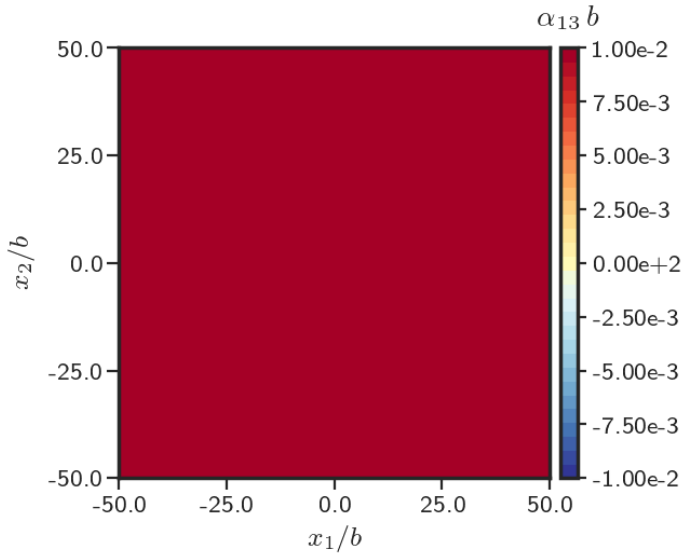

Figure 5.17: Spatially uniform α_{13} distribution.

The total Burgers vector of the dislocation distribution is $\boldsymbol{b} = \int_\Omega \alpha_{13}\, \boldsymbol{e}_1\, dA = 100b\boldsymbol{e}_1$. The external boundary of the domain is considered to be traction free. In the linear setting, the stress field is calculated by solving for $\boldsymbol{f}$ (or $\boldsymbol{z}$) as described in Sec. 4.1.4.3. The stress field in the nonlinear setting is obtained by solving the ECDD system (Eqs. (3.31) and (3.32)).

Figures 5.18a and 5.18b show the stress field T_{12} obtained from the geometrically linear theory for the Saint-Venant-Kirchhoff and the Neo-Hookean materials, respectively. It can be seen that the stress fields vanish in the entire domain. Figures 5.19a and 5.19b show the magnitude of the stress field in the domain for the Saint-Venant-Kirchhoff and the Neo-Hookean materials, respectively. Hence, the linear calculation predicts vanishing stress field for a spatially homogeneous dislocation distribution in the domain.

Figures 5.20a and 5.20b show the stress field T_{12} obtained from the geometrically nonlinear FDM theory for the Saint-Venant-Kirchhoff and the Neo-Hookean materials, respectively. The stress field is non-zero in the domain for both the materials in the nonlinear setting. A stress free dislocation distribution for the finite deformation case is presented in Section 5.6.

We remark here that although we demonstrated the contrasting predictions of linear and nonlinear theory for isotropic materials, the result holds true for any material with

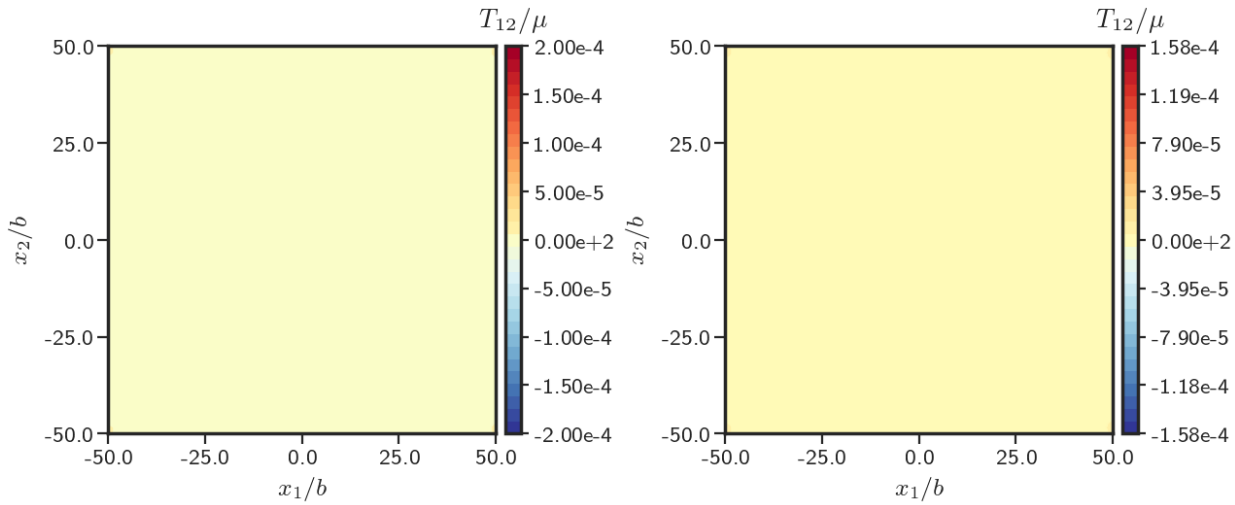

(a) (b)

Figure 5.18: Stress field for spatially uniform distribution of α_{13} in the linear setting for a) Saint-Venant-Kirchhoff material b) Neo-Hookean material.

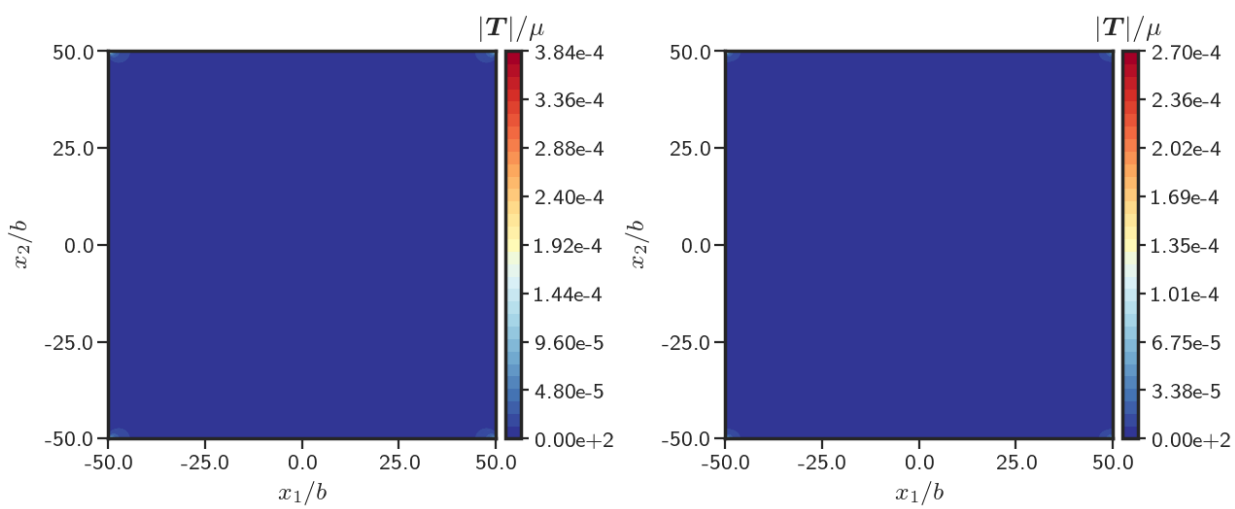

(a) (b)

Figure 5.19: Cauchy stress norm for spatially uniform distribution of α_{13} in the linear setting for a) Saint-Venant-Kirchhoff material b) Neo-Hookean material.

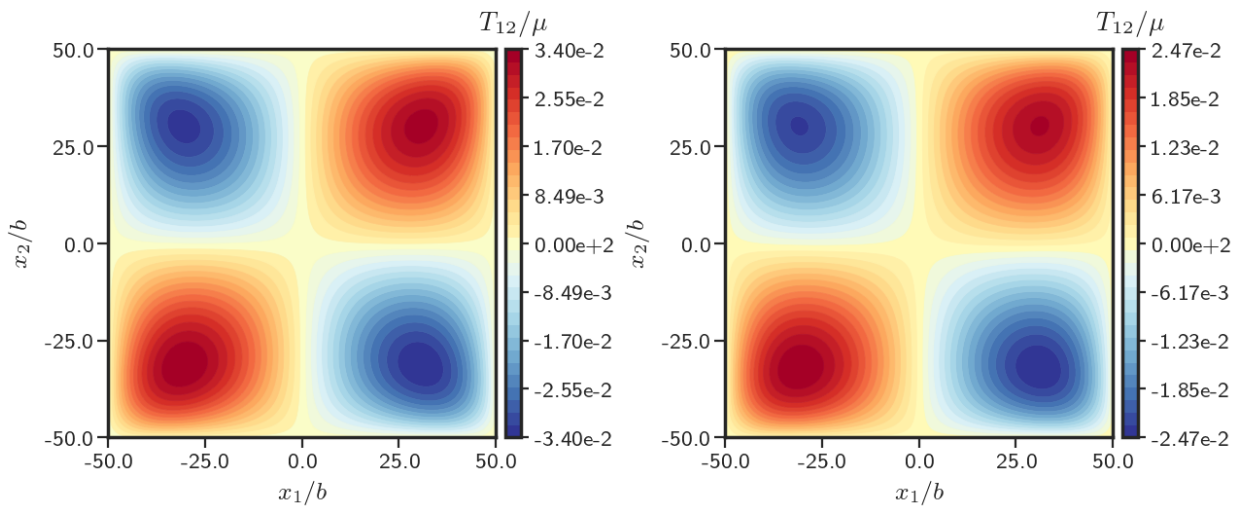

(a) (b)

Figure 5.20: Finite deformation stress field for spatially uniform distribution of α_{13} for a) Saint-Venant-Kirchhoff material b) Neo-Hookean material.

non-homogeneous and/or anisotropic elastic modulus $\mathbb{C}$.

5.5 Volume change due to dislocations

A fundamental question that was asked by Toupin and Rivlin [TR60] concerns the change in volume of a body when dislocations are introduced; linear elastic theory is not capable of capturing this volume change, due to the fact that the average value of each of the infinitesimal strain components of a self-equilibrated stress field in a body vanishes. However, it has been observed experimentally that the volume of the body changes upon the introduction of dislocations [Zen42] and the prediction by linear elastic theory (of no volume change) does not seem to be in agreement with experimental observations. Toupin and Rivlin [TR60] used a second-order approximation of nonlinear elasticity to give explicit expressions for the changes in average dimensions of elastic bodies resulting from the introduction of dislocations.

Here, we use FDM to capture this volume change. The problem is set up in a two dimensional plane strain setting as follows: A body Ω of dimensions $[-10b, 10b] \times [-10b, 10b]$ is discretized with a uniform mesh of 200×200 elements. The boundaries are assumed to be

traction free. Table 5.4 presents the values of material constants used for the simulation.

Parameter	Value
E	200 GPa
ν	.30

Table 5.4: Parameter values used for calculating volume change.

The % volume change (per unit length along the axis of body) is then calculated as

$$V_{curr} = \int_{\boldsymbol{\Omega}} dV \tag{5.14a}$$

$$V_{ref} = = \int_{\boldsymbol{\Omega}} det(\boldsymbol{W})\, dV \tag{5.14b}$$

$$\Delta V = V_{ref} - V_{curr}; \quad \%\Delta V = \frac{|\Delta V|}{V_{curr}} \times 100. \tag{5.14c}$$

V_{ref} and V_{curr} denote the volume of the reference and the current configurations, respectively. The volume change is calculated from Eq. (5.14) as follows: The ECDD system (Eqs. (3.31) and (3.32)) is solved on the current configuration to obtain the inverse elastic distortion field for a given distribution of dislocations in the domain. The % change in volume is then quantified from Eq. (5.14c).

Number of Cores	$\%\Delta V$
1	.1019
2	.2064
4	.3013
6	.3902
8	.6025

(a)

Number of Cores	$\%\Delta V$
2	.1793
4	.2938
6	.3523
8	.5873

(b)

Table 5.5: Volume change in body when the resultant strength of all the dislocations is a) positive b) zero.

Table 5.5a shows the % change in the area of the body consequent upon the introduction of multiple dislocations of the same sign, distributed in the body as shown in figures 5.21. Table 5.5b shows the % change in the area of the body due to the introduction of multiple pairs of dislocations such that the total Burgers vector of all dislocations is $\mathbf{0}$, distributed

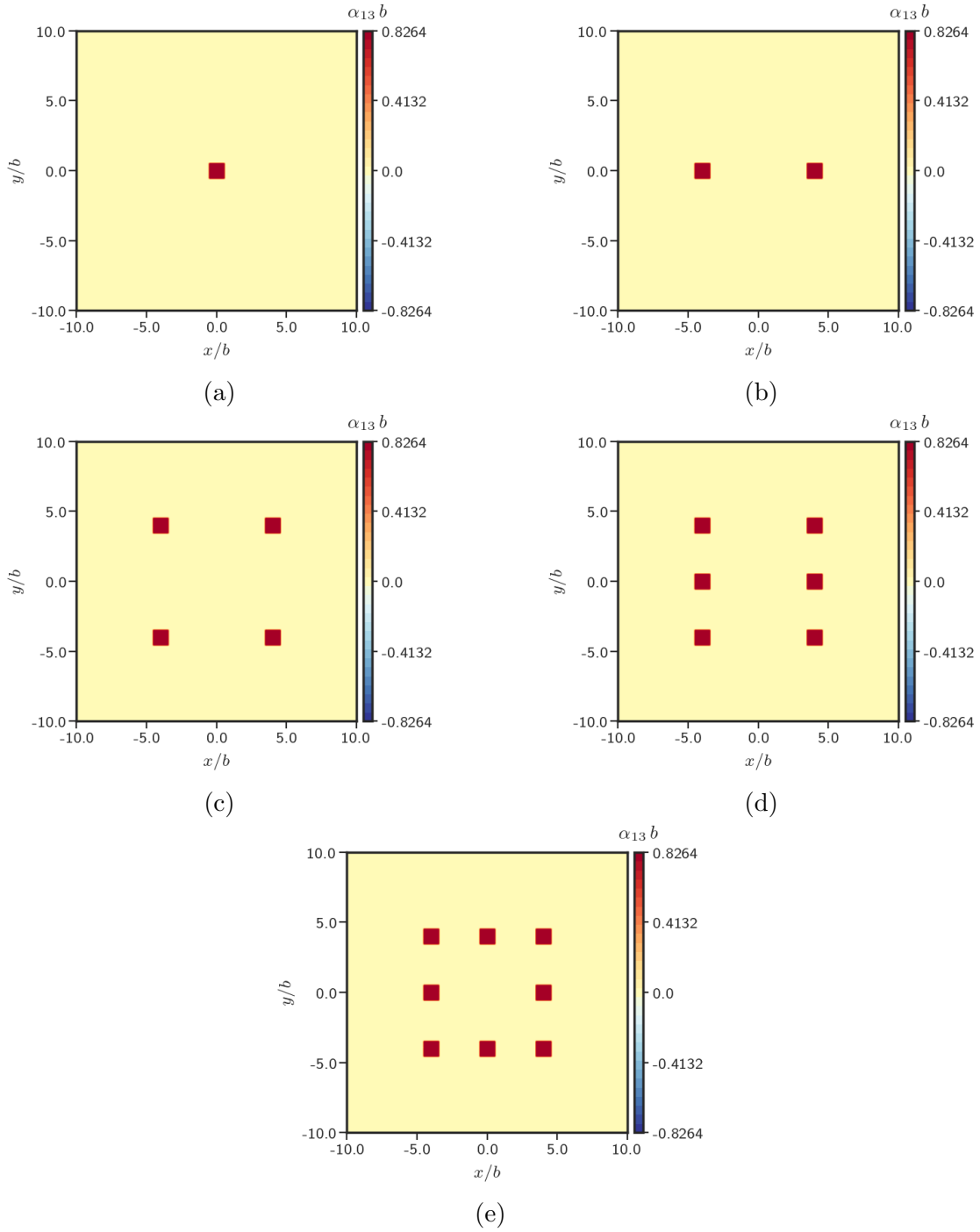

Figure 5.21: Dislocation density $\boldsymbol{\alpha}$ distribution for the case when the total strength of all dislocations is positive a) 1 core b) 2 cores c) 4 cores d) 6 cores e) 8 cores.

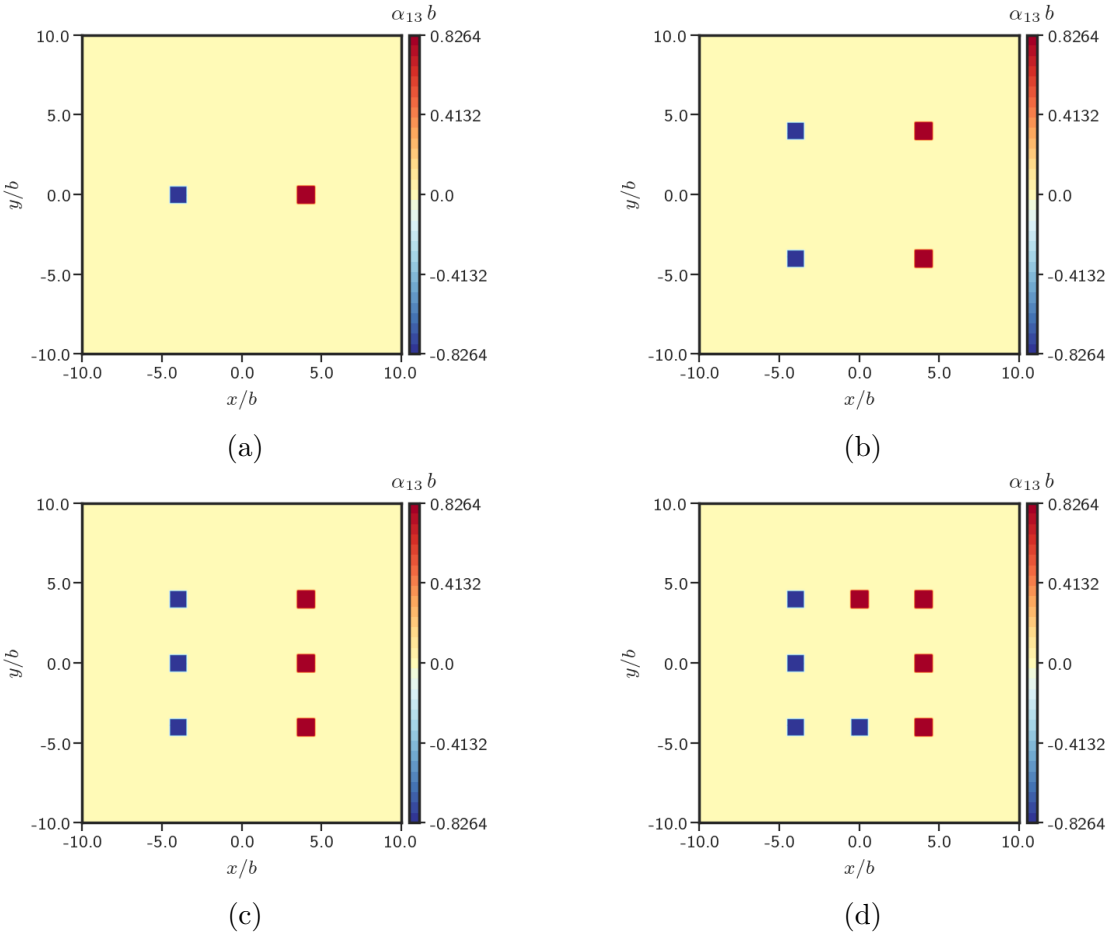

Figure 5.22: Dislocation density $\boldsymbol{\alpha}$ distribution for the case when the total Burgers vector is zero a) 2 cores b) 4 cores c) 6 cores d) 8 cores.

in the body as shown in figure 5.22. Each pair in figure 5.22 utilizes positive and negative straight edge dislocation.

Tables 5.5a and 5.5b demonstrate that the change in volume upon introduction of dislocations as quantified by finite deformation FDM is very small for both the cases. Moreover, we see that this volume change is not linear w.r.t the number of cores i.e. for the first case, the change in area in the presence of 6 dislocations is not the same as 6 times the change in area when only a single dislocation is present. The nonlinearity of the ECDD system and interaction among the dislocations cause the deviation from linear response to give smaller values.

This study suggests that for an isotropic Saint-Venant-Kirchhoff material, the volume change calculated with nonlinear theory is very small and therefore the linear theory prediction of no volume change is a very good approximation.

5.5.1 Reference configurations

Consider a case when a single dislocation is assumed to be present in the body resulting in the development of an elastic distortion tensor field $\boldsymbol{F}^e$ in the domain. It can be shown analytically that if the dislocation core is removed from the body and a cut made that runs from the boundary of the core to the external boundary to produce a simply connected body, then there exists a deformation $\boldsymbol{y}$ of this simply connected configuration such that $grad\boldsymbol{y} = \boldsymbol{W}$ holds, where $\boldsymbol{W} =: \boldsymbol{F}^{e-1}$. The reference configuration can then be obtained by mapping this 'hollowed and cut' current configuration by the field $\boldsymbol{y}$. Moreover, the field $\boldsymbol{y}$ has two important properties: i) the jump in the value of $\boldsymbol{y}$ along the cut surface is equal to the Burgers vector of the embedded dislocation in the original body and, ii) the jump in $\boldsymbol{y}$ is independent of the cut surface chosen [ZA18].

We now show that this topological property is preserved in the framework of (computational) FDM. More interestingly, we are easily able to do similar calculations for a body containing multiple dislocations when the current configuration cannot be rendered simply-

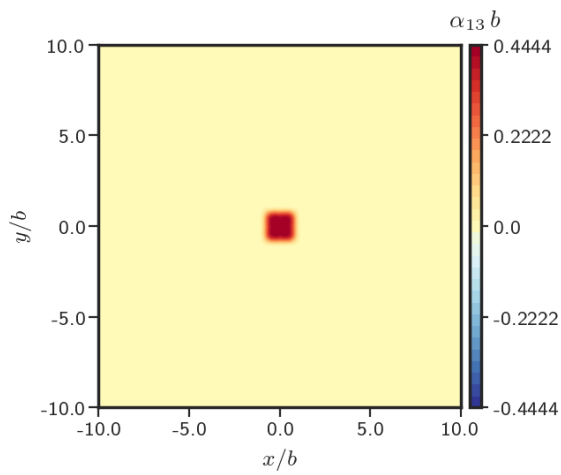

Figure 5.23: Dislocation density α_{13} on the current configuration Ω

connected by a single cut - in this case we show that the jump in $\boldsymbol{y}$ is not constant along the boundary, corresponding to the cuts, of the simply-connected domain, in contrast to the single dislocation single-cut case.

The calculations of this section also highlight an important feature of the ECDD formulation. If the dislocation stress problem for specified dislocation density is formulated classically, i.e., involving only an (inverse) deformation field, it is clear that there is massive non-uniqueness of solutions for the same stress field; ECDD suffers from no such ambiguity and lends itself to robust computation.

5.5.1.1 Burgers vector along $\boldsymbol{e}_1$

Consider a case when a single dislocation with Burgers vector, $\boldsymbol{b} = b\boldsymbol{e}_1$ is assumed to be present in the body Ω as shown in Figure 5.23. We now solve the ECDD Eq. (3.31) and (3.32) on this current configuration to determine the distribution of $\boldsymbol{W}$ in the domain. We then remove the core from the body and make it simply connected by making a horizontal cut that runs from the core to the boundary as shown in Figure 5.24a. Next, the field $\boldsymbol{y}$ is obtained on this simply connected configuration such that $grad\boldsymbol{y} = \boldsymbol{W}$ holds. We map the simply connected configuration by the field $\boldsymbol{y}$ to get the reference configuration for the horizontal cut which is shown in Figure 5.24b.

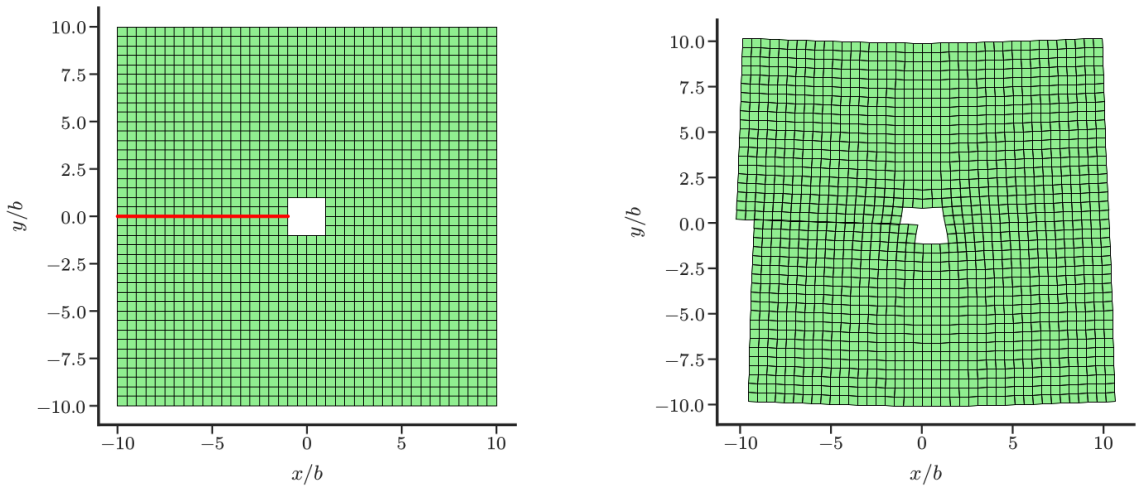

(a) (b)

Figure 5.24: a) Ω is made simply connected- core is removed and a horizontal cut is made b) reference configuration when the chosen cut surface is horizontal.

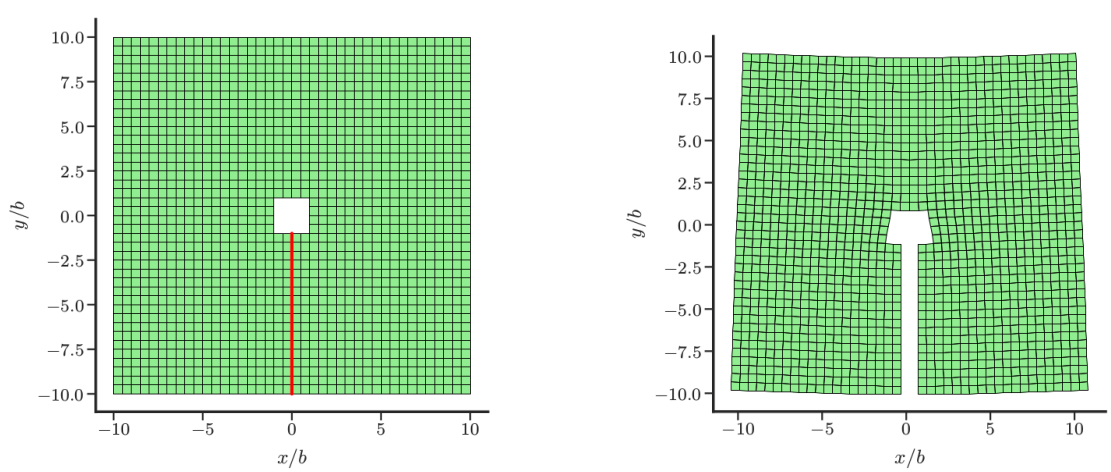

(a) (b)

Figure 5.25: a) Ω made simply connected- core is removed and a vertical cut (from top) is made b) Corresponding reference configuration.

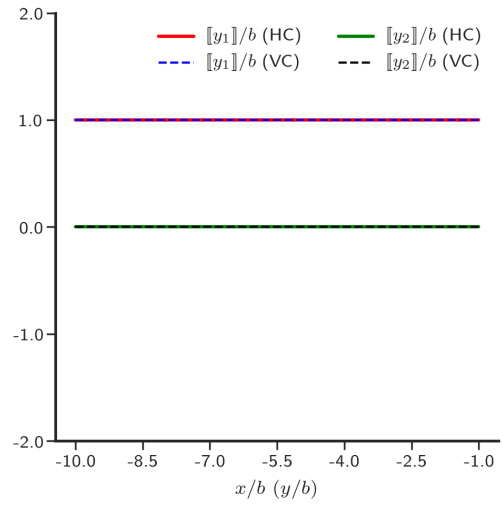

Figure 5.26: Jump in y_1 and y_2 across horizontal and vertical cut surface for the configurations shown in Figs. 5.24a and 5.25a. HC: Horizontal cut surface & VC: Vertical cut surface.

We now repeat the same procedure to get the reference configuration when a vertical cut is made from the bottom as shown in Figure 5.25a. The reference configuration for this case is shown in Figure 5.25b. It can be clearly seen that although the configurations 5.24a and 5.25a are related by a rigid rotation of 90° about $\boldsymbol{e}_3$ axis, the corresponding reference configurations are totally different. The cut surface slides in the tangential direction in the former case where as it opens up in the latter case. This is actually a consequence of the constraint that the (vectorial) jump has to remain constant along the cut surface.

Fig. 5.26 shows the plot of the jump in the value of the function $\boldsymbol{y}$ along the cut surface. As can be seen, the jump is constant along the cut surface and it is same for both the cuts (independent of cut surface). Moreover, this jump is exactly equal to the Burgers vector of the dislocation in the original body Ω.

As pointed out above, when the simply connected configurations were related by rigid rotations, the corresponding reference configurations are not related in the same way. In fact, they were entirely different. We demonstrate this non-uniqueness in the reference configurations in the presence of a single dislocation with Burgers vector $\boldsymbol{b} = b\boldsymbol{e}_1$ in the body in Fig. 5.27 for different cut surfaces.

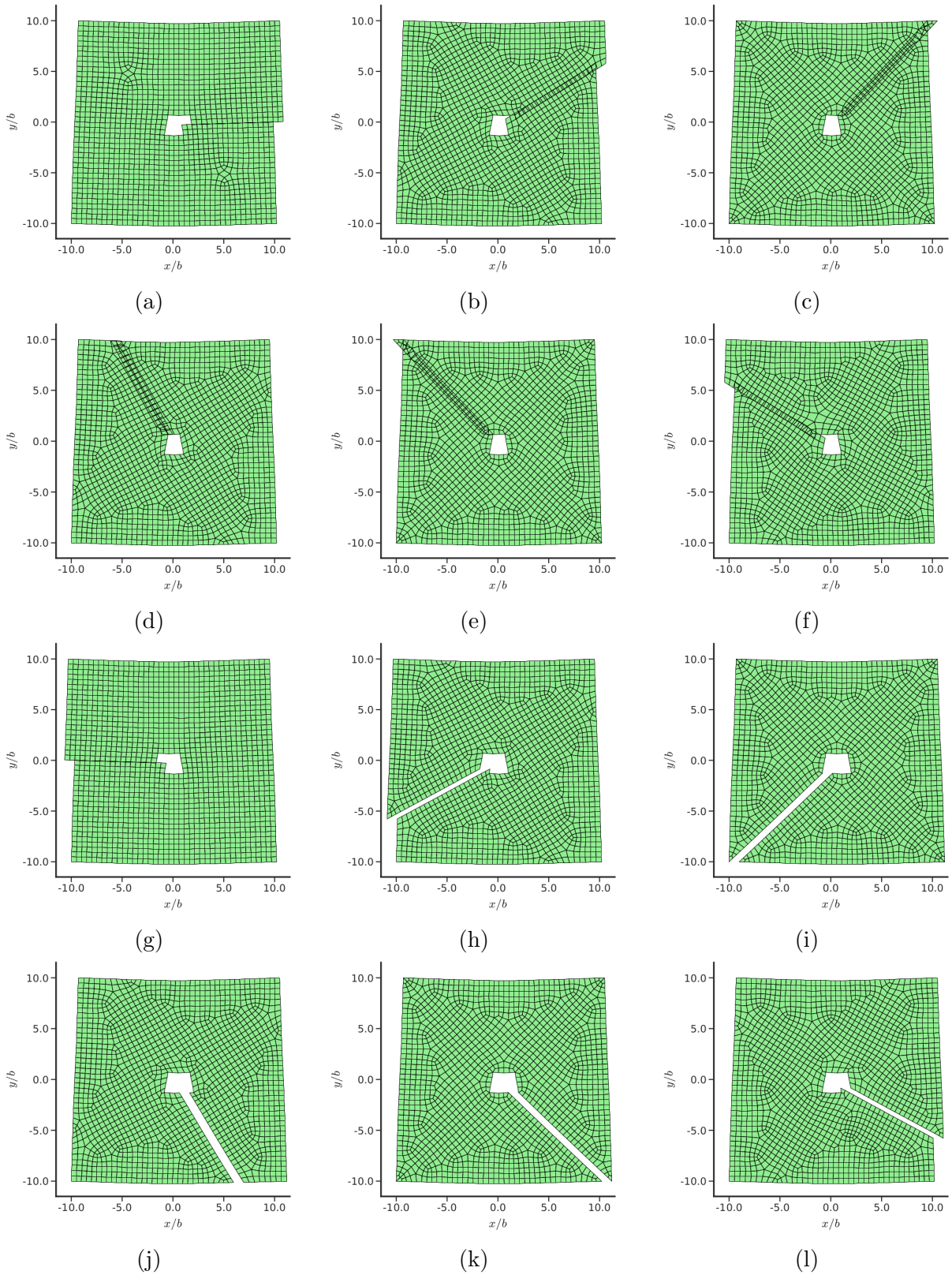

Figure 5.27: Reference configurations when the cut surface is drawn at varying angles from the x_1 axis a) 0° b) 30° c) 45° d) 120° e) 135° f) 150° g) 180° h) 210° i) 225° j) 300° k) 315° l) 330°.

Figure 5.27 shows the reference configurations for 12 different cuts chosen to make the body simply connected. However, we can see that none of the reference configurations are related by rigid rotations. It should be noted that the reference configurations are overlapping when the cut makes an angle between 0° and 180° with the axis. For other cases, the reference configuration opens up. However, the jump in the function $\boldsymbol{y}$ along each of the cut surface is same and constant. Moreover, it is equal to the Burgers vector of the dislocation involved.

5.5.1.2 Burgers vector in a general direction

We now consider a case wherein the Burgers vector of the dislocation density in the body is $\boldsymbol{b} = b(\boldsymbol{e}_1 - \boldsymbol{e}_2)$. Such a field requires the presence of two components of $\boldsymbol{\alpha}$, (α_{13} and α_{23}) as shown in Figures 5.28a and 5.28b, respectively. After solving for $\boldsymbol{W}$ on this current configuration from the ECDD equations, we remove the core from the body and make it simply connected by making a horizontal (vertical) cut (as shown earlier in figures 5.24a and 5.25a) that runs from the core to the boundary. We then solve for the field $\boldsymbol{y}$ on this simply connected configuration and map the simply connected configuration by the obtained field $\boldsymbol{y}$ to get the reference configuration[1]. Figures 5.29a and 5.29b show the obtained reference configuration when the cut is horizontal and vertical, respectively. We also plot the the jump in the value of the function $\boldsymbol{y}$ along the cut surface in Figure 5.30. As can be seen, the jump is again constant along the cut surface and it is independent of the cut surface. Moreover, the jump in each component is exactly equal to the Burgers vector component of the underlying dislocation density field.

5.5.1.3 Inverse deformations for multiple dislocations

The non-uniqueness in the reference configurations was demonstrated in the presence of a single dislocation earlier in 5.5.1.1. This section explores the possibility of obtaining non-unique reference configurations of a body with multiple dislocations. Figure 5.31 shows such

[1]The vector field $\boldsymbol{y}$ should be considered as one possible candidate inverse deformation consistent with the inverse elastic distortion $\boldsymbol{W}$.

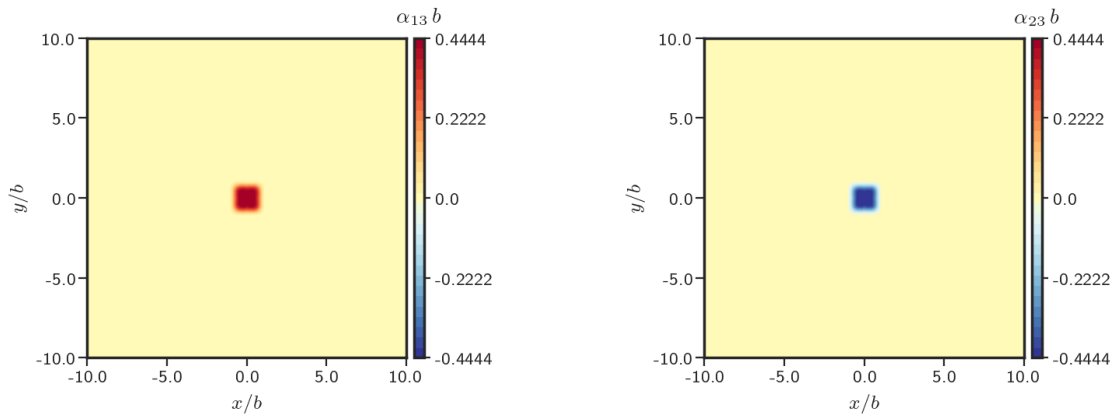

(a) (b)

Figure 5.28: Dislocation density on the current configuration a) α_{13} b) α_{23}

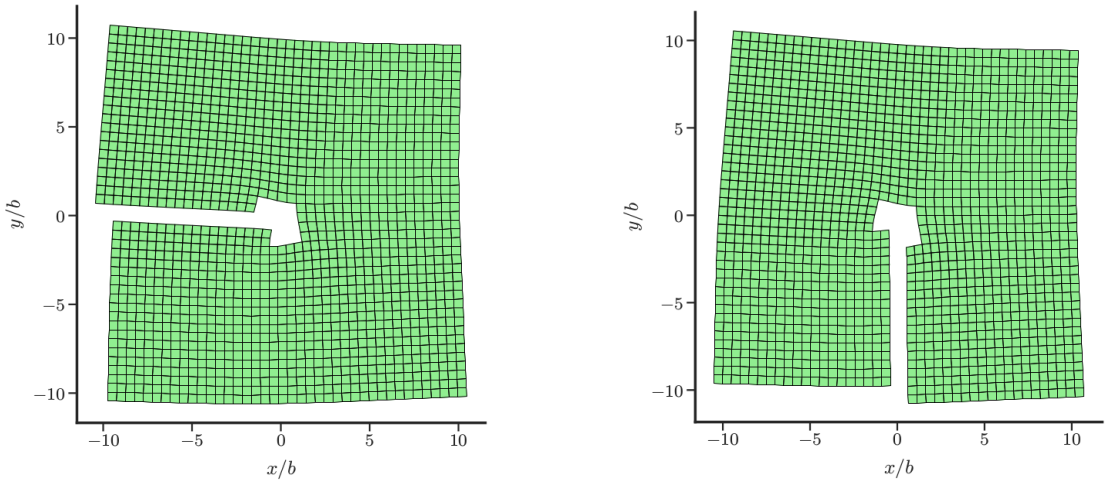

(a) (b)

Figure 5.29: Reference configuration when a) Horizontal cut is made from the left surface to the core as shown in Fig. 5.24a. b) Vertical cut is made from the bottom surface to the core as shown in Fig. 5.25a.

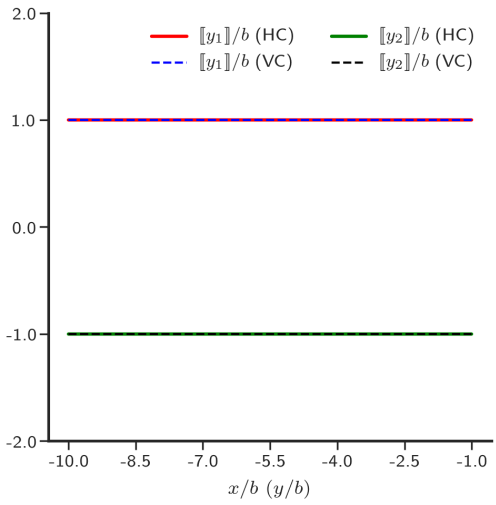

Figure 5.30: Jump in y_1 and y_2 across horizontal and vertical cut surface for the configurations shown in Figs. 5.24a and 5.25a. HC: Horizontal cut & VC: Vertical cut.

a scenario when 4 dislocations are assumed to be present in the body and multiple reference configurations, corresponding to different cuts, are obtained.

On the left panels of Figure 5.32[2], we show the simply connected configuration obtained by making several cuts (shown in red) on the 'hollowed' configuration shown in 5.31b. The corresponding reference configurations obtained by mapping by the field $\boldsymbol{y}$ are shown on the right in Figure 5.32.

As can be seen from these figures, the reference configuration is non-unique as it depends on the cut made inside the body to make it simply connected. Moreover, even when the cut-configurations differ by rigid rotations (for example 5.32a and 5.32i, and 5.32c and 5.32g), the corresponding reference configurations (5.32b and 5.32j, and 5.32d and 5.32h,) are totally different. Another important thing to note here is that unlike the case of the single dislocation, the jump in $\boldsymbol{y}$ is not constant along the cut in the presence of multiple dislocations, but constant along the cut between any two cores, in accord with the analytical values they should take in these examples of configurations with multiple cuts.

[2]Please note that Fig. 5.32 runs into two pages

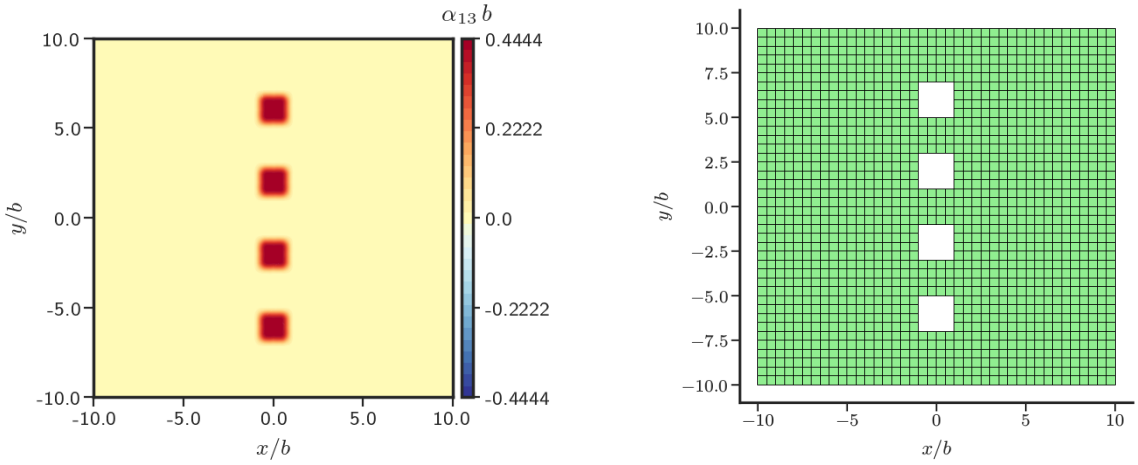

(a) (b)

Figure 5.31: a) Dislocation density distribution α_{13} for multiple cores b) configuration with cores removed.

5.6 Grain-boundary wall

A recent mathematically rigorous work [MSZ15] deduces, *assuming* certain total energy scalings and using Γ-convergence arguments, that the macroscopic limiting energy density of a nonlinear elastic body with dislocations is a sum of the *linear* elastic energy density and an additional term representing, roughly, a grain boundary energy. Thus, the limiting energy density is not rotationally invariant, and this cannot be physically appropriate as the observed phenomenon of polygonization shows [Nab67]. For example, dislocation cores can stack up to form a grain boundary giving rise to the presence of a piecewise-uniform finite rotation field and zero-stresses in the domain. To demonstrate that the energy density derived in [MSZ15] is not physically appropriate, we study the stress field of a special sequence of dislocations, wherein the dislocation cores stack up to form a dislocation wall in the limit.

We first study the stress field in the presence of a full dislocation wall in the polygonized domain. The problem is set up in a two dimensional plane strain setting as follows: Simulations are performed on a polygonized body as shown in Fig. 5.33. The body is assumed to behave as an isotropic Saint-Venant-Kirchhoff elastic material. A non-uniform mesh, highly

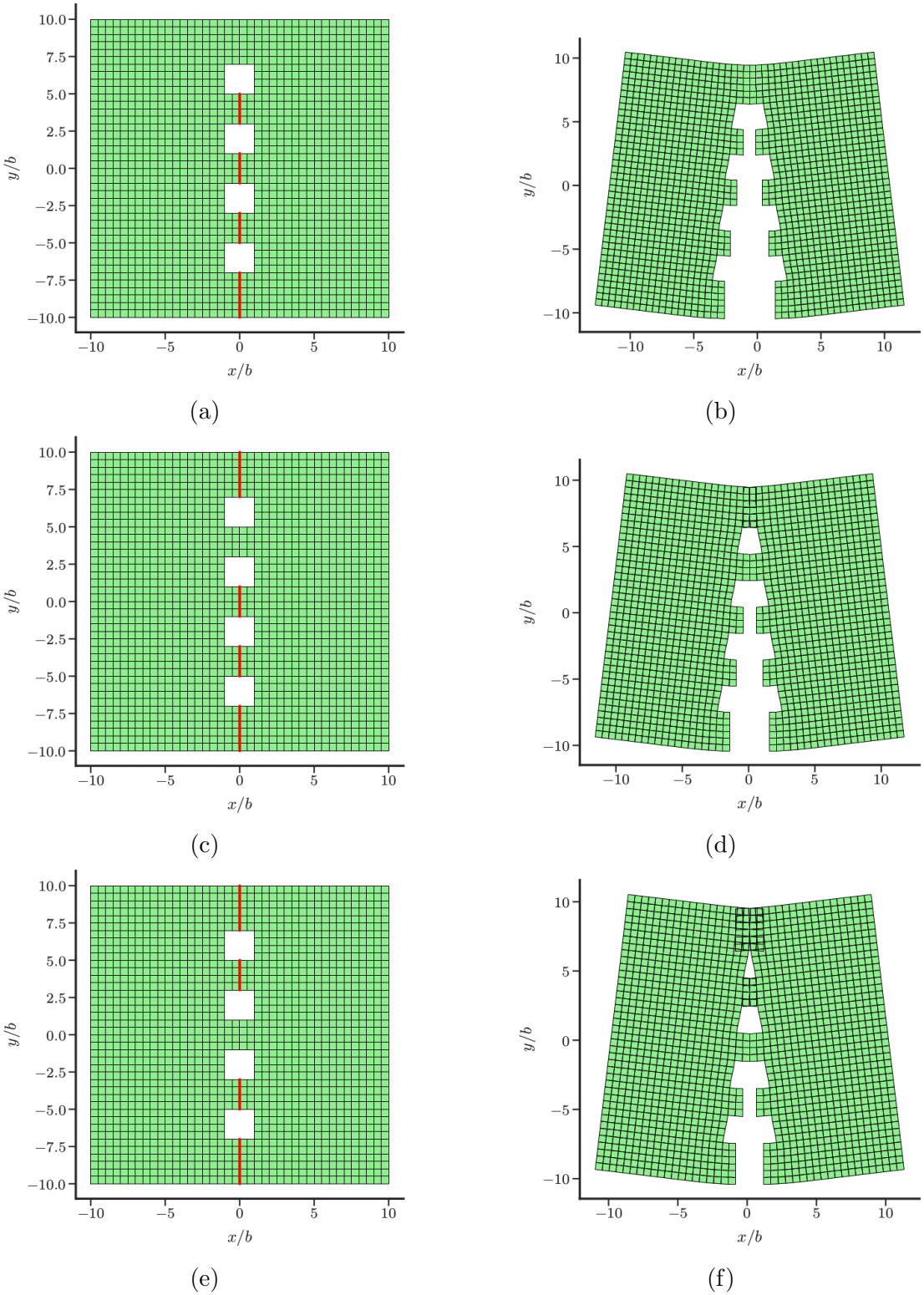
10.0
7.5
5.0
2.5
0.0
−2.5
−5.0
−7.5
−10.0
y/b
−10
−5
0
5
10
x/b
(a)
(b)
(c)
(d)
(e)
(f)

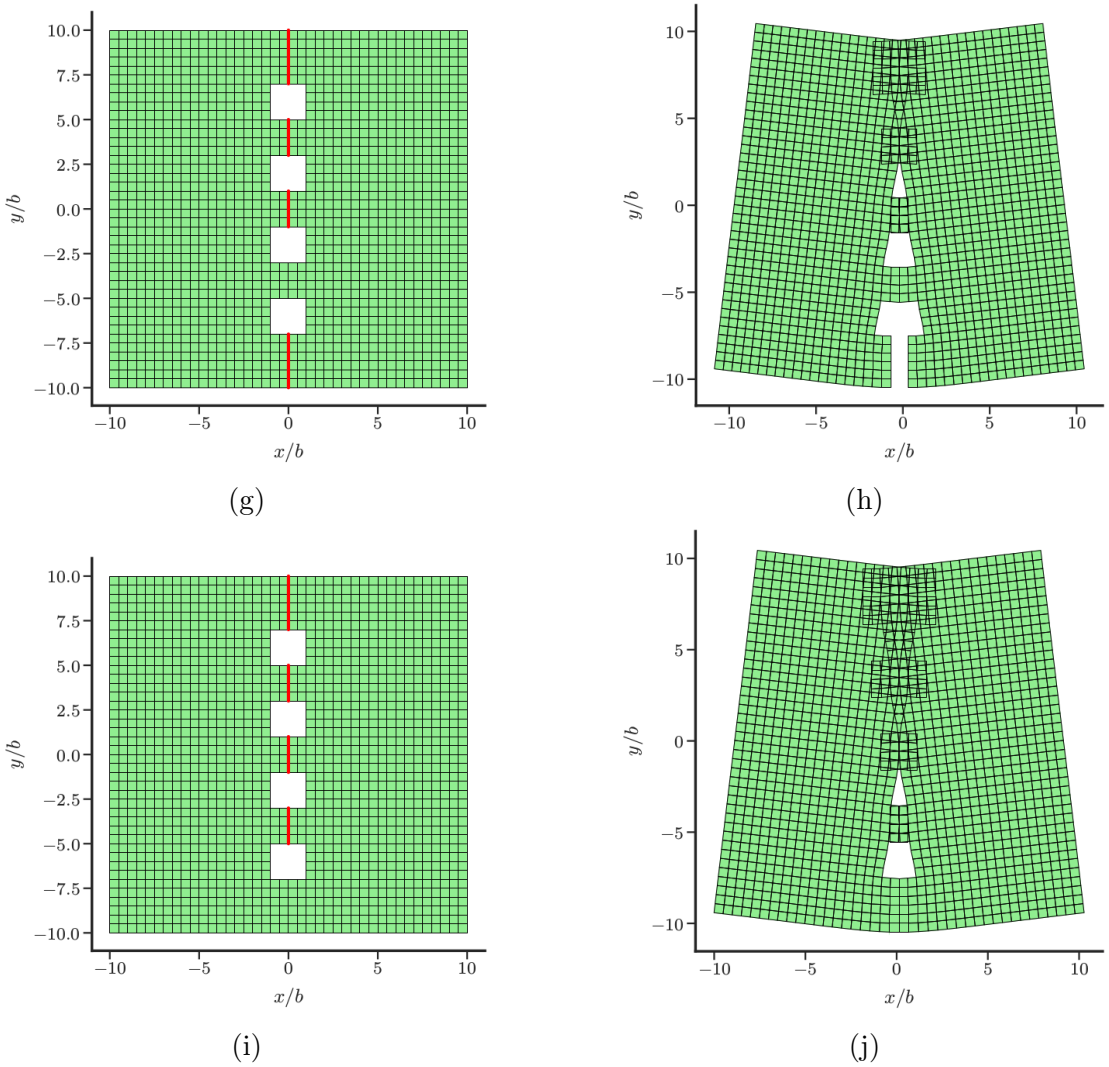

Figure 5.32: Non unique reference configurations (on the right) obtained for different simply connected configurations (on the left).

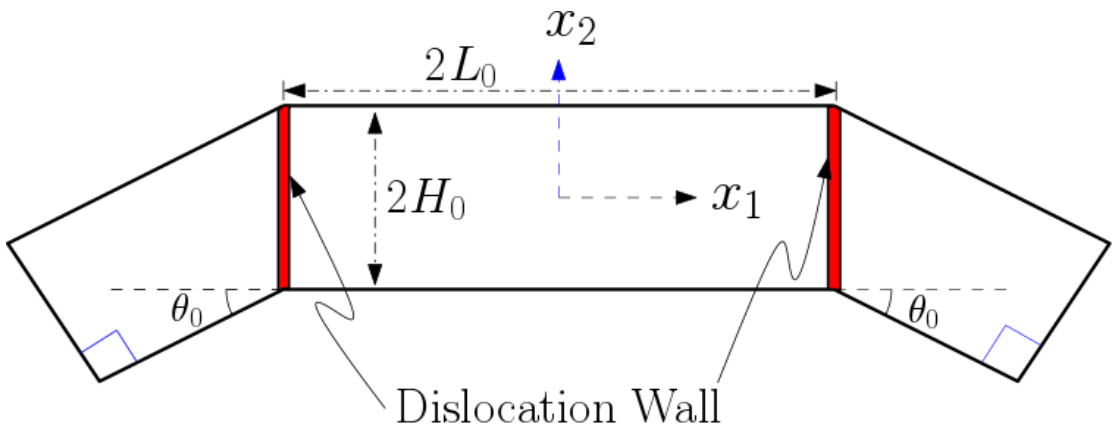

Figure 5.33: Schematic layout of a typical model geometry.

refined closer to the dislocation walls, with a total of 1 million elements is used to discretize the domain. Table 5.6 presents the values of the material constants used in the numerical simulation.

Parameter	Value
E	200 GPa
ν	.30

Table 5.6: Parameter values used for calculating stress field of a sequence of dislocation distributions.

In the limiting case, when the dislocation cores stack up to form a continuous grain boundary wall, the lattice on one side of the wall differs from the other side by a rigid rotation. We refer to this relative rigid rotation as the misorientation angle θ_0. Now, to construct the dislocation density for a given θ_0, we first write the inverse elastic distortion as a rotation field dependent on $\theta(\boldsymbol{x})$, defined in the full domain. We choose the following functional form of θ to generate two dislocation walls inside the polygonized domain with walls centered at $x_1 = -L_0$ and $x_1 = L_0$, respectively.

$$\theta(\boldsymbol{x}) = \frac{\theta_0}{2}\left(1 - \tanh(a\,x_1 + aL_0)\right) - \frac{\theta_0}{2}\left(1 + \tanh(a\,x_1 - aL_0)\right) \tag{5.15}$$

The value of $a = 4.2$ is chosen to ensure that the grain boundary wall width is less than b. Figure 5.34 shows a typical variation of theta in the domain for the polygonized domain

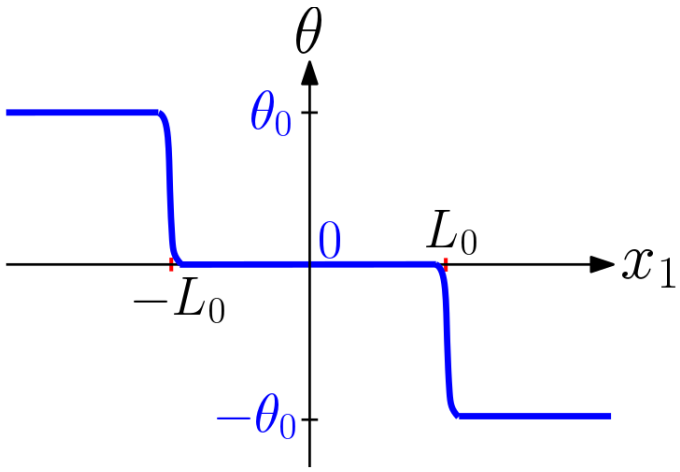

Figure 5.34: Variation of theta in the polygonized domain for dislocation walls centered at $x_1 = -L_0$ and $x_1 = L_0$.

shown in Fig. 5.33.

$$\boldsymbol{F}^e = \begin{bmatrix} \cos(\theta) & -\sin(\theta) & 0 \\ \sin(\theta) & \cos(\theta) & 0 \\ 0 & 0 & 1 \end{bmatrix} \tag{5.16}$$

The dislocation density is then calculated from the curl of this inverse elastic distortion field, $\boldsymbol{\alpha} = -curl(\boldsymbol{F}^{e-1})$. These localized gradients in θ over a small region give rise to localized dislocation density which corresponds to the presence of a full dislocation wall in the body. The α_{13} and α_{23} profiles on the polygonized domain for misorientation $\theta_0 = 5°$ is shown in figure 5.35a and 5.35b, respectively. For the case when $\theta_0 = 45°$, the α_{13} and α_{23} profiles are shown in figure 5.36a and 5.36b, respectively.

Since θ does not vary in the x_2 direction, $\boldsymbol{\alpha}$ is calculated as

$$\alpha_{13} = -\epsilon_{312} \left(\boldsymbol{F}^{e-1}\right)_{12,1} = \cos(\theta)\frac{d\theta}{dx}$$

$$\alpha_{23} = -\epsilon_{312} \left(\boldsymbol{F}^{e-1}\right)_{22,1} = \sin(\theta)\frac{d\theta}{dx}.$$

(a)

(b)

Figure 5.35: a) α_{13} b) α_{23} in the polygonized domain when misorientation $\theta_0 = 5°$.

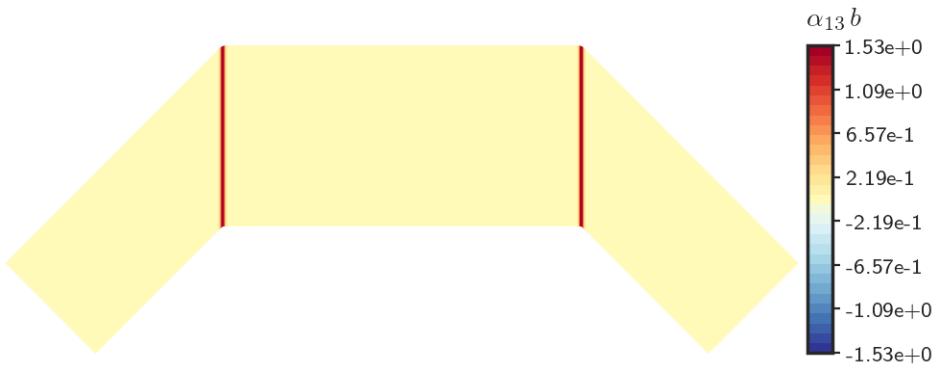

(a)

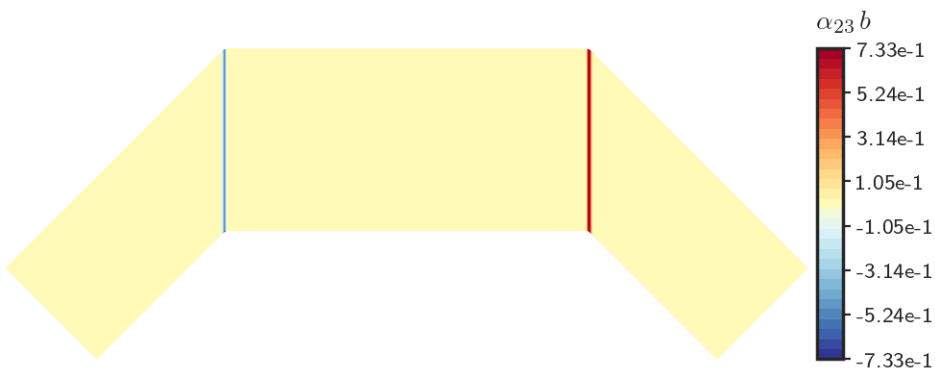

(b)

Figure 5.36: a) α_{13} b) α_{23} in the polygonized domain when misorientation $\theta_0 = 45°$.

Therefore, we notice that for small misorientations, $\alpha_{23} \approx \theta \frac{d\theta}{dx}$, which would be very small as compared to its evaluation at larger misorientations. It can also be seen from Figures 5.35b and 5.36b that α_{23} is large for the case when $\theta_0 = 45°$.

Once the dislocation density is prescribed, the ECDD system comprising Eqs. (3.31) and (3.32) is solved on the domain to determine the stress field. For this problem, the guess obtained from the linear theory is found to be inadequate to obtain a solution satisfying Eq. (3.14d). Therefore, we solve the problem by giving a guess which is closer to the exact solution. This guess is obtained by solving for $\boldsymbol{f}$ by using the Least-Squares finite element method, the objective functional for which is

$$J = \frac{1}{2} \int_{\Omega} ||grad\boldsymbol{f} + \boldsymbol{\chi} - \boldsymbol{F}^{e-1}||^2 dV,$$

wherein $\boldsymbol{F}^e$ is the rotation matrix corresponding to the prescribed misorientation, and $\boldsymbol{\chi}$ is known by solving the *div-curl* system (3.14b). The weak form is then given by

$$\begin{aligned} &\delta J_{\delta \boldsymbol{f}} = 0 \\ &\Rightarrow \int_{\Omega} grad\boldsymbol{f} : grad\delta\boldsymbol{f} = \int_{\Omega} (\boldsymbol{F}^{e-1} - \boldsymbol{\chi}) : grad\delta\boldsymbol{f} dV. \end{aligned} \tag{5.17}$$

$\boldsymbol{f}$ is fixed at one point in the domain to uniquely solve for it. Solving for $\boldsymbol{f}$ from the least squares method means $(\boldsymbol{F}^{e-1} - \boldsymbol{\chi})\,\boldsymbol{n} = grad\boldsymbol{f}\,\boldsymbol{n}$ holds on the external boundary weakly.

Figures 5.37a and 5.37b show the distribution of T_{12} in the domain for the cases $\theta_0 = 5°$ and $\theta_0 = 45°$ with the dislocation density fields corresponding to full walls, respectively. As can be seen, the shear stresses almost vanish in the entire domain for both the cases. To further verify vanishing of all the components of stress tensor $\boldsymbol{T}$, we define two measures of strain energy density in the domain as follows

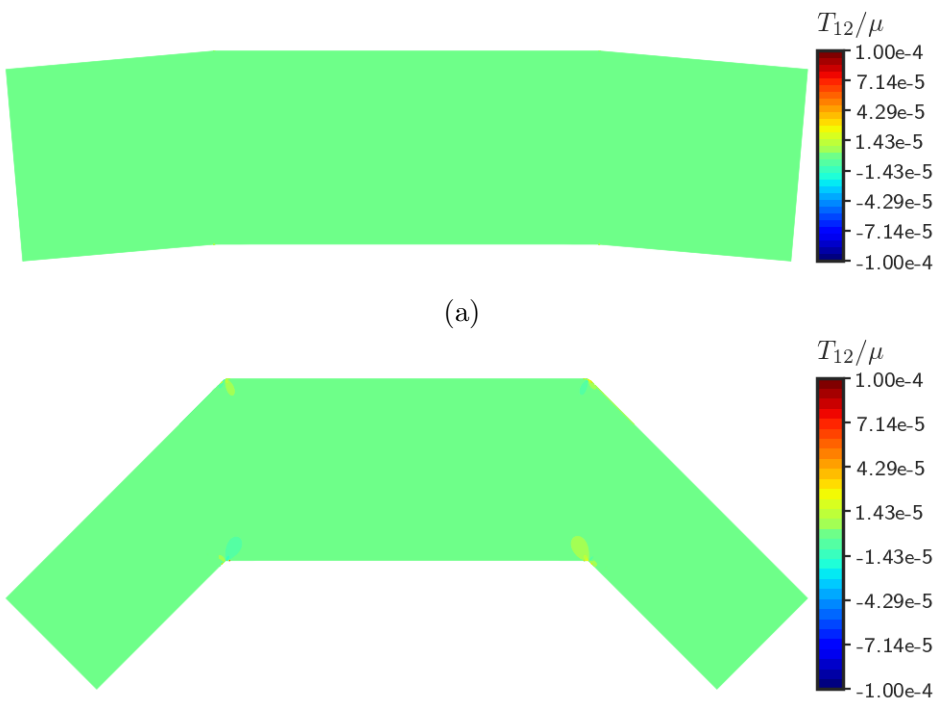

(a)

(b)

Figure 5.37: T_{12} in the polygonized domain. a) $\theta_0 = 5°$ b) $\theta_0 = 45°$.

$$\bar{\psi}_{fd} = \frac{1}{2\mu}\boldsymbol{E}^e : \mathbb{C} : \boldsymbol{E}^e \tag{5.18}$$

$$\bar{\psi}_{sd} = \frac{1}{2\mu}\boldsymbol{U}^e : \mathbb{C} : \boldsymbol{U}^e \tag{5.19}$$

$$\boldsymbol{U}^e = \boldsymbol{F}^e - \boldsymbol{I}.$$

In the above, $\boldsymbol{U}^e$ denotes the small deformation elastic distortion field, $\bar{\psi}_{fd}$ and $\bar{\psi}_{sd}$ denote the finite and small deformation strain energy density, respectively.

Figures 5.38a and 5.38b show the distribution of finite deformation strain energy density $\bar{\psi}_{fd}$ in the domain for the cases $\theta_0 = 5°$ and $\theta_0 = 45°$, respectively. For both the cases, it can be seen that the negligible magnitude of $\bar{\psi}_{fd}$ distribution in the body demonstrate that the body is stress-free.

Figures 5.39a and 5.39b demonstrate that the small deformation theory predicts non-zero

(a)

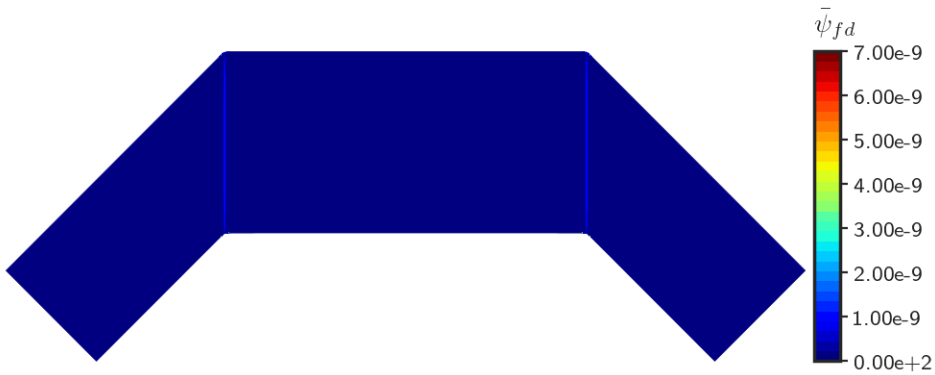

(b)

Figure 5.38: Finite deformation strain energy density $\bar{\psi}_{fd}$ in the polygonized domain a) $\theta_0 = 5°$ b) $\theta_0 = 45°$.

strain energy distribution even when the elastic distortion $\boldsymbol{F}^e$ is a rigid rotation. Therefore, we conclude that the finite deformation theory accurately predicts zero strain energy fields while the small deformation theory fails to do so, with the approximation being better for small misorientation.

We now demonstrate the stress and energy density field paths induced by a sequence of dislocation distributions, going from one core to a full wall. We calculate the stress fields in a rectangular domain of size $100b \times 50b$. A uniform mesh of $(0.1b)^2$ sized elements is used to discretize the domain. The $\theta(\boldsymbol{x})$ resulting in the presence of a wall of single dislocations stacked vertically centered at $x_1 = 0$ is given by

$$\theta(\boldsymbol{x}) = \frac{\theta_0}{2}\left(1 - \tanh(a\, x_1)\right) \tag{5.20}$$

where θ_0 is the relative misorientation of the lattice across the wall. The curl of the inverse

(a)

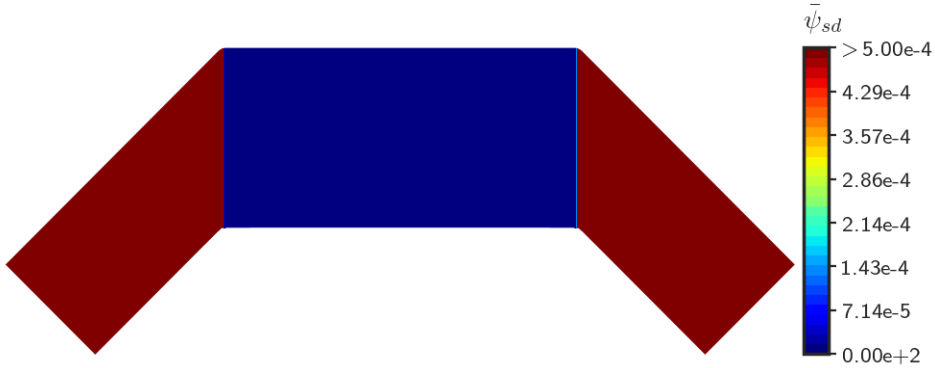

(b)

Figure 5.39: Small deformation strain energy density $\bar{\psi}_{sd}$ in the polygonized domain a) $\theta_0 = 5°$ b) $\theta_0 = 45°$. In (b), for the region where $\psi_{sd} > 5 \times 10^{-4}$, the value is 0.4.

elastic distortion field as given in Eq. (5.16) gives the dislocation density corresponding to the full wall. The dislocation density corresponding to a single core amounts to prescribing this dislocation density only in a region of height b. The dislocation density corresponding to multiple cores in the body can then be prescribed by taking the dislocation density corresponding to a single core and aligning it vertically with the previous ones. For this particular problem, when the number of cores is less than 40, we obtain the initial guess to the Newton-Raphson method from the small deformation equilibrium problem which is solved on the current configuration for the given dislocation density field as discussed in Sec. 4.1.4.3. However, for the number of cores beyond 40, the initial guess is obtained by solving Eq. (5.17) (corresponding to a full dislocation wall). The number of cores in the body is denoted by n_c.

The chosen sequence of positions and number (of cores) for the α_{13} component of dislocation density is shown in Figure 5.40. α_{23} is similarly placed and its values are assigned

accordingly.

The same sequence (both position and number) is chosen when the misorientation is 45°. However, the magnitude of components of dislocation density of individual cores change.

Figures 5.41 and 5.42 show the variation of the T_{12} shear stress field with the number of cores when the misorientation is 5° and 45°, respectively. The stress distribution is significant when the cores do not form a full wall. In the limit, the stress field is again zero as already shown in Figs. 5.37a and 5.37b. The stress, in most parts of the body, is very small when the cores form a continuous wall, except for a boundary effect where the wall meets the exterior boundary. This small boundary effect can further be shown to reduce with mesh refinement as shown in Figures 5.43a and 5.43b for $\theta_0 = 5°$ and $\theta_0 = 45°$, respectively.

Figures 5.44 and 5.45 show the finite deformation strain energy density $\bar{\psi}_{fd}$ in the body when the misorientation is 5° and 45°, respectively. Similar to the Figures 5.38a and 5.38b presented earlier, we notice that $\bar{\psi}_{fd}$ again becomes negligible for the case when the dislocations arrange to form a full grain boundary wall.

Figures 5.46a and 5.46b show the effect of mesh refinement on the finite deformation strain energy density $\bar{\psi}_{fd}$ in the presence of grain boundary walls for misorientations 5° and 45°, respectively. We can see that the strain energy density in the domain decreases further on refinement.

For $\theta_0 = 45°$, an important thing to note from Figures 5.42 and 5.45 is that there is a drastic change in the stress and the strain energy distributions when the number of cores n_c exceed 40. The variation (for both T_{12} and $\overline{\psi}_{fd}$) which was spreadout in the entire domain suddenly becomes localized near the core and the boundary when $n_c > 40$. It is clear that when the number of (same sign) dislocations in the body increases from 0 the stress and energy have to increase. It is also clear that the full wall must represent a stress and energy free configuration. Whether the transition between these behaviors has to be an abrupt 'phase transition', as indicated by our calculations, is an interesting question for further study.

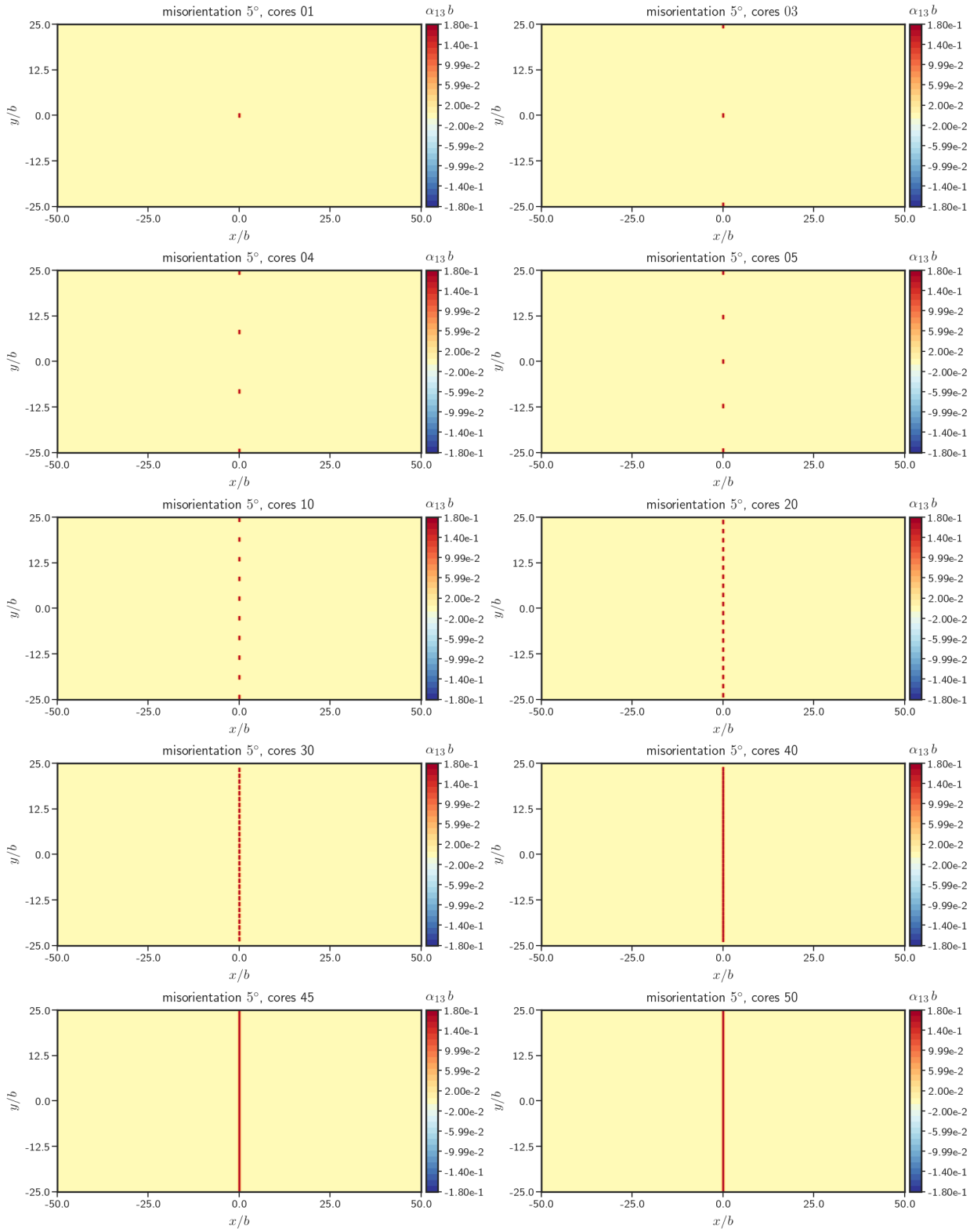

Figure 5.40: Position of dislocation cores α_{13} field in the body when misorientation is 5° for different number of dislocation cores.

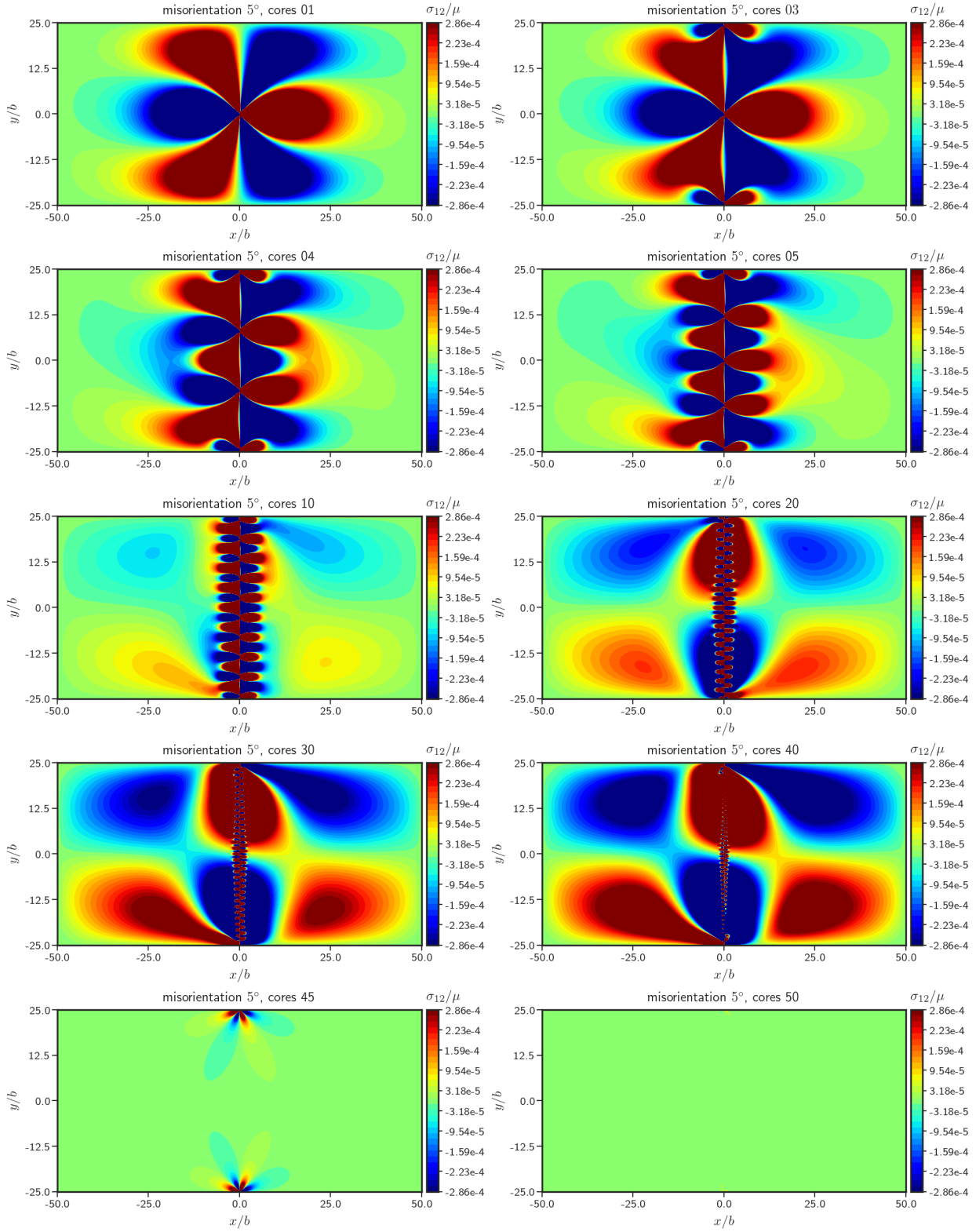

Figure 5.41: T_{12} distribution in the body when $\theta_0 = 5°$ for different number of dislocation cores, all plotted on the same scale.

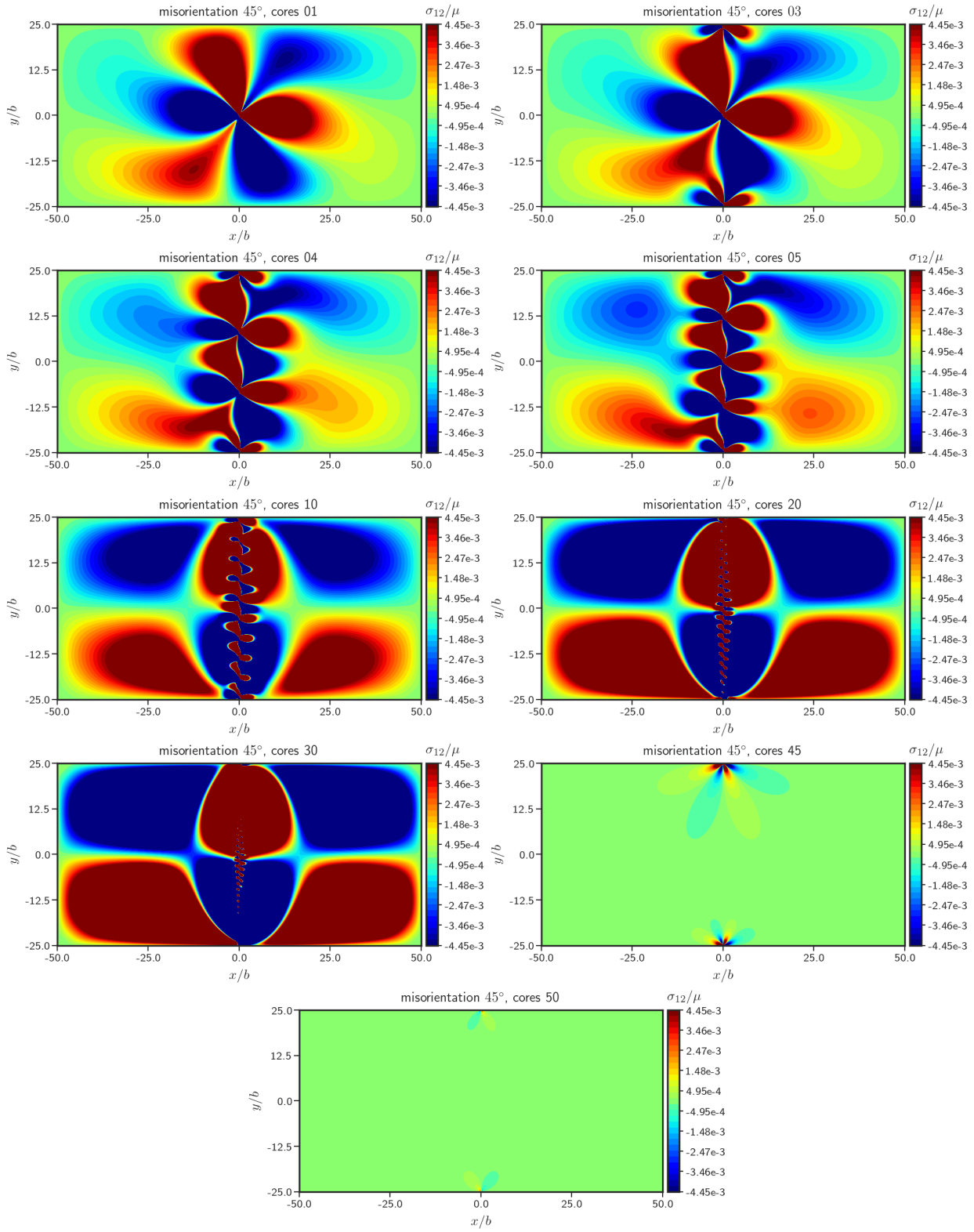

Figure 5.42: T_{12} distribution in the body when $\theta_0 = 45°$ for different number of dislocation cores, all plotted on the same scale.

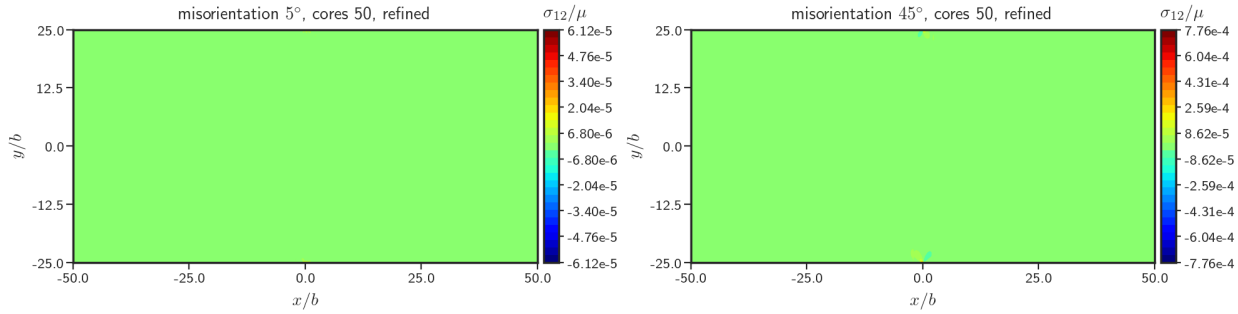

(a) (b)

Figure 5.43: T_{12} on a refined mesh when dislocations arrange to form a full grain boundary wall a) $\theta_0 = 5°$ b) $\theta_0 = 45°$.

Figures 5.47a and 5.47b show the mapped $\boldsymbol{e}_1$ vectors by the elastic distortion field on the current configuration. We can see that the lattice on the left of the dislocation wall is rigidly rotated w.r.t. the lattice on the right by the prescribed misorientation angle.

Also, we calculate the change in volume as described in Sec. 5.5. For the cases when the cores combine to form a full grain boundary wall, the % change in volume comes out to be 0 to a very high precision (10 decimal places), further ensuring that the deformation is just a rigid rotation in the domain.

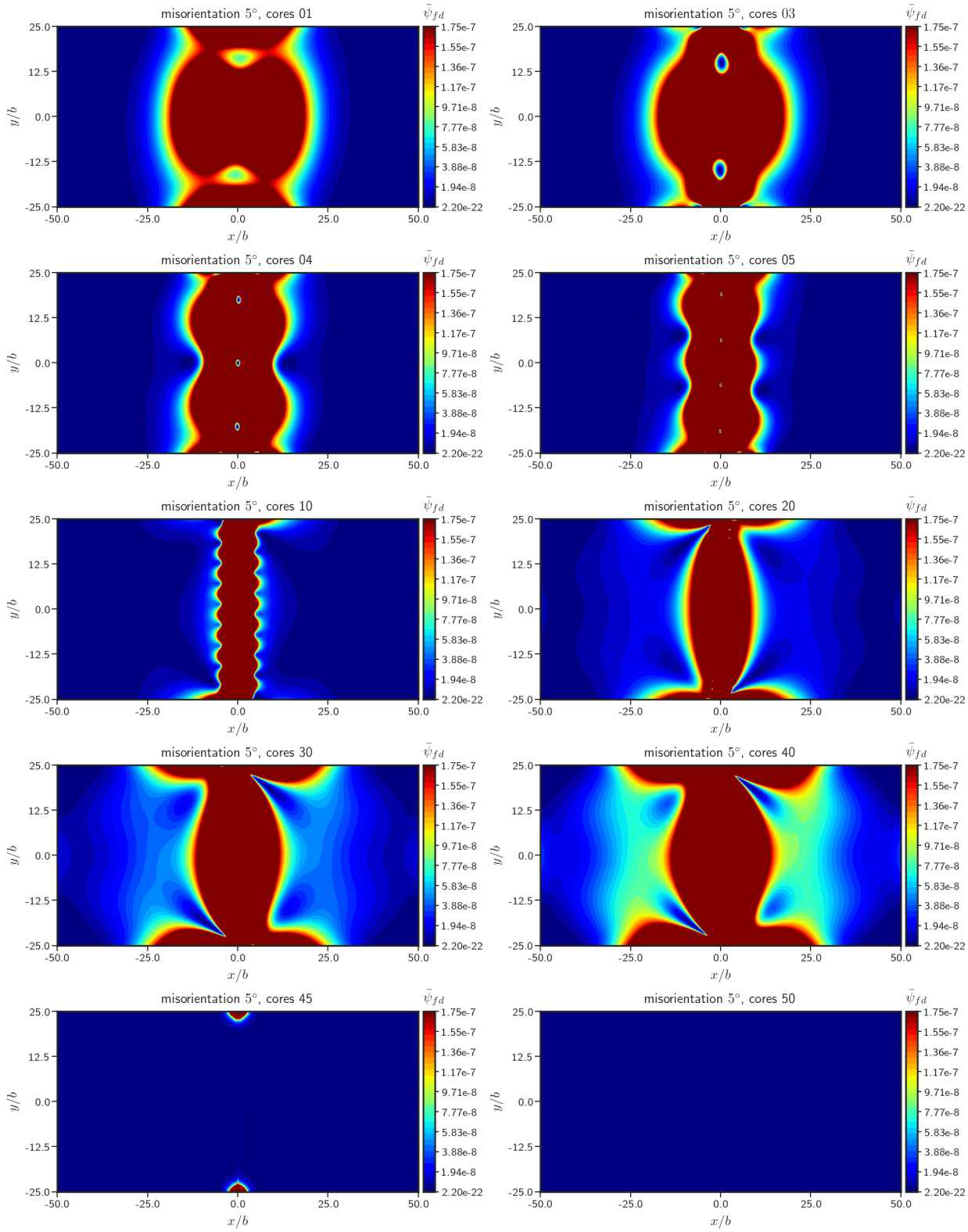

Figure 5.44: $\bar{\psi}_{fd}$ distribution when $\theta_0 = 5°$ for different number of dislocation cores, all plotted on the same scale.

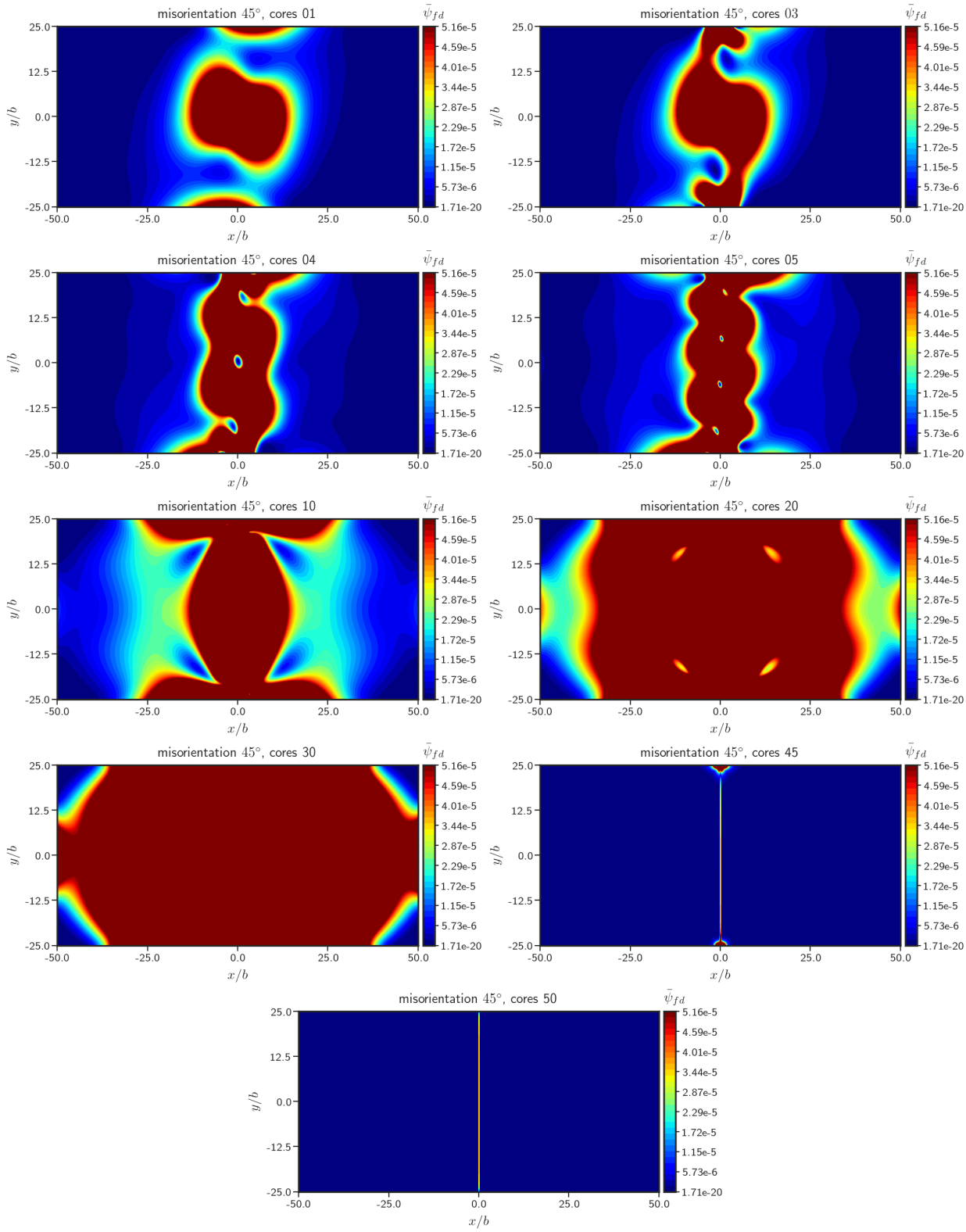

Figure 5.45: $\bar{\psi}_{fd}$ distribution when $\theta_0 = 45°$ for different number of dislocation cores, all plotted on the same scale.

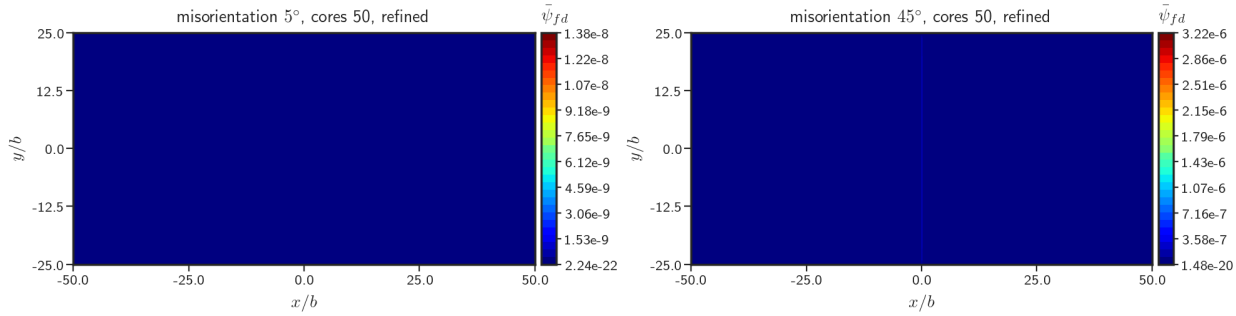

(a) (b)

Figure 5.46: $\bar{\psi}_{fd}$ on a refined mesh when dislocations arrange to form a full grain boundary wall a) 5° b) 45°.

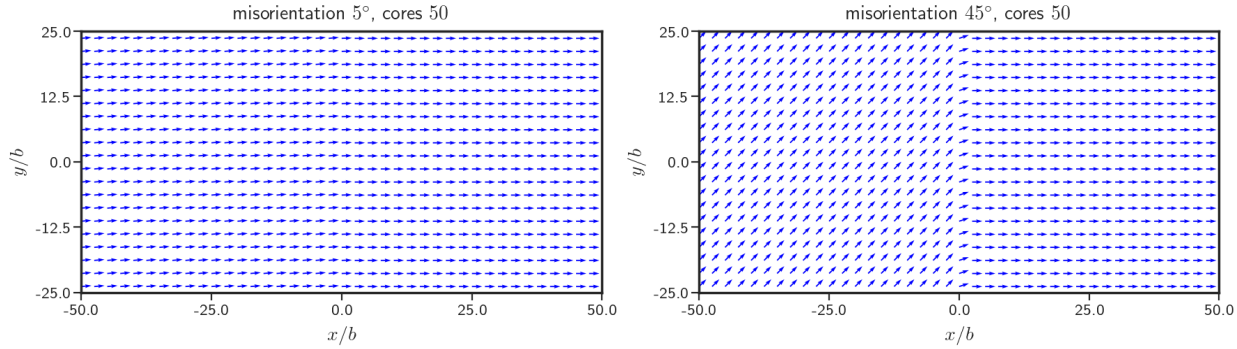

(a) (b)

Figure 5.47: Mapping of $\boldsymbol{e}_1$ vectors by elastic distortion field $\boldsymbol{F}^e$.

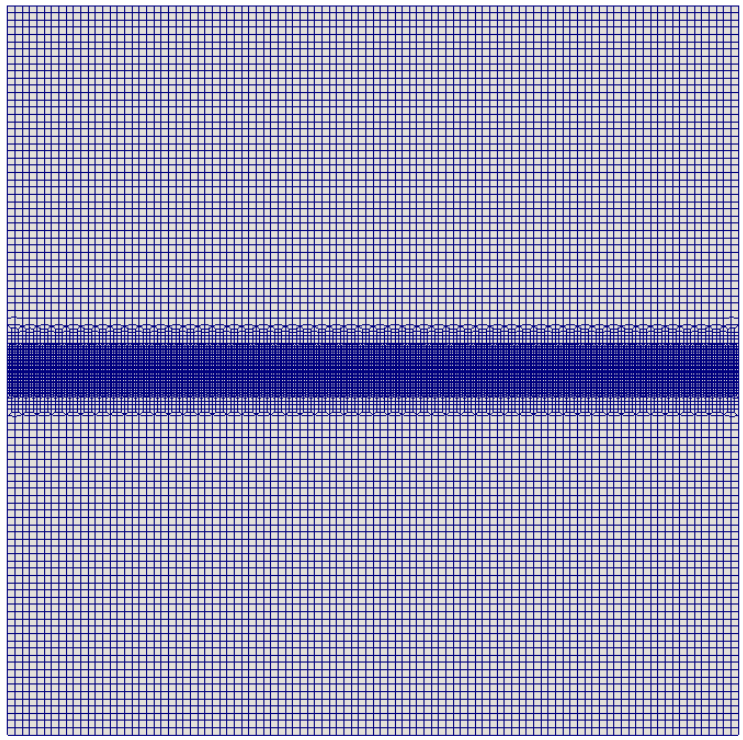

Figure 5.48: Mesh with $23,000$ elements for dynamic problems

5.7 (Stress-uncoupled) FDM with inertia

In this section, we present some results of calculations where inertia is accounted for in the numerical formulation. The full algorithm for the dynamic case appears in Table 4.2. The results presented here are for the case when the dislocation velocity is uncoupled to the underlying stress field. We study two problems:

- A single edge dislocation dynamically moving in the $\boldsymbol{e}_1$ direction at constant velocity. The solution reflects similarities to the longitudinal propagation of dynamic shear bands.

- Two dislocations of opposite sign moving towards each other with prescribed speeds and annihilate.

Although the dislocation velocity is uncoupled to the underlying stress field, the dislocation density evolution is coupled to the evolving deformation of the body through the

gradient of the material velocity field $\boldsymbol{v}$ which makes the problem nonlinear.

In the formulation, b is a fundamental length scale that correlates with the core size. At the atomistic scale, b denotes the Burgers vector of the full dislocation in the material. At the mesoscale, it could be a length scale related to the core-size of a shear band, a measurable quantity.

A non-uniform mesh, shown in figure 5.48, that is highly refined in a layer where the dislocation density will evolve is chosen for both the problems. Table 5.7 presents the values of the material constants used for the simulations presented in this section.

Parameter	Value
E	$200GPa$
ν	.30

Table 5.7: Parameter values used for modeling dynamics of single dislocation.

5.7.1 Single dislocation

The problem is set up as follows: a single edge dislocation with a Burgers vector $\boldsymbol{b} = b\boldsymbol{e}_1$ is considered in a domain of dimensions $[-20b, 20b] \times [-20b, 20b]$. The edge dislocation is modeled by prescribing an initial dislocation density tensor $\boldsymbol{\alpha}$ of the form

$$\begin{aligned} \alpha_{13}(x_1, x_2, t = 0) &= \varphi_0 \left(1 - tanh^2 \left(\frac{|\boldsymbol{x} - \boldsymbol{p}|}{b}\right)\right) \\ \alpha_{ij}(x_1, x_2, t = 0) &= 0 \text{ if i} \neq 1 \text{ and j} \neq 3. \end{aligned} \tag{5.21}$$

φ_0 is a constant chosen to give a dislocation of strength b by ensuring $\int_{A_0} \alpha_{13}\, dA = b$, where A_0 is any area patch in the domain at $t = 0$ that encloses the dislocation. x_1 and x_2 are the in-plane coordinates of any point $\boldsymbol{x}$ in the domain and $\boldsymbol{p}$ denotes the initial position of the dislocation. At all times, the dislocation is assumed to be moving with a constant velocity $\boldsymbol{V} = \frac{v_s}{2.0}\boldsymbol{e}_1$, where v_s is the shear wave speed of the body. For the computation presented below, $\boldsymbol{p}$ is taken to be $\boldsymbol{0}$. The system is then evolved by following the algorithm given in Table 4.2.

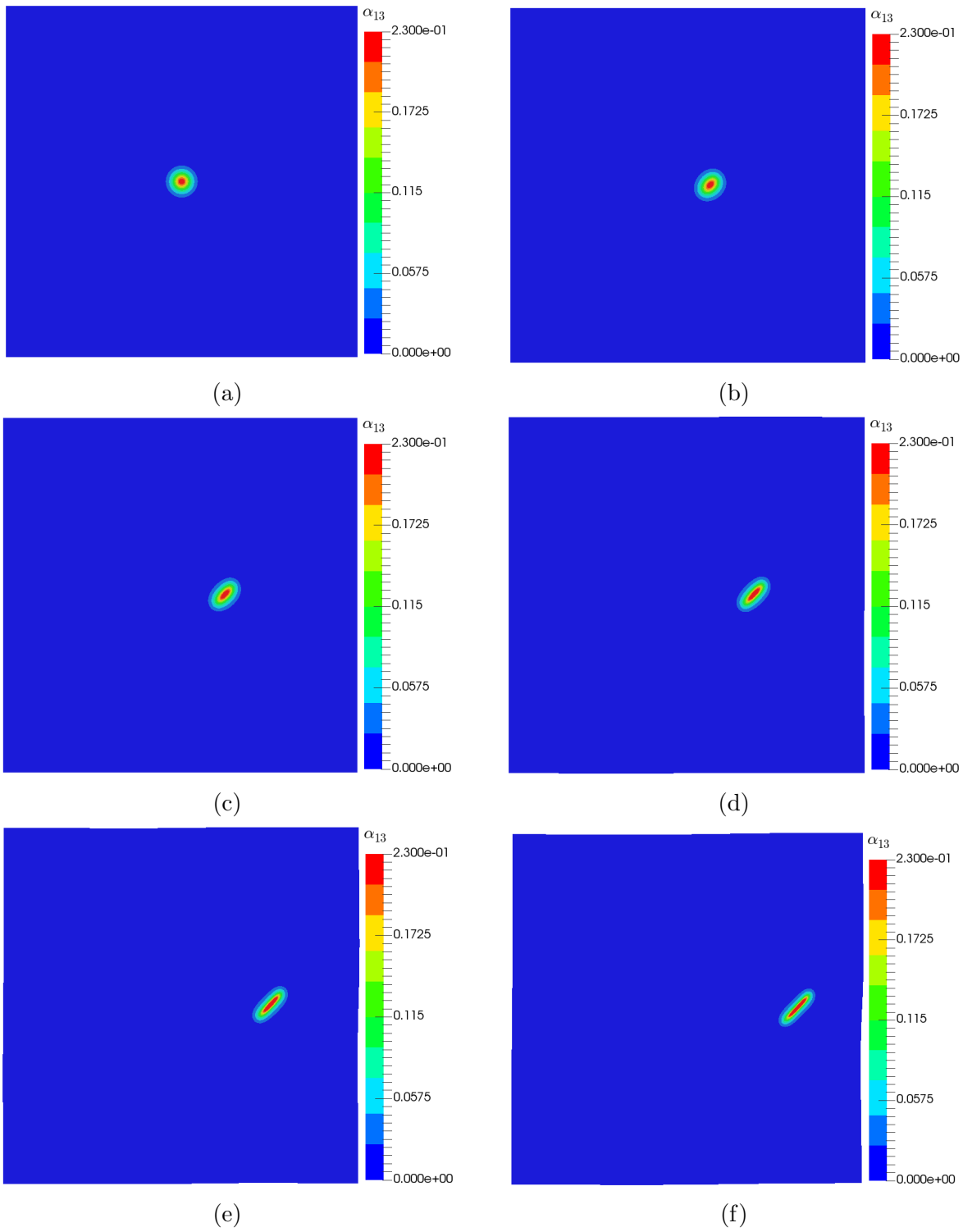
α_{13}
2.300e-01
0.1725
0.115
0.0575
0.000e+00
(a)
(b)
(c)
(d)
(e)
(f)

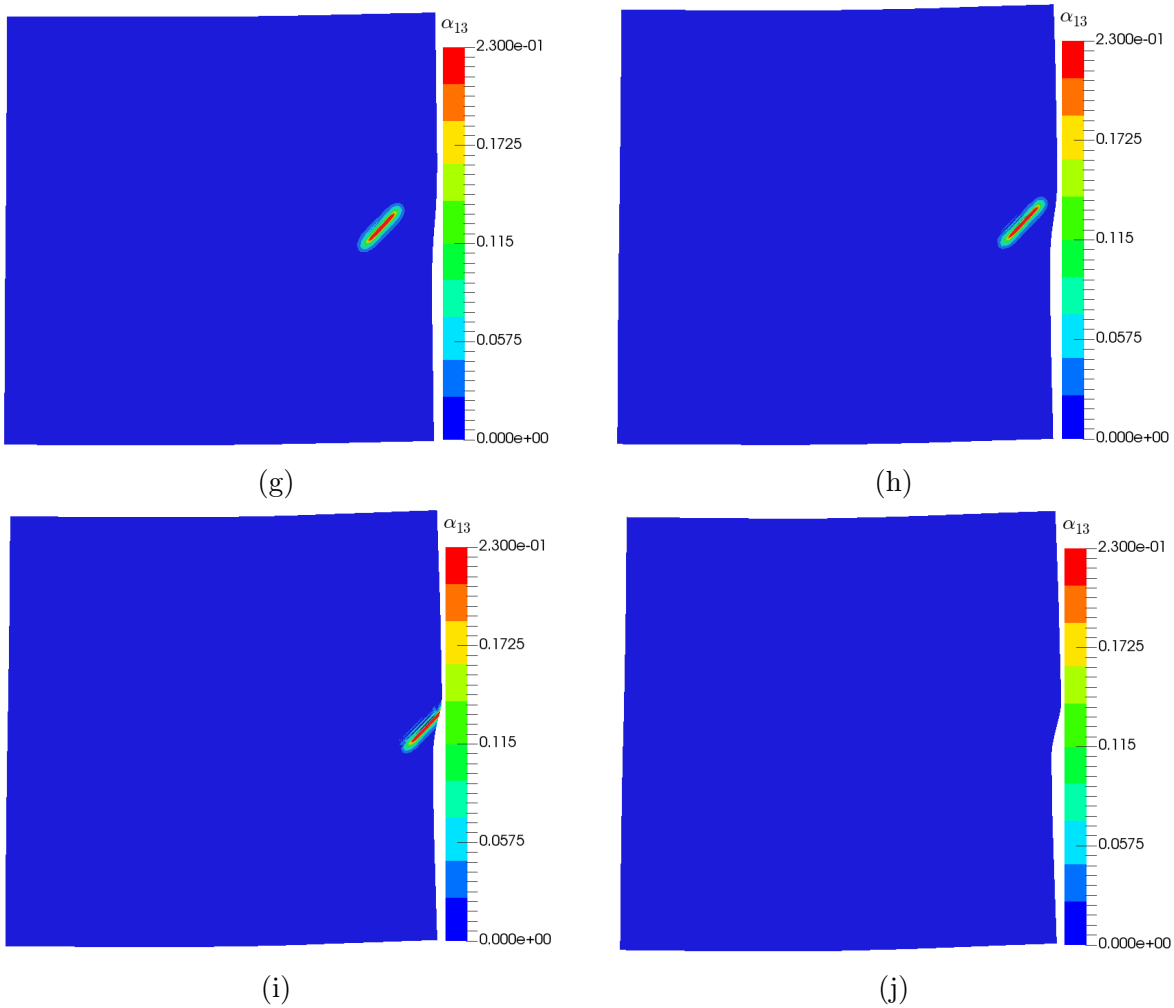

Figure 5.49: Position of dislocation core at different times t^* a) 0 b) 3 c) 6 d) 9 e) 12 f) 15 g) 18 h) 21 i) 24 j) 30

Figure 5.49 shows the dislocation position at various non-dimensional times $t^* = \frac{t\,v_s}{b}$, where t is the dimensional time. We can see the formation of a slip step when the dislocation exits the body in 5.49j. Another interesting feature to note here is that as the evolution progresses, the dislocation density is not radially symmetric anymore, and tilts towards the right. The distribution is almost elliptical with major axis along the direction of tilting. The tight coupling of the dislocation transport equation Eq. (3.14a) to the underlying material velocity field $\boldsymbol{v}$ through its gradient $\boldsymbol{L}$ in the finite deformation case gives rise to such a distribution.

Furthermore, the tilt towards the right is because of the positive $(\boldsymbol{\alpha} \times \boldsymbol{V})_{12}$ component of the plastic strain rate generated by the motion of the dislocation. Therefore, a negative dislocation ($\boldsymbol{b} = -b\boldsymbol{e}_1$) moving in the $-\boldsymbol{e}_1$ direction also tilts towards the right as the plastic strain rate component is still positive which can be seen in Fig. 5.51.

Figure 5.50 shows the evolution of the F_{12} component of the deformation gradient $\boldsymbol{F}$ in the domain at the corresponding times. There is an accumulation of shear deformation in the wake of the moving dislocation. The body is permanently deformed when the dislocation exits the body with a clear region where slip occurred, mimicking a shear band.

5.7.2 Multiple dislocations

The problem is set up as follows: Two edge dislocations with Burgers vectors $\boldsymbol{b}^1 = b\boldsymbol{e}_1$ and $\boldsymbol{b}^2 = -b\boldsymbol{e}_1$ are considered in a domain of dimensions $[-20b, 20b] \times [-20b, 20b]$. The edge dislocations are modeled by prescribing an initial dislocation density tensor $\boldsymbol{\alpha}$ of the form

$$\alpha_{13}(x_1, x_2, t = 0) = \varphi_0 \left(tanh^2 \left(\frac{|\boldsymbol{x} - \boldsymbol{p}|}{b} \right) - tanh^2 \left(\frac{|\boldsymbol{x} - \boldsymbol{q}|}{b} \right) \right)$$

$$\alpha_{ij}(x_1, x_2, t = 0) = 0 \text{ if i} \neq 1 \text{ and j} \neq 3.$$

The value of φ_0 is assumed to be the same as in Eq. (5.21) which ensures the strength of each dislocation to be b. $\boldsymbol{p}$ and $\boldsymbol{q}$ are the initial position vectors of the two dislocations. In

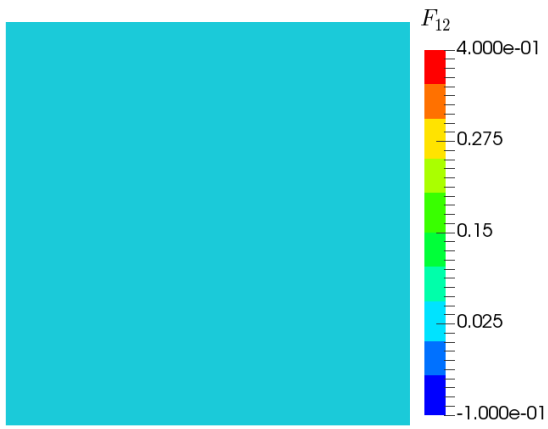
F_{12}
4.000e-01
0.275
0.15
0.025
-1.000e-01

(a)

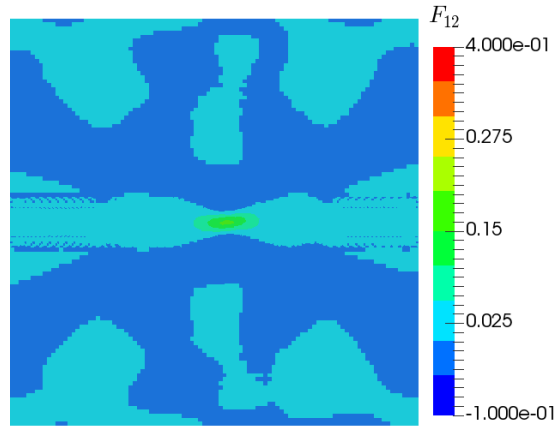
F_{12}
4.000e-01
0.275
0.15
0.025
-1.000e-01

(b)

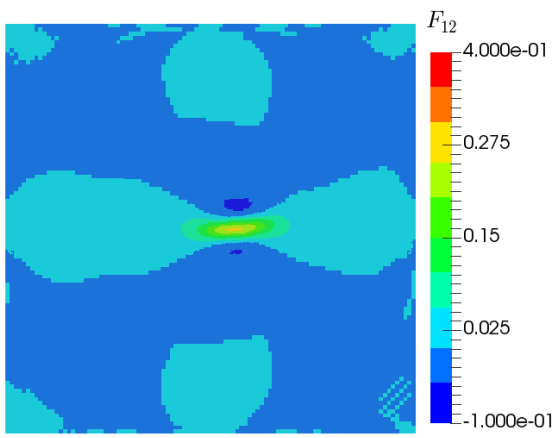
F_{12}
4.000e-01
0.275
0.15
0.025
-1.000e-01

(c)

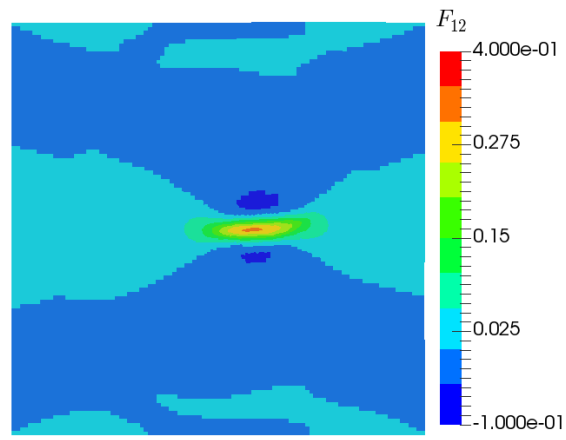
F_{12}
4.000e-01
0.275
0.15
0.025
-1.000e-01

(d)

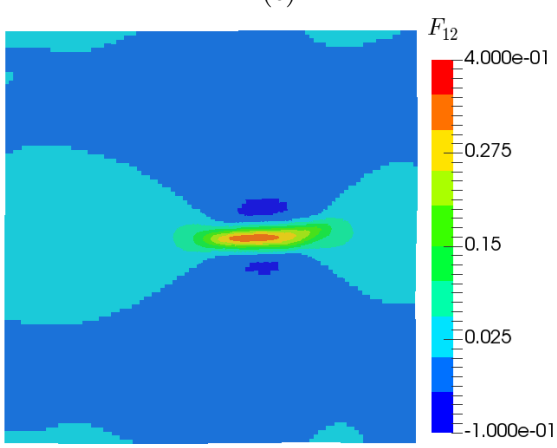
F_{12}
4.000e-01
0.275
0.15
0.025
-1.000e-01

(e)

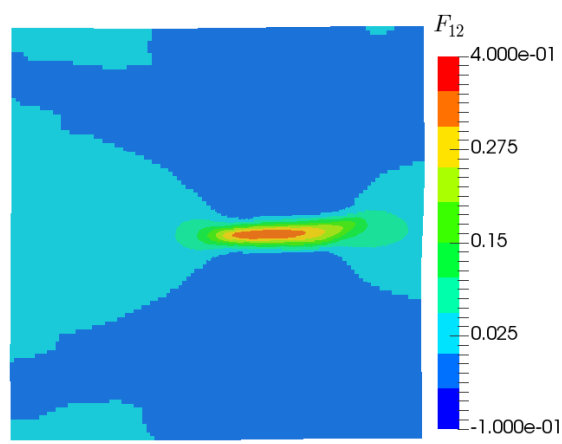
F_{12}
4.000e-01
0.275
0.15
0.025
-1.000e-01

(f)

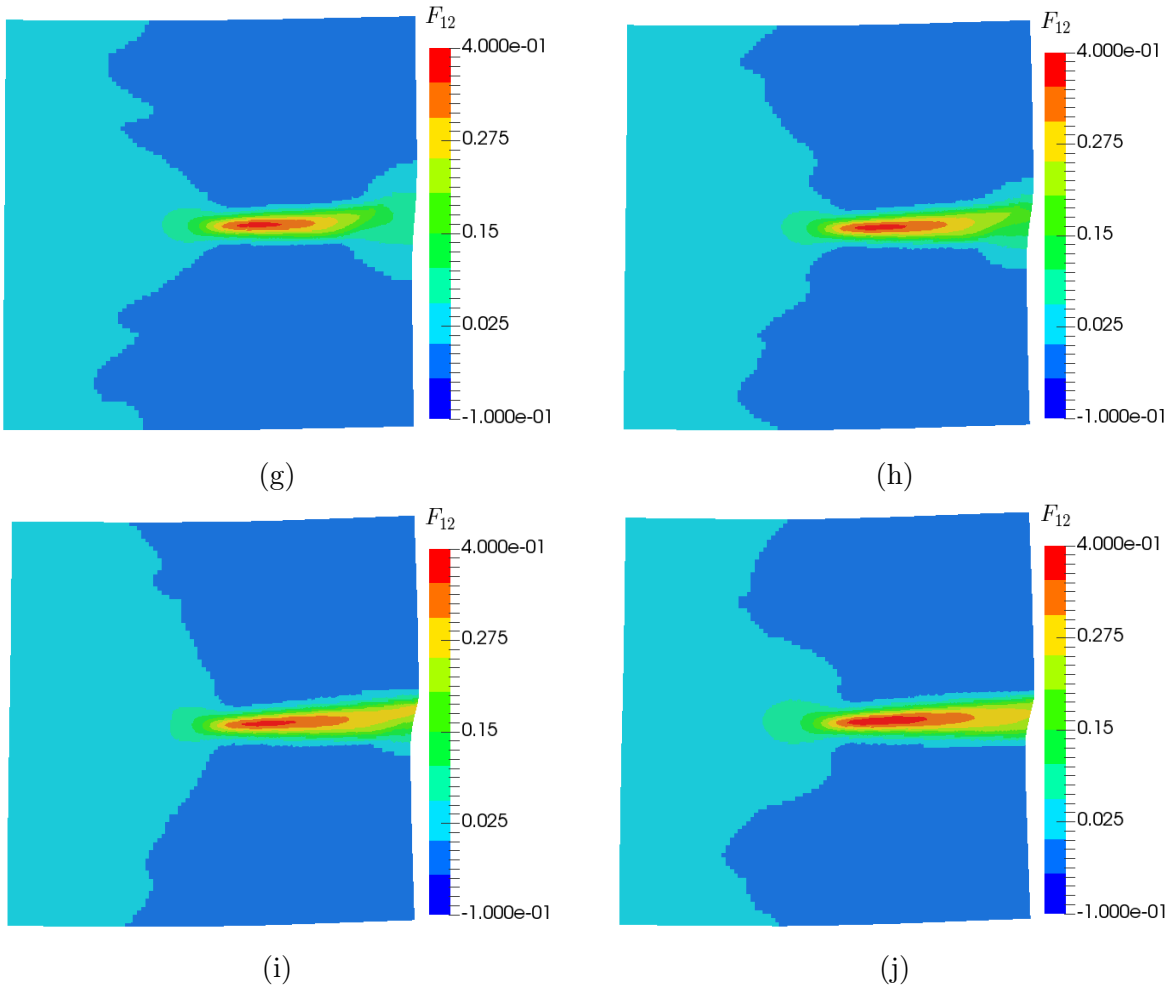

Figure 5.50: F_{12} in the domain at different times, t^* a) 0 b) 3 c) 6 d) 9 e) 12 f) 15 g) 18 h) 21 i) 24 j) 30.

the computed example below, $\boldsymbol{p}$ and $\boldsymbol{q}$ are taken as $-5b\boldsymbol{e}_1$ and $5b\boldsymbol{e}_1$, respectively. At all times, each dislocation is assumed to be moving with a prescribed velocity given by

$$\boldsymbol{V}^i = \frac{v_s}{2.0}\boldsymbol{e}_2 \times \boldsymbol{l}^i \tag{5.22}$$

where $\boldsymbol{l}^i = \frac{1}{|\boldsymbol{b}^i|}(\boldsymbol{b}^i \otimes \boldsymbol{e}_3)^T\boldsymbol{e}_1$ is the line direction of the ith dislocation. Therefore, the positive and negative dislocations move in the $\boldsymbol{e}_1$ and $-\boldsymbol{e}_1$ directions, respectively, at the same constant speed. The system is then evolved by following the algorithm given in Table 4.2.

Figure 5.51 shows the dislocation positions at various non-dimensional times, t^*. It can be seen that the two dislocations of opposite sign annihilate each other leaving behind a slipped embryo along the path of the dislocations in the domain. This is demonstrated in Figure 5.52 which shows the evolution of the F_{12} component of the deformation gradient in the domain at the corresponding times.

As noted in [VBAF06], for a $1d$ small deformation case (dislocation evolution is uncoupled to stress field and material velocity gradient), when dislocation densities of opposite sign meet, a discontinuity (shock) develops, grows, and finally disappears. Here, we have presented a full finite deformation scheme that is able to qualitatively resolve the shock and model the result of the interaction, which is that the dislocations are annihilated.

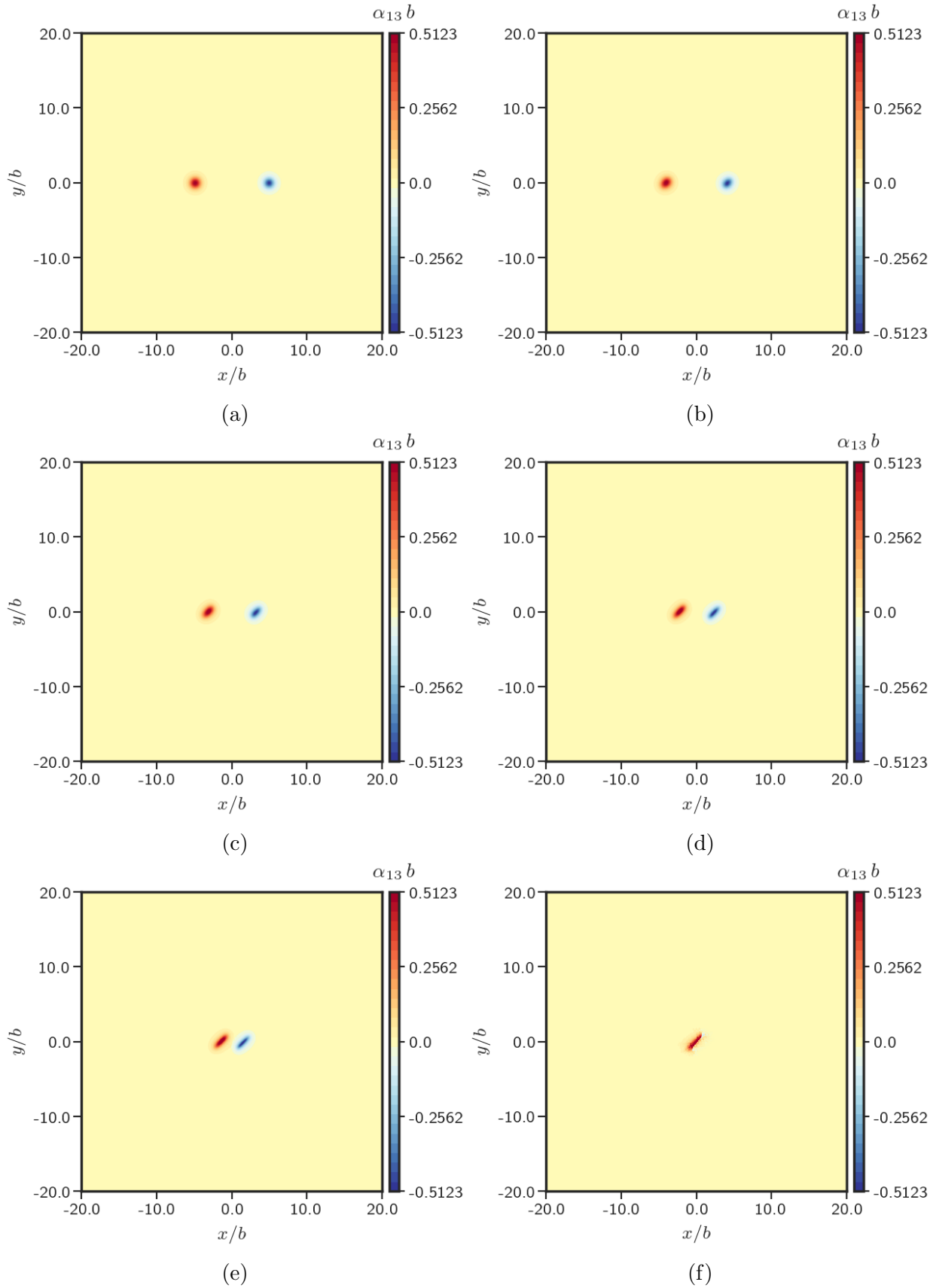
$\alpha_{13}\, b$
0.5123
0.2562
0.0
-0.2562
-0.5123
20.0
10.0
0.0
-10.0
-20.0
y/b
x/b
(a)
(b)
(c)
(d)
(e)
(f)

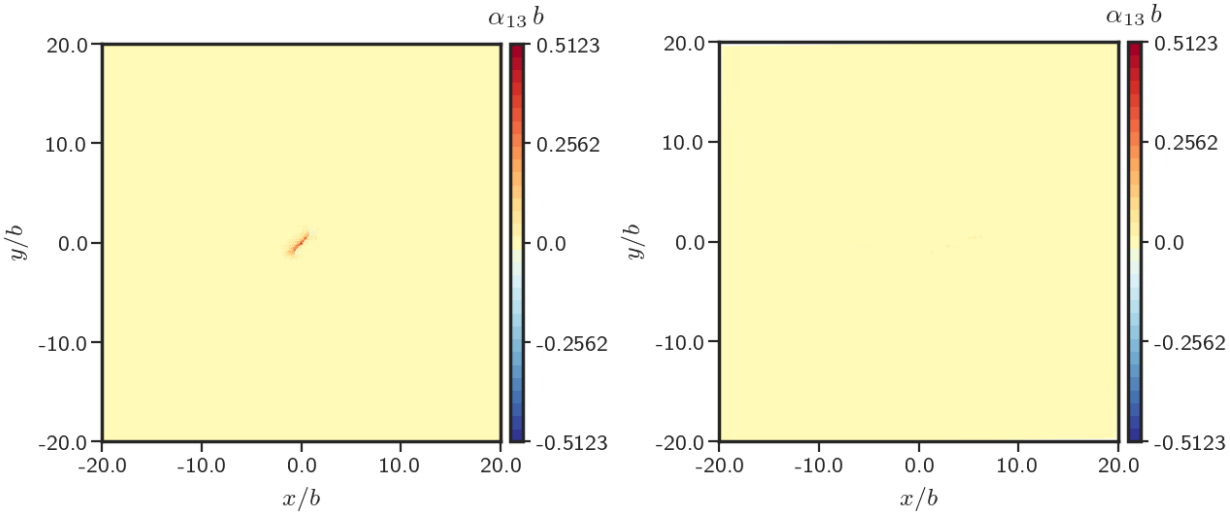

(g) (h)

Figure 5.51: Position of dislocation core at different times, t^* a) 0 b) 1.5 c) 3 d) 4.5 e) 6 f) 12 g) 18 h) 24.

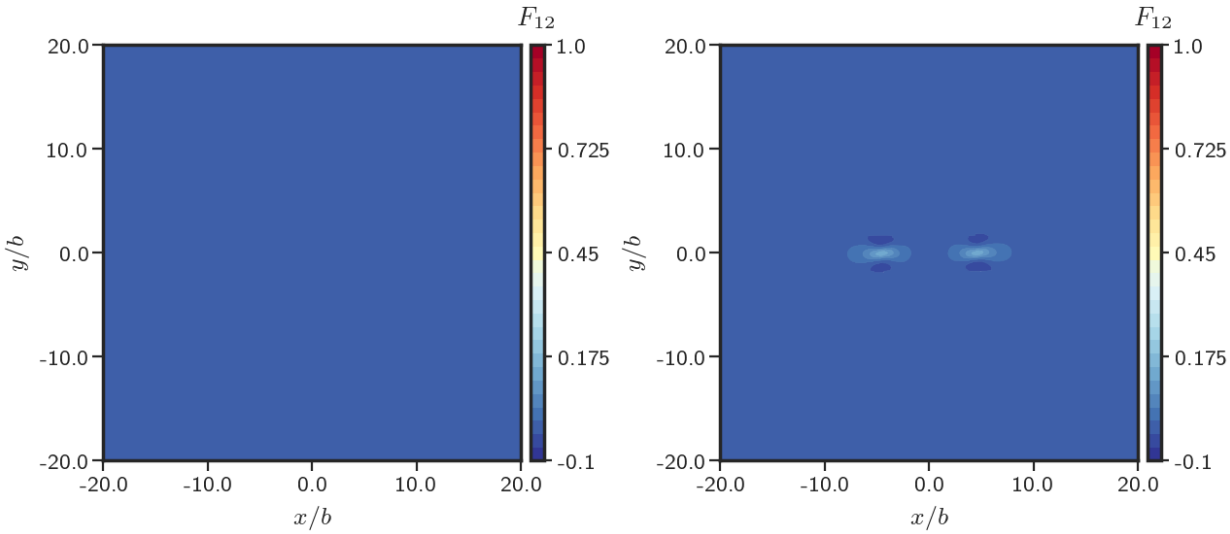
F_{12}
1.0
0.725
0.45
0.175
-0.1
20.0
10.0
0.0
-10.0
-20.0
y/b
x/b

(a)

F_{12}
1.0
0.725
0.45
0.175
-0.1
20.0
10.0
0.0
-10.0
-20.0
y/b
x/b

(b)

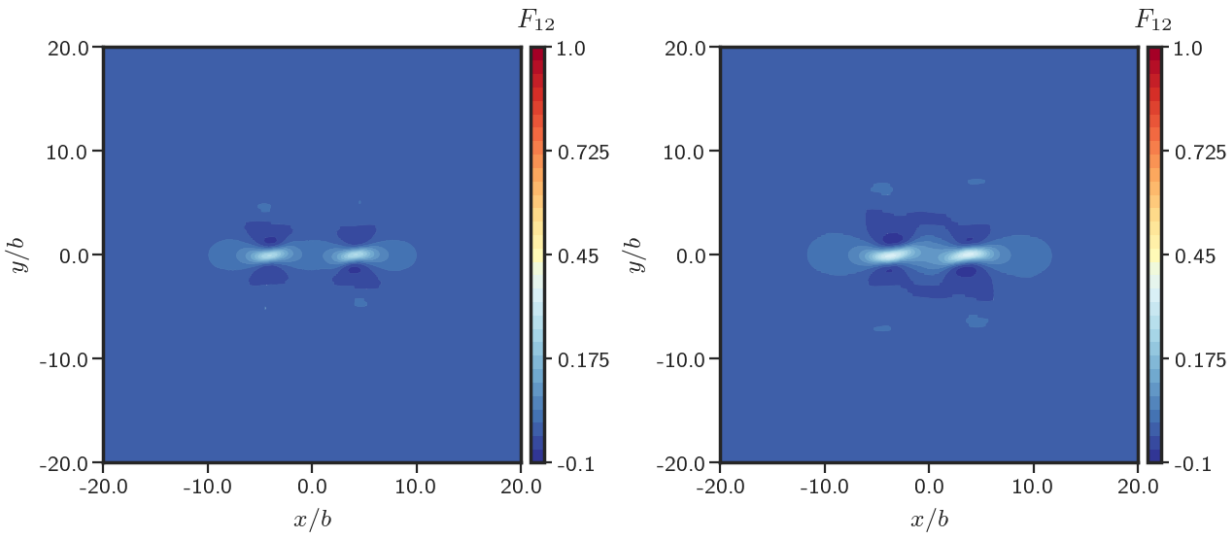
F_{12}
1.0
0.725
0.45
0.175
-0.1
20.0
10.0
0.0
-10.0
-20.0
y/b
x/b

(c)

F_{12}
1.0
0.725
0.45
0.175
-0.1
20.0
10.0
0.0
-10.0
-20.0
y/b
x/b

(d)

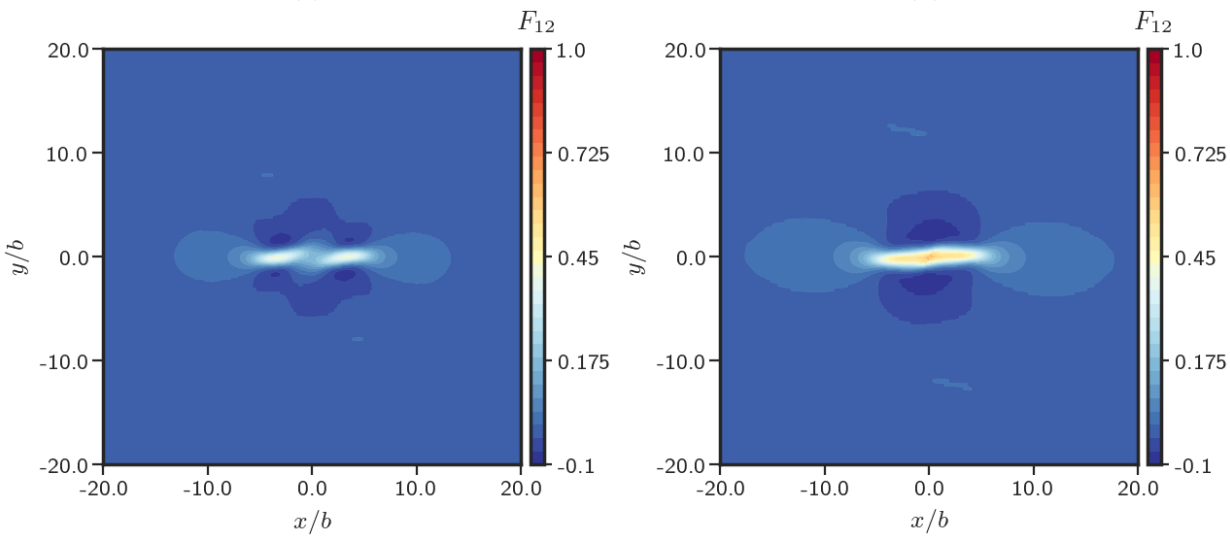
F_{12}
1.0
0.725
0.45
0.175
-0.1
20.0
10.0
0.0
-10.0
-20.0
y/b
x/b

(e)

F_{12}
1.0
0.725
0.45
0.175
-0.1
20.0
10.0
0.0
-10.0
-20.0
y/b
x/b

(f)

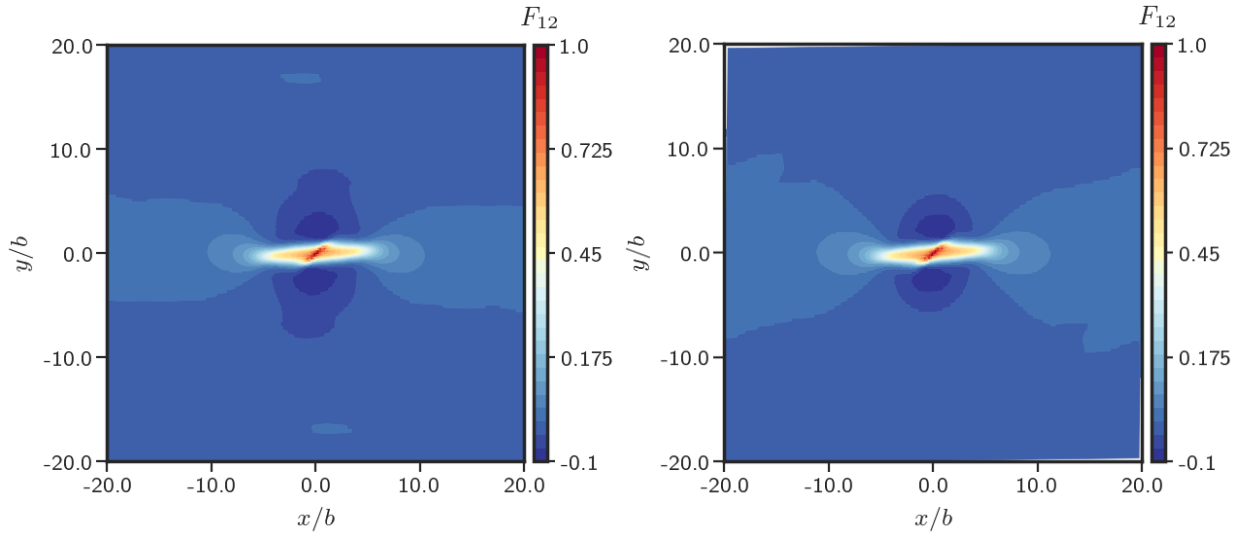

(g) (h)

Figure 5.52: F_{12} in the domain at different times, t^* a) 0 b) 1.5 c) 3 d) 4.5 e) 6 f) 12 g) 18 h) 24.

Chapter 6

Influence of inclusion size on material strength: MFDM

In this section, we present the results for an elastoplastic problem where we demonstrate that, for a given volume fraction of hard inclusions, the strengthening of the metal is greater for smaller particle size.

The experiments performed in Ebeling et. al [EA66] used a copper-silicon alloy for different particle sizes and volume fractions of SiO_2. The samples were then oriented for single slip and subjected to tensile loading. Their experimental results demonstrated that the strength of these alloys was greater than that of copper single crystals and this enhancement in strength depended on the size, spacing, and volume fraction of the inclusions. Moreover, for a given volume fraction of inclusion particles, the strength was enhanced much more when the inclusion sizes were small as compared to large inclusion sizes.

Several studies have qualitatively modeled the same phenomena under simple shearing motion using different continuum models [YGVdG04, BNVdG01, RWF11]. Here, we use the MFDM formulation to demonstrate this effect with elastic inclusions in a rate-dependent elastic-plastic material. Table 5.3 presents the material parameters for this simulation.

Parameter	Value
E	70 GPa
ν	.17

(a)

Parameter	Value
$\hat{\Gamma}$	$1s^{-1}$
$\hat{\gamma}_0$	$1s^{-1}$
m	20
b	$2.05\mathring{A}$
g_0	.050 GPa
g_s	.210 GPa
Θ_0	.3925 GPa
k_0	20
l	$0.1\,\mu m$
E	200 GPa
ν	.30

(b)

Table 6.1: Parameter values used for the simulations a) Inclusion b) Matrix.

The problem set up and boundary conditions for the overall simple shearing motion are similar to the description already given in Sec. 5.1. Simulations are performed on domain sizes of $(5\,\mu m)^2$ and $(50\,\mu m)^2$. A uniform grid of 128×128 elements is taken to mesh the

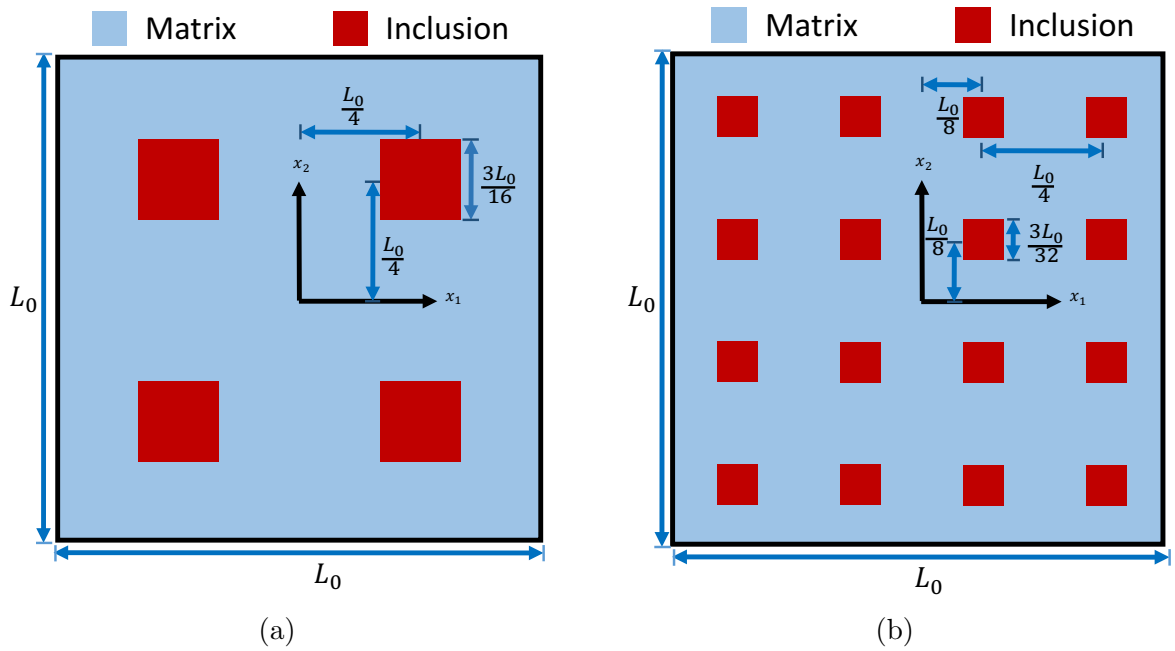

Figure 6.1: Schematic layout of the geometry with a) 4 inclusions b) 16 inclusions.

domain. The volume fraction of the inclusion is taken to be around 14%. Two cases are considered as shown in Fig. 6.1: i) 4 large inclusions and ii) 16 small inclusions. We use the J_2 plasticity model (3.23) for the plastic strain rate due to SSDs.

Figure 6.2 show the stress-strain response (τ vs. Γ) of the body. MFDM is able to model the dependence of the mechanical response of the material on the size of the reinforcing particles.

Figures 6.3 and 6.4 show the distribution of the dislocation density for the $(5\,\mu m)^2$ and $(50\,\mu m)^2$ domain sizes, respectively. It can be seen that for the $(5\,\mu m)^2$ sample size, the average dislocation density norm in the domain is greater when the inclusions are smaller in size. For the larger sample size, we see that the magnitude of dislocation density is smaller as compared to the $(5\,\mu m)^2$ domain size and therefore not much hardening is produced.

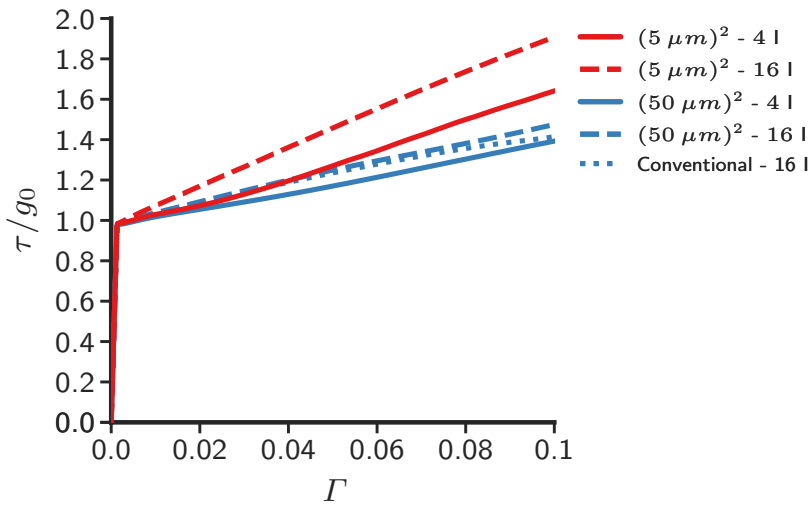

Figure 6.2: Size effect using J_2 MFDM due to the presence of inclusions. I: Inclusion.

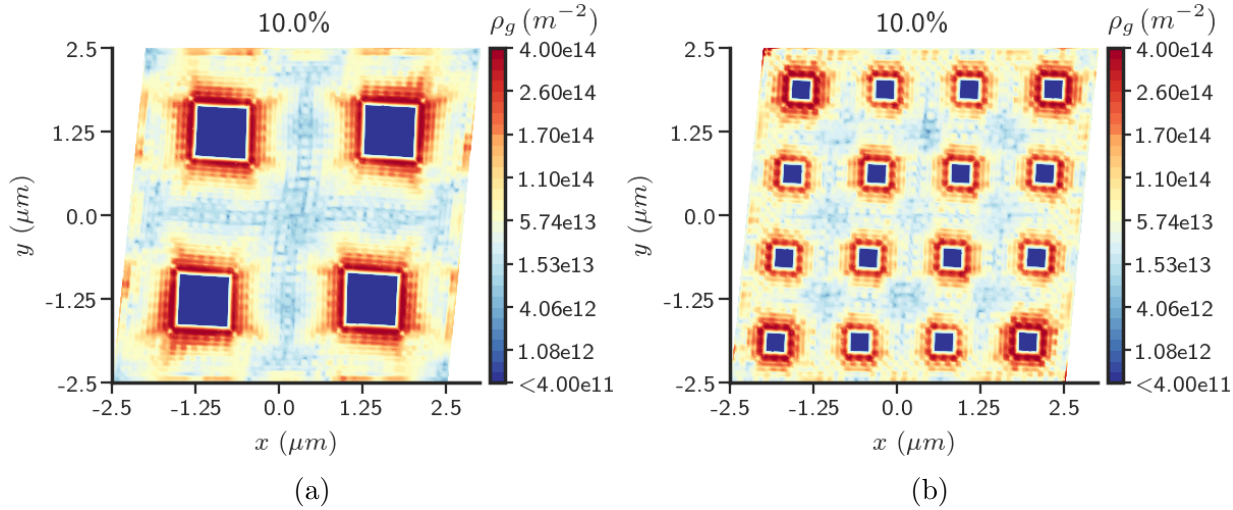

Figure 6.3: Dislocation density at 10% strain when the size of inclusions is decreased keeping the volume fraction same for $(5\,\mu m)^2$ domain size a) 4 inclusions b)16 inclusions.

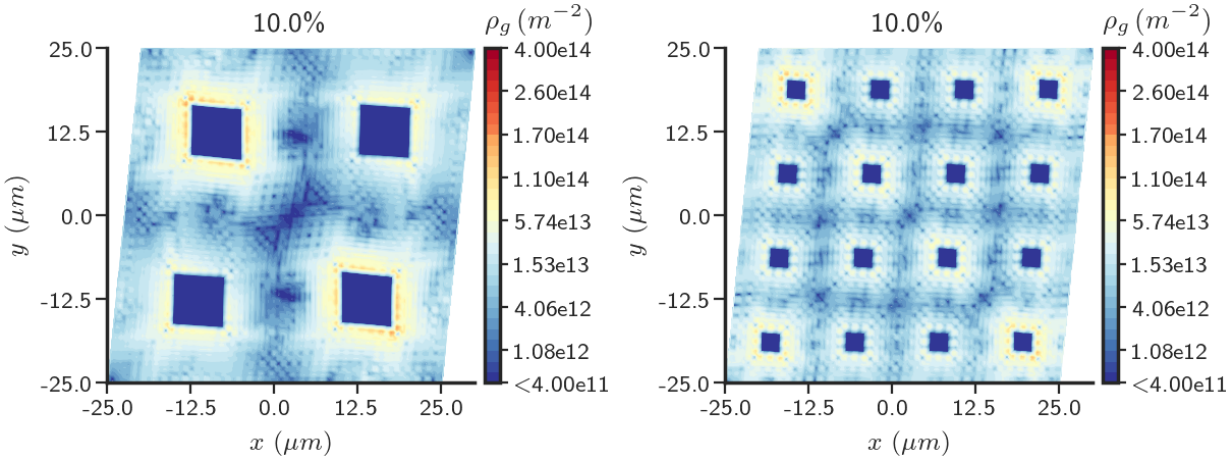

(a) (b)

Figure 6.4: Dislocation density at 10% strain when the size of inclusions is decreased keeping the volume fraction same for $(50\,\mu m)^2$ domain size a) 4 inclusions b)16 inclusions.

This page intentionally left blank.

Chapter 7

Size effect & dislocation patterning in crystal plasticity MFDM

In this chapter, we demonstrate size effects and the emergence of dislocation patterns and dipolar dislocation walls using crystal plasticity MFDM. Stressed dislocation pattern formation in crystal plasticity at finite deformation is also demonstrated. The dislocation microstructures emerge without any consideration of latent hardening or constitutive assumptions related to cross-slip. Crystal orientation effects on the pattern formation and mechanical response are also demonstrated.

Simulations are performed on square domains of sizes $(1\,\mu m)^2$, $(5\,\mu m)^2$, and $(100\,\mu m)^2$. The details of the meshes employed are given in Table 7.1 with rationale presented in Sec. 7.3. Velocity b.c.s corresponding to overall simple shear are imposed for a plane strain problem. At any point $P = (x_1, x_2)$ on the boundary a velocity of $v_2 = 0$ and $v_1 = \hat{\Gamma} y(x_2)$ is imposed, where $y(x_2)$ is the height of the point P from the bottom surface as shown in the schematic of the problem in Figure 7.1. $\hat{\Gamma}$ is the applied shear strain rate. The initial ($t = 0$) slip system orientation will be denoted by the parameter θ_0.

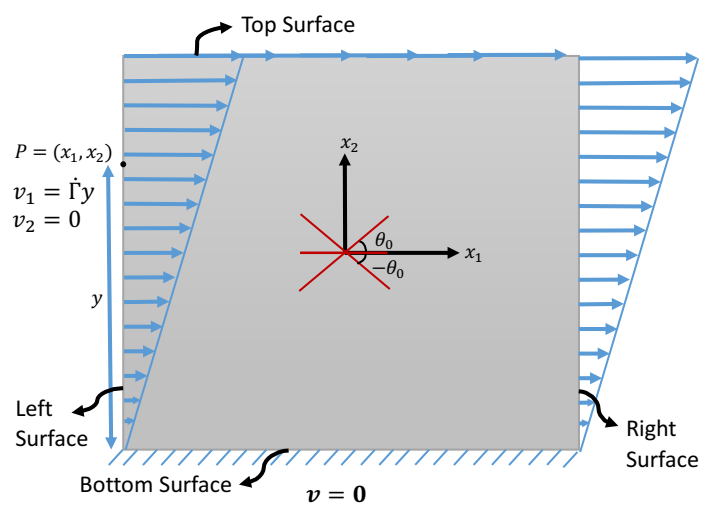

Figure 7.1: Schematic layout of a typical model geometry.

Sample Size	Mesh
$(1\,\mu m)^2$	70×70
$(5\,\mu m)^2$	70×70
$(100\,\mu m)^2$	70×70

Table 7.1: Details of finite element mesh used in computations.

Parameter	Value
b	4.05Å
g_0	17.3 MPa
g_s	161 MPa
Θ_0	392.5 MPa
m	.03
E	62.78 GPa
ν	.3647
$\hat{\Gamma}$	$1\,s^{-1}$
$\hat{\gamma}_0$	$1\,s^{-1}$
k_0	20
l	$\sqrt{3} \times 0.1\,\mu m$

Table 7.2: Default parameter values used in computations.

The strain Γ at any time t is given as $\Gamma = \hat{\Gamma}\,t$. All material parameters used in the simulations are presented in Table 7.2.

7.1 Dislocation microstructure and size effect in multiple slip

For multiple slip, we assume that there are 3 slip systems present in the crystal, oriented at ${\theta_0}^\circ$, $-{\theta_0}^\circ$, and 0° from the x axis as shown above in Fig. 7.1. The slip directions and normals for the 3 slip systems are given as

$$\boldsymbol{m}_0^1 = (\cos(\theta_0), \sin(\theta_0)) \qquad \boldsymbol{n}_0^1 = (-\sin(\theta_0), \cos(\theta_0))$$

$$\boldsymbol{m}_0^2 = (\cos(0), \sin(0)) \qquad \boldsymbol{n}_0^2 = (-\sin(0), \cos(0))$$

$$\boldsymbol{m}_0^3 = (\cos(\theta_0), -\sin(\theta_0)) \qquad \boldsymbol{n}_0^3 = (\sin(\theta_0), \cos(\theta_0)).$$

Thus, θ_0 characterizes the orientation of all the slip systems at $t = 0$.

7.1.1 Size effect

We demonstrate size effects in elastic-plastic material behavior up to large strains for both the plastically constrained and unconstrained cases defined in Section 3.4.

Figure 7.2 shows the averaged stress-strain (τ vs. Γ) response for all the domain sizes and both boundary conditions (plastically constrained and unconstrained), demonstrating the 'smaller is harder' size effect under simple shear. These results are in qualitative agreement with experimental observations [FMAH94, LHT+12, SWBM93, EA66].

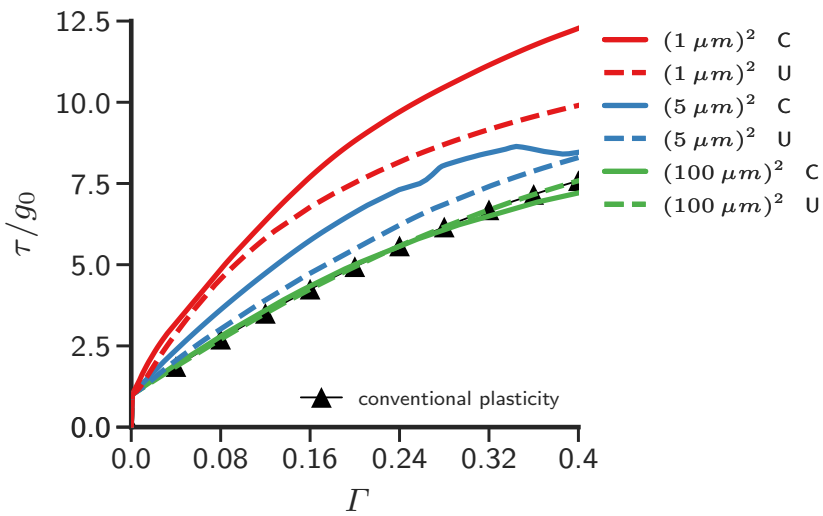

Figure 7.2: Size effect under simple shear. C: Constrained Boundaries U: Unconstrained Boundaries.

For the unconstrained case, the response of the larger domain size of $(100\,\mu m)^2$ overlaps the conventional plasticity solution. This is expected as the larger sample develops no inhomogeneities in deformation and therefore $|\boldsymbol{\alpha}| \approx 0$. However, the smaller domain sizes $(1\,\mu m)^2$ and $(5\,\mu m)^2$ develop inhomogeneity at small strains of (approximately) 0.5% and 1.7%, respectively. This (controlled) instability leads to deviation from the homogeneous solution, which in turn increases the local hardening, resulting in harder response than the

conventional solution. This instability of the time-dependent spatially homogeneous simple shearing solution for the MFDM theory is discussed in [RA06, DAS16] at small deformation.

The $(1\,\mu m)^2$ domain size for the plastically constrained case displays the hardest response. This is because the constrained boundary conditions lead to gradients in the plastic strain rate, $\boldsymbol{L}^p$, near the boundaries, as explained below, and these gradients are larger for the smaller domain sizes (by simple scaling arguments), this resulting in greater hardening through (3.33), apart from associated internal stress effects. Of course, the presence of $\boldsymbol{\alpha}$ also gives rise to additional plastic strain rate of the form $\boldsymbol{\alpha} \times \boldsymbol{V}$ in MFDM which is a softening effect, but the net effect is one of hardening in overall response.

We now explain the reason for the development of inhomogeneity in the $\boldsymbol{\alpha}$ field with the onset of plasticity for the case of constrained boundary conditions. This emergence of inhomogeneity can be attributed to the fact that the no-flow boundary condition induces gradients in $\boldsymbol{L}^p$ which lead to the evolution of $\boldsymbol{\alpha}$ in the domain. For example, taking $\boldsymbol{n} = \boldsymbol{e}_2$ on the top boundary with $\boldsymbol{\alpha} = \boldsymbol{0}$ instantaneously, a no-flow boundary implies

$$
\begin{aligned}
&(\boldsymbol{L}^p \times \boldsymbol{n}) = \boldsymbol{0} \text{ on } \partial\Omega \\
\implies &\begin{bmatrix} 0 & 0 & L^p_{11} \\ 0 & 0 & L^p_{21} \\ L^p_{33} & 0 & 0 \end{bmatrix} = \boldsymbol{0}
\end{aligned}
\tag{7.1}
$$

on the top/bottom boundary whereas there is no such constraint on $\boldsymbol{L}^p$ in the interior of the domain. This induces a gradient in the L^p_{21} and L^p_{11} components of the plastic strain rate $\boldsymbol{L}^p$ in the x_2 direction near the top and bottom boundaries, which contributes to the development of α_{23} and α_{13} in the domain. On the left and right boundaries similar considerations hold, but weakened with the progress of deformation, as can be seen below. The normal, $\boldsymbol{n} = (n_1, n_2)$,

changes direction with deformation and

$$
\begin{aligned}
&(\boldsymbol{L}^p \times \boldsymbol{n}) = \mathbf{0} \text{ on } \ \partial\Omega \\
\implies &\begin{bmatrix} 0 & 0 & L^p_{11}n_2 - L^p_{12}n_1 \\ 0 & 0 & L^p_{21}n_2 - L^p_{22}n_1 \\ L^p_{33}n_2 & L^p_{33}n_1 & 0 \end{bmatrix} = \mathbf{0}
\end{aligned}
\tag{7.2}
$$

which implies that at small deformation ($n_1 = \pm 1, n_2 = 0$), L^p_{12} is constrained at the boundary. This gives rise to a gradient of L^p_{12} in the x_1 direction which contributes to the development of α_{13}. As the normal changes direction, the linear constraints $L^p_{11}n_2 - L^p_{12}n_1 = 0$ and $L^p_{21}n_2 - L^p_{22}n_1 = 0$ have to hold which allow more freedom in accommodating deformation but, nevertheless, gradients do develop.

Before moving on to presenting the results for the emergence of dislocation patterns in the presence of external loads, we verify that the solution for the larger domain size is close to the one obtained from conventional plasticity theories. For the larger domain size of $(100\,\mu m)^2$ with unconstrained boundaries, the dislocation density norm at 40% strain is small and homogeneous, which is similar to the prediction of conventional plasticity theories. The stress strain curve therefore also overlaps the conventional plasticity result as shown in Fig. 7.2.

7.1.2 Dislocation microstructure

We now present results of stressed dislocation patterns in crystal plasticity at finite deformation using MFDM. Fig. 7.4 shows the norm of the dislocation density, ρ_g, at various strains for the $(1\,\mu m)^2$ domain size for plastically constrained boundaries. It can be observed that

- Microstructural patterns start developing even before 2% strain for the $(1\,\mu m)^2$ domain size. This is demonstrated in Fig. 7.3 which indicates that the $|\boldsymbol{\alpha}|$ becomes inhomogeneous at very early stages of deformation (strains ¡ $\approx 0.4\%$) and has a variation of an

order of magnitude in the interior of the domain.

- The distribution at 5% strain seems to resemble the blocky structure as shown in [JW84].

- The dislocation density magnitude increases in the domain up to 10% strain. However, ρ_g diminishes in the interior with increasing strain and becomes quite small at 40% strain.

- At 60% strain, the sample develops two prominent (dipolar) dislocation walls enclosing a distinct region of low dislocation density (by nearly two orders of magnitude), forming a dislocation cell-like structure. The dipolar nature of the walls is confirmed by looking at the magnitude of the individual dislocation components, α_{13} and α_{23} as shown in Figures 7.5a and 7.5b respectively.

- The Burgers vector, $\boldsymbol{b}$, content of any area patch A is given by

$$\boldsymbol{b} = \int_A \boldsymbol{\alpha n}\, dA.$$

An important point to note here is that in the case of plastically constrained boundaries, there is no flux of ED or SD from the boundary into the domain. Therefore, in the absence of any inflow or outflow flux of dislocations, and the $\boldsymbol{\alpha}$ evolution being a conservation law (3.14a) for Burgers vector, the total Burgers vector content of the whole body has to remain constant in time. Since, the initial Burgers vector content was $\mathbf{0}$ (dislocation free at $t = 0$), the dislocation microstructure needs to be such that the Burgers vector (for the whole domain) remains $\mathbf{0}$ at all times, which makes the appearance of a distribution with opposite signs inevitable as shown in Figure 7.5. Of course, that dipolar walls should be produced is not a consequence of the conservation law and a somewhat realistic outcome of our model.

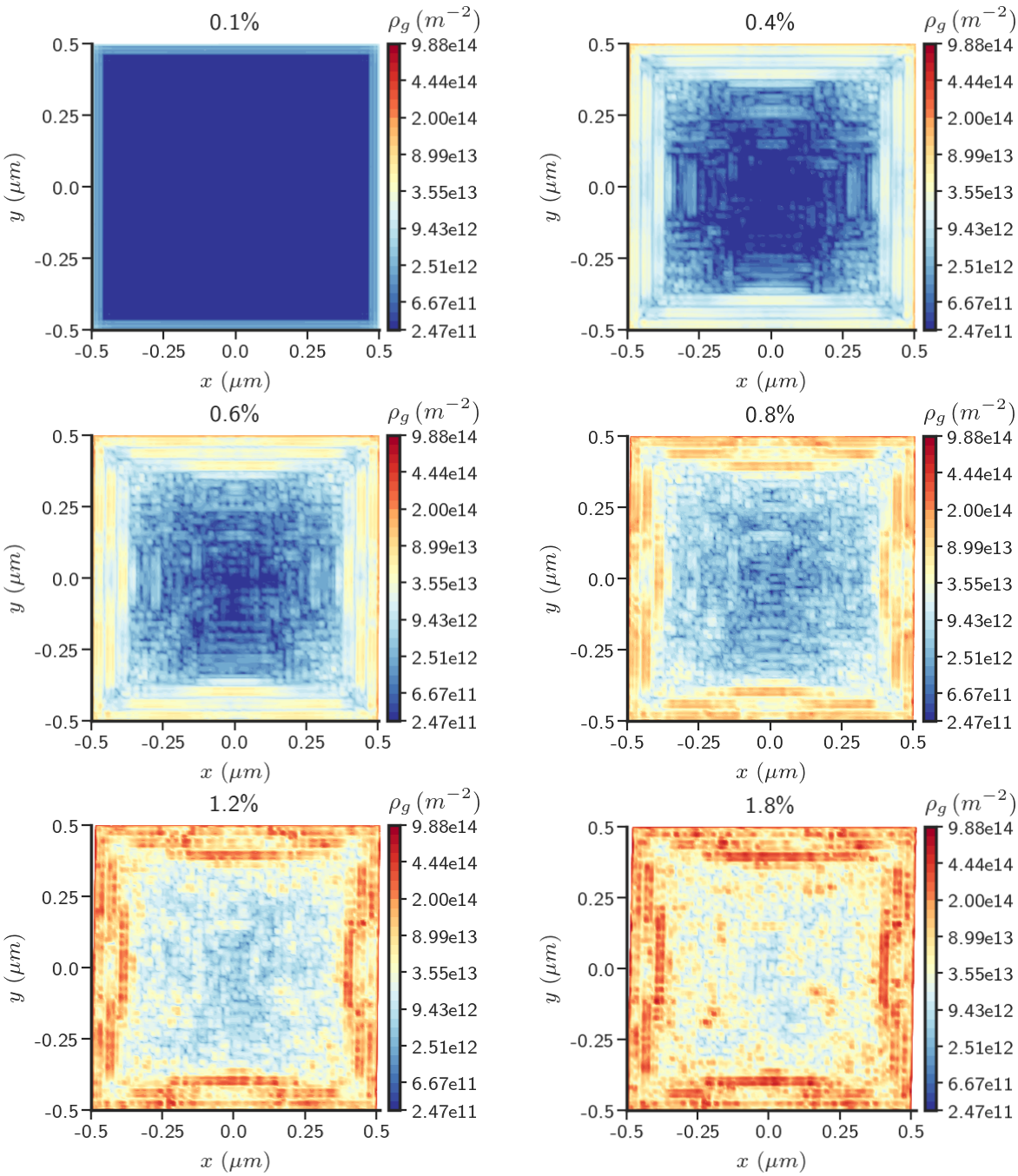

Figure 7.3: ρ_g for the $(1\,\mu m)^2$ domain size at different strains with plastically constrained boundaries and $\theta_0 = 30°$ ($n_{sl} = 3$).

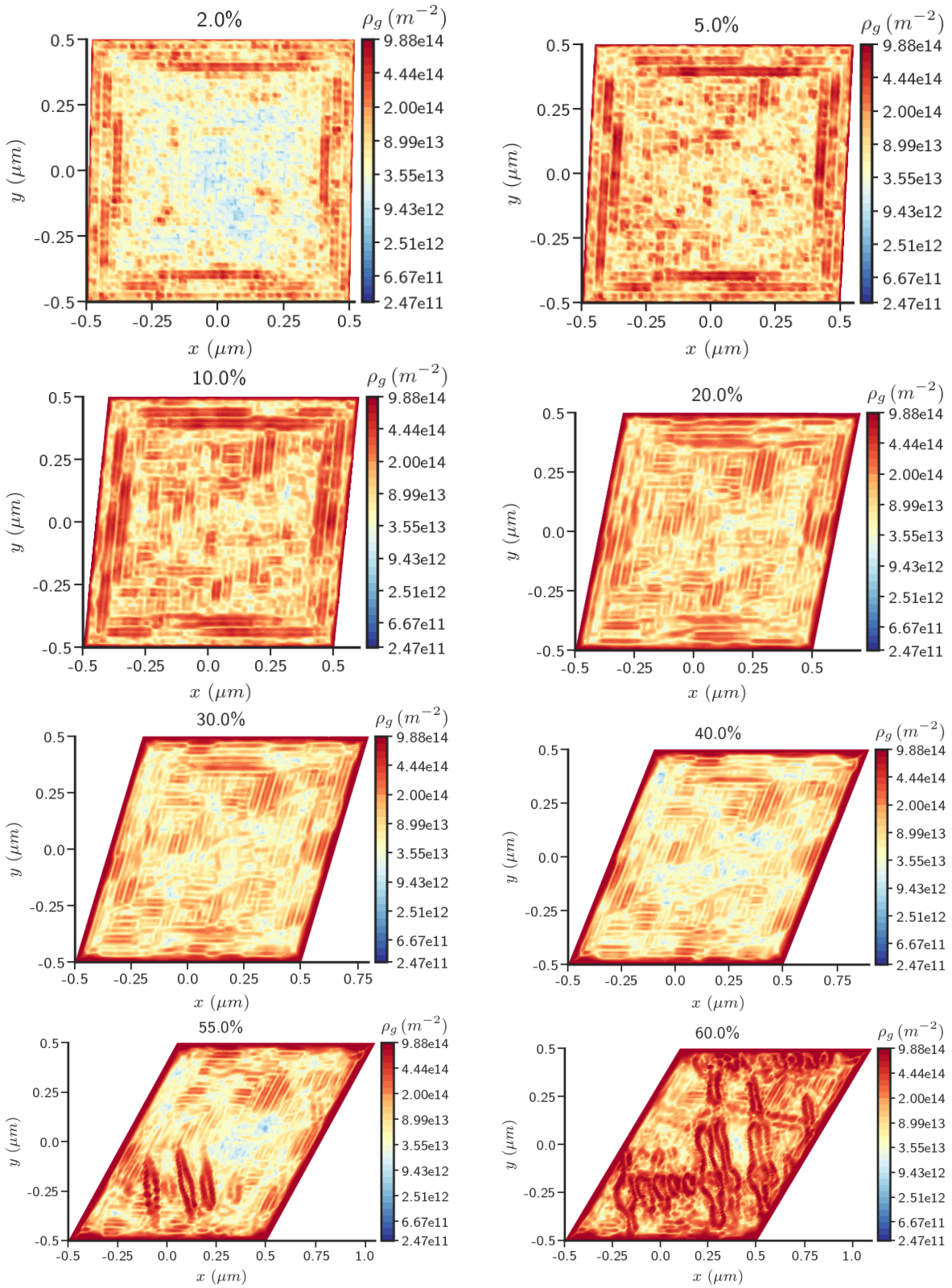

Figure 7.4: ρ_g for the $(1\,\mu m)^2$ domain size at different strains with plastically constrained boundaries and $\theta_0 = 30°$ ($n_{sl} = 3$).

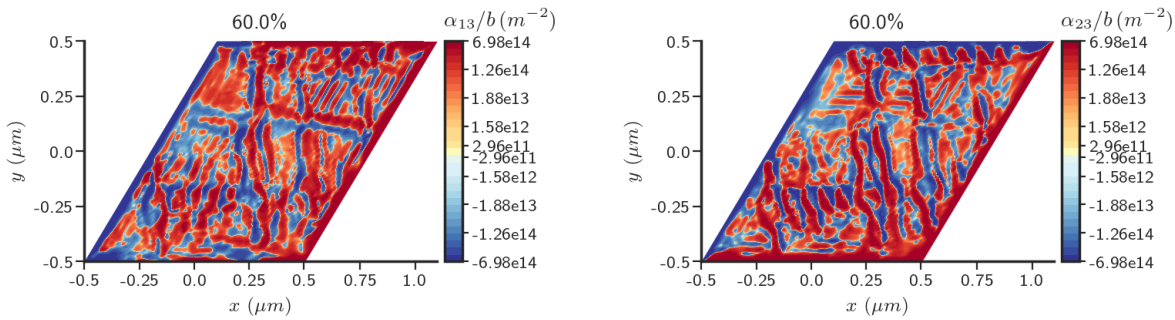

(a) (b)

Figure 7.5: a) α_{13} b) α_{23} for the $(1\,\mu m)^2$ domain size at 60% strain with plastically constrained boundaries and $\theta_0 = 30°$ ($n_{sl} = 3$). The corresponding ρ_g is shown in Fig. 7.4.

The microstructural patterns for the domain size of $(5\,\mu m)^2$ are significantly different from those of $(1\,\mu m)^2$ domain size. Figure 7.6 shows the comparison of the microstructure obtained for the $(1\,\mu m)^2$ and $(5\,\mu m)^2$ domain sizes at 40% strain. The dislocation density is generated because of the constrained boundary conditions (as explained earlier in the discussion surrounding (7.1) and (7.2)) for both the domain sizes, but for the $(5\,\mu m)^2$ domain the accumulation occurs only near the boundary. The difference can be understood by noting that the sum of the widths of the two boundary layers in the $(5\,\mu m)^2$ domain add up to almost the entire linear dimension of the $(1\,\mu m)^2$ domain. Assuming the patterns have an intrinsic length scale in the submicron range, as substantiated by the $(1\,\mu m)^2$ results, dislocation patterns are likely to occur within the boundary layers of the $(5\,\mu m)^2$ domain.

At finite strains, the accumulation of dislocations develops an asymmetry along the boundaries for the $(5\,\mu m)^2$ domain size. This is because of the change in orientation of the boundary normal with deformation at the left and right boundaries. This is corroborated by Figure 7.7 where the dislocation density distribution is symmetric at small applied strain (the asymmetry in Fig. 7.7 persists at large applied strain).

7.1.3 *ssd* distribution

A large part of the plastic strain rate at mesoscales comes from expansion of unresolved dislocation loops that constitute SD. The *ssd*, ρ_s, given by Eq. (3.34) in MFDM, is propor-

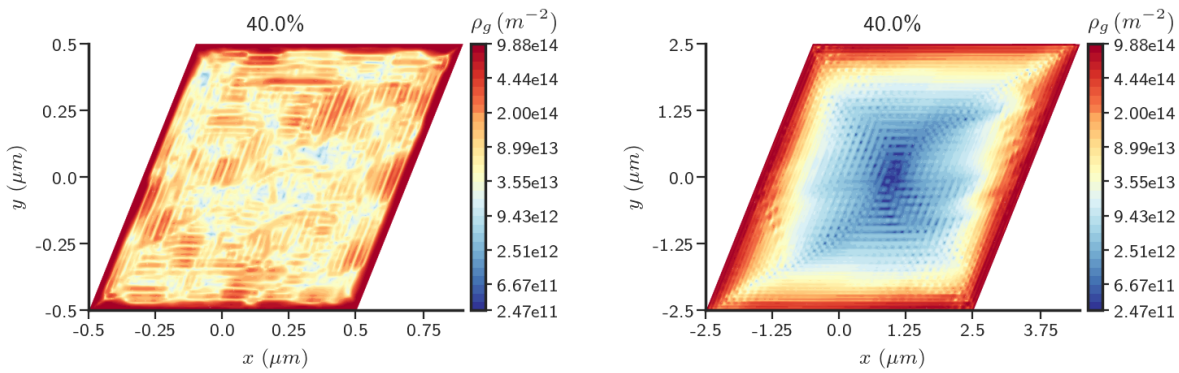

(a) (b)

Figure 7.6: Comparison of ρ_g for the a) $(1\,\mu m)^2$ b) $(5\,\mu m)^2$ sample sizes with plastically constrained boundaries at 40% strain and $\theta_0 = 30°$ ($n_{sl} = 3$).

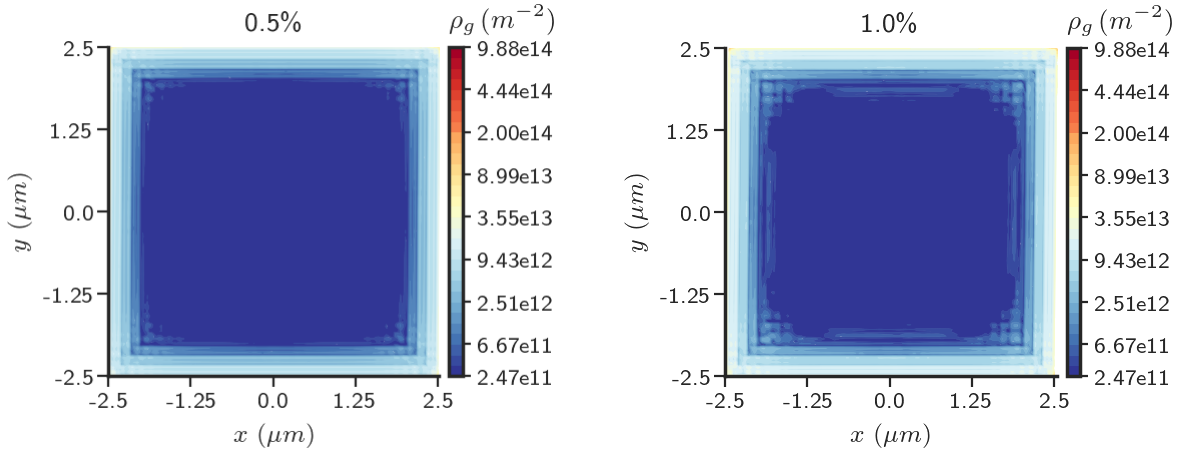

(a) (b)

Figure 7.7: ρ_g distribution for the $(5\,\mu m)^2$ domain size with plastically constrained boundaries at a) 0.5% b) 1% strain and $\theta_0 = 30°$ ($n_{sl} = 3$).

tional to the root-mean-square of the SD. Figure 7.8 presents the distribution of *ssd* in the domain for the $(1\,\mu m)^2$ sample size with plastically constrained boundaries. The distribution is mildly patterned in the domain, with magnitude increasing with strain. There is a variation of at least an order of magnitude in the domain at all strain levels.

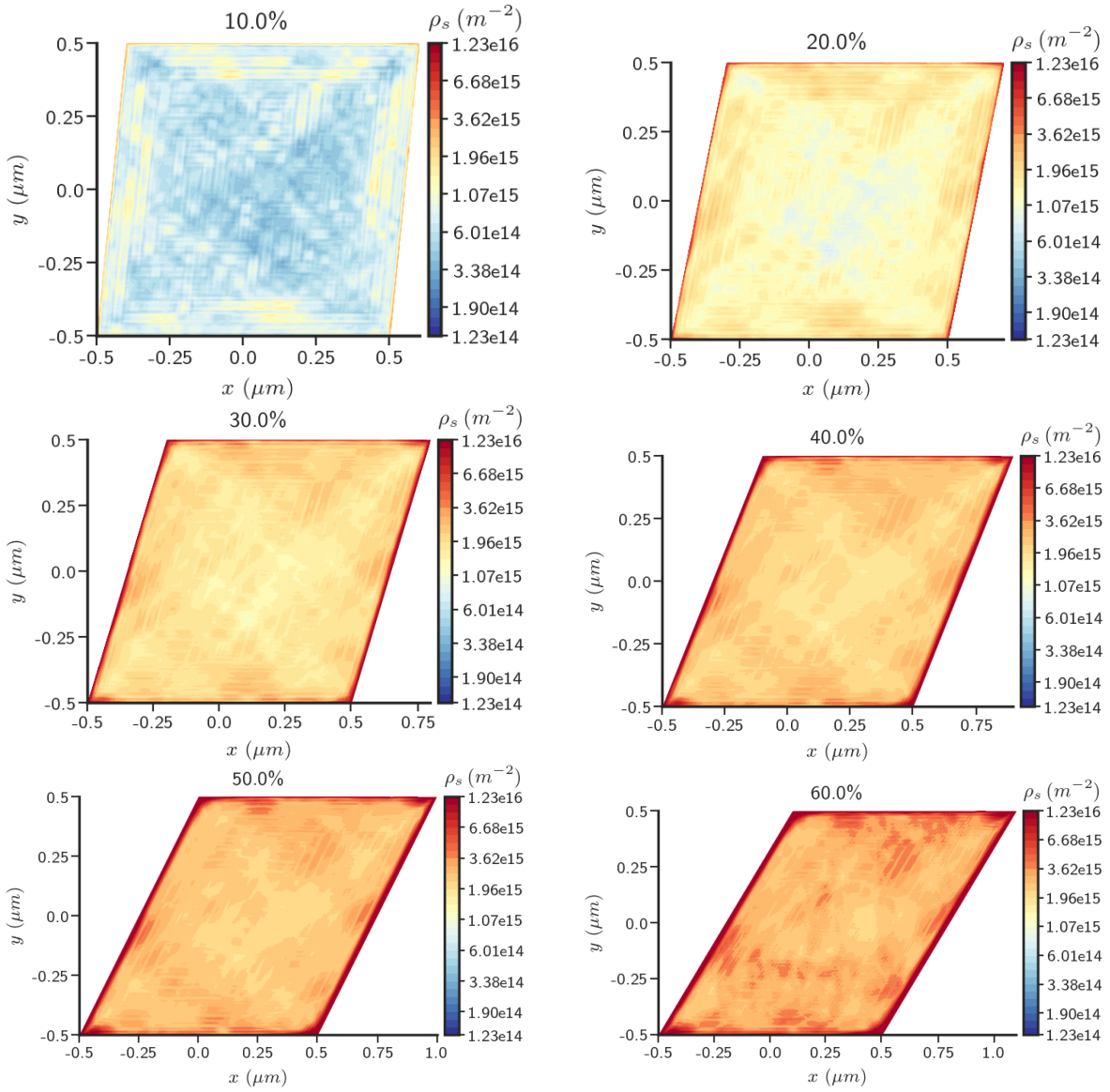

Figure 7.8: *ssd* distribution for the $(1\,\mu m)^2$ domain size at different strains with plastically constrained boundaries and $\theta_0 = 30°$ ($n_{sl} = 3$).

7.1.4 Unloaded stressed microstructures

The $(1\,\mu m)^2$ domain is unloaded from 60% strain by reversing the loading direction. The boundary conditions for velocity are taken as $v_2 = 0$ and $v_1 = -\hat{\Gamma} y$ until τ (averaged stress on the top surface) becomes zero. Then, we decrease the nodal reaction forces steadily over time until a tolerance of $\max_j\{\text{abs}(F_j)\} < 10^{-4} \times (g_0\, h)$ is reached, where $\{\text{abs}(F_j)\}$ refers to the absolute value of the jth entry in the nodal reaction force array $\{F\}$, defined in Sec. 4.2, with size equal to number of degrees of freedom where (material) velocity Dirichlet-boundary conditions are applied, and h is the element size. Thereafter, we let the system achieve thermodynamic equilibrium by requiring all evolution, i.e., of $\boldsymbol{\alpha}$, $\boldsymbol{f}$, g, to become small. Hence, if at all, these microstructures evolve very slowly.

The ρ_g distribution on the unloaded configuration is shown in Fig. 7.9a. The α_{13} and α_{23} components of the dislocation density tensor are shown in Figures 7.9b and 7.9c, respectively.

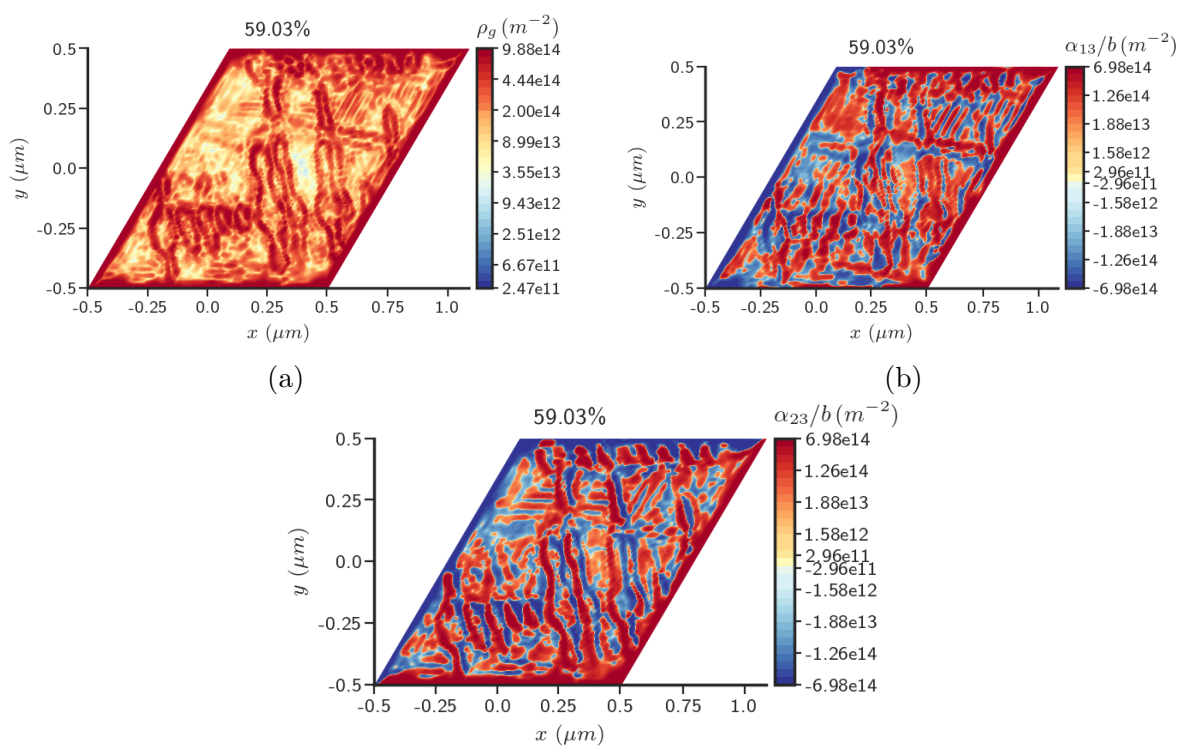

Figure 7.9: Unloaded, stressed microstructure a) ρ_g b) α_{13} c) α_{23} for the $(1\,\mu m)^2$ domain size with plastically constrained boundaries and $\theta_0 = 30°$ ($n_{sl} = 3$).

In Fig. 7.10, we plot the elastic energy density in the domain, given by $\rho\phi$ (3.20), before and after the unloaded equilibration. The energy density variation in the body after unloaded equilibration is at least an order of magnitude smaller in most of the interior of the domain than the energy density before unloading.

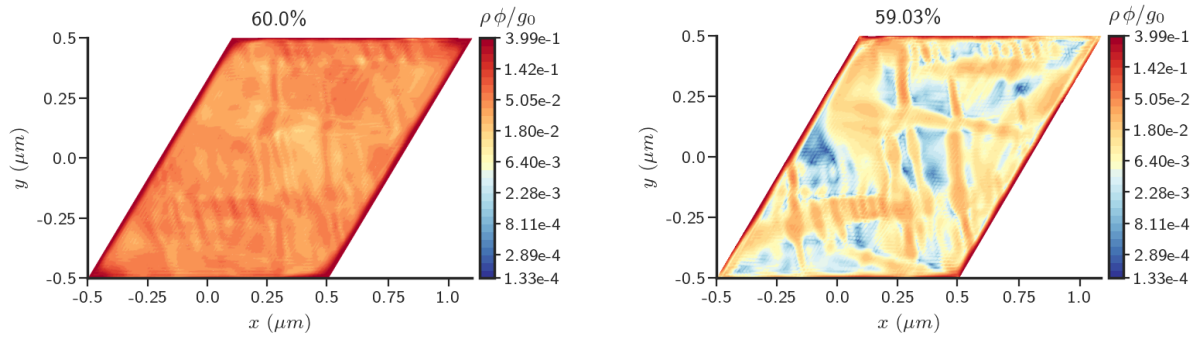

(a) (b)

Figure 7.10: Elastic energy density for the unloaded $(1\,\mu m)^2$ domain size with plastically constrained boundaries and $\theta_0 = 30°$ ($n_{sl} = 3$) a) before b) after unloading.

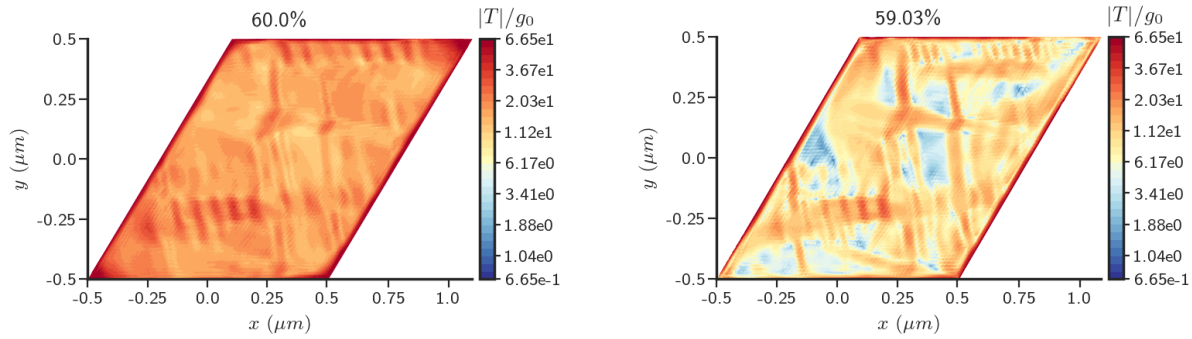

(a) (b)

Figure 7.11: Cauchy stress norm for the $(1\,\mu m)^2$ domain size with plastically constrained boundaries and $\theta_0 = 30°$ ($n_{sl} = 3$) a) before b) after unloading.

Figure 7.11 shows the non-dimensionalized norm of the stress field in the domain before and after unloaded equilibration. It can be seen that the body is not stress-free after equilibration, and is stressed upto ≈ 6 times the initial yield strength g_0. The corresponding plastic strain rate magnitudes, $\hat{\gamma}^k$ for k^{th} slip system, are found to be negligible, $\frac{\hat{\gamma}^k}{\hat{\gamma}_0} \approx 10^{-8}$.

Hence, we conclude that the unloaded stressed microstructures are kinetically trapped, (computational) metastable equilibrium solutions of the theory.

We remark that *the entire class of ED distributions arising from spatially heterogeneous rotation distributions in unloaded bodies constitute exact equilibria of our model*, since they result in vanishing stress fields. This results in vanishing $\hat{\gamma}^k$ on any slip system which implies $\boldsymbol{V} = \boldsymbol{0}$ and $\boldsymbol{L}^p = \boldsymbol{0}$ from (3.30) and (3.25), respectively, and consequently $\boldsymbol{\alpha}, \boldsymbol{f}, g$ cease to evolve from such states.

7.1.5 Microstructure with unconstrained boundary conditions

We demonstrate that the emergence of patterning for the $(1\,\mu m)^2$ domain size is not dependent on the condition that the boundaries be plastically constrained. Figure 7.12 shows the dislocation pattern in the $(1\,\mu m)^2$ domain size at different strains with unconstrained boundaries ($\theta_0 = 30°, n_{sl} = 3$). After an initial burst at relatively small strains, the patterns again become pronounced at 60% strain as was the case for constrained boundaries presented Fig. 7.4.

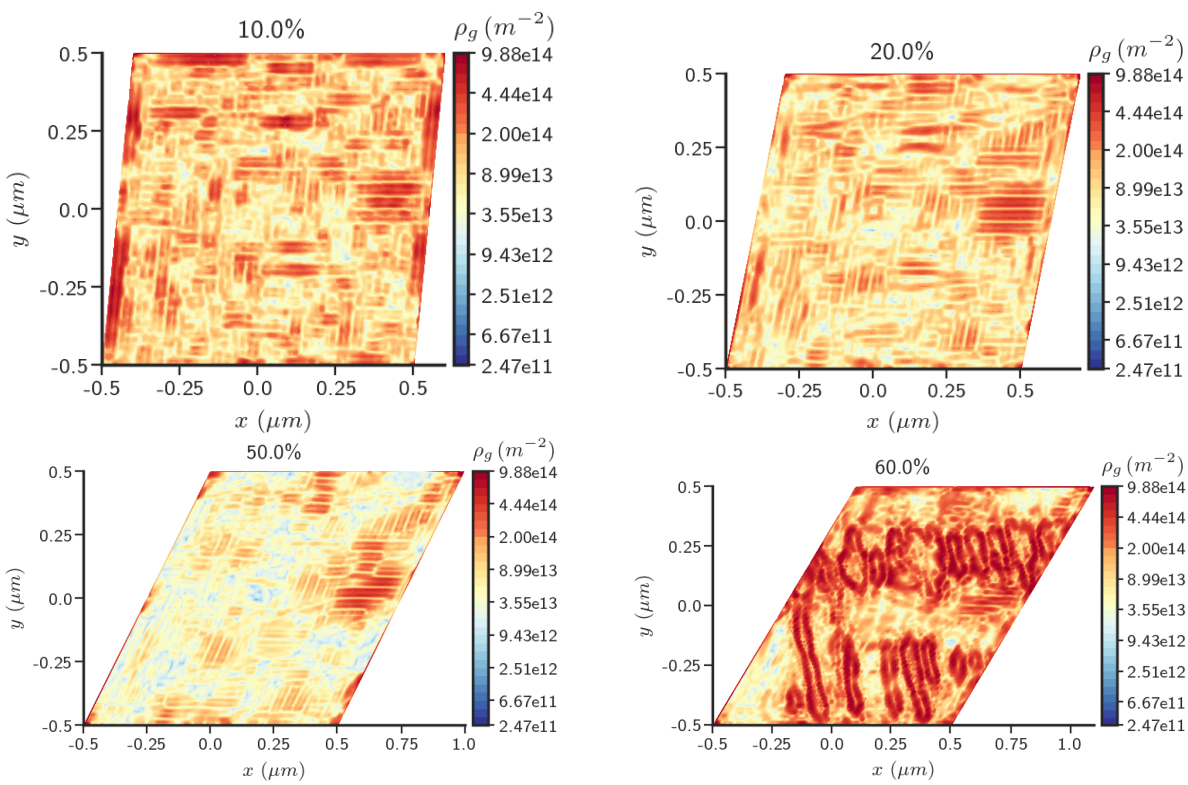

Figure 7.12: ρ_g at different strains for the $(1\,\mu m)^2$ domain size with plastically unconstrained boundaries and $\theta_0 = 30°$ ($n_{sl} = 3$).

7.1.6 Effect of slip system orientation on microstructure and stress response

We now explore the question of variation in the microstructural patterns when the initial lattice orientation, θ_0, is changed. Keeping all parameters as in Table 7.2 except for setting θ_0 to 45°, we obtain microstructural patterns for the $(1\,\mu m)^2$ domain size shown below in Fig. 7.13 that are very similar to the microstructure in Fig. 7.4 obtained for $\theta_0 = 30°$. This is because the applied averaged simple shear deformation can be accommodated by three independent slip systems regardless of orientation (in fact two suffices for incompressible velocity fields).

Figure 7.14 presents a comparison of the stress-strain plots for the $(1\,\mu m)^2$ domain size when the orientation of the slip system is changed from $\theta_0 = 30°$ to $\theta_0 = 45°$. This change in orientation results in a harder stress-strain response which can also be seen in corresponding responses modeled by conventional theory.

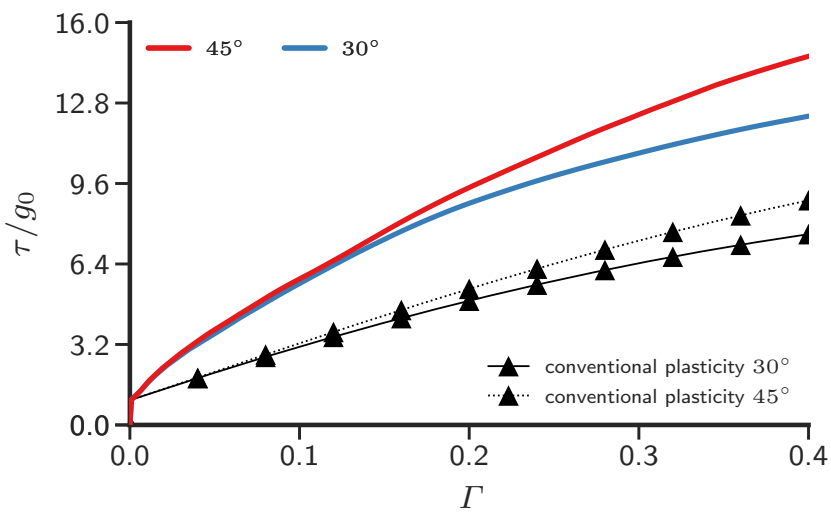

Figure 7.14: Stress-strain response for the $(1\,\mu m)^2$ domain size for $\theta_0 = 30°$ and $\theta_0 = 45°$ ($n_{sl} = 3$).

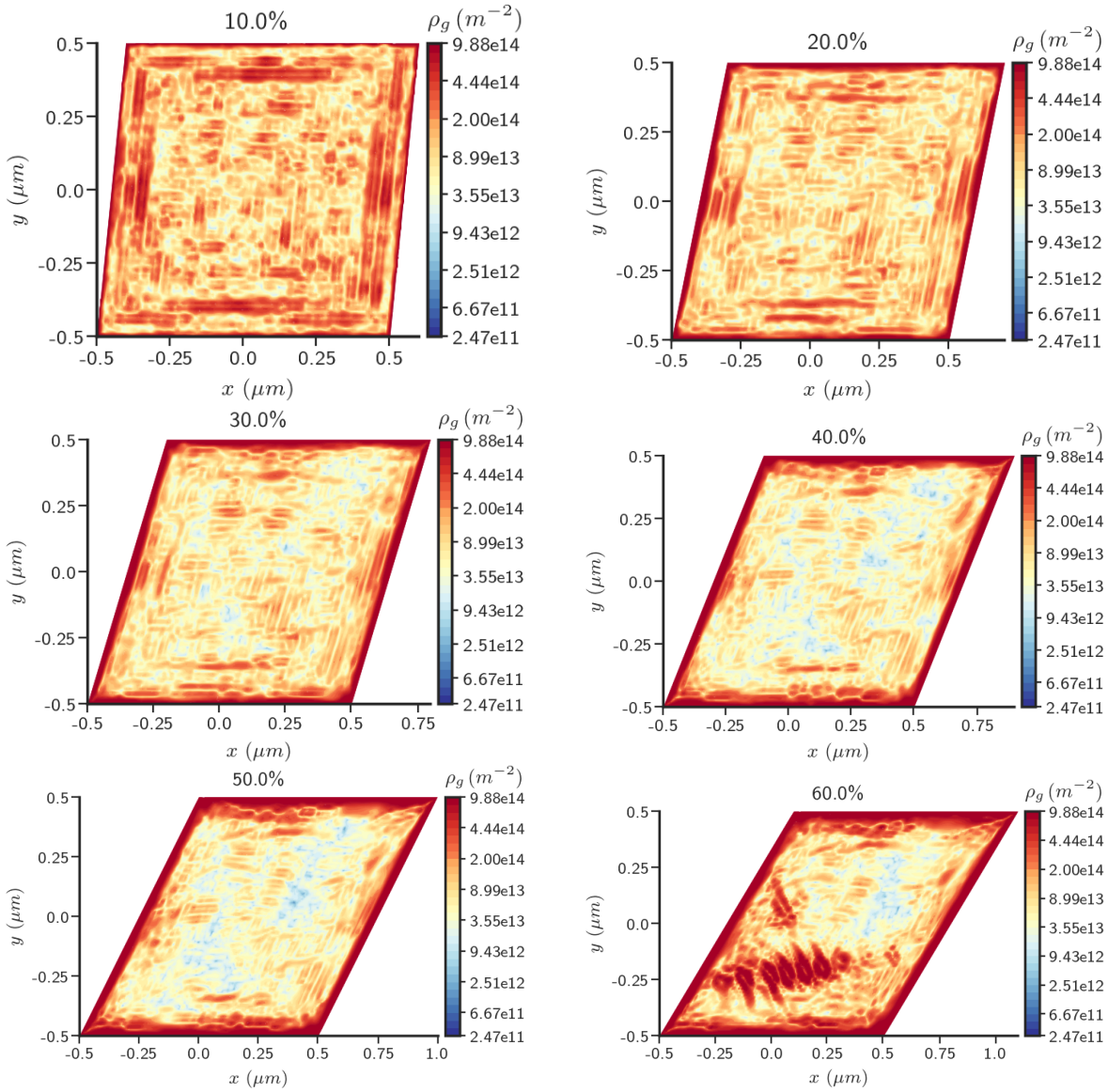

Figure 7.13: ρ_g distribution for the $(1\,\mu m)^2$ domain size at different strains with plastically constrained boundaries and $\theta_0 = 45°$ ($n_{sl} = 3$).

7.2 Dislocation microstructure in single slip

Motivated by the approximate invariance of the microstructural patterns with respect to crystal orientation and our conjecture in Sec. 7.1.6 that the issue is related to the accommodation of the applied average deformation (rate) field by the plastic slip systems available, we now consider a body with only a single slip system. The hypothesis to be tested is that in this scenario the applied deformation cannot be accommodated, thus leading to higher stresses and elastic incompatibilities, the degree of which should depend on the slip system orientation with respect to the applied simple shear. By 'accommodation' here we mean that the tensorial direction of the simple shearing motion defined by the applied boundary conditions can be represented as a linear combination of the evolving slip-system dyads of the material, assuming active slip systems.

As before, the initial orientation of the slip system will be defined by θ_0, which is the angle of the slip direction from the x_1 axis. The initial slip direction and normal for the slip system is given as

$$\boldsymbol{m}_0^1 = (\cos(\theta_0), \sin(\theta_0)) \qquad\qquad \boldsymbol{n}_0^1 = (-\sin(\theta_0), \cos(\theta_0)).$$

7.2.1 Dislocation microstructure

We plot the microstructure for the $(5\,\mu m)^2$ domain size at 5% strain in Figure 7.15 for $\theta_0 = 30°$. We can see that for the case of a single slip system, the patterns in the $(5\,\mu m)^2$ domain size are very different from those for the 3-slip-systems case (shown in Fig. 7.6b). This can be attributed to the fact the the deformation now is much more constrained due to the presence of only a single slip system. In contrast to Fig. 7.6b, cell structures form in the interior of the domain at 5% strain. Therefore, these observations substantiate our conjecture related to accommodation.

Figure 7.16 shows the individual components of the dislocation density tensor for $(5\,\mu m)^2$

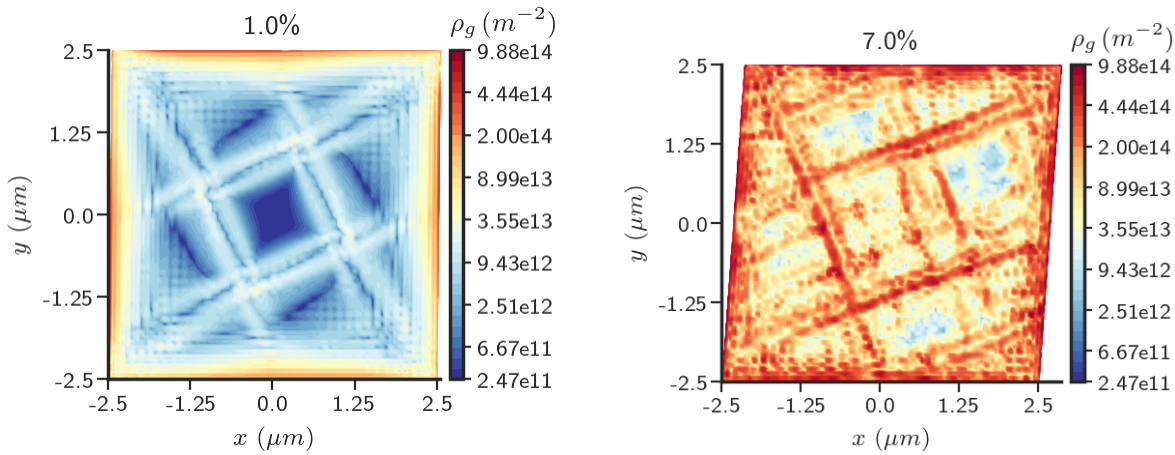

Figure 7.15: ρ_g for the $(5\,\mu m)^2$ domain size at 1% and 7% strain with plastically constrained boundaries and $\theta_0 = 30°$ ($n_{sl} = 1$).

domain size at 5% strain. We can notice monopolar walls, of both types (α_{13} and α_{23}) of dislocations, forming in the interior of the domain. If we relate these to the norm of the dislocation density tensor shown in Fig. 7.15, we can see that these monopolar walls are the boundary of the cell structure formed in the center of the domain. Of note is also the dipolar wall in kink orientation [Asa83, Sec. IV A] to the primary (and only) slip plane.

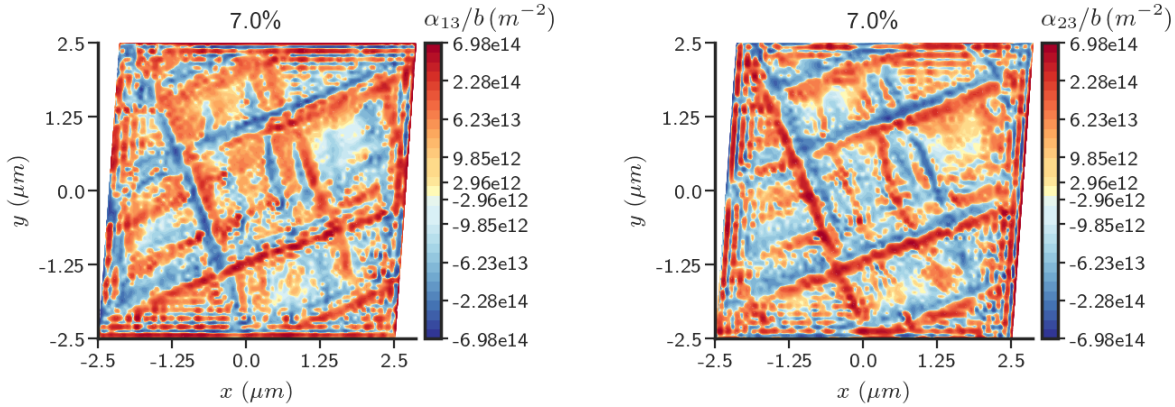

(a) (b)

Figure 7.16: a) α_{13} b) α_{23} for the $(5\,\mu m)^2$ domain size at 7% strain with plastically constrained boundaries and $\theta_0 = 30°$ ($n_{sl} = 1$).

7.2.2 Effect of slip system orientation on microstructure and stress response

Here we explore the change in the microstructural pattern for the $(5\,\mu m)^2$ domain size when the orientation of the slip system is changed from 30° to 45°. Figure 7.17 shows the obtained patterns for $\theta_0 = 45°$. It can be seen that the ρ_g becomes significant only at strains larger than 5%. This is because at small deformation, the resolved shear stress on the slip system, with instantaneous orientation denoted by θ, is given as $\tau = \boldsymbol{m} \cdot \boldsymbol{T}\boldsymbol{n} = T_{12}\cos(2\theta)$ which is small for $\theta \approx 45°$ so that the applied deformation has to be elastically accommodated. As the deformation progresses, the lattice rotation affects the slip system orientation θ. This change in orientation of the slip system produces a small plastic strain rate on it and results in the development of ED because of the plastically constrained boundary condition as explained earlier in the discussion surrounding (7.1) and (7.2). However, even though the plastic strain gradients are large, the plastic strain itself is small enough to not cause any noticeable change from elastic behavior in the stress-strain response.

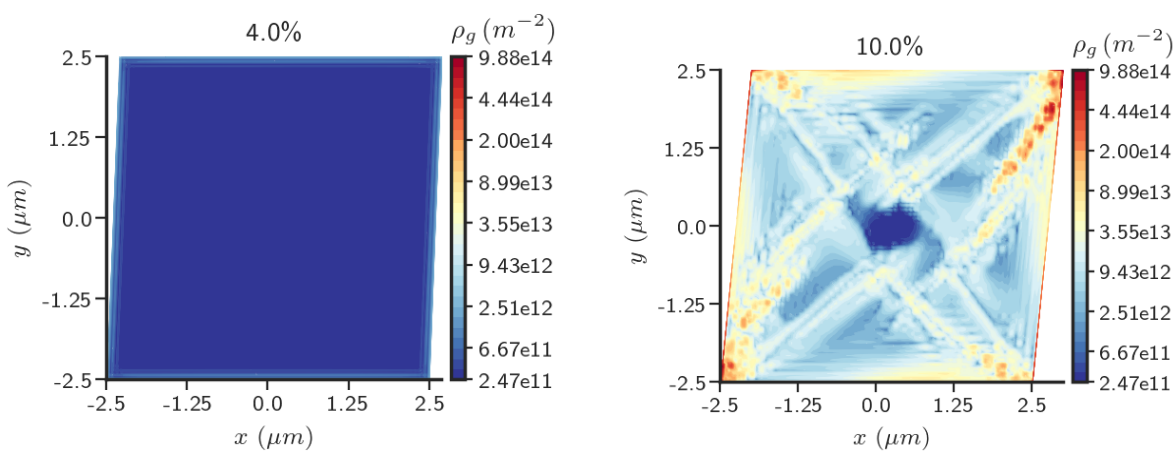

Figure 7.17: ρ_g for the $(5\,\mu m)^2$ domain size at different strains with plastically constrained boundaries and $\theta_0 = 45°$ ($n_{sl} = 1$).

A comparison of the stress-strain behavior for the $(5\,\mu m)^2$ domain size when the initial orientation θ_0 of the slip system is changed from 30° to 45° is presented in Fig. 7.18. As can be seen, the response is almost 50 times harder than the corresponding data shown in

Fig. 7.2. As already explained above, this is the result of the elastic accommodation of the initial deformation.

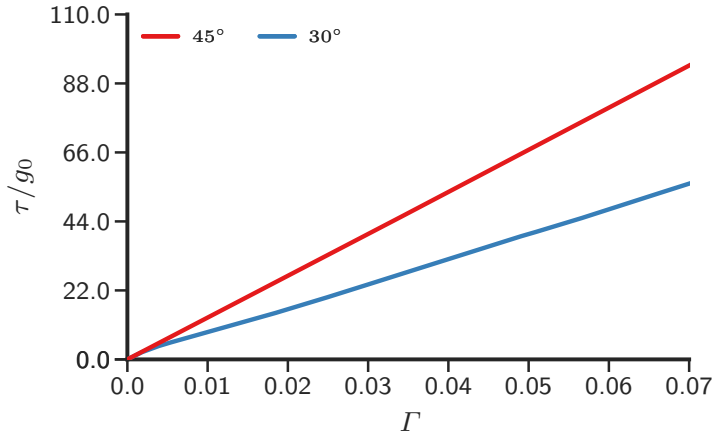

Figure 7.18: Stress-strain response for the $(5\,\mu m)^2$ domain size for plastically constrained boundaries and $\theta_0 = 30°$ and $\theta_0 = 45°$ ($n_{sl} = 1$).

7.3 Convergence

This section deals with the study of convergence in stress-strain response and microstructural patterns obtained in Sec. 7.1 ($n_{sl} = 3$).

7.3.1 Stress-strain response

We study the convergence of the stress-strain responses for the $(1\,\mu m)^2$ and $(5\,\mu m)^2$ domain sizes with plastically constrained boundaries. The details of the meshes used in this section are as follows. For the $(1\,\mu m)^2$ and $(5\,\mu m)^2$ domain sizes, we use two uniform meshes of 70×70 and 140×140 elements, referred to as the coarse and fine meshes, respectively.

The averaged stress-strain plot for the case when the initial orientation θ_0 is 30° is plotted in Fig. 7.19. The stress strain plots (almost) overlap upto 40% strain for $(1\,\mu m)^2$ domain size. The maximum difference (at 40% strain) in the stress-strain curve is 1.2%, and the difference at (28%) strain is 1.8% for the smaller sample. For the case when $\theta_0 = 45°$, the stress-strain plots for the $(1\,\mu m)^2$ sample size overlap up to 40% strain and there is no

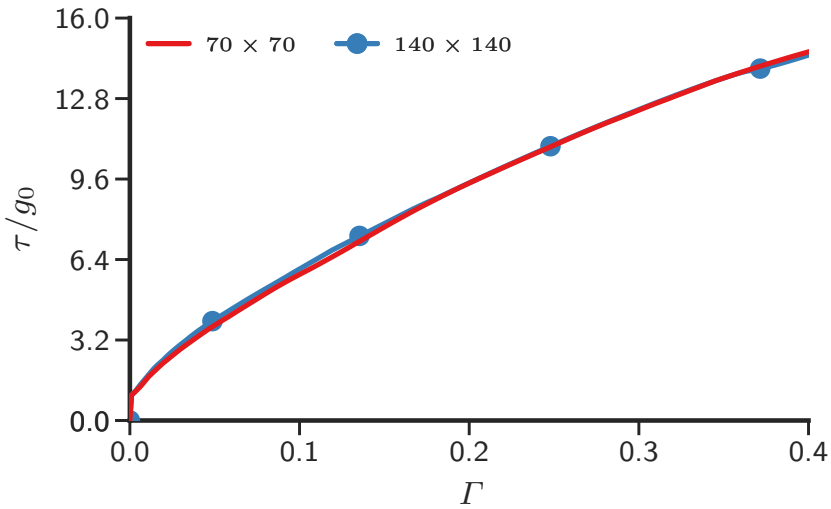

Figure 7.20: Convergence in stress-strain response for the $(1\,\mu m)^2$ domain size with plastically constrained boundaries for coarse and fine meshes ($\theta_0 = 45°, n_{sl} = 3$).

discernible difference between the results obtained using coarse and fine meshes as shown in Fig. 7.20.

The unconstrained cases represent a more conservative simulation scenarios with smaller gradients than the constrained case, and hence the same mesh sizes suffice for them.

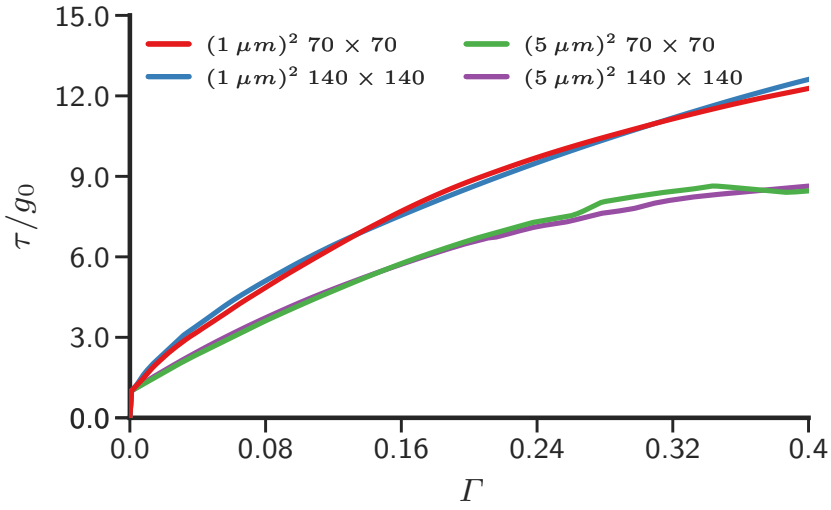

Figure 7.19: Convergence in stress-strain response for the $(1\,\mu m)^2$ and $(5\,\mu m)^2$ domain sizes with plastically constrained boundaries for coarse and fine meshes ($\theta_0 = 30°, n_{sl} = 3$).

7.3.2 Dislocation microstructure

We discuss convergence of the microstructural patterns for the specific case of Sec. 7.1 wherein $n_{sl} = 3$ and $\theta_0 = 30°$ (we believe that the same arguments apply to Sec. 7.2 as well).

The norm of the dislocation density ρ_g and the components of $\boldsymbol{\alpha}$ (α_{13} and α_{23}) for the $(1\,\mu m)^2$ domain size at 60% strain for the coarse mesh are shown in Figures 7.21a, 7.21b, and 7.21c, respectively. The localized concentrations are not aligned with the mesh. Moreover, the signed components are spread over more than 2 elements in the mesh. Similar observation can also be made for the microstructure on the refined mesh, as shown in Fig. 7.21d.

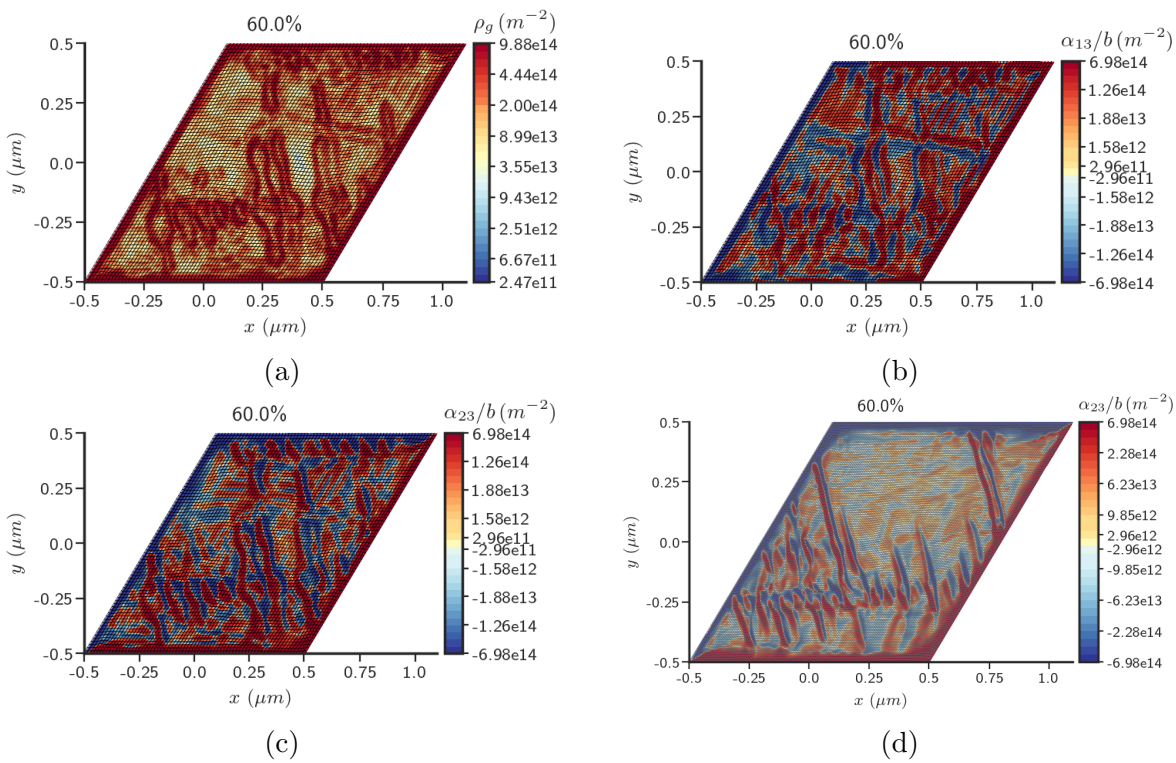

Figure 7.21: Microstructure for the $(1\,\mu m)^2$ domain size at 60% strain with plastically constrained boundaries and $\theta_0 = 30°$ ($n_{sl} = 3$): a) ρ_g b) α_{13} c) α_{23} computed with the coarse mesh, d) α_{23} computed with the fine mesh.

However, it is also clear, from a comparison of Figs. 7.4 and 7.22, that even though the stress-strain curves converge for the coarse and the fine meshes, the microstructures are not converged for the mesh sizes considered. Nevertheless, we show that there are similarities in

the microstructures obtained for the fine and coarse meshes considered at different levels of applied strain, as shown in Figure 7.23.

7.4 A necessary condition for microstructural patterns

Our model predicts inhomogeneous distributions of dislocations leading to the formation of microstructural patterns such as dipolar dislocation walls and cell structures. The discussion surrounding (7.1) and (7.2) explains the reason for the generation of dislocation density in the constrained case, but the results of the unconstrained case in Sec. 7.1.5 begs the question of the real reason for the development of patterns in MFDM.

In [RA06], using the small deformation variant of MFDM, mild patterns were obtained for the $(1\,\mu m)^2$ domain size with constrained and unconstrained boundaries. To understand the issue, a simplified system in 1 space dimension was analyzed in [RA06, Sec. 4.2.1] and linearized weak hyperbolicity of the homogeneous state was pointed out as a possible reason for giving rise to a (controlled) instability making the system sensitive to perturbations and leading to the formation of patterns. The homogeneous state may be thought of as a situation where the $\boldsymbol{\alpha}$ and g evolution equations ((3.14a) and (3.33) respectively) are uncoupled from each other instantaneously, which leads to the hypothesis that $k_0 = 0$ may lead to the suppression of patterns.

This hypothesis, i.e. $k_0 = 0$ suppresses patterns, was tested in [DAS16] using a simple 1-d ansatz, and it was again observed that the microstructure vanishes in the absence of any coupling between the dislocation transport (3.14a) and the strength evolution equations (3.33).

Here, we test the same hypothesis in the finite deformation setting. $k_0 = 0$ is assumed, with all other parameters taken from Table 7.2 along with $\theta_0 = 30°$ and $n_{sl} = 3$. Figure 7.24 shows the distribution of ρ_g at different strains under such a scenario. Comparing Fig. 7.24 with Fig. 7.4, we notice that the dislocation patterns entirely change when $k_0 = 0$; they

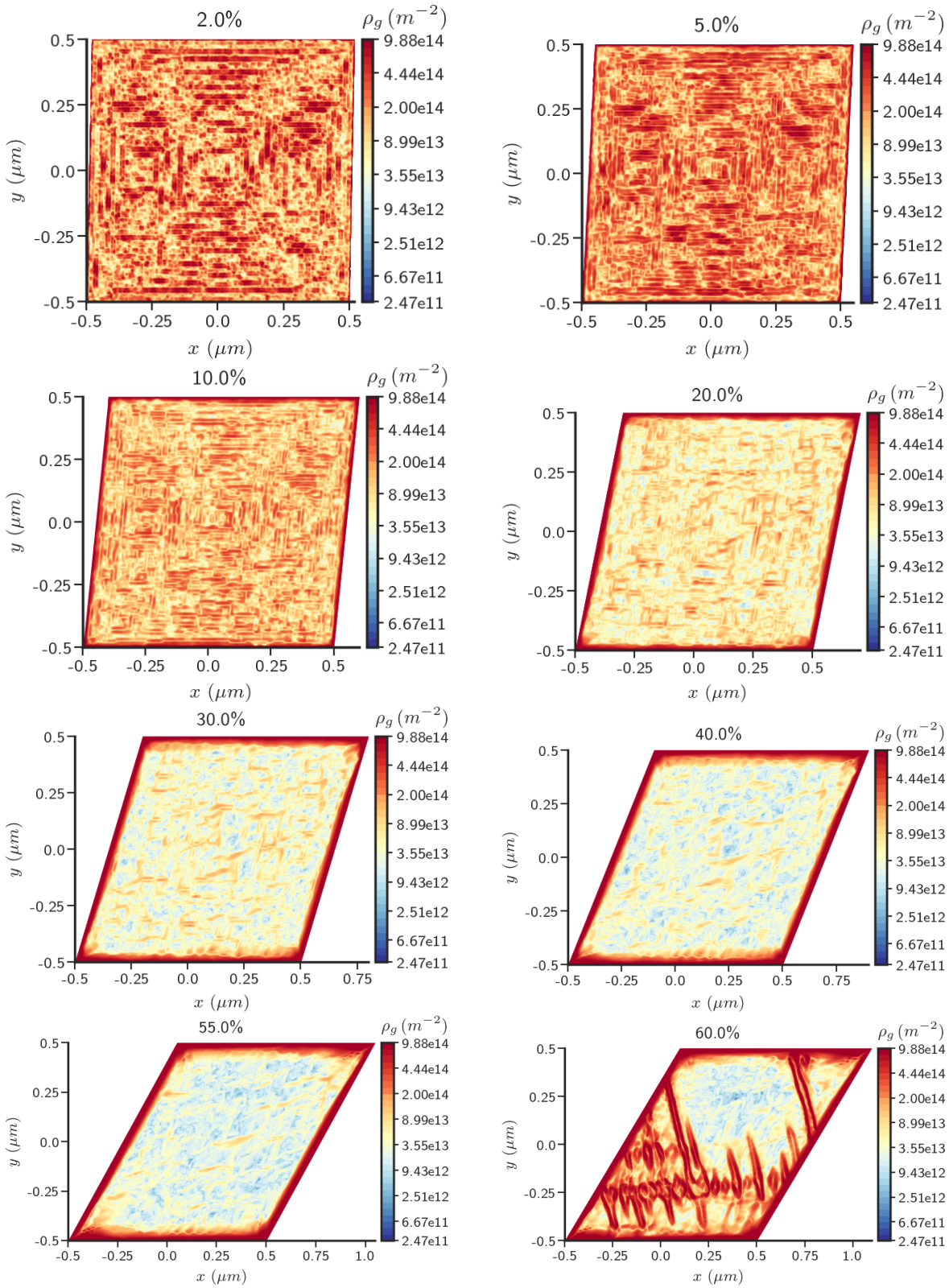

Figure 7.22: ρ_g for the $(1\,\mu m)^2$ domain size at different strains with plastically constrained boundaries on the fine mesh with $\theta_0 = 30°$ ($n_{sl} = 3$).

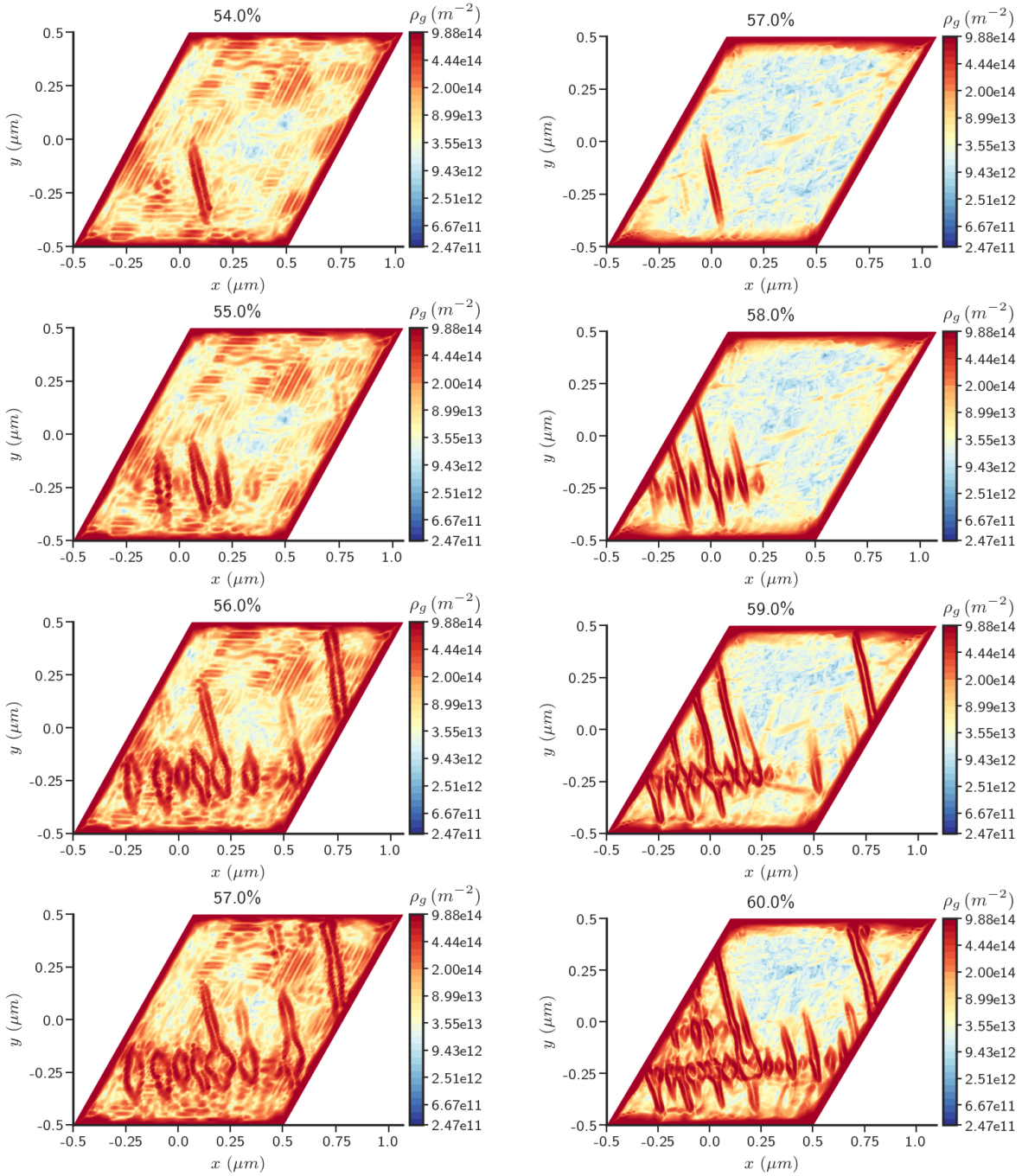

Figure 7.23: Results from the coarse mesh on left, and the fine mesh on right: Similarity of patterns for the $(1\,\mu m)^2$ domain size with plastically constrained boundaries and $\theta_0 = 30°$ ($n_{sl} = 3$).

are mildly patterned with much of the dislocations accumulated near the boundary similar to the case of the $(5\,\mu m)^2$ sample size shown in Fig. 7.6b. Therefore, we conclude that a necessary condition for patterning in full finite deformation MFDM is the coupling between equations of dislocation transport and evolution of strength evolution through $k_0 \neq 0$.

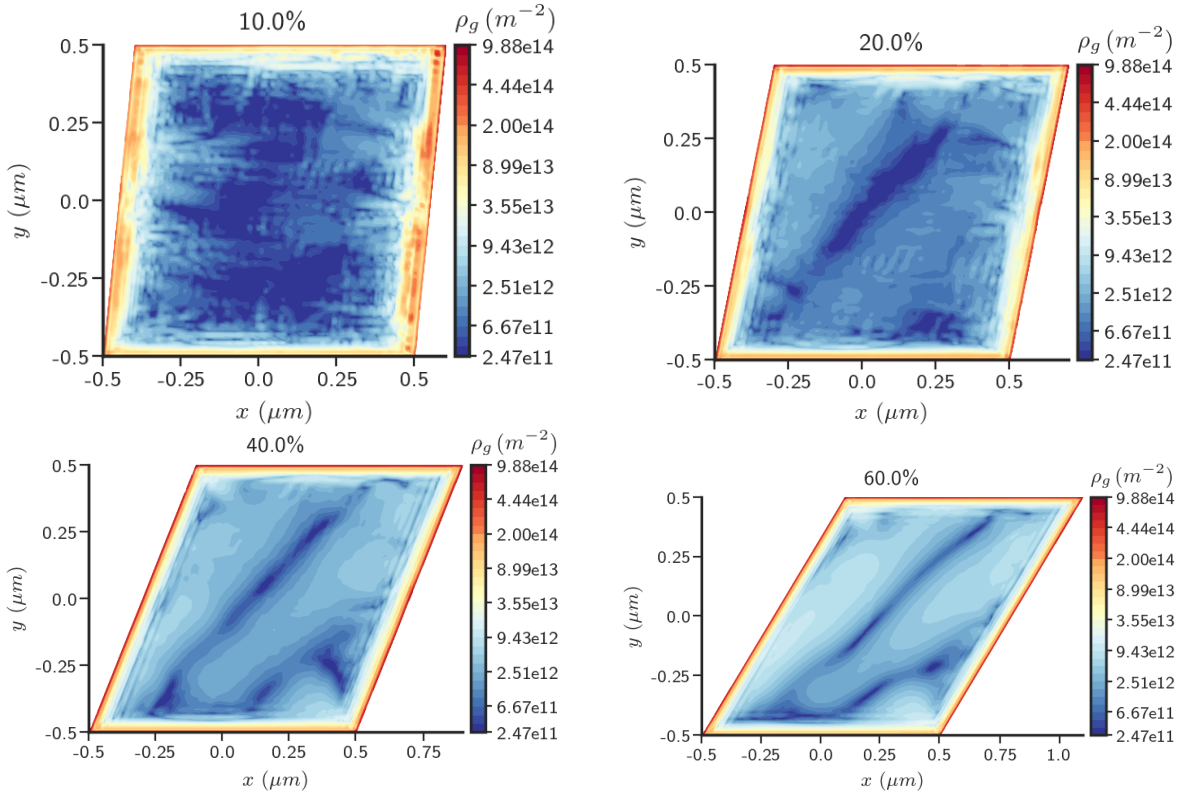

Figure 7.24: Distribution of ρ_g for the $(1\,\mu m)^2$ domain size at different strains with $k_0 = 0$ and plastically constrained boundaries ($\theta_0 = 30°$, $n_{sl} = 3$).

7.5 Effect of the length scale, l

Here, we look at the effect of l, defined in (3.25), on the microstructure obtained during simple shearing of the $(1\,\mu m)^2$ sample size with constrained boundaries, $\theta_0 = 30°$, and $n_{sl} = 3$, with all other parameters as in Table 7.2.

We first look at the variation in stress-strain response for different values of l shown in Fig. 7.25. A decrease in the value of l results in stronger response. As already explained, this is due to the fact that a larger l decreases the magnitude of $\boldsymbol{\alpha}$ in the domain and

consequently leads to smaller hardening (3.33). Next we look at the effect of l on the microstructural patterns shown in Figure 7.26. It can be seen that increasing the value of l makes a noticeable difference in the applied strain where qualitatively similar patterns of dislocations are formed. We notice that for $l = 2.5 \times 0.1\mu m$ we get several dislocation cells in the domain at 65% strain. Similar and even more intense structures can be noticed for $l = \sqrt{2} \times 0.1\mu m$ at 53% strains. Therefore, we can conclude that similar microstructures form at comparatively smaller strains as l is decreased, and the distribution has higher magnitude on average as well.

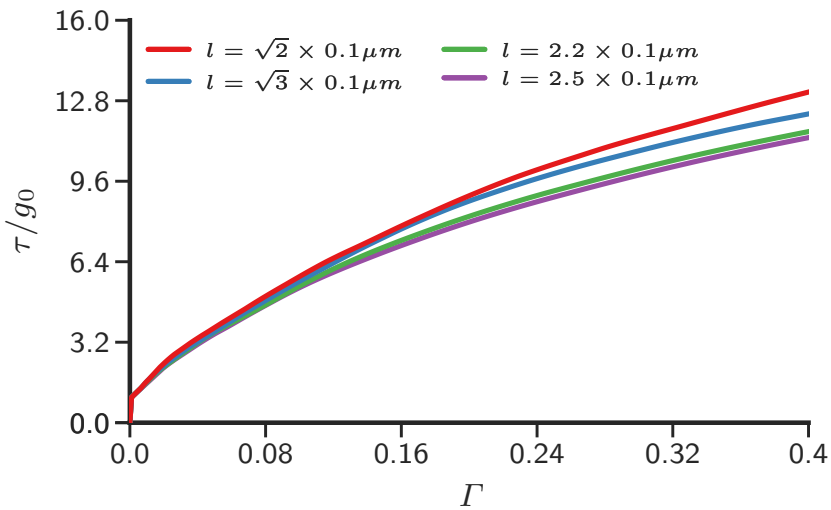

Figure 7.25: Stress strain response for different values of l for the $(1\,\mu m)^2$ domain size with plastically constrained boundaries ($\theta_0 = 30°$, $n_{sl} = 3$).

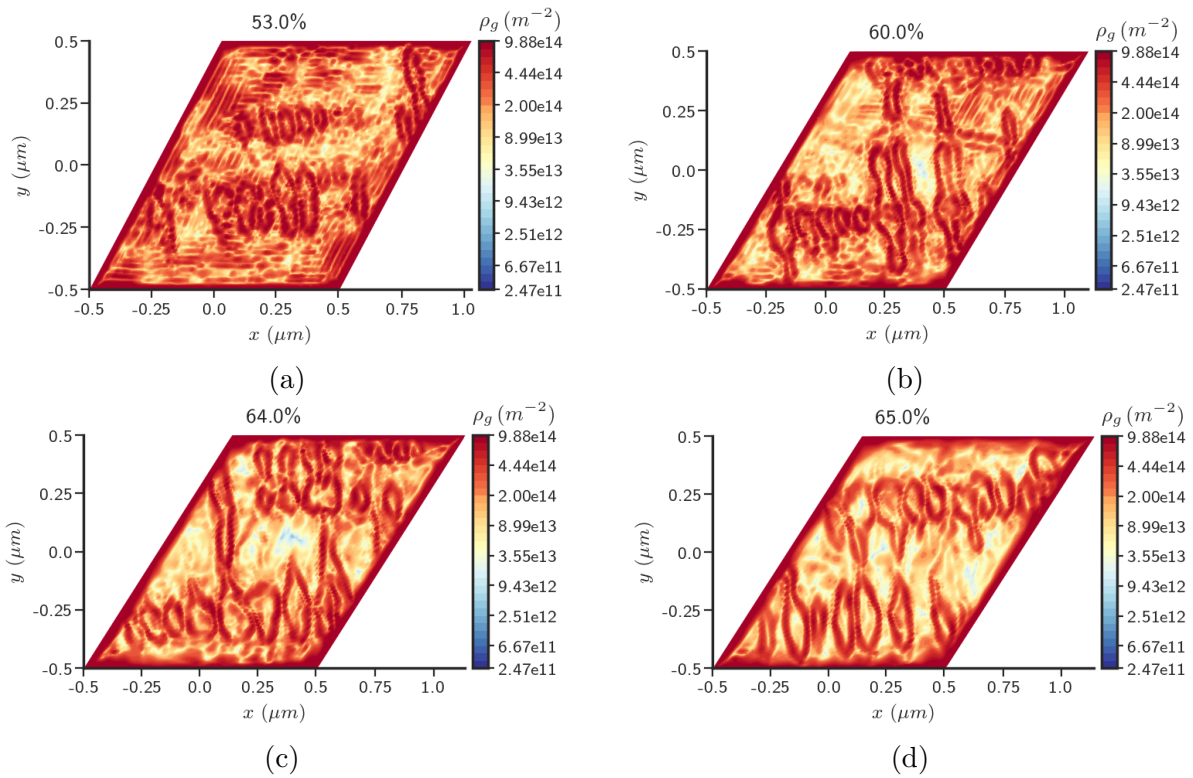

Figure 7.26: Distribution of ρ_g for the $(1\,\mu m)^2$ domain size with plastically constrained boundaries ($\theta_0 = 30°$, $n_{sl} = 3$) a) $l = \sqrt{2} \times 0.1\,\mu m$ b) $l = \sqrt{3} \times 0.1\,\mu m$ c) $l = 2.2 \times 0.1\,\mu m$ d) $l = 2.5 \times 0.1\,\mu m$.

This page intentionally left blank.

Chapter 8

Stress-coupled propagation of shear bands using FDM

Adiabatic shear bands are narrow, localized zones of large plastic deformation which are widely observed in metals and metallic alloys under intense dynamic loading. Due to their impact on materials under extreme conditions, they have been of immense interest to the scientific and engineering communities, and several experimental programs have been executed to explore the phenomenon of shear band formation in materials. Conventional elasto-viscoplastic theories by themselves are incapable of modeling shear band dynamics as they do not have the kinematical feature necessary for the longitudinal propagation of shear bands due to plastic flow.

Due to the incapability of conventional theories to model longitudinal shear band propagation, several works [ZRR96, MLL07, LLR+02] involve various ad-hoc extra failure criteria (critical strain rate or temperature based) that force shear band propagation along with the further assumption that the solid loses its strength, and a non-Newtonian viscous fluid constitutive equation is used to model its behavior. Our simple goal is to explore if shear band propagation can be attained relying on the fundamental kinematics of (averaged) dislocation motion in a *solid*. The fact that a dislocation is an *observed*, often static, boundary between differently strained regions on a slip plane may be modeled by the energy density of the body having preferred strained states. We use this realization in our modeling of the energy density of the theory. Recent observations of Rittel [RLV08] related to dynamic recrystallization being a precursor to shear band propagation may also be taken as evidence supporting this hypothesis at the mesoscale. Therefore, our aim is to model shear band propagation in a material on the basis of the essential kinematics of the model combined with standard constitutive response rather than ad-hoc criteria that force the longitudinal propagation of the shear band tip.

In our model, there is no role of a coherent global reference configuration. To model single dislocation non-equilibrium behavior we need to include another tensor valued *state* descriptor beyond the fields $\boldsymbol{W}$, $\boldsymbol{\alpha}$, and the current positions $\boldsymbol{x}$ on the body, much like strains related to modeling stacking fault energies, that we denote by the symbol $\boldsymbol{P}$. This

state variable is assumed to evolve as

$$\dot{\boldsymbol{P}}\boldsymbol{P}^{-1} = (\boldsymbol{\alpha} \times \boldsymbol{V} + \boldsymbol{L}^p)\, \boldsymbol{F}^e, \tag{8.1}$$

which can be justified from the kinematics of locally homogeneous deformations with velocity gradient given by the right hand side of the expression. We do not invoke the relation $\boldsymbol{F} = \boldsymbol{F}^e\boldsymbol{P}$ needing the definition $\boldsymbol{F}$ from an unknown global reference configuration and constraining the product $\boldsymbol{F}^e\boldsymbol{P}$ to equal the deformation gradient from this reference, with only the additive decomposition of the velocity gradient (3.18) considered a fundamental relation.

We model the shear banding process by first getting a dislocation core to come to equilibrium and then making it propagate longitudinally in the presence of an external force, leaving a shear band in its wake. The motion of the core under the application of force is based on the premise that the plastic distortion tensor field has to evolve in a fashion which is consistent with the dislocation density. The possibility of modeling a shear band in this manner was demonstrated in [ZAWB15] where a 1-d ansatz for the plastic distortion was utilized for its evolution in a predetermined layer in an otherwise $2d$ domain. We generalize the approach presented therein, without applying any restriction to the evolution of dislocation density or plastic distortion to a layer. This is a significant extension as it now requires solving a *multidimensional* nonlinear wave propagative *system* with a degenerate parabolic second order singular perturbation for the plastic distortion. The motion of the core under the application of the force is based on the premise that the plastic distortion tensor field has to evolve in a fashion which is consistent with the dislocation density.

8.1 Thermodynamics in terms of free energy or Dissipation

The thermodynamics for MFDM in terms of an entropy function is presented in [Ach11] and for FDM, but without the state variable $\boldsymbol{P}$, in [Ach04]. The aim here is to get the driving force for the dislocation velocity field $\boldsymbol{V}$ by requiring the dissipation in the system to be non-negative [cf., DAS16, ZAWB15]. The dissipation is calculated as done before in Sec. 3.3, but here we augment the free energy of the system ψ by an additional term $\eta(\boldsymbol{P})$ as

$$\psi := \psi(\boldsymbol{W}, \boldsymbol{\alpha}, \boldsymbol{P}) = \phi(\boldsymbol{W}) + \Upsilon(\boldsymbol{\alpha}) + \underbrace{\eta(\boldsymbol{P})}_{\text{extra term}} .$$

η is a non-convex multi-well function which embodies the fact that certain states are more preferred than others. A simplified example representing single slip is of the form

$$\eta(\boldsymbol{P}) = \frac{C}{\rho^*}\left\{1 - cos\left(\frac{2\pi \boldsymbol{P}_{12}}{\overline{\omega}}\right)\right\}$$

where C and $\overline{\omega}$ are constants.

In effect, the energy from stresses and the core term tries to smooth out concentration of dislocation density $\boldsymbol{\alpha}$, while the driving force from the non-convex η term promotes setting up sharp gradients in $\boldsymbol{P}$. Therefore, the balance between these thermodynamic driving forces will lead to an equilibrium width of the dislocation density, referred to as the core width. Following the details in Sec. 3.3, the dissipation in the body at any time t is given by

$$\begin{aligned} D &= \int_\Omega \boldsymbol{T} : \boldsymbol{L}\, dV - \int_\Omega \rho\, \dot{\overline{(\phi(\boldsymbol{W}) + \eta(\boldsymbol{P}) + \Upsilon(\boldsymbol{\alpha}))}} dV \\ &= \int_\Omega \boldsymbol{T} : \boldsymbol{L}\, dV - \int_\Omega \rho \left(\frac{\partial \phi(\boldsymbol{W})}{\partial \boldsymbol{W}} : \dot{\boldsymbol{W}} + \frac{\partial \eta(\boldsymbol{P})}{\partial \boldsymbol{P}} : \dot{\boldsymbol{P}} + \frac{\partial \Upsilon(\boldsymbol{\alpha})}{\partial \boldsymbol{\alpha}} : \dot{\boldsymbol{\alpha}} \right) dV. \end{aligned}$$

Using the evolution equations for $\boldsymbol{W}$, $\boldsymbol{\alpha}$, and $\boldsymbol{P}$ and the energy function definitions, we

get

$$D = \int_{\Omega} \left[\boldsymbol{T} + \rho \boldsymbol{W}^T \frac{\partial \phi}{\partial \boldsymbol{W}} + \rho \epsilon (\boldsymbol{\alpha} : \boldsymbol{\alpha}) \mathbf{I} - \rho \epsilon \boldsymbol{\alpha}^T \boldsymbol{\alpha} \right] dV - \int_{\partial \Omega} \rho \epsilon \boldsymbol{\alpha} : ((\boldsymbol{\alpha} \times \boldsymbol{V} + \boldsymbol{L}^p) \times \boldsymbol{n}) \, d\boldsymbol{A}$$
$$- \int_{\Omega} \rho \boldsymbol{X} \left[\left(\frac{\partial \phi}{\partial \boldsymbol{W}} + \frac{\partial \eta}{\partial \boldsymbol{P}} \boldsymbol{P}^T \boldsymbol{F}^{eT} - \epsilon \, curl \boldsymbol{\alpha} \right)^T \boldsymbol{\alpha} \right] \cdot \boldsymbol{V} \, dV.$$

Given the above form of the dissipation, the constitutive form of $\boldsymbol{V}$ that render the dissipation non-negative gives

$$\boldsymbol{V} \;\parallel\; \rho \boldsymbol{X} \left[\left(-\frac{\partial \phi}{\partial \boldsymbol{W}} + \epsilon \, curl \boldsymbol{\alpha} - \underbrace{\frac{\partial \eta}{\partial \boldsymbol{P}} \boldsymbol{P}^T \boldsymbol{F}^{eT}}_{\text{extra term}} \right)^T \boldsymbol{\alpha} \right], \tag{8.2}$$

where the symbol $\parallel$ refers to 'parallel'. At small deformation, this can be written as

$$\boldsymbol{V} \;\parallel\; \rho \boldsymbol{X} \left[\left(\boldsymbol{T} + \epsilon \, curl \boldsymbol{\alpha} - \frac{\partial \eta}{\partial \boldsymbol{P}} \right)^T \boldsymbol{\alpha} \right]. \tag{8.3}$$

Therefore, it can be noted that the addition of the function η in the free energy density adds an additional term in the driving force for $\boldsymbol{V}$. In this work, the non-dimensional drag in the driving force for $\boldsymbol{V}$ is assumed to be 0.0297 which ensures that the speed dislocations in our model is same as in discrete dislocation methodology [ZAWB15, Sec. 4.2].

Using FDM to model shear band propagation produces a system of coupled nonlinear equilibrium, transport, and diffusion equations. Having a stable, computationally efficient, and robust numerical scheme for such a system of coupled equations presented severe, novel, numerical challenges. We demonstrate our scheme for longitudinal stress coupled shear band propagation in the context of the small deformation, quasi-static force balance setting. The adopted scheme (Sec. 8.2) for plastic distortion and dislocation density evolution can be accommodated with no extensions into a fully dynamic force balance computation. We now present two numerical formulations that were unsuccessful before going on to explain the problem set up and the final algorithm used.

- <u>Locally evolving $\boldsymbol{U}^p$ at the integration points</u>: A simple way to evolve $\boldsymbol{U}^p$ in time is to numerically integrate it locally at integration points as an ODE with $\boldsymbol{\alpha}$ and $\boldsymbol{V}$ treated as known data. The value of the plastic distortion field at any time $t + \Delta t$ is then given as $\boldsymbol{U}^{p,t+\Delta t} = \boldsymbol{U}^{p,t} + \Delta t(\boldsymbol{\alpha} \times \boldsymbol{V})$. While this approach succeeds in the stress-uncoupled version of the equation, an inherent problem with such an approach is that the evolution algorithm may not produce a smooth $\boldsymbol{U}^p$ field in the domain, especially in the core, and, much more importantly, the constraint $curl\boldsymbol{U}^p = -\boldsymbol{\alpha}$ may not hold with time. So, even if an equilibrium of the core is achieved, its motion on the application of an externally applied stress field is not possible since the evolution equation of $\boldsymbol{U}^p$, $\dot{\boldsymbol{U}}^p = \boldsymbol{\alpha} \times \boldsymbol{V}$ with $curl\boldsymbol{U}^p \neq -\boldsymbol{\alpha}$ loses its nature of a first order wave equation. Therefore, this way of numerically evolving $\boldsymbol{U}^p$ in the domain fails to model the motion of the dislocation core leaving a localized shear band in its wake.

- <u>Helmholtz decomposition of $\boldsymbol{U}^p$</u>: Using the Helmholtz decomposition, $\boldsymbol{U}^p$ can be written as $\boldsymbol{U}^p = \boldsymbol{\chi} + grad\boldsymbol{w}$, where $curl\boldsymbol{\chi} = -\boldsymbol{\alpha}$. Since $\boldsymbol{\chi}$ at any time $t + \Delta t$ can be calculated from the dislocation density $\boldsymbol{\alpha}^{t+\Delta t}$, an evolution equation for $\boldsymbol{w}$ can then be derived as follows:

$$\begin{aligned} & div\,\dot{\boldsymbol{U}}^p = div(\boldsymbol{\alpha} \times \boldsymbol{V}) \\ \Longrightarrow \quad & div\,grad\dot{\boldsymbol{w}} = div(\boldsymbol{\alpha} \times \boldsymbol{V}) \quad (\text{using } div\dot{\boldsymbol{\chi}} = \boldsymbol{0}). \end{aligned} \tag{8.4}$$

$\boldsymbol{U}^p$ at time $t + \Delta t$ can then be given as $\boldsymbol{U}^{p,t+\Delta t} = \boldsymbol{\chi}^{t+\Delta t} + \text{grad}\,\boldsymbol{w}^{t+\Delta t}$. However, the problem in evolving $\boldsymbol{U}^p$, for this particular problem, by such an evolution scheme is that, while being a consistent scheme, it nevertheless results in the development of $\boldsymbol{U}^p$ components other than those which correspond to the non-zero plastic strain rate components of $\boldsymbol{\alpha} \times \boldsymbol{V}$, i.e. the scheme accumulates errors and is not accurate. For example, with $(\alpha \times V)_{12}$ being the only non zero component of plastic strain rate consistent with the $\boldsymbol{\alpha}$ evolution, we find that using the Helmholtz decomposition, $\boldsymbol{\chi}$

always develops a χ_{11} component and this needs to be negated by the $grad\boldsymbol{w}$ field, which does not materialize, even when higher order interpolation is used for the $\boldsymbol{w}$ field.

8.2 Variational formulation

The failure of the two schemes above suggested the following insights:

1. These schemes were able to transport $\boldsymbol{\alpha}$ well, but the $\boldsymbol{U}^p$ field, used crucially in the non-convex function η, could not be discretely transported adequately for its curl to remain consistent with the dislocation core represented by $\boldsymbol{\alpha}$.

2. For success, it would be important to firmly impose $curl\boldsymbol{U}^{p,t+\Delta t} = -\boldsymbol{\alpha}^{t+\Delta t}$, using the computed values of $\boldsymbol{U}^{p,t}$, $\boldsymbol{\alpha}^t$, $\boldsymbol{\alpha}^{t+\Delta t}$, and $\boldsymbol{V}^t$ as data to define the approximation $\boldsymbol{U}^{p,t+\Delta t}$ such that the solution for $curl\boldsymbol{U}^p = -\boldsymbol{\alpha}$ is not underconstrained.

The equation for the evolution of $\boldsymbol{U}^p$ in the small deformation case is

$$\dot{\boldsymbol{U}^p} = \boldsymbol{\alpha} \times \boldsymbol{V},$$

along with the constraint

$$curl(\boldsymbol{U}^p) = -\boldsymbol{\alpha}.$$

After $\boldsymbol{\alpha}$ has been evolved from its conservation law as explained in Sec. 4.1.3, we need to evolve $\boldsymbol{U}^p$ to get its value at the end of a time increment $(t + \Delta t)$ assuming that $\boldsymbol{\alpha}^t$ and $\boldsymbol{V}^t$ are known. Appendix C shows that using the Least-Squares formulation (Eq. C.1) to solve for $\boldsymbol{U}^p$ gives a unique solution (in a slightly more general setting) with only the natural boundary condition enforced by the Least-Squares scheme. With this data we define the discrete value of $\boldsymbol{U}^{p,t+\Delta t}$ as $\boldsymbol{U}^{p,t+\Delta t} = \boldsymbol{U}^{p,t} + \Delta t\, \Theta\, \boldsymbol{\alpha}^{t+\Delta t} \times \boldsymbol{V}^t$, where Θ is a scalar field.

Thus, the exact solution for Θ is 1 in the limit $\Delta t \to 0$ and we use the following Least Squares functional to solve for the field over finite time steps:

$$J(\Theta) = \frac{1}{2}\int_\Omega (\Theta - 1)^2 dV + \frac{P}{2}\int_\Omega \left(curl(\boldsymbol{U}^{p,t+\Delta t}(\Theta)) + \boldsymbol{\alpha}^{t+\Delta t}\right) : \left(curl(\boldsymbol{U}^{p,t+\Delta t}(\Theta)) + \boldsymbol{\alpha}^{t+\Delta t}\right) dV,$$

where $P >> 1$. We rewrite the functional as

$$J(\Theta) = \frac{1}{2}\int_\Omega (\Theta - 1)^2 dV + \frac{P}{2}\int_\Omega |(curl(\boldsymbol{U}^{p,t} + \Delta t\, \Theta\, \boldsymbol{\alpha}^{t+\Delta t} \times \boldsymbol{V}^t) + \boldsymbol{\alpha}^{t+\Delta t})|^2\, dV.$$

We again use the Least Squares finite element method and use its Euler-Lagrange equation to solve for Θ as follows:

$$\begin{aligned} &\delta J_{\delta\Theta} = 0 \\ \implies &\int_\Omega (\Theta - 1)\delta\Theta\, dV + P\int_\Omega \big[(curl(\boldsymbol{U}^{p,t} + \Delta t\, \Theta\, \boldsymbol{\alpha}^{t+\Delta t} \times \boldsymbol{V}^t) + \boldsymbol{\alpha}^{t+\Delta t}) : \\ &\qquad\qquad curl(\Delta t\, \delta\Theta\, \boldsymbol{\alpha}^{t+\Delta t} \times \boldsymbol{V}^t)\big]\, dV = 0. \end{aligned}$$

Using $curl(\boldsymbol{U}^{p,t}) = -\boldsymbol{\alpha}^t$ eliminates the need for involving the evolving approximation of $\boldsymbol{U}^p$ in the solution for Θ. Therefore we get the weak form as

$$\begin{aligned} \int_\Omega (\Theta - 1)\, \delta\Theta\, dV + P\int_\Omega \big((curl(\Delta t\, \Theta\, \boldsymbol{\alpha}^{t+\Delta t} \times \boldsymbol{V}^t) + \boldsymbol{\alpha}^{t+\Delta t} - \boldsymbol{\alpha}^t) : \\ curl(\Delta t\, \delta\Theta\, \boldsymbol{\alpha}^{t+\Delta t} \times \boldsymbol{V}^t)\big)\, dV = 0. \end{aligned} \tag{8.5}$$

Once Θ is known, we update the value of $\boldsymbol{U}^p$ at the integration points as

$$\boldsymbol{U}^{p,t+\Delta t} = \boldsymbol{U}^{p,t} + \Theta\Delta t(\boldsymbol{\alpha}^{t+\Delta t} \times \boldsymbol{V}^t).$$

Next we describe the algorithm that is used to evolve the system for this particular problem.

8.2.1 Algorithm for quasistatic case with $\boldsymbol{U}^p$ evolution for small deformation

The algorithm for the quasistatic case with $\boldsymbol{U}^p$ evolution is presented in Table 8.1.

Given: material properties, initial conditions, boundary conditions, and applied loading conditions.
Step 1: Finding the initial stress field on the body in as-received configuration. At small deformation, $curl\boldsymbol{U}^e = \boldsymbol{\alpha}$ and $curl\boldsymbol{U}^p = -\boldsymbol{\alpha}$, which implies that $\boldsymbol{U}^e$ and $\boldsymbol{U}^p$ differ by a gradient field i.e. $\boldsymbol{U}^e = \boldsymbol{U}^p + grad\boldsymbol{w}$. • Since $\boldsymbol{U}^p$ is known, we solve the equilibrium equation $div(\mathbb{C}\boldsymbol{U}^e) = \boldsymbol{0}$ to solve for the field $\boldsymbol{w}$ in the domain as described in the Sec. 4.1.4.3 • $\boldsymbol{U}^e$ can then be calculated as $\boldsymbol{U}^e = grad\boldsymbol{w} + \boldsymbol{U}^p$ to get stresses in the domain at $t = 0$ given by $\boldsymbol{T} = \mathbb{C} : \boldsymbol{U}^e$. • The dislocation density in the domain is initialized by evaluating $curl\boldsymbol{U}^e$ in the domain. • Solve for $\boldsymbol{\chi}$ from the now known dislocation density distribution $\boldsymbol{\alpha}$ as described in Sec. 4.1.2.
Step 2: Quasistatic loading analysis: Assume that the state at time-step k is known: $\boldsymbol{x}^k$, $\boldsymbol{\alpha}^k$, $\boldsymbol{z}^k$, $\boldsymbol{\chi}^k$, $\boldsymbol{v}^k$, $\boldsymbol{V}^k$, $\boldsymbol{L}^p$, Δt^k, PH^k To get the state at time step $k+1$ the following is done: • $\boldsymbol{\alpha}^{k+1}$ is calculated by solving alpha evolution equation using Galerkin-Least-Squares FEM as shown in Sec. 4.1.3. • $\boldsymbol{U}^{p,k+1}$ is obtained as described in Sec. 8.2. • Solve for $\boldsymbol{\chi}^{k+1}$ from the given dislocation density distribution $\boldsymbol{\alpha}^{k+1}$ as described in Sec. 4.1.2. • Finally, the equilibrium equation is solved on the new configuration to get $gradz$ as described in Sec. (4.1.4.3). The stresses are then given as $\boldsymbol{T} = \mathbb{C} : \boldsymbol{U}^e$ where $\boldsymbol{U}^e = grad\boldsymbol{z} - \boldsymbol{\chi}$. • PH^{k+1} is updated on the new configuration.
Cutback to step k and use half time-step to come to step $k+1$ if following holds at any Gauss point in the domain. $\lvert\boldsymbol{\alpha}^{k+1} \times \boldsymbol{V}^{k+1} + \boldsymbol{L}^{p\,k+1}\rvert_\infty \times \Delta t^k > 0.002$
if no cut back happens, then the state is accepted. $\Delta\, t^{k+1}$ is calculated as described in (4.11) and this algorithm is repeated to get state at increment $k+2$.

Table 8.1: Quasistatic (M)FDM algorithm with $\boldsymbol{U}^p$ evolution.

The elasticity of the material is modeled as isotropic linear elastic. The problem set up is as follows: we prescribe the initial condition for $\boldsymbol{U}^p_{12}$ in a layer of thickness b as a hyperbolic tangent function given by

$$\boldsymbol{U}^p_{12}(\boldsymbol{x}, t=0) = \frac{\bar{\omega}}{2}\left(1 + tanh(ax_1)\right), \tag{8.6}$$

where we choose $\overline{\omega} = 1$, and $a = \sqrt{\frac{\mu}{4\epsilon}}$. The initial dislocation density in the domain is then given as $\boldsymbol{\alpha} = -curl\boldsymbol{U}^p$. Table 8.2 presents the values of material constants used in modeling of shear band propagation. The non-dimensionalized time is given as $t^* = t\frac{V_s}{b}$.

Parameter	Value
ϵ	1
$\overline{\omega}$	1
C	$\frac{\mu\overline{\omega}^2}{\pi^2}$
E	200 GPa
ν	.30

Table 8.2: Parameter values used for modeling shear bands.

Figure 8.1a shows the α_{13} prescribed in the domain at $t^* = 0$. Figure 8.1b shows its distribution along $x_2 = 0$. Figures 8.2a and 8.2b show the U^p_{12} in the domain and along the $x_2 = 0$ respectively.

We then follow the algorithm outlined in Table 8.1 to let the system evolve until the rate of evolution of α_{13} becomes small and the core is then said to have equilibrated. Figures 8.4a and 8.4b present the equilibrated α_{13} and the corresponding $\boldsymbol{U}^p$. As can be seen in 8.4c, the non-dimensional rates for the evolution of α_{13} are 10^{-3} or smaller. Figure 8.4d shows the shear stress component T_{12} in the domain at equilibrium.

Figures 8.3a and 8.3b show the stress field in the domain at $t^* = 0$ and at equilibrium respectively. As can be seen, there is no noticeable change in the stress field outside the core.

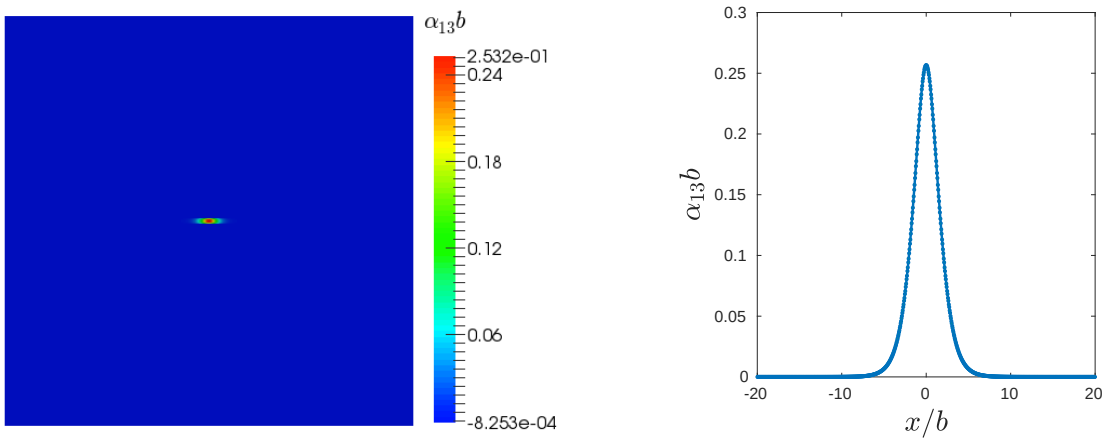

(a) (b)

Figure 8.1: At $t = 0$. a) α_{13} in the domain b) α_{13} along $x_2 = 0$

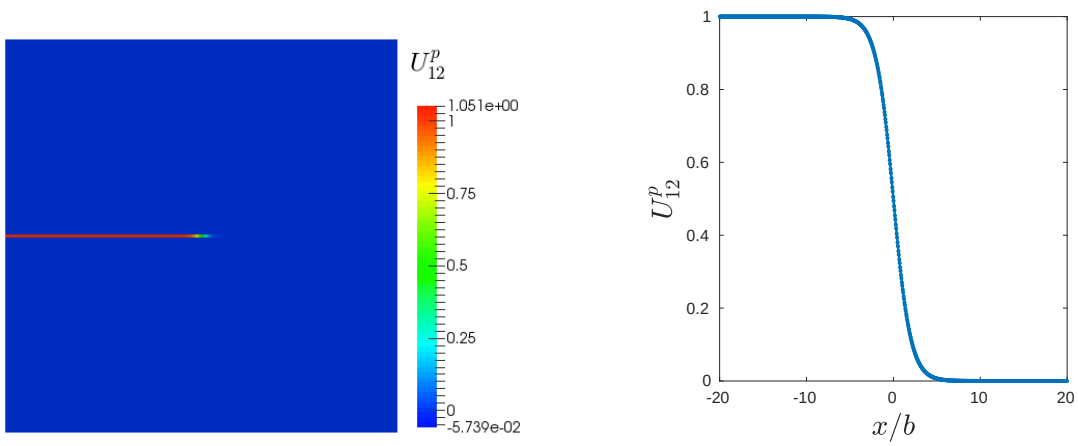

(a) (b)

Figure 8.2: At $t = 0$. a) U_{12}^p in the domain b) U_{12}^p along $x_2 = 0$

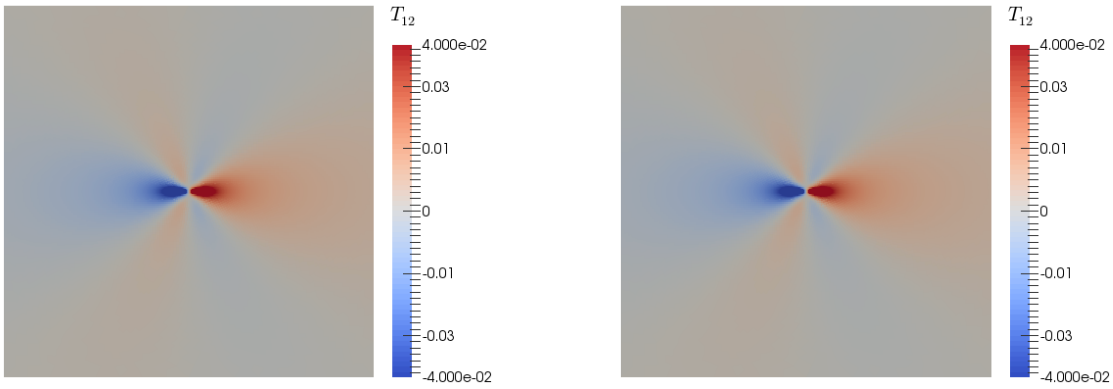

(a) (b)

Figure 8.3: T_{12} in the domain at a) $t^* = 0$ b) equilibrium

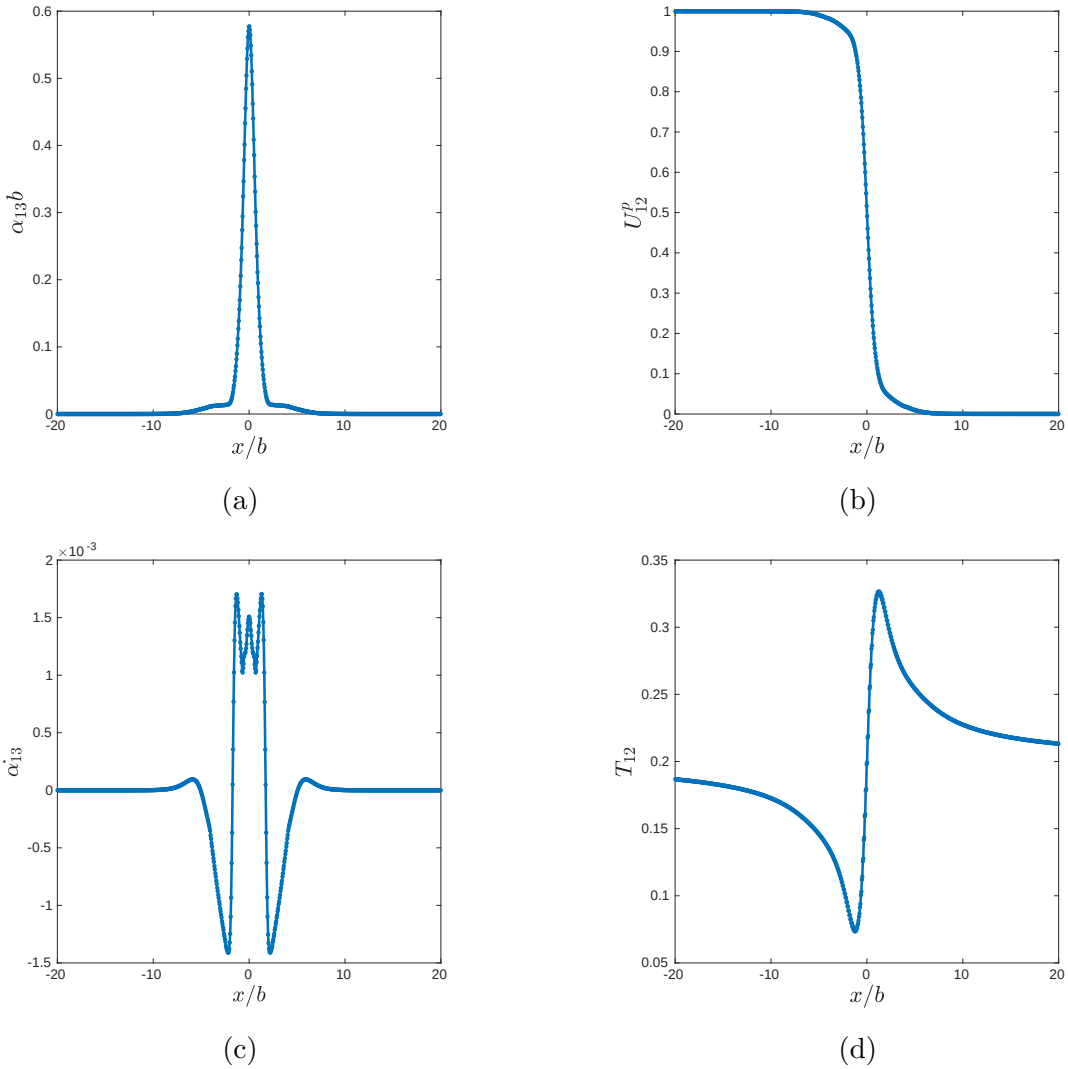

Figure 8.4: a) α_{13} b) U_{12}^p c) $\dot{\alpha}_{13}$ d) T_{12} in the domain at equilibrium.

After equilibrium is attained, we apply a shear traction of magnitude 0.2μ on the outer boundary of the domain. This corresponds to the superposition of a homogeneous stress field of $T_{12} = 0.2\mu$ on the body.

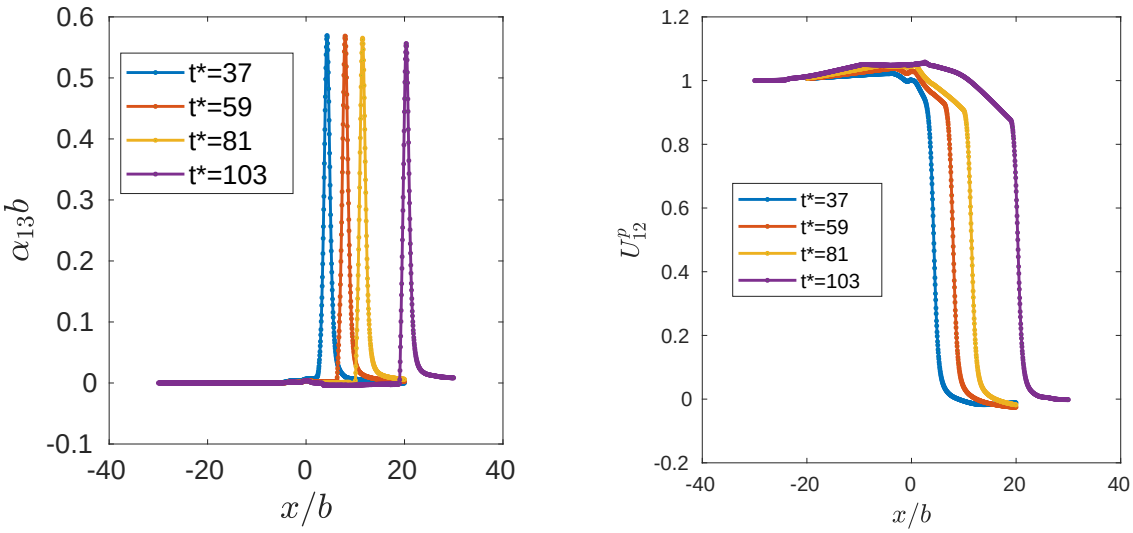

(a) (b)

Figure 8.5: a) α_{13} b) U^p_{12} along $x_2 = 0$ at different times during the motion.

Figure 8.5a presents the position of the dislocation core at different times. We can see that dislocation moves in the $\boldsymbol{e}_1$ direction under the application of external force. The evolution of plastic distortion along $x_2 = 0$ can be seen from figure 8.5b at different times. We observe that a localized shear deformation arises along the path as the core moves longitudinally upon the application of external force. Although, some numerical errors accumulate in the evolution of $\boldsymbol{U}^p$ in the domain, it does not affect the propagation of the core. This demonstrates the successful modeling of the longitudinal propagation of the shear band in a *fully coupled, multidimensional, and nonlinear setting.*

To show that the dislocation density and the plastic distortion are localized along the path of the shear band, the dislocation density and the plastic distortion fields in the domain are presented in figure 8.6 at various times during the propagation.

Although, we have presented the results under the quasi-static and small deformation assumptions, this stands as a first theoretical-computational implementation of the longi-

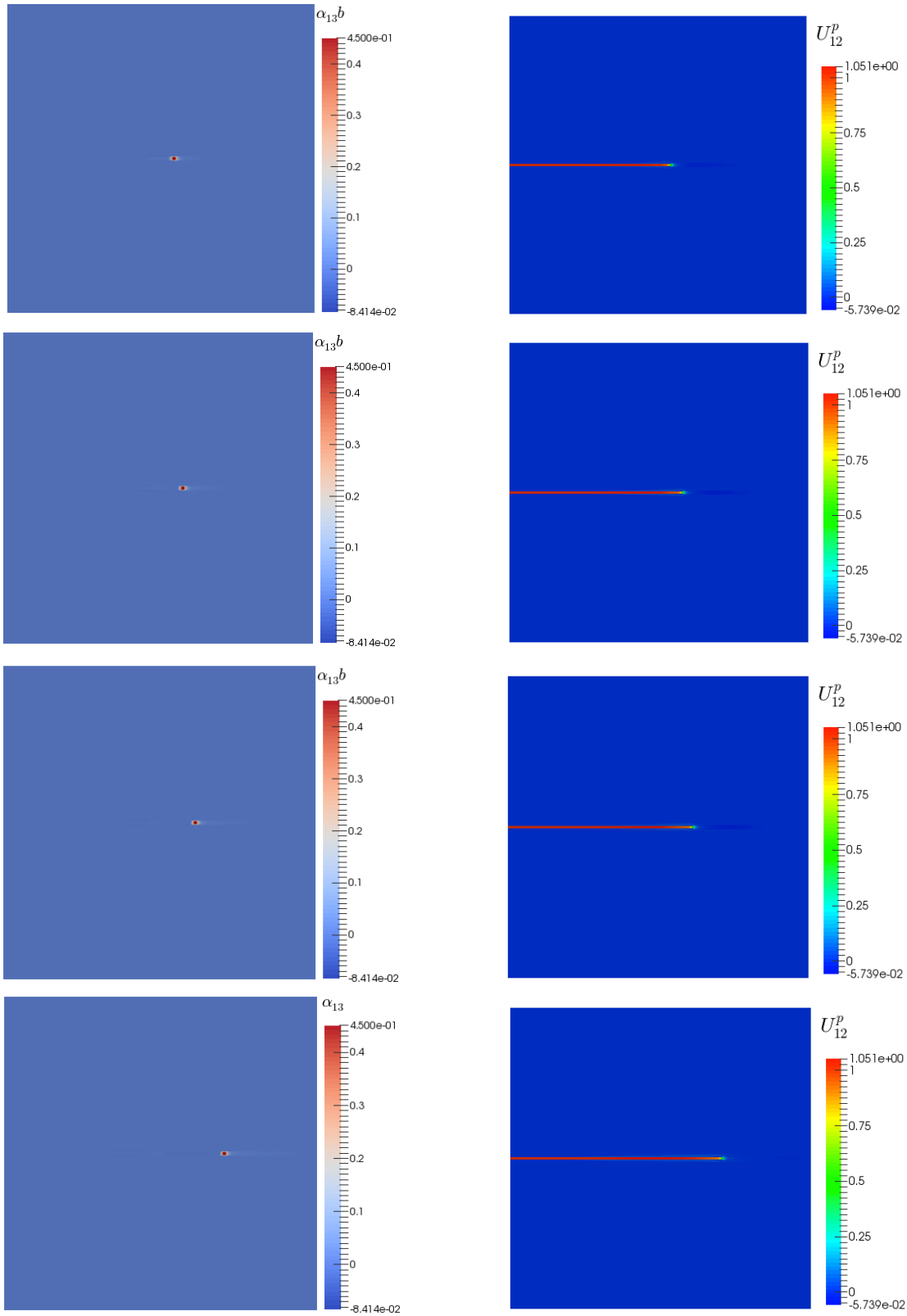

Figure 8.6: Left: α_{13} and Right: U_{12}^p in the domain at various times t^* (starting from top) 37, 59, 81, 140

tudinal propagation of shear bands in the literature that does not involve ad-hoc failure criteria as well as an invocation of solid and fluid behavior behind the shear band tip [ZRR96, MLL07, LLR+02]. Moreover, the scheme is robust enough to accommodate the modeling of shear bands with inertia.

This page intentionally left blank.

Chapter 9

Conclusion and future work

In this chapter, a brief summary of the research work presented in the thesis and possible avenues of future research using the developed framework are discussed.

9.1 Conclusion

This research presented results of a first model of mesoscale crystal and J_2 plasticity of unrestricted geometric and material nonlinearity where fields of dislocation distributions can be explicitly calculated and dislocation transport, and its attendant plastic strain rate, is fundamentally accounted. In the first part of the research, staggered numerical algorithms for the quasi-static and dynamic cases for finite deformation MFDM theory were devised and implemented in a finite element framework. The implementation is quite efficient, and a typical 2-d simulation up to 60% strain on the meshes shown in Table 7.2 takes an average wall-clock time of 5 hours when running on 1 node comprising 24 processors.

The second part involved the use of the developed computational tool to study problems of significant scientific interest, after verification of the numerical formulation and algorithm through stringent numerical tests. The computational tool was used to quantify the change in the volume in the body upon introduction of dislocations. The sharply contrasting predictions of the geometrically linear and nonlinear FDM theories for the stress field of a spatially homogeneous dislocation distribution were also demonstrated. We study the stress-field path followed in a body corresponding to a sequence of dislocation starting from a single dislocation to a stress-free dislocation wall constituting a grain boundary. Furthermore, we show large differences in the stress field of single edge dislocation obtained from finite deformation FDM and small deformation analytical solution. The numerical calculations show large difference for distances upto $10b$ from the dislocation core and suggest careful calibration of the analytical result from Molecular Dynamics.

We also demonstrated dislocation patterning in a full-fledged, geometrically nonlinear model of crystal/J_2 plasticity MFDM. Intricate spatial patterning, crystal orientation (only

for crystal plasticity MFDM) and size effects, the occurrence of stressed dislocation microstructures both under applied loads and in unloaded bodies were demonstrated in a rate-dependent setting with the simplest possible isotropic model of work hardening. Interesting and realistic microstructural features of plastic response have been shown to be within the qualitative purview of the model, which may be considered a minimal enhancement of classical crystal/J_2 plasticity to account for what are commonly known as geometrically necessary dislocations. Finally, the potential and generality of MFDM are demonstrated by applying it to study the phenomenon of longitudinally propagating shear bands in materials which stands as a first theoretical-computational implementation in the literature that does not involve any ad-hoc failure criteria to model longitudinal propagation of shear bands.

9.2 Future work

In the future, the framework can be used to model several more problems in computational plasticity such as strain localization in rate-independent materials as observed in [PAN82, PAN83, NALP85], response of polycrystal aggregates [HH95], and size effect in torsion of circular wires [FMAH94, LHT+12], all at finite deformation. Also, the modeling of shear bands at finite deformation with or without inertia as well as temperature driven changes of preferred plastic distortion (apart from stress driven changes as shown in Chapter 8) can be studied. It will also be interesting to study the dislocation patterning in a full 3D body. The model can also be used to study microstructure development in the body under fatigue loading. Another interesting study would be to understand the reason why the standard slipping rate from crystal plasticity (un-symmetrized Eq. 3.25) causes instability in the model.

Another interesting research area to explore would be the extension of the algorithm presented for the shear band propagation Sec. 8.2 to include i) dynamics with inertia, ii) finite deformation, iii) multidimensional shear band motion, and iv) understanding the degree

of freedom required in the Least-Squares formulation to accurately solve the problem in the case of multidimensional motion, i.e. is it always true that a scalar field will suffice.

The future work can also focus on modeling dislocation patterning which accompanies deformation microstructures like shear bands [AR77, PAN83, Pei83, OR99, AO03] and patchy slip [PCC55, Cah51] arising from the effects of strong latent hardening [Asa83, Bas93].

Comparison with experiment of the evolving cellular and wall patterns formed can also be the subject of future work. A comprehensive large-scale computational study of the nature of convergence of the observed patterns in our work awaits further study, including whether weaker notions of convergence [FKMT17, FLM17] will be required. Also, the significance and utility of the work of the French school of Mathematical Morphology [e.g., Jeu13, Ang17] in understanding and characterizing the intricate patterns displayed by our model appears to be another interesting area of future research.

Appendices

Appendix A

Calculation of $\frac{\partial \boldsymbol{T}}{\partial \boldsymbol{F}^e}$

A.1 Saint-Venant Kirchhoff material

For a Saint-Venant Kirchhoff material whose stress response is given by Eq. (3.21), the partial derivative of $\boldsymbol{T}$ w.r.t. $\boldsymbol{F}^e$ can be obtained as

$$
\begin{aligned}
T_{ij} &= F^e_{ik}\mathbb{C}_{klrs}E_{rs}F^{eT}_{lj} \\
\frac{\partial T_{ij}}{\partial F^e_{mn}} &= \frac{\partial F^e_{ik}}{\partial F^e_{mn}}\mathbb{C}_{klrs}E_{rs}F^e_{jl} + F^e_{ik}\mathbb{C}_{klrs}\frac{\partial E_{rs}}{\partial F^e_{mn}}F^e_{jl} + F^e_{ik}\mathbb{C}_{klrs}E_{rs}\frac{\partial F^e_{jl}}{\partial F^e_{mn}} \\
E^e_{rs} &= \frac{1}{2}\left(F^{eT}_{rp}F^e_{ps} - \delta_{rs}\right) \implies \frac{\partial E^e_{rs}}{\partial F^e_{mn}} = \frac{1}{2}(\delta_{rn}F^e_{ms} + F^e_{mr}\delta_{sn}) \\
\frac{\partial T_{ij}}{\partial F^e_{mn}} &= \delta_{im}\mathbb{C}_{nlrs}E_{rs}F^e_{jl} + \frac{1}{2}F^e_{ik}\mathbb{C}_{klrs}\left[F^e_{ms}\delta_{rn} + F^e_{mr}\delta_{ns}\right]F^e_{jl} + F^e_{ik}\mathbb{C}_{knrs}E_{rs}\delta_{jm}.
\end{aligned}
$$

A.2 Neo-Hookean material

For the Neo-Hookean Material whose stress is given by Eq. (3.22), the partial derivative of $\boldsymbol{T}$ w.r.t. $\boldsymbol{F}^e$ can be obtained as

$$
\begin{aligned}
T_{ij} &= \mu(F^e_{ik}F^{eT}_{kj} - \delta_{ij}) \\
\frac{\partial T_{ij}}{\partial F^e_{mn}} &= \mu\left(\frac{\partial F^e_{ik}}{\partial F^e_{mn}}F^e_{jk} + F^e_{ik}\frac{\partial F^e_{jk}}{\partial F^e_{mn}}\right) \\
&= \mu\left(\delta_{im}F^e_{jn} + F^e_{in}\delta_{jm}\right)
\end{aligned}
$$

Appendix B

Calculation of $\frac{\partial \boldsymbol{T}}{\partial \boldsymbol{H}}$

B.1 Saint-Venant Kirchhoff material

At small deformation, writing $\boldsymbol{F}^e = \boldsymbol{I} + \boldsymbol{U}^e$, the linearised stress for Saint-Venant Kirchhoff material is then given as

$$
\begin{aligned}
T_{ij} &= F^e_{ik}\mathbb{C}_{klrs}E_{rs}F^{eT}_{lj} \\
T_{ij} &= \frac{1}{2}(\delta_{ik} + U^e_{ik})\mathbb{C}_{klrs}\left[(\delta_{ar} + U^e_{ar})(\delta_{as} + U^e_{as}) - \delta_{rs}\right](\delta_{jl} + U^{eT}_{lj}) \\
&\approx \frac{1}{2}\mathbb{C}_{klrs}(U^e_{rs} + U^e_{sr}) \\
&\approx \mathbb{C}_{klrs}U^e_{rs}
\end{aligned}
$$

wherein the symmetry in the last two indices of $\mathbb{C}$ has been used. Writing $\boldsymbol{H} = grad\boldsymbol{z}$, $\frac{\partial \boldsymbol{T}}{\partial \boldsymbol{H}}$ can then be calculated as

$$
\begin{aligned}
\frac{\partial T_{ij}}{\partial H_{ab}} &= \frac{\partial T_{ij}}{\partial U^e_{pq}}\frac{\partial U^e_{pq}}{\partial H_{ab}} \\
&= \mathbb{C}_{klrs}\delta_{pr}\delta_{qs}\delta_{pa}\delta_{qb} \\
&= \mathbb{C}_{klab}.
\end{aligned}
$$

B.2 Neo-Hookean material

For Neo-Hookean material whose stress response is given by (3.22), the linearised stress can be calculated as:

$$
\begin{aligned}
\boldsymbol{T} &= \mu(\boldsymbol{F}^e \boldsymbol{F}^{eT} - \boldsymbol{I}) \\
T_{ij} &= \mu(F^{eT}_{ip} F^e_{pj} - \delta_{ij}) \\
&= \mu((\delta_{pi} + U^e_{pi})(\delta_{pj} + U^e_{pj}) - \delta_{ij}) \\
&\approx \mu(U^e_{ij} + U^e_{ji})
\end{aligned}
$$

Writing $\boldsymbol{H} = grad\boldsymbol{z}$, $\frac{\partial \boldsymbol{T}}{\partial \boldsymbol{H}}$ can then be calculated as

$$
\begin{aligned}
\frac{\partial T_{ij}}{\partial H_{ab}} &= \frac{\partial T_{ij}}{\partial U^e_{pq}} \frac{\partial U^e_{pq}}{\partial H_{ab}} \\
&= \mu(\delta_{ip}\delta_{jq} + \delta_{jp}\delta_{iq})\delta_{pa}\delta_{qb} \\
&= \mu(\delta_{ia}\delta_{jb} + \delta_{ja}\delta_{ib})
\end{aligned}
$$

Appendix C

Uniqueness proof

In this section, we show that using the Least-Squares method to solve for $\boldsymbol{U}^p$ from the constraint $curl\boldsymbol{U}^p = -\boldsymbol{\alpha}$ along with its evolution equation $\dot{\boldsymbol{U}}^p = \boldsymbol{\alpha} \times \boldsymbol{V}$ in one time step has a unique solution. Using the forward Euler method to denote $\dot{\boldsymbol{U}}^p = \frac{\boldsymbol{U}^p - \boldsymbol{U}^{p,t}}{\Delta t}$, the Least-Squares functional is given by (no superscripts denote fields at time $t + \Delta t$)

$$\begin{aligned} J = \frac{P}{2} \int_\Omega (curl\boldsymbol{U}^p + \boldsymbol{\alpha}) : (curl\boldsymbol{U}^p + \boldsymbol{\alpha})\, dV \\ + \frac{1}{2} \int_\Omega \left(\frac{\boldsymbol{U}^p - \boldsymbol{U}^{p,t}}{\Delta t} - \boldsymbol{\alpha}^t \times \boldsymbol{V}^t \right) : \left(\frac{\boldsymbol{U}^p - \boldsymbol{U}^{p,t}}{\Delta t} - \boldsymbol{\alpha}^t \times \boldsymbol{V}^t \right)^2 dV. \end{aligned} \tag{C.1}$$

where P is a constant with dimensions of $length^2 \times time^{-2}$. P is chosen such that the first term of the objective functional (C.1) is much larger than the second. $\boldsymbol{\alpha}^t$ and $\boldsymbol{V}^t$ denote the dislocation density and its velocity at time t. The fields are assumed to be known at time t. The weak form for the functional (C.1) is given as

$$R = \delta J_{|\delta \boldsymbol{U}^p} = 0$$

$$R = P \int_\Omega (curl\boldsymbol{U}^p + \boldsymbol{\alpha}) : curl\delta\boldsymbol{U}^p\, dV + \frac{1}{\Delta t} \int_\Omega \left(\frac{\boldsymbol{U}^p - \boldsymbol{U}^{p,t}}{\Delta t} - \boldsymbol{\alpha}^t \times \boldsymbol{V}^t \right) : \delta\boldsymbol{U}^p\, dV = 0.$$

To get the strong form, we integrate the weak form by parts to get

$$P^* \int_\Omega curl(curl\boldsymbol{U}^p + \boldsymbol{\alpha}) : \delta\boldsymbol{U}^p \, dV + P^* \int_{\partial\Omega} ((curl\boldsymbol{U}^p + \boldsymbol{\alpha}) \times \boldsymbol{n}) : \delta\boldsymbol{U}^p \, dA$$
$$+ \int_\Omega \boldsymbol{U}^p : \delta\boldsymbol{U}^p \, dV - \int_\Omega (\boldsymbol{U}^{p,t} + \Delta t \boldsymbol{\alpha}^t \times \boldsymbol{V}^t) : \delta\boldsymbol{U}^p \, dV = 0,$$

where $P^* = P(\Delta t)^2$. The strong form of the equations is then given by

$$P^* \, curl(curl\boldsymbol{U}^p + \boldsymbol{\alpha}) + \boldsymbol{U}^p = (\boldsymbol{U}^{p,t} + \Delta t \boldsymbol{\alpha}^t \times \boldsymbol{V}^t), \tag{C.2}$$

along with the natural boundary conditions

$$(curl\boldsymbol{U}^p + \boldsymbol{\alpha}) \times \boldsymbol{n} = \boldsymbol{0}. \tag{C.3}$$

We now prove that the system (Eqs. (C.2) and (C.3)) has a unique solution. We assume that $\boldsymbol{U}_1^p$ and $\boldsymbol{U}_2^p$ are two solutions that satisfy the above system. Then the difference $\tilde{\boldsymbol{U}}^p = \boldsymbol{U}_1^p - \boldsymbol{U}_2^p$ satisfies the equations

$$P^* \, curl(curl\tilde{\boldsymbol{U}}^p) + \tilde{\boldsymbol{U}}^p = \boldsymbol{0} \quad \text{on} \quad \Omega \tag{C.4}$$
$$curl\tilde{\boldsymbol{U}}^p \times \boldsymbol{n} = \boldsymbol{0} \quad \text{on} \quad \partial\Omega.$$

Multplying equation (C.4) by $\tilde{\boldsymbol{U}}^p$ and integrating on the domain we get

$$\int_\Omega P^* \, curl(curl\tilde{\boldsymbol{U}}^p) : \tilde{\boldsymbol{U}}^p \, dV + \int_\Omega \tilde{\boldsymbol{U}}^p : \tilde{\boldsymbol{U}}^p \, dV = 0$$
$$\implies P^* \int_\Omega curl\tilde{\boldsymbol{U}}^p : curl\tilde{\boldsymbol{U}}^p \, dV - \int_{\partial\Omega} \underbrace{curl\tilde{\boldsymbol{U}}^p \times \boldsymbol{n}}_{\boldsymbol{0}} \, dA + \int_\Omega \tilde{\boldsymbol{U}}^p : \tilde{\boldsymbol{U}}^p \, dV = 0$$
$$\implies curl\tilde{\boldsymbol{U}}^p = \boldsymbol{0} \text{ and } \tilde{\boldsymbol{U}}^{\mathbf{p}} = \boldsymbol{0}. \qquad \square$$

Bibliography

[AB96] A. Acharya and J. L. Bassani. On non-local flow theories that preserve the classical structure of incremental boundary value problems. In *IUTAM Symposium on Micromechanics of Plasticity and Damage of Multiphase Materials*, pages 3–9. Springer, 1996.

[AB00a] A. Acharya and J. L. Bassani. Lattice incompatibility and a gradient theory of crystal plasticity. *Journal of the Mechanics and Physics of Solids*, 48(8):1565–1595, 2000.

[AB00b] A. Acharya and A. J. Beaudoin. Grain-size effect in viscoplastic polycrystals at moderate strains. *Journal of Mechanics and Physics of Solids*, 48(10):2213–2230, 2000.

[ABB03] A. Acharya, J. L. Bassani, and A. Beaudoin. Geometrically necessary dislocations, hardening, and a simple gradient theory of crystal plasticity. *Scripta Materialia*, 48(2):167–172, 2003.

[ABD+17] D. Arndt, W. Bangerth, D. Davydov, T. Heister, L. Heltai, M. Kronbichler, M. Maier, J-P. Pelteret, B. Turcksin, and D. Wells. The `deal.II` library, version 8.5. *Journal of Numerical Mathematics*, 2017.

[AC12] A. Acharya and S. J. Chapman. Elementary observations on the averaging of dislocation mechanics: dislocation origin of aspects of anisotropic yield and plastic spin. *Procedia IUTAM*, 3:301–313, 2012.

[Ach01] A. Acharya. A model of crystal plasticity based on the theory of continuously distributed dislocations. *Journal of Mechanics and Physics of Solids*, 49(4):761–784, 2001.

[Ach03] A. Acharya. Driving forces and boundary conditions in continuum dislocation mechanics. *Proceedings of the Royal Society of London A: Mathematical, Physical and Engineering Sciences*, 459(2034):1343–1363, 2003.

[Ach04] A. Acharya. Constitutive analysis of finite deformation field dislocation mechanics. *Journal of Mechanics and Physics of Solids*, 52(2):301–316, 2004.

[Ach07] A. Acharya. Jump condition for gnd evolution as a constraint on slip transmission at grain boundaries. *Philosophical magazine*, 87(8-9):1349–1359, 2007.

[Ach08] A. Acharya. A counterpoint to cermelli and gurtins criteria for choosing the correctgeometric dislocation tensor in finite plasticity. In *IUTAM Symposium on theoretical, computational and modelling aspects of inelastic media*, pages 99–105. Springer, 2008.

[Ach11] A. Acharya. Microcanonical entropy and mesoscale dislocation mechanics and plasticity. *Journal of Elasticity*, 104(1-2):23–44, 2011.

[Ach18] A. Acharya. Stress of a spatially uniform dislocation density field. *Journal of Elasticity*, pages 1–5, 2018.

[ADKL01] P. R. Amestoy, I. S. Duff, J. Koster, and J.-Y. L'Excellent. A fully asynchronous multifrontal solver using distributed dynamic scheduling. *SIAM Journal on Matrix Analysis and Applications*, 23(1):15–41, 2001.

[Ang17] J. Angulo. Convolution in (max, min)-algebra and its role in mathematical morphology. In *Advances in Imaging and Electron Physics*, volume 203, pages 1–66. Elsevier, 2017.

[AO03] S. Aubry and M. Ortiz. The mechanics of deformation–induced subgrain–dislocation structures in metallic crystals at large strains. *Proceedings of the Royal Society of London A: Mathematical, Physical and Engineering Sciences*, 459(2040):3131–3158, 2003.

[APBB04] A. Arsenlis, D. M. Parks, R. Becker, and V. V. Bulatov. On the evolution of crystallographic dislocation density in non-homogeneously deforming crystals. *Journal of the Mechanics and Physics of Solids*, 52(6):1213–1246, 2004.

[AR77] R. J. Asaro and J. R. Rice. Strain localization in ductile single crystals. *Journal of Mechanics and Physics of Solids*, 25(5):309–338, 1977.

[AR06] A. Acharya and A. Roy. Size effects and idealized dislocation microstructure at small scales: Predictions of a Phenomenological model of Mesoscopic Field Dislocation Mechanics: Part I. *Journal of Mechanics and Physics of Solids*, 54(8):1687–1710, 2006.

[AS95] A. Acharya and T. G. Shawki. Thermodynamic restrictions on constitutive equations for second-deformation-gradient inelastic behavior. *Journal of the Mechanics and Physics of Solids*, 43(11):1751–1772, 1995.

[Asa83] R. J. Asaro. Micromechanics of crystals and polycrystals. In *Advances in Applied Mechanics*, volume 23, pages 1–115. Elsevier, 1983.

[Ash70] M.F. Ashby. The deformation of plastically non-homogeneous materials. *Philosophical Magazine*, 21(170):399–424, 1970.

[AT11] A. Acharya and L. Tartar. On an equation from the theory of field dislocation mechanics. *Bulletin of the Italian Mathematical Union*, 9:409–444, 2011.

[ATSB04] A. Acharya, H. Tang, S. Saigal, and J. L. Bassani. On boundary conditions and

plastic strain-gradient discontinuity in lower-order gradient plasticity. *Journal of the Mechanics and Physics of Solids*, 52(8):1793–1826, 2004.

[AZ15] A. Acharya and X. Zhang. From dislocation motion to an additive velocity gradient decomposition, and some simple models of dislocation dynamics. *Chinese Annals of Mathematics, Series B*, 36(5):645–658, 2015.

[BAA+17] S. Balay, S. Abhyankar, M. F. Adams, J. Brown, P. Brune, K. Buschelman, L. Dalcin, V. Eijkhout, W. D. Gropp, D. Kaushik, M.G. Knepley, D. A. May, L. C. McInnes, K. Rupp, B. F. Smith, S. Zampini, H. Zhang, and H. Zhang. PETSc Web page http://www.mcs.anl.gov/petsc, 2017.

[Bab97] M. Babic. Average balance equations for granular materials. *International Journal of Engineering Science*, 35(5):523–548, 1997.

[BAC+00] A. J. Beaudoin, A. Acharya, S. R. Chen, D. A. Korzekwa, and M. G. Stout. Consideration of grain-size effect and kinetics in the plastic deformation of metal polycrystals. *Acta Materialia*, 48(13):3409–3423, 2000.

[Bas93] J. L. Bassani. Plastic flow of crystals. In *Advances in Applied Mechanics*, volume 30, pages 191–258. Elsevier, 1993.

[Bas01] J. L. Bassani. Incompatibility and a simple gradient theory of plasticity. *Journal of the Mechanics and Physics of Solids*, 49(9):1983–1996, 2001.

[BB66] S. J. Basinski and Z. S. Basinski. The nature of the cold worked state. In *Recrystalization, Grain Growth, and Textures, papers presented at a seminar of the American Society for Metals, Metals Park, Ohio, USA*, 1966.

[BBS55] B. A. Bilby, R. Bullough, and E. Smith. Continuous distributions of dislocations: a new application of the methods of non-riemannian geometry. *Proceed-*

ings of the Royal Society of London A: Mathematical, Physical and Engineering Sciences, 231(1185):263–273, 1955.

[BNVdG01] J. L. Bassani, A. Needleman, and E. Van der Giessen. Plastic flow in a composite: a comparison of nonlocal continuum and discrete dislocation predictions. *International Journal of Solids and Structures*, 38(5):833–853, 2001.

[BWG11] C. Burstedde, L. C. Wilcox, and O. Ghattas. `p4est`: Scalable algorithms for parallel adaptive mesh refinement on forests of octrees. *SIAM Journal on Scientific Computing*, 33(3):1103–1133, 2011.

[Cah51] R. W. Cahn. Slip and polygonization in aluminium. *Journal of the Institute of Metals*, 79:129–158, 1951.

[CCPS10] Y. S. Chen, W. Choi, S. Papanikolaou, and J. P. Sethna. Bending crystals: emergence of fractal dislocation structures. *Physical Review Letters*, 105(10):105501, 2010.

[CG01] P. Cermelli and M. E. Gurtin. On the characterization of geometrically necessary dislocations in finite plasticity. *Journal of the Mechanics and Physics of Solids*, 49(7):1539–1568, 2001.

[CHB09] J. A. Cottrell, T. J. R. Hughes, and Y. Bazilevs. *Isogeometric analysis: toward integration of CAD and FEA*. John Wiley & Sons, 2009.

[DAS16] A. Das, A. Acharya, and P. Suquet. Microstructure in plasticity without nonconvexity. *Computational Mechanics*, 57(3):387–403, 2016.

[Den04] C. Denoual. Dynamic dislocation modeling by combining peierls nabarro and galerkin methods. *Physical Review B*, 70(2):024106, 2004.

[Den07] C. Denoual. Modeling dislocation by coupling peierls–nabarro and element-free

galerkin methods. *Computer Methods in Applied Mechanics and Engineering*, 196(13-16):1915–1923, 2007.

[DNVdG03] V. S. Deshpande, A. Needleman, and E. Van der Giessen. Finite strain discrete dislocation plasticity. *Journal of the Mechanics and Physics of Solids*, 51(11-12):2057–2083, 2003.

[EA66] R. Ebeling and M. F. Ashby. Dispersion hardening of copper single crystals. *Philosophical Magazine*, 13(124):805–834, 1966.

[EM84] Y. Estrin and H. Mecking. A unified phenomenological description of work hardening and creep based on one-parameter models. *Acta Metallurgica*, 32(1):57–70, 1984.

[Esh56] J. D. Eshelby. The continuum theory of lattice defects. *Solid state physics*, 3:79–144, 1956.

[FH01] N. A. Fleck and J. W. Hutchinson. A reformulation of strain gradient plasticity. *Journal of the Mechanics and Physics of Solids*, 49(10):2245–2271, 2001.

[FKMT17] U. S. Fjordholm, R. Käppeli, S. Mishra, and E. Tadmor. Construction of approximate entropy measure-valued solutions for hyperbolic systems of conservation laws. *Foundations of Computational Mathematics*, 17(3):763–827, 2017.

[FLM17] U. S. Fjordholm, S. Lanthaler, and S. Mishra. Statistical solutions of hyperbolic conservation laws: Foundations. *Archive for Rational Mechanics and Analysis*, 226(2):809–849, 2017.

[FMAH94] N. A. Fleck, G. M. Muller, M. F. Ashby, and J. W. Hutchinson. Strain gradient plasticity: Theory and experiment. *Acta Metallurgica et Materialia*, 42(2):475–487, 1994.

[Fox66] N. Fox. A continuum theory of dislocations for single crystals. *IMA Journal of Applied Mathematics*, 2(4):285–298, 1966.

[GB99] I. Groma and P. Balogh. Investigation of dislocation pattern formation in a two-dimensional self-consistent field approximation. *Acta Materialia*, 47(13):3647–3654, 1999.

[GBB06] M. G. D. Geers, W. A. M. Brekelmans, and C. J. Bayley. Second-order crystal plasticity: internal stress effects and cyclic loading. *Modelling and Simulation in Materials Science and Engineering*, 15(1):S133, 2006.

[GR14] M. E. Gurtin and B. D. Reddy. Gradient single-crystal plasticity within a mises–hill framework based on a new formulation of self-and latent-hardening. *Journal of the Mechanics and Physics of Solids*, 68:134–160, 2014.

[Gro97] I. Groma. Link between the microscopic and mesoscopic length-scale description of the collective behavior of dislocations. *Physical Review B*, 56(10):5807, 1997.

[Gur02] M. E. Gurtin. A gradient theory of single-crystal viscoplasticity that accounts for geometrically necessary dislocations. *Journal of the Mechanics and Physics of Solids*, 50(1):5–32, 2002.

[Gur08] M. E. Gurtin. A finite-deformation, gradient theory of single-crystal plasticity with free energy dependent on densities of geometrically necessary dislocations. *International Journal of Plasticity*, 24(4):702–725, 2008.

[HCB05] T. J. R. Hughes, J. A. Cottrell, and Y. Bazilevs. Isogeometric analysis: Cad, finite elements, nurbs, exact geometry and mesh refinement. *Computer methods in applied mechanics and engineering*, 194(39-41):4135–4195, 2005.

[HFH89] T. J. R. Hughes, L. P. Franca, and G. M. Hulbert. A new finite element formulation for computational fluid dynamics: VIII. the Galerkin/Least-Squares

method for advective-diffusive equations. *Computer Methods in Applied Mechanics and Engineering*, 73(2):173–189, 1989.

[HH95] N. Hansen and D. A. Hughes. Analysis of large dislocation populations in deformed metals. *physica status solidi (a)*, 149(1):155–172, 1995.

[HH00] D. A. Hughes and N. Hansen. Microstructure and strength of nickel at large strains. *Acta Materialia*, 48(11):2985–3004, 2000.

[HH12] F. J. Humphreys and M. Hatherly. *Recrystallization and related annealing phenomena*. Elsevier, 2012.

[HHOT93] A. K. Head, S. D. Howison, J. R. Ockendon, and S. P. Tighe. An equilibrium theory of dislocation continua. *SIAM review*, 35(4):580–609, 1993.

[Hil58] R. Hill. A general theory of uniqueness and stability in elastic-plastic solids. *Journal of the Mechanics and Physics of Solids*, 6(3):236–249, 1958.

[HL82] J. P. Hirth and J. Lothe. Theory of dislocations. 1982.

[Hoc16] T. Hochrainer. Thermodynamically consistent continuum dislocation dynamics. *Journal of the Mechanics and Physics of Solids*, 88:12–22, 2016.

[Hun07] J. D. Hunter. Matplotlib: A 2d graphics environment. *Computing In Science & Engineering*, 9(3):90–95, 2007.

[HZG07] T. Hochrainer, M. Zaiser, and P. Gumbsch. A three-dimensional continuum theory of dislocation systems: kinematics and mean-field formulation. *Philosophical Magazine*, 87(8-9):1261–1282, 2007.

[IRD15] N. Irani, J. J. C. Remmers, and V. S. Deshpande. Finite strain discrete dislocation plasticity in a total Lagrangian setting. *Journal of the Mechanics and Physics of Solids*, 83:160–178, 2015.

[IRG15] M. Iyer, B. Radhakrishnan, and V. Gavini. Electronic-structure study of an edge dislocation in aluminum and the role of macroscopic deformations on its energetics. *Journal of the Mechanics and Physics of Solids*, 76:260–275, 2015.

[Jeu13] D. Jeulin. Analysis and modeling of 3d microstructures. *Mathematical Morphology: From Theory to Applications*, pages 421–444, 2013.

[Jia13] B. Jiang. *The Least-Squares Finite Element Method: Theory and applications in computational fluid dynamics and electromagnetics*. Springer Science & Business Media, 2013.

[JOP+] E. Jones, T. E. Oliphant, P. Peterson, et al. SciPy: Open source scientific tools for Python, 2001–. [Online; accessed ¡today¿].

[JW84] N. Y. Jin and A. T. Winter. Dislocation structures in cyclically deformed [001] copper crystals. *Acta Metallurgica*, 32(8):1173–1176, 1984.

[KN63] A. Kelly and R. B. Nicholson. Precipitation hardening. *Progress in Materials Science*, 10:151 – 391, 1963.

[Krö81] E. Kröner. Continuum theory of defects. In R. Balian, M. Kléman, and J.-P. Poirier, editors, *Physics of Defects, Les Houches Summer School Proceedings*, volume 35, pages 217–315. North-Holland, Amsterdam, 1981.

[KT08] M. Kuroda and V. Tvergaard. A finite deformation theory of higher-order gradient crystal plasticity. *Journal of the Mechanics and Physics of Solids*, 56(8):2573–2584, 2008.

[LHT+12] D. Liu, Y. He, X. Tang, H. Ding, P. Hu, and P. Cao. Size effects in the torsion of microscale copper wires: Experiment and analysis. *Scripta Materialia*, 66(6):406–409, 2012.

[LLR+02] S. Li, W. K. Liu, A. J. Rosakis, T. Belytschko, and W. Hao. Mesh-free galerkin simulations of dynamic shear band propagation and failure mode transition. *International Journal of solids and structures*, 39(5):1213–1240, 2002.

[LS06] S. Limkumnerd and J. P. Sethna. Mesoscale theory of grains and cells: crystal plasticity and coarsening. *Physical Review Letters*, 96(9):095503, 2006.

[M+10] W. McKinney et al. Data structures for statistical computing in python. In *Proceedings of the 9th Python in Science Conference*, volume 445, pages 51–56. Austin, TX, 2010.

[MAH79] H. Mughrabi, F. U. Ackermann, and K. Herz. Persistent slipbands in fatigued face-centered and body-centered cubic metals. In *Fatigue mechanisms*. ASTM International, 1979.

[MC95] Q. Ma and D. R. Clarke. Size dependent hardness of silver single crystals. *Journal of Materials Research*, 10(4):853–863, 1995.

[McK11] W. McKinney. pandas: a foundational python library for data analysis and statistics. *Python for High Performance and Scientific Computing*, pages 1–9, 2011.

[MHS81] H. Mughrabi, K. Herz, and X. Stark. Cyclic deformation and fatigue behaviour of α-iron mono-and polycrystals. *International Journal of fracture*, 17(2):193–220, 1981.

[MK81] H. Mecking and U. F. Kocks. Kinetics of flow and strain-hardening. *Acta Metallurgica*, 29(11):1865–1875, 1981.

[MLL07] S. N. Medyanik, W. K. Liu, and S. Li. On criteria for dynamic adiabatic shear band propagation. *Journal of the Mechanics and Physics of Solids*, 55(7):1439–1461, 2007.

[MR75] R. M. McMeeking and J. R. Rice. Finite-element formulations for problems of large elastic-plastic deformation. *International Journal of Solids and Structures*, 11(5):601–616, 1975.

[MSZ15] S. Muller, L. Scardia, and I. C. Zeppieri. Gradient theory for geometrically nonlinear plasticity via the homogenization of dislocations. *Analysis and Computation of Microstructure in Finite Plasticity*, 78:766–778, 2015.

[Mur63] T. Mura. Continuous distribution of moving dislocations. *Philosophical Magazine*, 8(89):843–857, 1963.

[Mur89] T. Mura. Impotent dislocation walls. *Materials Science and Engineering: A*, 113:149–152, 1989.

[MW76] H. Mughrabi and C. Wüthrich. Asymmetry of slip and shape changes during cyclic deformation of α-iron single crystals. *Philosophical Magazine*, 33(6):963–984, 1976.

[Nab67] F. R. N. Nabarro. Theory of crystal dislocations. 1967.

[NALP85] A. Needleman, R. J. Asaro, J. Lemonds, and D. Peirce. Finite element analysis of crystalline solids. *Computer Methods in Applied Mechanics and Engineering*, 52(1-3):689–708, 1985.

[NH03] C. F. Niordson and J. W. Hutchinson. Non-uniform plastic deformation of micron scale objects. *International journal for numerical methods in engineering*, 56(7):961–975, 2003.

[NLRS15] N. A. Nystrom, M. J. Levine, R. Z. Roskies, and J. R. Scott. Bridges: A uniquely flexible hpc resource for new communities and data analytics. In *Proceedings of the 2015 XSEDE Conference: Scientific Advancements Enabled*

by Enhanced Cyberinfrastructure, XSEDE '15, pages 30:1–30:8, New York, NY, USA, 2015. ACM.

[NPR74] J. C. Nagtegaal, D. M. Parks, and J. R. Rice. On numerically accurate finite element solutions in the fully plastic range. *Computer methods in applied mechanics and engineering*, 4(2):153–177, 1974.

[NR04] C. F. Niordson and P. Redanz. Size-effects in plane strain sheet-necking. *Journal of the Mechanics and Physics of Solids*, 52(11):2431–2454, 2004.

[NT05] C. F Niordson and V. Tvergaard. Instabilities in power law gradient hardening materials. *International Journal of Solids and Structures*, 42(9-10):2559–2573, 2005.

[Nye53] J. F. Nye. Some geometrical relations in dislocated crystals. *Acta Metallurgica*, 1(2):153–162, 1953.

[Oli] T. E. Oliphant. NumPy: A guide to NumPy. USA: Trelgol Publishing, 2006–. [Online; accessed ¡today¿].

[OR99] M. Ortiz and E. A. Repetto. Nonconvex energy minimization and dislocation structures in ductile single crystals. *Journal of the Mechanics and Physics of Solids*, 47(2):397–462, 1999.

[PAN82] D. Peirce, R. J. Asaro, and A. Needleman. An analysis of nonuniform and localized deformation in ductile single crystals. *Acta metallurgica*, 30(6):1087–1119, 1982.

[PAN83] D. Peirce, R. J. Asaro, and A. Needleman. Material rate dependence and localized deformation in crystalline solids. *Acta Metallurgica*, 31(12):1951–1976, 1983.

[PAR11] S. Puri, A. Acharya, and A. D. Rollett. Controlling plastic flow across grain boundaries in a continuum model. *Metallurgical and Materials Transactions A*, 42(3):669–675, 2011.

[PCC55] G. R. Piercy, R. W. Cahn, and A. H. Cottrell. A study of primary and conjugate slip in crystals of alpha-brass. *Acta Metallurgica*, 3(4):331–338, 1955.

[PDA11] S. Puri, A. Das, and A. Acharya. Mechanical response of multicrystalline thin films in mesoscale field dislocation mechanics. *Journal of the Mechanics and Physics of Solids*, 59(11):2400–2417, 2011.

[Pei83] D. Peirce. Shear band bifurcations in ductile single crystals. *Journal of the Mechanics and Physics of Solids*, 31(2):133–153, 1983.

[Pur09] S. Puri. *Modeling dislocation sources and plastic flow through grain boundaries in mesoscopic field dislocation mechanics*. PhD thesis, Carnegie Mellon University, 2009.

[RA70] K. G. Russell and M. F. Ashby. Slip in aluminum crystals containing strong, plate-like particles. *Acta Metallurgica*, 18(8):891–901, 1970.

[RA05] A. Roy and A. Acharya. Finite element approximation of field dislocation mechanics. *Journal of the Mechanics and Physics of Solids*, 53(1):143–170, 2005.

[RA06] A. Roy and A. Acharya. Size effects and idealized dislocation microstructure at small scales: predictions of a phenomenological model of mesoscopic field dislocation mechanics: Part II. *Journal of the Mechanics and Physics of Solids*, 54(8):1711–1743, 2006.

[Ree06] R. C. Reed. *The Superalloys: Fundamentals and Applications*. Cambridge University Press, 2006.

[RLV08] D. Rittel, P. Landau, and A. Venkert. Dynamic recrystallization as a potential cause for adiabatic shear failure. *Physical review letters*, 101(16):165501, 2008.

[RVdVG14] S. Rudraraju, A. Van der Ven, and K. Garikipati. Three-dimensional isogeometric solutions to general boundary value problems of toupins gradient elasticity theory at finite strains. *Computer Methods in Applied Mechanics and Engineering*, 278:705–728, 2014.

[RWF11] T. Richeton, G. F. Wang, and C. Fressengeas. Continuity constraints at interfaces and their consequences on the work hardening of metal–matrix composites. *Journal of the Mechanics and Physics of Solids*, 59(10):2023–2043, 2011.

[SE98] J. S. Stölken and A. G. Evans. A microbend test method for measuring the plasticity length scale. *Acta Materialia*, 46(14):5109–5115, 1998.

[SWBM93] N. A. Stelmashenko, M. G. Walls, L. M. Brown, and Y. V. Milman. Microindentations on W and Mo oriented single crystals: an STM study. *Acta Metallurgica et Materialia*, 41(10):2855–2865, 1993.

[SZ15] S. Sandfeld and M. Zaiser. Pattern formation in a minimal model of continuum dislocation plasticity. *Modelling and Simulation in Materials Science and Engineering*, 23(6):065005, 2015.

[TCD+14] J. Towns, T. Cockerill, M. Dahan, I. Foster, K. Gaither, A. Grimshaw, V. Hazlewood, S. Lathrop, D. Lifka, G. D. Peterson, R. Roskies, J. R. Scott, and N. Wilkins-Diehr. XSEDE: Accelerating scientific discovery. *Computing in Science & Engineering*, 16(5):62–74, Sept.-Oct. 2014.

[TCDH95] M. C. Theyssier, B. Chenal, J. H. Driver, and N. Hansen. Mosaic dislocation structures in aluminium crystals deformed in multiple slip at 0.5 to 0.8 T_M. *Physica Status Solidi (a)*, 149(1):367–378, 1995.

[Tou62] R. A. Toupin. Elastic materials with couple-stresses. *Archive for Rational Mechanics and Analysis*, 11(1):385–414, 1962.

[TR60] R. A. Toupin and R. S. Rivlin. Dimensional changes in crystals caused by dislocations. *Journal of Mathematical Physics*, 1(1):8–15, 1960.

[VBAF06] S. N. Varadhan, A. J. Beaudoin, A. Acharya, and C. Fressengeas. Dislocation transport using an explicit galerkin/least-squares formulation. *Modelling and Simulation in Materials Science and Engineering*, 14(7):1245, 2006.

[W+18] M. Waskom et al. mwaskom/seaborn: v0.9.0 (july 2018), July 2018.

[Wil67] J. R. Willis. Second-order effects of dislocations in anisotropic crystals. *International Journal of Engineering Science*, 5(2):171–190, 1967.

[WVM+18] Y. M. Wang, T. Voisin, J. T. McKeown, J. Ye, N. P. Calta, Z. Li, Z. Zeng, Y. Zhang, W. Chen, T. T. Roehling, et al. Additively manufactured hierarchical stainless steels with high strength and ductility. *Nature materials*, 17(1):63, 2018.

[XEA15] S. Xia and A. El-Azab. Computational modelling of mesoscale dislocation patterning and plastic deformation of single crystals. *Modelling and Simulation in Materials Science and Engineering*, 23(5):055009, 2015.

[YG12] A. Yavari and A. Goriely. Riemann–cartan geometry of nonlinear dislocation mechanics. *Archive for Rational Mechanics and Analysis*, 205(1):59–118, 2012.

[YGVdG04] S. Yefimov, I. Groma, and E. Van der Giessen. A comparison of a statistical-mechanics based plasticity model with discrete dislocation plasticity calculations. *Journal of the Mechanics and Physics of Solids*, 52(2):279–300, 2004.

[YVdGG04] S. Yefimov, E. Van der Giessen, and I. Groma. Bending of a single crystal:

discrete dislocation and nonlocal crystal plasticity simulations. *Modelling and Simulation in Materials Science and Engineering*, 12(6):1069, 2004.

[ZA18] C. Zhang and A. Acharya. On the relevance of generalized disclinations in defect mechanics. *Journal of the Mechanics and Physics of Solids*, 119:188–223, 2018.

[ZAP18] C. Zhang, A. Acharya, and S. Puri. Finite element approximation of the fields of bulk and interfacial line defects. *Journal of the Mechanics and Physics of Solids*, 114:258–302, 2018.

[ZAWB15] X. Zhang, A. Acharya, N. J. Walkington, and J. Bielak. A single theory for some quasi-static, supersonic, atomic, and tectonic scale applications of dislocations. *Journal of the Mechanics and Physics of Solids*, 84:145–195, 2015.

[Zen42] C. Zener. Theory of lattice expansion introduced by cold work. *Transactions Of The American Institute Of Mining And Metallurgical Engineers*, 147, 1942.

[Zha15] X. Zhang. *Field Dislocation Mechanics with applications in atomic, mesoscopic and tectonic scale problems.* PhD thesis, Carnegie Mellon University, Pittsburgh, 2015.

[ZRR96] M. Zhou, G. Ravichandran, and A. J. Rosakis. Dynamically propagating shear bands in impact-loaded prenotched plates–ii. numerical simulations. *Journal of the Mechanics and Physics of Solids*, 44(6):1007–1032, 1996.